UNIVERSITY OF Southampton

University of Southampton Research Repository
ePrints Soton

http://eprints.soton.ac.uk

University of Southampton

Faculty of Engineering, Science and Mathematics

School of Electronics and Computer Science

A Deep Sea Lab On a Chip Chemical Sensor

By Alan Taberham

Doctor of Philosophy

May 2010

ABSTRACT

UNIVERSITY OF SOUTHAMPTON

FACULTY OF ENGINEERING, SCIENCE AND MATHEMATICS
SCHOOL OF ELECTRONICS AND COMPUTER SCIENCE

<u>Doctor of Philosophy</u>

A DEEP SEA LAB ON A CHIP CHEMICAL SENSOR
by Alan Taberham

The measurement of chemical concentrations within the oceans is crucial for our understanding of its biogeochemical processes. Such data is vital for; studies of climate and environment change; natural resource management; assessment of pollution, human impact and biodiversity. Current measurement methods (sampling and large *in situ* instrumentation) cannot provide the quantity and quality of biogeochemical data that is required. The factors limiting the widespread collection of quality data include, sample degradation/contamination, instrument size, cost and insufficient sensitivity.

New technologies allow the manufacture of Lab On a Chip (L.O.C.) devices that can be used as small, low-cost and low power sensors. There are numerous demonstrations of these devices in the laboratory where it is possible to use standard bench top equipment to operate them. Within the National Oceanography Centre Southampton and the Nanoscale System Integration Research Group at Southampton University it has been proposed that integrated L.O.C. devices could be used autonomously and remotely in the marine environment. These innovative micro-devices could provide *in situ* real time synoptic data on processes with temporal and spatial scales smaller than currently sampled. This report details the development, laboratory testing and field trial of the world's first deep sea *in situ* L.O.C. chemical sensor. Preparatory work for the design of the next generation of marine L.O.C. devices including low-cost fabrication in fluoropolymer materials (which are naturally robust and chemically resistant) is also presented.

The L.O.C. devices within this study use a reagent based colorimetric protocol to determine the concentration of a chemical within a sea-water sample. The optical absorption when the reagent is mixed with a sample is proportional to the chemical concentration and is measured using a double beam spectrophotometer. This method can be used in the metrology of a number of

chemical species including nutrients and pollutants and therefore this technology is generic. The detection of nitrite and nitrate at a wavelength of 540nm is used as a proof of concept within this report. Nitrite samples are combined with α-napthylamine and sulphanilamide to form a coloured dye. The absorption of the dye is proportional to the nitrite concentration. Nitrate is reduced to nitrite using a cadmium column and then measured in same manner. The L.O.C. devices are fabricated using negative photolithography on photosensitive epoxy resin. Micro channels measuring 500 by 500μm are used to create micromixers, optical detection paths and fluid delivery ports on a device with a footprint of 45 by 45mm. The absorption is measured with low powered portable electronics, a modulated light emitting diode source and photodiode detector both coupled to polymer fibres. The mixer uses a three dimensional split and recombine technique to ensure effective mixing of the chemicals and sample.

On the laboratory bench the sensor was capable of continuously sampling nitrite concentration levels in sea-water at **60μl/min** with a limit of detection of **47.6nM** and a precision of 89.3nM at 15μM. Once reconfigured it was capable of detecting nitrate in seawater, at the same flow rates with a limit of detection of **1.75μM** and a precision of 9.26μM at 100μM. An *in situ* version of the sensor, packaged within a pressure compensated housing measuring Ø120mm by 300mm, was deployed in the mid-Atlantic. It provided key functionality and construction methodologies for future generation devices. These trials also identified the developments necessary for the sensor to work as efficiently at depths of 1500m as on the laboratory bench.

TABLE OF CONTENTS

LIST OF FIGURES

LIST OF TABLES

DECLARATION OF AUTHORSHIP

I, Alan Taberham, declare that the thesis entitled 'A Deep Sea Lab On a Chip Sensor' and the work presented in it are my own. I confirm that:

- this work was done wholly or mainly while in candidature for a research degree at this University;

- where any part of this thesis has previously been submitted for a degree or any other qualification at this University or any other institution, this has been clearly stated;

- where I have consulted the published work of others, this is always clearly attributed;

- where I have quoted from the work of others, the source is always given. With the exception of such quotations, this thesis is entirely my own work;

- I have acknowledged all main sources of help;

- where the thesis is based on work done by myself jointly with others, I have made clear exactly what was done by others and what I have contributed myself;

- parts of this work have been published as:

Taberham, A., Kraft, M., Mowlem, M. and Morgan, H. (2008) Fabrication of Lab-on-Chip devices from Fluoropolymers. *J Micromech. Microeng.*

Taberham, A., Mowlem, M., Kraft, M. and Morgan, H. (2007) Fabrication of Lab on Chip devices from fluoropolymers. In: *Proc. Micromechanics Europe*, September 2007, Guimaraes, Portugal.

Signed: *Alan Taberham*

Date: *May 2010*

ACKNOWLEDGEMENTS

- Strenuis Ardua Cedunt -

ACROYMNS

Term	Acronym
Alternating current	A.C.
Arbitrary fluorescence units	A.F.U.
Array for real-time geostrophic oceanography	A.R.G.O.
Atlantic network of interdisciplinary moorings and time-series for Europe	A.N.I.M.A.T.E.
Autonomous profiling explorer	A.P.E.X.
Autonomous underwater vehicle	A.U.V.
Avalanche photodiode	A.P.D.
Biological micro electro-mechanical systems	Bio.M.E.M.S.
Bio-luminescence	B.L.
Capillary electrophoresis	C.E.
Charge coupled device	C.C.D.
Chemi-luminescence	C.L.
Compact disc	C.D.
Complementary metal oxide semiconductor	C.M.O.S.
Computational fluid dynamics	C.F.D.
Conductivity, temperature and depth	C.T.D.
Configurable chemical analyser	C.C.A.
Cyclic olefin copolymer	C.O.C.
Decimal points	D.P.
Deep reactive ion etching	D.R.I.E
Degrees Celsius	^{o}C
Deoxyribonucleic acid	D.N.A.
Digital to analogue convertor	D.A.C.
Direct current	D.C.
Dissolved organic nitrogen	D.O.N.
Dissolved oxygen	D.O.
Dots per inch	D.P.I.
Electromagnetic	E.M.
Electron beam lithography	E.B.L.
Electro-osmotic flow	E.O.F.
Fluorescein isothiocyanate	F.I.T.C.
Fluorinated Ethylene Propylene	F.E.P.
Fluoroethylene propylene	F.E.P.
Glass transition temperature	T_g
Global climate observing system	G.C.O.S
Global ocean observing system	G.O.O.S.
Graphical user interface	G.U.I.
Harmful algae blooms	H.A.B's
Hydrofluoric acid	H.F.
Instrument detection limit	I.D.L.
Integrated circuit	I.C.
Internal diameter	I.D.
International union of pure and applied chemistry	I.U.P.A.C.
Lab On a Chip	L.O.C.
Laser induced breakdown spectroscopy	L.I.B.S.
Laser spark spectroscopy	L.A.S.S.
Light amplification by stimulated emission of radiation	L.A.S.E.R.

Term	Acronym
Light emitting diode	L.E.D.
Liquid core waveguide	L.C.W.
Liquid waveguide capillary cell	L.W.C.C.
Lithography, electroplating and moulding	L.I.G.A.
Mean time to failure	M.T.T.F.
Method detection limit	M.D.L.
Methyl ether ketone peroxide	M.E.K.P.
Micro electromechanical systems	M.E.M.S.
Micro laser induced fluorescence	μ.L.I.F.
Micro particle image velocimetry	μ.P.I.V.
Micro systems technology	M.S.T.
Micro total analytical systems	μ.T.A.S.
MicroMolar	μM
MilliQ	M.Q.
N-(1-naphthyl) ethylenediamine	N.E.D.
NanoMolar	nM
National environment research council	N.E.R.C.
Near infra-red	N.I.R.
Orthophthaldialdehyde	O.P.A.
Outside diameter	O.D.
Particulate organic nitrogen	P.O.N.
Photo multiplier tube	P.M.T.
Polycarbonate	P.C.
Polychloro-trifluoroethylene	P.C.T.F.E.
Polydimethylsiloxane	P.D.M.S.
Polymerase chain reaction	P.C.R.
Polymethylmethacrylate	P.M.M.A.
Polytetrafluoroethylene	P.T.F.E.
Polytetrafluoroethylene	P.T.F.E.
Power supply unit	P.S.U.
Printed circuit board	P.C.B.
Profiling autonomous lagrangian circulation explorer	P.A.L.A.C.E
Radio frequency	R.F.
Reactive ion etching	R.I.E.
Refractive index	R.I.
Relative fluorescence units	R.F.U.
Reverse flow injection analysis	r.F.I.A.
Reverse transcription polymerase chain reaction	R.T.-P.C.R.
Revolutions per minute	R.P.M.
Scanning probe imaging processor	S.P.I.P.
Segmented flow analysis	S.F.A.
Spectral analysis system	S.E.A.S.
Split and recombine	S.A.R.
Sub miniature version A	S.M.A.
Tagged image file format	T.I.F.F.
Texas advanced optoelectronic solutions	T.A.O.S.
Three dimensions	3D
Total internal reflection	T.I.R.
Two dimensions	2D
Ultra-violet	U.V.

1. INTRODUCTION

1.1 Objectives and outcomes of the PhD study

The purpose of this doctoral study was to develop *in situ* Lab On a Chip (L.O.C.) chemical sensor technologies for the detection of nitrite and nitrate in seawater. It did not include the development of pumping or flow control technologies for these microfluidic systems. The innovative L.O.C. technologies in this study are a precursor to the fabrication of a fully integrated, miniaturised sensor that could be used to detect a wide range of chemicals including; nitrite; nitrate; ammonium; silicate; phosphate; manganese and iron. The sensor needed to combine microfluidic principles and differential optical spectroscopy to facilitate the detection of these chemicals within a small footprint. To maximise the number of deployment scenarios and scientific impact it needed to be fabricated from rugged, low cost materials and be able to operate at ocean depths. Measurement of the effectiveness of the sensor was to be provided by logging performance characteristics in both laboratory and *in situ* settings.

The outcome of this study is that a L.O.C. sensor has been constructed and successfully used to determine the concentration of nitrite and nitrate in seawater within the laboratory and during sea trials. The study has achieved its low cost aims with direct material costs for the microfluidic and optical detection systems of fifty pounds. Production of the microfluidics in a novel low-cost, mechanically strong, chemical resistant and shock resistant all polymer construct has also been achieved.

1.2 Novelty and Contribution

The L.O.C. sensors presented in this study provide an important framework and understanding for the further integration of ancillary components by identifying previously unknown performance dependencies for the deployment of L.O.C. devices in the ocean. Other novel aspects of the research presented are:

- The development of a high performance integrated L.O.C. for nitrite and nitrate metrology in seawater. The L.O.C. chemical sensor combined three dimensional micro-mixers, two optical detection paths and fluidic ports for external connections. Along with low power light emitting diodes and photodiode detectors it was capable of detecting nanomolar concentrations of nitrite and nitrate in seawater during continuous flow in the laboratory. Other L.O.C. devices published for the metrology of nitrite (Section 2.6.2) are tested under controlled conditions using clean water and need ancillary laboratory equipment to function.

- The world's first deep sea L.O.C. system. *In situ* L.O.C. devices were tested in the Atlantic Ocean and continued to operate up to the maximum tested depth of 1518m. This is the first example of a L.O.C. nitrate and nitrite sensor operating at depth, and sampling seawater directly from the ocean. The limited number of L.O.C. devices previously presented in the literature which have been tested in the ocean, are not able to operate at depth or in a harsh ocean environment [**1**].

- The fabrication of thin film microfluidic devices using fluoropolymer substrates. Fluoropolymers were used in the creation of microfluidic devices with an all polymer construct (fluoropolymer substrate and epoxy thin film) that are chemically resistant, can have self-integrated waveguides and are cheap to fabricate. Their resistance to shock, construction flexibility and cost make them an ideal solution for *in situ* sensors. Alternative polymer materials currently available such as Polymethylmethacrylate (P.M.M.A.) or Polydimethylsiloxane (P.D.M.S.) cannot offer the same level of chemical resistance, or minimal moisture absorption that fluoropolymers offer. The novel aspects of this work were highlighted in a peer reviewed article published in the Journal of Micromechanics and Microengineering (as per Section 1.2.1). This is the first reported fabrication of microfluidic devices using fluoropolymer substrates.

1.2.1   Publications

Taberham, A., Kraft, M., Mowlem , M. and Morgan, H. (2008) Fabrication of Lab-on-Chip devices from Fluoropolymers. *J Micromech. Microeng.*

Taberham, A., Mowlem, M., Kraft, M. and Morgan, H. (2007) Fabrication of Lab on Chip devices from fluoropolymers. In: *Proc. Micromechanics Europe*, September 2007, Guimaraes, Portugal.

Mowlem, M., Holmes, D., Benazzi, G., Morgan, H., Kraft, M., Taberham, A., Chavagnac, V., Hass, C., Statham, P. and Burkhill, P. (2006) Micro system technology for marine measurement. In: *Oceans'06 MTS/IEEE-Boston,* 2006, Boston, Massachusetts .

1.3   Scientific relevance

This section details the scientific reasoning for the detection of nitrite (NO_2^-) and nitrate (NO_3^-). It begins by explaining the relevance of nitrite and nitrate in the nitrogen cycle and the influences or impact human activities can have. This leads into a description of the subsequent effects that can be caused by alterations to the nitrogen cycle.

As an objective of this study is to develop a L.O.C. sensor for monitoring the concentration of the nitrite and nitrate in oceans, lakes and rivers the content of the section is biased as such. However it also covers the effects that an increase in nitrite and nitrate levels in consumer supply water can have on human health as this is one of the alternative uses for a sensor.

1.3.1   The nitrogen cycle

The three principle forms of nitrogen that control biological productivity are nitrite, nitrate and ammonium. Their concentration levels and those of other nitrogen containing molecules (listed in Table 1.1) are regulated by complex reduction and oxidation (redox) reactions. These reactions and the flux of nitrogen between the land, atmosphere, ocean and sediments can be described by a biogeochemical process called the nitrogen cycle. The processes which govern the nitrogen cycle are illustrated in Figure 1.1.

Species	Molecular formula	Oxidation number of nitrogen
Nitrate ion	NO_3^-	+V
Nitrite ion	NO_2^-	+III
Nitrous oxide gas	N_2O	+I
Nitric oxide gas	NO	+II
Nitrogen gas	N_2	0
Ammonia gas	NH_3	-III
Ammonium ion	NH_4^+	-III
Organic amine	RNH_2	-III

Table 1.1 – Oxidised states of nitrogen and their molecular formula [2].

Figure 1.1 – Diagram of the nitrogen cycle extrapolated from S. Libes et al [2] showing the flux between the land, atmosphere, ocean and sediments.
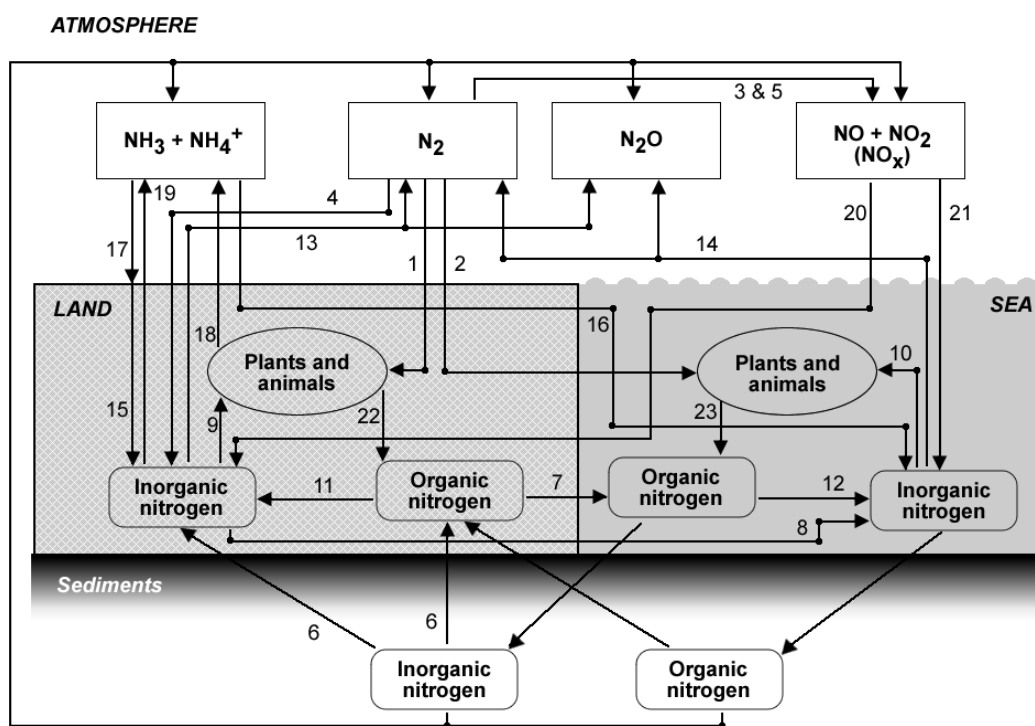
Number	Process	Number	Process
1	N fixation – land	13	Denitrification – land
2	N fixation – ocean	14	Denitrification – sea
3	N fixation – atmospheric	15	NH$_4^+$ fallout, rainout and washout – land
4	N fixation – industrial	16	NH$_4^+$ fallout, rainout and washout – sea
5	N fixation – combustion	17	N from fossil fuel
6	Weathering process	18	NH$_4^+$ volatilisation – plants and animals
7	Organic N runoff	19	NH$_4^+$ volatilisation – soil
8	Inorganic N runoff	20	NO$_x$ fallout, rainout and washout – land
9	Assimilation – land	21	NO$_x$ fallout, rainout and washout – sea
10	Assimilation – sea	22	To organic pool – land
11	Mineralisation – land	23	To organic pool – sea
12	Mineralisation – sea		

The main biological redox reactions that are involved within the marine (and also non-marine) environment are nitrogen fixation, ammonification [3,4], nitrification and denitrification [5]. These are shown as numbers 1-5 (fixation), 11-12 (ammonification), 18-19 (nitrification) and 13-14 (denitrification) in Figure 1.1. The total flux from the atmosphere and rivers to the ocean is 270 Tg N per year [6]. Nitrogen fixation is the conversion of nitrogen gas to ammonia (then quickly protonated to ammonium) and happens through high or low energy fixation. High energy nitrogen fixation which is caused by lightening, cosmic radiation and meteorite trails, accounts for approximately 10% of the nitrogen naturally entering the nitrogen cycle. Low energy or

biological fixation (Equation 1.1) from microorganisms accounts for 90% [7,8]. These organisms can be found in both soil (Rhizobium, Azobacter and Clostridium) and water (Cyanobacteria) or both (Nostoc and Calothrix).

$$N_2 + 8H^+ \rightarrow 2NH_3 + H_2$$ *Equation 1.1*

Ammonification (Equation 1.2) is the aerobic or anaerobic degradation by organisms (heterotropic bacteria and proteolytic enzymes) of dissolved organic nitrogen (D.O.N.) that has been produced by the remineralisation of particulate organic nitrogen (P.O.N.). The bacteria and enzymes convert amino acids and proteins found in dead biomass to ammonia (inorganic nitrogen) [8].

$$NH_2 + H \rightarrow NH_3$$ *Equation 1.2*

Ammonia is oxidised to nitrite and nitrate by a process called nitrification. It is a two step process with ammonia first being converted to nitrite (Equation 1.3) by bacteria (Nitrosomonas [9]) and subsequently oxidised to nitrate by Nitrobacter (Equation 1.4).

$$NH_3 + O_2 \rightarrow NO_2^- + 3H^+ + 2e^-$$ *Equation 1.3*

$$NO_2^- + H_2O \rightarrow NO_3^- + 2H^+ + 2e^-$$ *Equation 1.4*

$$NO_3^- + 10e^- + 12H^+ \rightarrow N_2 + 6H_2O$$ *Equation 1.5*
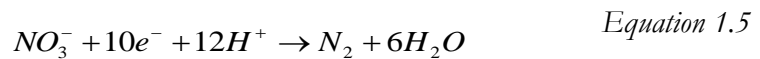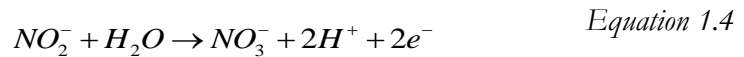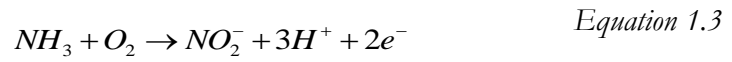
Denitrification is when nitrates are reduced to nitrogen (Equation 1.5) by facultative anaerobes (organisms that normally use oxygen for respiration but in its absence use nitrogen oxides). These organisms, mostly heterotropic bacteria, flourish in an aerobic environment but switch to denitrification in an anaerobic environment.

1.3.1.1   The role of nitrite and nitrate in the nitrogen cycle

Primary production is the creation of organic compounds utilising atmospheric carbon dioxide (CO_2) and light or chemical energy. It is limited by the availability of nutrients (including nitrogenous nutrients) within the ocean. Phytoplankton, macroalgae, and chemoautolithtropic bacteria [2] are the main primary producers and require nitrogen for growth (nitrate most important element after carbon) [10,11]. Only a few marine organisms (photoautotroph's) can fix nitrogen (N_2) directly so the needs of most are met through the absorption, or assimilation, of

dissolved species such as nitrite, nitrate, ammonium and urea [2]. The concentrations of nitrite, nitrate and ammonium are therefore limiting factors in primary production within the ocean.

1.3.1.2 Human influences on the nitrogen cycle

Human activity alters the nitrogen cycle by fixing nitrogen gas from the atmosphere (currently at a rate equal to the natural terrestrial biosphere [2] of approximately 210 teragrams per year [7]) and by the production of nitrogen oxides (NO and NO_2) during combustion (i.e. power production). The manufacture of nitrogenous fertilisers begins with nitrogen fixation (through the Haber-Bosch process) to produce ammonia gas. This is processed to create nitrate, nitrite and ammonium inorganic fertilisers that are spread on agricultural or domestic land. Through leaching, run off or misuse these products are carried into water courses, estuaries (in which they are the primary source of nitrate and nitrite [12]) and out into the coastal waters. Nitrites and nitrates that have been created by the fixation of atmospheric nitrogen are also routinely added to meat products as a preservative [13,14]. Human waste or sewage also has an effect on the nitrogen cycle as it contains high levels of ammonia. The sewage is normally treated to decrease ammonia levels but this increases the nitrate and nitrite levels within the purified effluent output. Both treated and untreated sewage is discharged into rivers, estuaries and oceans.

1.3.1.3 Impact of changes to the nitrogen cycle

Small changes to a single part of the nitrogen cycle can have a dramatic knock on effect. This section explores three of the scenario's that could result from changes to nitrite or nitrate levels in the ocean, freshwater or estuaries.

1.3.1.3.1 Global warming

Changes in the nitrogen cycle cause alterations to marine productivity which effects carbon cycling and the rate of carbon sequestration. Micro-organisms (e.g. phytoplankton) are vital in the sequestration of carbon into organic rich rocks like shale and mudstones [3,4]. Therefore global changes in their population can affect the role of these organisms in this process that helps maintain oxygen and carbon dioxide levels within the atmosphere.

1.3.1.3.2 Eutrophication

Large changes in the levels of nitrite, nitrate or ammonium in fresh or sea water can result in pollution or be a key indicator of its presence. Nitrite is an important indicator for organic pollution in water [15,16,4]. The accumulation of organic waste leads to an increase in sedimentary microbial activity, decreased oxygen levels and an increase in ammonia and nitrite concentrations within the water [17]. An increase in the concentration of nitrite and nitrate in slow flowing water (i.e. lakes) promotes excessive growth rates in organisms leading to reduced

dissolved oxygen and light levels. Low oxygen concentrations, high ammonia and high pH (pH 7-8) promotes the transient build up of nitrite through the inhibition of Nitrobactor Microbes that are responsible for the oxidation of nitrite to nitrate. This is part of the eutrophication process and leads to a decrease in the number of fish and biodiversity.

1.3.1.3.3 Harmful algae blooms

An increase in nitrite and nitrate can lead to the creation of harmful algae blooms (H.A.B's) [5]. H.A.B's (a sudden increase in the population of microalgae that are considered directly or indirectly harmful to humans) can cause shellfish poisoning, red tides, reduction in water quality and the death of marine mammals and fish [15].

1.3.2 Direct effects of nitrite and nitrate on human health

Determining the concentration of nitrite in drinking water is important as high levels can have significant health implications for humans. The maximum permissible level in the United Kingdom is 10.9μM as higher concentrations can lead to methemoglobinemia (blue baby syndrome) in infants [18].

With long term exposure it is possible for nitrite to combine with secondary natural amines [18,19] at a physiological pH to form N-nitrosamines (within food products and the human digestive system [19]) which are carcinogens in a variety of animals and suspected cancer (gastric and stomach) causing compounds in humans [15,16,20,21]). However there is no conclusive evidence that has linked nitrosamines with cancer. Traces of nitrate within drinking water may also lead to methemoglobinemia in infants [18] because the low acidity in an infant's stomach promotes nitrate reducing micro organisms that reduce nitrate to nitrite.

Nitric oxide (NO) formed in human tissues acts as an important biological mediator and cell signalling molecule in various physiological functions, including neuro transmission and endothelium-dependant vasorelaxation [22]. It is also produced in inflammatory processes and host defence reactions [23]. The nitric oxide produced, has a short half life in biological fluid (i.e. blood) of 130 seconds at pH 7.4 [24]. It is rapidly oxidised to nitrite and then nitrate by heme-containing proteins [25] (Equation 1.6). Due to its short half life, its oxidised products, nitrite and nitrate, are normally used as markers for its presence in medical diagnostics.

$$4NO + O_2 + 2H_2O \rightarrow 4NO_2^- + 4H^+ \qquad \textit{Equation 1.6}$$
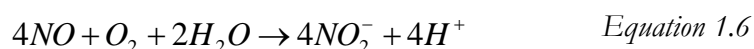
As there is no local mechanism within the urinary tract to produce nitrite, its presence in urine samples normally indicates a bacterial urinary infection. The bacteria convert nitrate in the urine

to nitrite which is then detected by a simple dipstick test (based on the Griess reaction [26]). Increase in urinary nitrate indicates systemic formation of nitrous oxide in connection with diseases, such as infective gastroenteritis, or under conditions such as cardiac and renal allograft rejections [18].

1.4   Commercial opportunities

There are two reasons why it is necessary to examine the commercial opportunities resulting from the development of a low cost, miniature, chemical sensor. Firstly, to provide a business case to a potential commercial partner or sponsor and secondly, to identify additional deployment opportunities outside the oceanographic focus of the study.

To provide a sensor network that is capable of providing the spatial and temporal resolutions that the scientific community requires will involve collaboration (whether that be through project sponsorship or licensing agreements) with a commercial partner so that the necessary numbers of sensors can be fabricated at an acceptable cost. Therefore the number of industry sectors that can be targeted by the sensor, and hence the numbers sold, has a great deal of relevance due to cost quantity benefits. An overview of potential industry sectors for a sensor is presented in Table 1.2 below. The largest market for a portable, low cost chemical sensor is currently within the water quality sector. In the United Kingdom (UK) this is the remit of the Environment Agency who have a monitoring obligation from European Union (EU) and UK legislation. Over 80% of their water monitoring is collection and laboratory analysis of water samples [27]. This has large inefficiencies due to mass transport of bottles to centralised laboratories, delays in getting the results, sample degradation and overall expense. Production of a portable or *in situ* sensor would therefore allow immediate assessment of water quality and ensure a rapid and appropriate response.

Industry Sector	Example companies
Scientific community	WETlabs
Environmental monitoring authorities	Environment Agency
Water companies	Thames Water, Southern Water
Healthcare	Philips, Honeywell
Defence	QinetiQ, DoD

Table 1.2 – Potential industry sectors and companies that could be partnered with to commercially develop a micro sensor.

1.5   Report overview

This section provides context and an overview of the work, undertaken during this doctoral study, which is presented in this report. It also includes a short description of the content of each of the chapters.

Chapters one and two provide background material for this research by detailing context and novelty (Chapter 1) and reviewing relevant techniques, technologies and literature (Chapter 2). The latter also details the performance required for oceanographic applications. Chapter's three to six outline the development and characterisation of the technology. Chapter 3 presents the fabrication of low-cost robust generic L.O.C. devices using fluoropolymers. The design, development and evaluation of three prototype L.O.C. systems for nitrite metrology, as an example of a generic colourmetric analyser, is presented in Chapter 4. Each prototype enables higher performance absorption measurements as part of an iterative process and staged knowledge increase. Chapter 5 details the development, characterisation and deep sea deployment of a L.O.C. device for nitrate and nitrite metrology. Chapter 6 provides a brief overview of the other chemical species that can be detected by the sensor and presents a design through which this could be accomplished.

The thesis is summarised by a conclusion (Chapter 7) setting out the achievements of the study and providing a description of key data and sensor performance characteristics. Future implications and further investigations necessary to improve the performance of the sensor are also highlighted.

2. LITERATURE AND BACKGROUND

Current oceanographic sampling techniques and sensors are unable to provide sufficient data to resolve complex oceanographic processes [**28**]. This chapter identifies why *in situ* sensors would enable these measurements and how they would be deployed into the ocean. It also reviews current chemical sensing techniques and relevant prior art in Lab On a Chip sensing systems.

2.1   Current sampling methods

Data from the ocean can be gained by either performing *in situ* analysis (Section 2.3) or by collecting samples which are subsequently analysed in a laboratory. The spatial resolution and quantity of laboratory analysed results is poor and samples can degrade during transport (the chemical or biological compositions change leading to problems with quality). As results are not available in real time episodic and transient events are often completely missed [**29**]. Modern technology facilitates *in situ* analysis which increases the spatial resolution and quantity of data available.

Large volumes of data are important due to the scale and complexity of the ocean as oceanographic processes (such as phytoplankton blooms) occur over a range of time (<1 sec → 1 year) and distances (<1mm → 1000km). Figure 2.1 illustrates the difference in the time and distance between the processes needed to assess global climate problems. Assessing geographically distributed processes on small timescales as well as transient events requires high temporal and spatial resolution of measurements. This can only be adequately satisfied by *in situ* sensors [**29**].
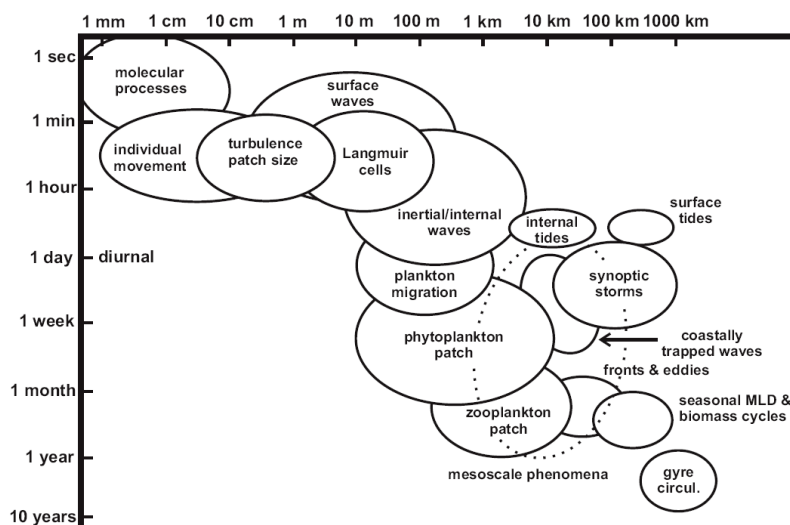
*Figure 2.1 – Time and space scales for ocean processes illustrating the high temporal and spatial resolutions of measurements required to asses global climate problems [**29,30**].*

2.2   Performance parameters

Performance parameters are required to compare designs, and to evaluate suitability for use in any application. The use of standardised performance parameters is not prevalent in the literature, however they do allow quantitative assessment and may be derived (even if approximately) from data that is presented. Performance parameters are used in this study throughout the design phases and to aid evaluation and comparison of results. They can describe attributes of a system at a high level (i.e. size or cost) or quantify low level engineering detail (i.e. dispersion in a microchannel). A combination of low level parameters will dictate the performance of the sensor at a high level and both viewpoints are necessary in engineering design and analysis. The parameters defined in this section provide insight into the difficulties associated with creating a deep sea L.O.C. sensor and set down criteria on which performance will be measured. A summary table (Table 2.3) at the end of the section defines the desired value of the key parameters in an *in situ* L.O.C. system.

2.2.1   Pressure resistance

The primary purpose of the sensor is to provide concentration measurements at varying depths within the ocean. Pressure in the deep sea is typically 70MPa though it is approximately 110MPa in the deepest regions [31]. Primary production and many biogeochemical processes are most active in the upper 1000m (~10MPa) [32,33] therefore to provide maximum scientific benefit the sensor created in this doctoral study should be rated to at least this depth.

2.2.2   Weight

If the sensor is deployed in the ocean then the ideal is for it to have neutral buoyancy. This can be easily achieved through the use of materials such as syntactic foam. However in other deployment situations weight becomes more of a critical performance criterion. A high weight will restrict the portability and therefore possible applications. The majority of the weight is expected to be from the battery and any fluid storage onboard. It was the intention of the doctoral study to ensure the weight of the sensor is less than or equivalent to commercial systems. Section 2.5 provides an overview of the systems currently available.

2.2.3   Size

The smaller the size of the sensor the increased number of deployment options and market opportunities that are available. Although preliminary sensor packages created by this doctoral study are not 'miniature' further component integration, design iterations and use of products developed in parallel studies will enable further size reduction. The first generation of sensor is a

testing board for the novel devices developed in this study and can be further refined into a 'pint size' sensor and beyond.

2.2.4 Cost

One of the objectives of the doctoral study is to develop and test a low cost sensor package as well as a low cost L.O.C. device (<£1,000). For this reason it is necessary to examine fabrication routes, packaging and component pricing. The lower the cost the larger the quantity of sensors that could be deployed and the lower the spatial resolution of results that can be achieved. A lower cost per device also allows additional and innovative market penetration (for example; ship bilges and consumer supply monitoring). Priced below one thousand pounds sterling the sensor would be significantly cheaper than other similarly performing commercial sensors on the market (see Table 2.4).

2.2.5 Power consumption

To enable use on small platforms, which have a limited payload (including for extra batteries) and power (e.g. A.P.E.X floats), power consumption must be minimised. The sensor should have power consumption comparable to that of commercial systems (see Table 2.4).

2.2.6 Reagent consumption

A sensor will only be able to detect chemical concentrations whilst there is sufficient reagent to mix with the sample and form an azo dye (as described in Section 2.4.1.1). Therefore higher reagent consumption will decrease the lifetime of the sensor or increase the size of its storage container. Non continuous sampling methods can be used to decrease reagent consumption and increase the sensor lifetime.

2.2.7 Lifetime

Factors affecting the lifetime of the sensor include; biofouling, power and reagent consumption, measurement drift and material compatibility. An increase in lifetime will give an increased temporal span of data (therefore, add greater value to the data) and will increase maintenance intervals. It is expected that the lifetime of any production sensor will be up to one year (assuming an external power source).

2.2.8 Sensitivity

The sensitivity (an absolute quantity) is the change in the response divided by the corresponding change in stimulus. It can be calculated from Equation 2.1.

$$m = \frac{\Delta y}{\Delta x}$$

Equation 2.1

Where m is the sensitivity, Δy is the change in response (e.g. absorption), and Δx is the change in stimulus (e.g. concentration). The change in the stimulus must be large compared with the resolution of the sensor.

2.2.9   Resolution

The resolution (a relative quantity) is the smallest change, in the value of a quantity being measured by a measuring system, which causes a perceptible change in the corresponding indication [**34**]. If a sensor has a high resolution this does not necessarily mean that it has a high sensitivity and vice versa. The resolution of a sensor may be dependent on factors such as noise. In this study the resolution of each data point is calculated using the standard deviation equation (Equation 2.2) for a number of samples (n) where x is the value for sample n.

$$S = \left(\frac{1}{n-1} \sum_{i=1}^{n} \left(x_i - \bar{x} \right)^2 \right)^{\frac{1}{2}} \text{ where } \quad \bar{x} = \frac{1}{n} \sum_{i=1}^{n} x_i$$

Equation 2.2

2.2.10   Accuracy

In the context of a L.O.C. chemical sensor the accuracy refers to its ability to provide a correct reading that reflects the concentration of the chemical that is being measured. As long as the sensor is precise (see Section 2.2.11) this can be calibrated for by creating calibration curves with certified concentration standards during and/or before deployment (assuming the offset is constant). Accuracy is measured in this report by comparing readings between the sensor and a separate commercial system.

2.2.11   Precision

The sensor needs to be able to consistently provide the same measurement reading for the same chemical concentration (for example; a repeat test using the same matrix and concentration). It must provide the exact same measurement each time. This will be especially relevant if multiple sensors are produced and it is necessary to correlate their readings. The precision of the sensor is measured throughout the study by experiment repetition and presented as the standard deviation (Equation 2.2) of a number of absorption values at the same concentration.

2.2.12 Limit of detection

The limit of detection (L.O.D.) is described as the value of the measurands at which the probability of detection reaches a specified level of confidence [34]. The limit of detection (assuming that it is the maximum value of either the Instrument Detection Limit (I.D.L.) – electronic noise, detector sensitivity; or the method detection limit (M.D.L.) – limit of the detection of a analyte using a specific analytical technique in a specific matrix) can be calculated using the International Union of Pure and Applied Chemistry (I.U.P.A.C.) method [35] as per Equation 2.3.

$$C_L = \frac{(k.s_B)}{m} \qquad \qquad \textit{Equation 2.3}$$

Where S_B is the standard deviation of the blank, C_L is the limit of detection, k is the certainty level (scientific standard of 3) and m is the sensitivity as determined from Equation 2.1. The sensor must be able to detect concentrations of scientific interest otherwise it will be limited to regions of high concentration. Table 2.1 provides an overview of the typical concentrations of chemical species in surface ocean, deep ocean, estuarine and coastal regions. The sensitivity must be as high as possible to give the best L.O.D. and resolution. The L.O.D. and the sensitivity should also be lower than other commercial systems presented in Section 2.5. The lower the L.O.D. and higher the sensitivity the more insights that can be gained into ocean processes.

	Region	Range (µM)
Nitrite	Surface ocean	0.0001 - 0.2
	Deep ocean	0.0001 - 0.05
	Estuarine	0.5 - 1.5
	Coastal	0.1 – 2
Nitrate	Surface ocean	0.1 - 2.5
	Deep ocean	2 – 40
	Estuarine	10 – 400
	Coastal	0.1 - 80
Ammonia	Surface ocean	0.05 - 1.5
	Deep ocean	0.02 - 0.06
	Estuarine	0 - 600
	Coastal	5 - 30
Phosphate	Surface ocean	0.05 - 1.5
	Deep ocean	0.002 - 0.005
	Estuarine	0 - 600
	Coastal	5 - 30
Silicate	Surface ocean	0.1 - 3
	Deep ocean	3 - 200
	Estuarine	10 - 75
	Coastal	0.1 - 35
'dissolved' Fe	Surface ocean	0.00002 - 0.0025
	Deep ocean	0.0004 - 0.001
	Estuarine	0.7 - 1.5
	Coastal	0.0001 - 0.001

*Table 2.1 – Typical ranges of chemical concentrations for chemical species that a miniaturised L.O.C. sensor could be used to detect in oceans or estuaries [**2,34,36,37**].*

2.2.13   Time response

The time response or 'step response' of a sensor is the duration between the instant when a quantity value at the input of the sensor is subjected to a step change between two specified steady states and the instant when the corresponding indication settles within specified limits around its final steady value [**35**]. A value of 90% (T90) of the steady state value is normally used as a specified limit. The time response of a L.O.C. sensor will be affected by dispersion and smearing.

2.2.14   Minimum resolvable volume

This is a measure of the volume of a liquid that must flow through the sensor, following a step change in the quantity value at the input of the sensor, until the corresponding indicator settles within specified limits around its final steady value. The minimum resolvable volume of a L.O.C.

sensor will be affected by absorption cell volumes as well as the total dispersion in the system (including flushing) and smearing.

2.2.15 Effective flushing volume

On change of sample the volume of fluid required to remove all traces of the previous sample fluid is referred to as the effective flushing volume. It is affected by dispersion and dead volume within the fluidic pathways. A high effective flushing volume will cause a poor time response, high minimum resolvable volume and increase reagent consumption. Therefore the volume must be minimised.

2.2.16 Material compatibility

To analyse the concentration of chemicals within the sea it is assumed the sensor must be in contact with seawater. It has already been proposed that this sensor will be deployed for substantial periods of time (up to 1 year) and therefore materials within any fluidic pathways must absorb minimal quantities of seawater, and not be degraded by any chemicals used in the detection scheme. Additionally components must be compatible with any pressure compensating medium (e.g. coronation oil [38]).

2.2.17 Fouling resistance

Unlike clean or deionised (D.I.) laboratory water, with which the majority of L.O.C. devices are tested, seawater or fresh water contain a large number of micro organisms (for example; Phytoplankton and Zooplankton [31]) and Dissolved Organic Matter (D.O.M). The flow of seawater or fresh water through a device will lead to the adsorption of organic molecules (within a few seconds), adhesion of bacteria (within a few hours), and biofilm growth [39] on channel surfaces. Acidic conditions (pH<2) associated with the reagents used in the chemical detection of nitrite should prevent this growth in channels that contain these fluids. However fouling is expected to be most severe at the inlet of the system before reagents are mixed with the seawater.

Fine particle sediment (for example; clays and slits; 0. 1μm - >200μm) and large quantities of micro organisms or D.O.M. (for example; Plankton blooms) could also cause instantaneous partial or total blockage of the channels. This fouling would modify the local chemical environment and lead to erroneous results or simply stop the device all together. Table 2.2 gives an indication of how many particles could expect to be seen in a channel at a flow rate of 60μl/min. Due to the high risk of failure created by particles entering the sensor it is necessary to filter the water input. Larger particles (>25μm) pose the highest risk and therefore are the ones the filter needs to address. A filter used with a sensor must be capable of surviving extended deployment periods (>8hrs for a standard C.T.D. cast, and up to 1 year for mooring

deployments) without particulates causing flow rate changes leading to sensor drift, inaccuracy and eventually inoperability [**40,39**].

Region	Diameter of Particle (µm)	Particles per Hour (at 60µl/min)
Eastern Pacific Coastal	>2.9	43200
Eastern Pacific Coastal	>11	1080
Ocean	>25	0.36
Eastern Pacific Coastal	>84.5	28.7
Surface in Eastern Sound	50-110	1170
Sargasso sea, Bermuda	267-771	5.30×10^{-3}
Sargasso sea, Bermuda	267-771	1.61×10^{-5}

*Table 2.2 – The number of particles (over a wide range of diameters) that could be seen in the ocean [**41,42,43**] with a sensor sampling at 60µl per minute.*

2.2.18 Robustness

For ease of operation and reliability during deployment the sensor has to be robust. Unfamiliar users need to be able to handle the sensor with relative ease so a fragile device is not of any use. During deployment in harsh environments, such as the oceans or rivers, the sensor also needs to be able to survive inclement weather and initial shocks from placement (e.g. from a ship).

2.2.19 Dispersion

Taylor Aris dispersion, which causes sample band broadening, degrades the time response and increases the minimum resolvable volume. At low Reynolds numbers a parabolic velocity profile develops within a fluid (as shown in the velocity profile in Figure 2.2a) and is caused by the channels surface roughness. In the case of a fluid segment, diffusion then acts to broaden and therefore lengthen the sample. Figure 2.2b illustrates the effects of a parabolic velocity profile with and without diffusion. A consequence of Taylor Aris dispersion is a decrease in the sampling frequency, and an increase in reagent consumption and power consumption.
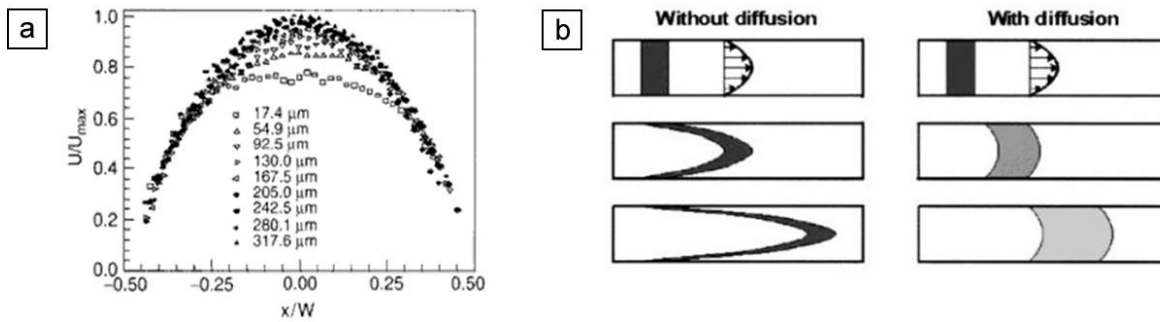
Figure 2.2a & b - Graph showing a parabolic velocity profile for Reynolds number of 20 with velocity plotted against channel position [44], b) the development of a parabolic profile without any diffusion and c) with diffusion [45].

2.2.20 Extent of mixing

The extent of mixing of fluids is a measure of the variation of the concentration across the fluid stream at an instant in time, following the input of two different concentrations of fluid. This is an important performance characteristic when assessing L.O.C. devices as a lower extent of mixing will reduce the sensitivity of the sensor. The extent of mixing over a period of time rather than at any one instance is also an important factor as a variable extent of mixing can reduce the precision. An increased mixing length (required to provide a higher extent of mixing) also increases dispersion (see Section 2.2.19).

2.2.21 Fluidic delay

The time between a sample of interest entering the sensor and it being analysed is referred to as the fluidic delay. It is caused by the time required for the fluid to travel along the channels inside a sensor. Although this parameter does not directly affect the performance of a sensor (assuming real time data is not required) a longer fluidic delay will lead to an increase in dispersion.

2.2.22 Pressure drop

Longer and narrower channels will result in an increased pressure drop. A greater pressure drop will increase the work required by the pump and hence increase energy consumption. An increase in energy consumption has the potential to decrease the maximum deployment length.

2.2.23 Effective absorption length

The length of the absorption cell (i.e. the part that the fluid flows through) is not necessarily the actual length that the light takes through the fluid. As any light source will have an angular intensity profile it will be reflected or refracted off channels walls or waveguides. If the effective

absorption length is shorter than the absorption cell length then this will decrease sensitivity, resolution and accuracy.

2.2.24 Stray light

Natural light or stray light from other sources (e.g. an additional spectrophotometric channel) can enter the detector and result in increased light intensity readings. This stray light will increase the L.O.D. and decrease the measurement range of the sensor.

2.2.25 Reaction kinetics

The length of time over which the reaction between a reagent and a chemical species of interest occurs (determined by reaction kinetics) affects the fluidic delay. For slower reactions a longer fluidic path length or slower flow rate is required, leading to an increase in the fluidic delay.

2.2.1 Summary

Many different parameters are linked to the performance and capability of a potential sensor for *in situ* deployment. Table 2.3 defines the desired value of the key parameters and provided an aid memoire in the design and performance assessment of the sensor work carried out in this study.

Parameter	Target value
Pressure resistance	>10MPa
Weight	<1Kg (L.O.C. components)
Size	<700(W)x500(D)x 850(H)
Cost	<£1000
Power consumption	<5.5W
Reagent consumption	<2μl/min
Lifetime	1 year (assuming external Power Supply Unit, P.S.U.)
Sensitivity	<1μM (Nitrite)
Resolution	<1μM (Nitrite)
Precision	<1μM (Nitrite)
Limit of detection	<1μM (Nitrite)
Measurement frequency	>1Hz

Table 2.3- Summary table of target values for the key design driver parameters identified in Section 2.2.

2.3 Deployment platforms

This section identifies five different platforms on which a miniature chemical sensor could be deployed and used to field test or trial the sensor in the ocean. Some of the platforms (specifically the profiling floats, see Section 2.3.4) could also be used for the mass deployment of later, more developed, sensor versions. The holding capacity, maximum payload, profiling speed and power

supply capabilities of each option is described and aids the design of a field testable and platform compatible sensor. Table 2.4 provides a summary of these criteria.

2.3.1 Rosette frame

A rosette frame or pylon is frequently used in oceanographic research as a sensor platform to take conductivity, temperature and depth (C.T.D.) measurements from a scientific research vessel at locations of interest around the globe. Instrumentation can be located on the robust frame and, in conjunction with water sampling bottles, (as shown in Figure 2.3a & b) provide a profile of the ocean up to a depth of 10km at a rate of 0 to 45 metres a minute.
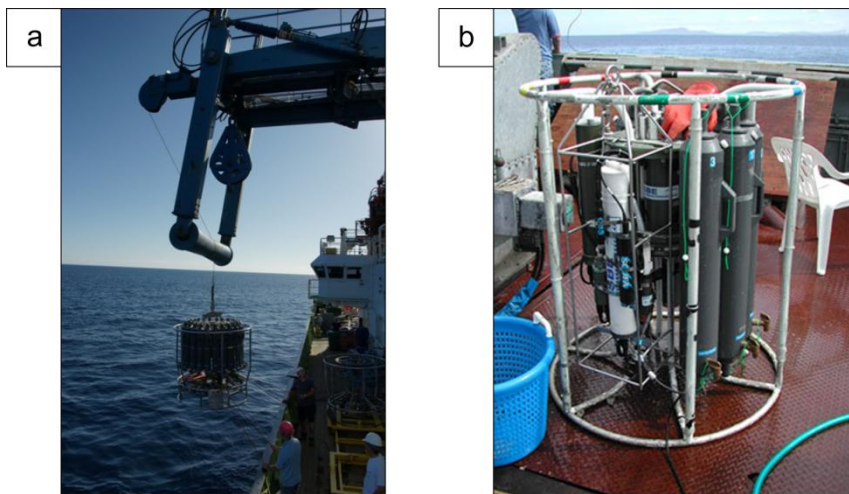
Figure 2.3a & b – a) Picture of a General Oceanics 24 bottle rosette frame being deployed in the Atlantic ocean and b) a close up of a smaller rosette frame with a selection of instruments attached [courtesy of the State of Alaska, Department of Environmental Conservation].

These frames provide a perfect prototype development platform as they can sustain a large amount of weight (up to approximately 100kg), have a large number of sensor mounting options and space, as well as providing parallel calibration or comparison measurements (e.g. using water sampling bottles). External power supplies (such as deep sea batteries) can also be mounted onto the frame. Disadvantages of this platform are that its deployment location is limited by that of the vessel which is carrying it, and the cost of running a vessel is high (>£10,000 a day).

2.3.2 Ferrybox

The objective of the FerryBox project, first operational in 2002 [46], is to provide cost effective ship born instrumentation that can help solve environmental problems. The FerryBox system is a fully automated flow through system with sensors and automatic analysers for the measurement of physical, biological and chemical parameters. It uses ferryboats and other ships of opportunity

as the carrier system [**47**]. A commercial FerryBox system is offered by Chelsea instruments (Aqualine, [**48**]) for approximately £50,000. The sensor station is approximately 700(W) x 500(D) x 850(H) mm with a total mass of 30kg and can log between one sample a second and one sample a day. For this study it can provide an existing platform to work from, using the existing power sources, data logging and telemetry and sample handling infrastructure. FerryBox would provide an ideal test bed for the sensor as it is based in a dry, easily accessed location within the ships engine room.

2.3.3   AutoSub

AutoSub is a National Environment Research Council (N.E.R.C.) project that has been operational since 1996 and combines numerous sensors (for example; an oxygen sensor and flow cytometer) into an Autonomous Underwater Vehicle (A.U.V) [**47**]. It is designed to carry a variety of interchangeable scientific instruments to depths up to 6000m (AutoSub 6000, as shown in Figure 2.4) and in locations previously inaccessible by conventional techniques (i.e. tow sensors, rosette frames or buoys).
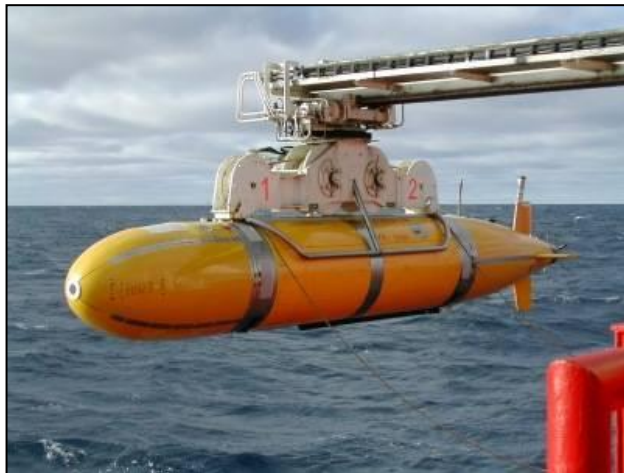
Figure 2.4 – Picture of the AutoSub being deployed in the ocean from a scientific vessel [courtesy of the National Oceanographic Centre, Southampton].

The maximum scientific cargo it can carry is $0.5m^3$ with a mass of 20kg (higher if the payload is neutrally buoyant) [**49**]. For long range (thousands of km) power consumption of the sensor would be restricted to <1W but under normal use an average of 50W is acceptable.

Whilst the FerryBox is restricted to existing shipping tracks, the AutoSub provides the study with an opportunity to gain data from hazardous and remote locations (i.e. ocean trenches, ice shelves).

2.3.4 Profiling autonomous lagrangian circulation explorer floats

Profiling Autonomous Lagrangian Circulation Explorer or P.A.L.A.C.E. floats (see Figure 2.5a for an illustrated cross section) are probes designed for ocean deployment in large numbers over large geographical areas. Currently they are not routinely fitted with biogeochemical sensor technology and only monitor temperature ($\pm0.005^\circ$C) and salinity (±0.01 p.s.u.) [50]. Their main function is to form a network of sensors deployed within the ocean called A.R.G.O. (array for real-time geostrophic oceanography) initiated by R. E. Davis 1991 [51]. They submerge to 2000m (at approximately 6m a minute) and use the principle of neutral buoyancy, developed by J. Swallow [52], to follow drift currents and then ascend to the surface whilst recording changes in temperature and salinity, as illustrated in Figure 2.5b. The global A.R.G.O. array of these floats contributes to the Global Ocean Observing System (G.O.O.S.) and Global Climate Observing System (G.C.O.S.) [53].
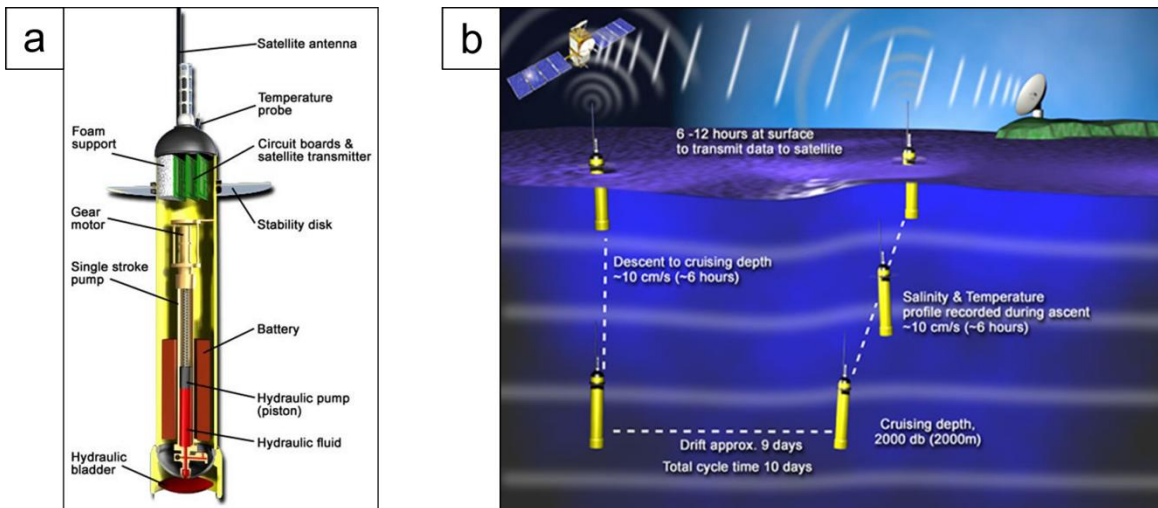
Figure 2.5a & b – a) Cross section of an Argo float where the main instrumentation is found above the stability disk, b) Cycle of the Argo Float [54].

A.R.G.O. is an international project that has deployed 3050 (January 2008) drifters (costing approximately £12,500 each) across all the oceans (with the exception of the Artic Ocean) [54]. It supports projects such as the environmental assessment in the Gulf of Alaska and monitoring of the subsurface salinity flows in the Indian Ocean. The floats can be modified to carry alternative sensors (e.g. oxygen, nitrite) to contribute to the data collection (restricted to payloads of less than 1Kg and power consumption of less than 0.1W). Whilst the floats themselves are large (1.3m x Ø0.17m) the maximum payload capability is relatively small ($\approx$120xØ70mm). They are designed with lifetimes of up to 2 years so they can provide long term data. The large numbers

and wide geographic distribution of these vehicles makes them an attractive target for the devices developed by this study.

2.3.5 Slocum gliders

Developed by (among others) the Webb Research Corporation these gliders (shown in Figure 2.6) are driven by variable buoyancy rather than traditional propeller propulsion. They can be programmed to patrol subsurface in a saw tooth vertical profile for weeks at a time surfacing only to transmit data [55]. Driven by electric batteries (15 – 30 days) or a thermal engine (5 years) they are capable of holding a 5 litre payload of sensors.

Figure 2.6 – A picture of three slocum gliders from the Webb Corporation [55] where the horizontal wings are the lift surfaces that enable forward motion.

The variable buoyancy propulsion system employed works using buoyancy change to cause vertical velocity and lift surfaces (e.g. wings) to create forward motion from the vertical momentum [56]. All devices deployed on the gliders would need to be low power (<1W) to maximise deployment time.

2.3.6 Summary

Comparing the performance parameters presented in Section 2.2 against the deployment platform specifications in this section (see Table 2.4 for a summary) it is possible to determine the most suitable platforms for sensor deployment.

Deployment platform	Holding Capacity (mm)	Payload (Kg)	Max. Power Consumption (W)	Profiling speed (m/min)	Deployment length
Rosette frame	1000(W)x500(D)x300(H)	100	<18W	0-45	hours - days
Ferry box	700(W) x 500(D) x 850(H)	30	n/a	≈679	months
AutoSub	790(W)x790(D)x790(H)	20	1W – 50W	0-120	hours
Floats	120xØ70	<1	<0.1W	6	up to 2 years
Slocum gliders	300 x Ø213	4	<1W	24	<1 month

Table 2.4 – Capabilities of the five deployment platforms identified for use in field testing a miniature chemical sensor.

All platforms identified, apart from the P.A.L.A.C.E. floats, provide a holding capacity and are capable of carrying a payload large enough (see Section 2.2.1) for a prototype sensor. Power consumption is limited (less than 1W) with both P.A.L.A.C.E. floats and Slocum Gliders. The speed at which the platform moves through the sampling medium limits the maximum spatial resolution of the sensor (i.e. difference between the sampling speed of the sensor and the speed at which it is moving through the medium). A sensor sampling at 60μl/min and with a minimum resolvable volume (Section 2.2.14) of 10μl on a ferry box platform (679m/min) will have a spatial resolution of 113m. If a higher spatial resolution (at that platform profiling speed) is required the sampling rate would have to increase or the minimum resolvable volume decrease. A higher profiling speed will also increase the time response of the sensor (Section 2.2.13).

As such the primary focus of this report was the production of a sensor to be deployed on a rosette frame. The frame provides a configurable platform for prototype development with abundant power and space and a variable profiling speed. For future deployment the P.A.L.A.C.E. floats provide the opportunity to deploy the sensors in thousands with a proven data collection and tracking mechanism.

2.4   Chemical sensing techniques

This section covers the theory of detection techniques that could be used in a nitrite or nitrate sensor. A further review has been presented by P. Auroux et. al. [57] and reports on many disciplines including chromatography, electrophoresis, luminescence, fluorescence and mass spectrometry.

2.4.1   Spectrophotometry

Spectrophotometry is the analysis of the attenuation of electromagnetic (E.M.) radiation. Every chemical element has a propensity to absorb photons at a certain wavelength. Measurement of this absorption is called absorption spectrophotometry [58]. When the number of unabsorbed

photons is measured it is called transmission spectrophotometry. If photons are reflected by a molecule instead of being absorbed or transmitted it is termed as scattering and the quantity of which is measured through reflection spectrophotometry [59].

2.4.1.1 Absorption, transmission and concentration

The concentration of a molecule in a solution is related to photon absorption by the Beer-Lambert-Bouger law. This section details the derivation of the law and relationship between absorption, transmission and concentration.

For monochromatic light the power absorbed (dP) by an infinitesimal slab (thickness of dz) is given by Equation 2.4 where P_z is the power entering the slab, is the effective absorption cross section of a molecule and N_A is Avogadro's constant. This is illustrated in Figure 2.7a & b.

$$-\frac{dP}{P_z} = \sigma N_A dz \qquad \textit{Equation 2.4}$$

Figure 2.7a & b - Diagram showing a) an overview of the terminology and b) the fundamental terms used in the derivation of the Beer-Lambert Bouger Law for light of power P_0 entering a sample.

Integrating Equation 2.4 between z=0 and z=b (Equation 2.5) gives Equation 2.6 (naperian version) or Equation 2.7 (decadic version) where b is the absorption path length, P_0 is the power entering the sample, P_T is that leaving then sample, c is the concentration of the medium, ε is the decadic molar absorption coefficient (wavelength dependant) and k is the naperian molar absorption coefficient (wavelength dependant).

$$-\int_{P_0}^{P_b} \frac{dP}{P} = \int_0^b \sigma N_A dz \qquad \textit{Equation 2.5}$$

$$-ln\left(\frac{P_T}{P_0}\right) = \sigma N_A b = kbc \qquad \textit{Equation 2.6}$$

$$-log\left(\frac{P_T}{P_0}\right) = \frac{\sigma N_A b}{2.303} = \varepsilon bc \qquad \textit{Equation 2.7}$$

The molar absorption coefficient (decadic - measured in $M^{-1}cm^{-1}$) is dependent on the type of molecule being detected and the wavelength of the incident light. It is a measurement of the absorption per molar concentration. The absorption of the sample is given by Equation 2.8 where A_D is the decadic absorbance and T is the light transmitted.

$$A_D = -log_{10}(T) = -log_{10}\left(\frac{P_T}{P_0}\right) = \varepsilon bc \qquad \textit{Equation 2.8}$$

The amount of light absorbed is proportional to the number of molecules in the medium the light passes through. Therefore the concentration of a molecule in the medium is directly proportional to the amount of light absorbed (illustrated in Figure 2.8a). The light transmitted (transmittance = P_T/P_0) reduces exponentially with concentration and absorbance (illustrated in Figure 2.8b & c).
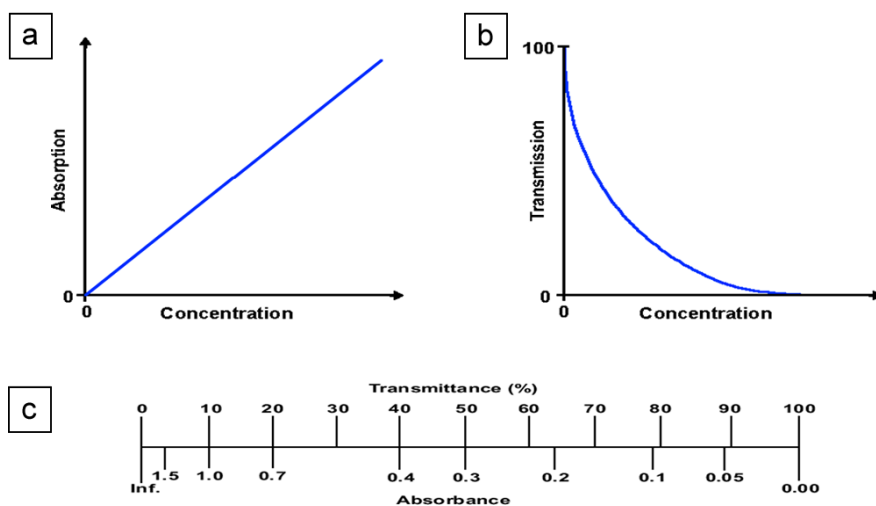
Figure 2.8a, b & c – Graph showing a) the linear relationship between absorption and concentration, b) the inversely proportional relationship of concentration to transmission, c) relationship between absorbance and transmission.

The Beer-Lambert-Bouger law only applies when molecules are evenly distributed and behave independently from other absorbing species in a solution. Non linearity in the relationship between absorption and concentration can occur for three reasons; a non-monochromatic (or polychromatic) light source [60,61]; using diffusive media and stray light.

The absorption of a medium measured using a light source emitting two wavelengths is given by Equation 2.9 where P_0' and P_0'' are the powers incident on the medium and $\varepsilon(\lambda')$ and $\varepsilon(\lambda'')$ are the molar absorption coefficients of the medium at the two wavelengths (λ' and λ'') [61].

$$A_1 = log_{10}\left(\frac{P_0' + P_0''}{P_0'10^{-\varepsilon(\lambda')bc} + P_0''10^{-\varepsilon(\lambda'')bc}}\right) \qquad \textit{Equation 2.9}$$

Figure 2.9 shows absorption versus concentration graph ($\varepsilon(\lambda')$=1.35x10^6 M^{-1}m^{-1}, $\varepsilon(\lambda'')$=1x10^4 M^{-1}m^{-1} b=0.01m, P_0'=1, P_0''=1) that has been plotted using The Mathworks™ Matlab$^©$ (see script in Appendix 8.5.1) using a monochromatic source and a polychromatic source. The deviation caused by a low bandwidth (<100nm) source would be minimal at the concentration ranges of nitrate, nitrite and ammonium found in the ocean (see Section 2.2.12 for typical concentrations).

Stray light (natural light or other light source) increases the L.O.D. and causes non linearity between absorption measurement and the concentration. The absorption of a medium where the power of the stray light measured is equal to P_{st} is given by Equation 2.10 and plotted in Figure 2.9. This and the change in absorption from scattering and reflectance of a medium can be factored out by using a reference medium (i.e. one without any absorbing molecules) and a differential absorption measuring system.

$$A = log_{10}\left(\frac{P_0 \times 10^{-\varepsilon\lambda bc} + P_{st}}{P_0}\right) \qquad \textit{Equation 2.10}$$
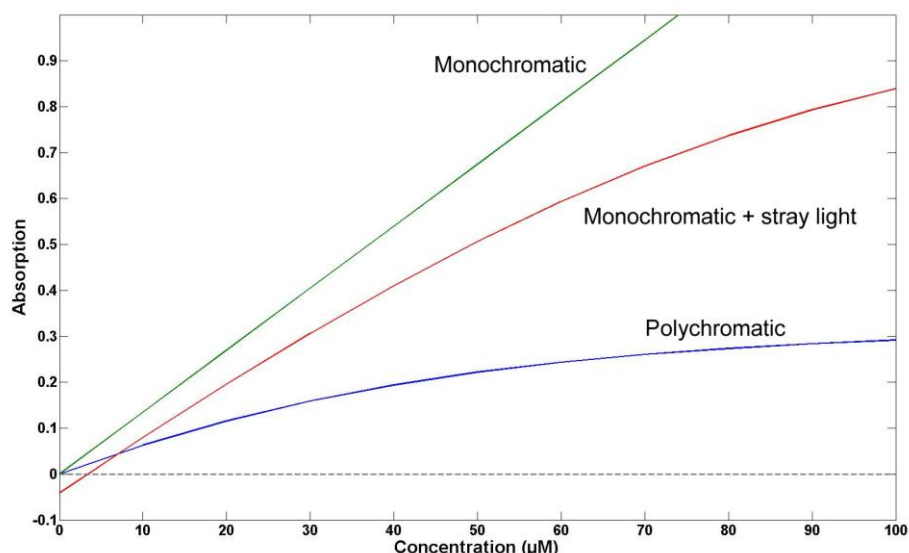
Figure 2.9 – Graph showing the deviation from the Beer-Lambert-Bouger law when measuring absorption using monochromatic and polychromatic light. The deviation caused by stray light is also plotted.

In commercial spectrophotometers the linear relationship between absorption and concentration remains valid until the absorption is greater than 3 or 4 as excitation source filters (used to narrow bandwidth to approximately 0.1nm) are used. These spectrophotometers are desktop based (>500x500x400mm) and most require a P.C. interface. Typical performance data can be found in Table 2.5.

Name	Detector	Wavelengths (nm)	Min. Absorption (A)	Reference
Shimadzu UV-3600	PbS, InGaAs & PMT	185-3300	0.00003	[62]
Jasco V-670	PMT, Pbs	190-3200	0.002	[63]
Camspec M550	Si	190-1100	0.002	[64]
Hach DR 5000	Si	190-1110	0.005	[65]
DU 800	Si	190-1100	0.005	[66]
Hitachi U4100	PMT, PbS	175-2600	0.002	[67]

Table 2.5 – An overview of commercial absorption spectrophotometry machine performance.

Nitrite (NO_2^-) in a solution can be detected directly though spectrophotometry (direct UV-Vis spectrophotometry, Section 2.4.1.2) and has an absorbance peak at 210 and 355nm [68] with a molar absorptivity (ε) of 560 and 23 $M^{-1}cm^{-1}$ [69,70] respectively. Nitrate (NO_3^-) is also commonly detected using this method [40,71]. Alternatively, nitrite can be reacted with a reagent to form chromophores (molecules that absorb energy within the visible (380nm to 780nm) spectrum [72])

the concentration of which can be measured using colourmetric spectrophotometry (Section 2.4.1.1).

2.4.1.2 Direct spectrophotometry

The concentration of nitrite in a seawater sample can be determined by calculating zero, first and second derivatives of absorption measurements from UV-Vis spectrophotometry. Curve fitting of the absorption spectrum can also be used. Zero derivative detection is purely a measurement of the absorption at a set wavelength (see Figure 2.10a for a graph of the absorption peak of nitrite at 210nm) whereas first derivative detection is the rate of change of absorption with wavelength. Second derivative detection is the rate of change of the first derivative. Both first and second derivative detection are limited to detecting nitrite in solution with a pH greater than 5 as in a more acidic environment the nitrite is turned to nitrous oxide and the absorbance reduced. This is not seen in seawater (which is slightly alkaline). Direct spectrophotometry systems do not rely on reagents and their running time is dependent on power consumption, biofouling and sensor drift.

For first derivative direct spectrophotometry the concentration of nitrite is calculated by using the absorption at multiple wavelengths to minimise the effect of other species on measurements. This is because first derivative detection of nitrite can be affected by the salinity of the water [40], and various salts (355nm [69]). Nitrate also has an absorbance peak at 203 & 302nm so can distort absorption levels of nitrite as the spectra overlap, as shown in Figure 2.10b.
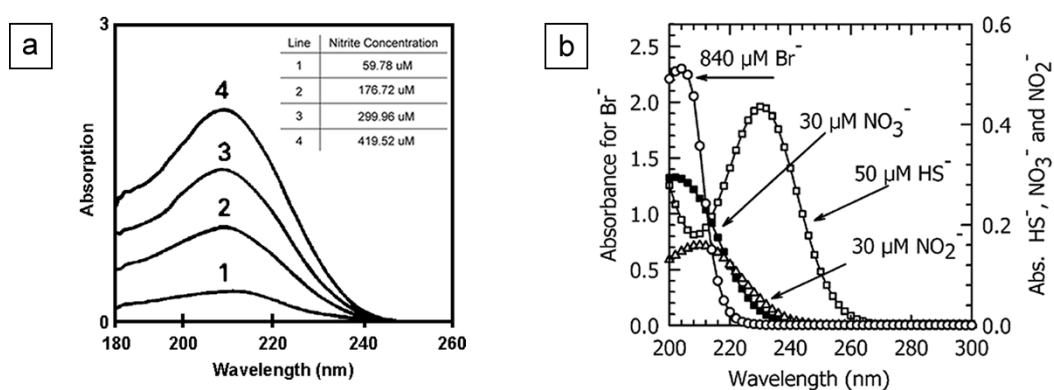
Figure 2.10a & b – a) A graph of the 210nm absorption peak of nitrite [68] b) Comparison of nitrate and nitrite spectra [71] showing the overlap between the two as well as with bromide and hydrosulfide.

Second derivative direct spectrophotometry facilitates the measurement of nitrite within a solution containing other species without the need for any reagents. It allows the simultaneous detection of both nitrite and nitrate [68,73] as the derivative spectrum can separate overlapped

absorption peaks. Nitrite exhibits a different concentration dependant variation in the second derivative absorbance so can be determined from nitrate at an isosbestic point. Commercial *in situ* sensor presented to date [71,40] have been capable of detecting low micro molar concentrations (see Section 2.5). N. Suzuki et al [68] showed a limit of detection of 4μM for nitrite but in distilled water and a laboratory setting.

A disadvantage of the technique is that the derivatisation of the spectra can amplify any noise and has a high dependence on instrumental conditions both of which lower the reproducibility of results [74]. Additionally any change in the composition of the medium being studied requires re-calibration and optimisation of the parameters making sea-water analysis difficult.

2.4.1.1 Colourmetric spectrophotometry

The most widely found method for colourmetric (or indirect) spectroscopic detection of nitrite uses the Griess reaction [26]. Nitrate and ammonium can also be detected through the Griess reaction using colourmetric spectrophotometry but require additional steps to reduce them to nitrite. These steps are detailed in Section 2.4.1.1.1. The Griess reaction is shown in Figure 2.11, where, under acidic conditions (pH<5), nitrite reacts with sulfanilic acid to form a diazonium cation (any compound that has a N_2^+ attached to an organic group). The diazonium cation then couples to α-napthylamine to form coloured chromophores (otherwise known as an azo dye).
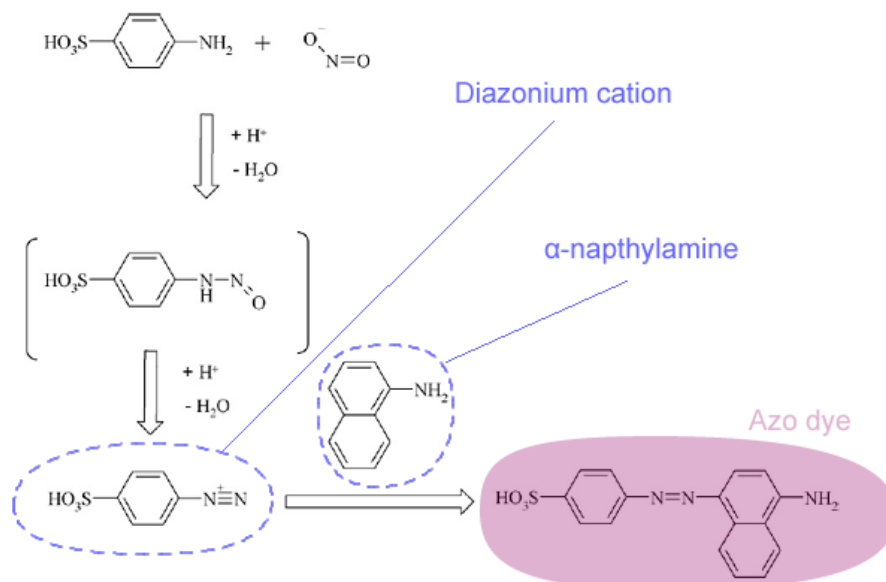
Figure 2.11 – The Griess reaction, under acidic conditions nitrite reacts with the amino group of sulfanilic acid to form the diazonium cation, which couples to a-napthylamine [24].

The absorption of the chromophore is directly proportional to the nitrite concentration. This facilitates nitrite and nitrate metrology using absorption spectrophotometery of the colourimetric product [75].

The Griess reaction, first developed in 1879, has many variants (listed in Table 2.6) and was initially used in the identification of nitrite in saliva and urine. The reactions can be used to detect concentrations from 0.001 (1nM) [76] to 391µM [18] however the low selectivity of some variants makes them unsuitable for use in non-laboratory situations. The most common variant of the Griess reaction uses N-(1-naphthyl) Ethylenediamine (N.E.D.) and it has several advantages over other coupling agents; reproducibility, higher speed of coupling, increased sensitivity, increased acid-solubility of azo dye and pH independence of the colour in the pH range 1-2 [75].

Reagent	Range (µM)	Peak Absorption λ_{max} (nm)	Reference
SA+NEDH	11 – 304	540	[77]
p-Aminophenyl mercaotoacetic acid	0.21 - 35	495	[78]
p-Aminoacetophenone+ NEDH	2 – 17	546	[79]
o-Nitroaniline + 1-Aminonaphthalene	2 - 15	545	[80]
PNA+ Phloroglucinol	0.09 - 0.87	420	[81]
PNA+Acetylacetone	11 - 304	490	[82]
Phosphomolybdenum blue	11 - 43	814	[83]
PNA+EA	1 - 130	507	[84]
SA+EAA	4 - 65	356	[84]
PAA+ Citrazinic acid	11 - 261	495	[85]
Leucocrystal violet	0.09 - 0.87	500	[86]
4,4'-Diaminostilbene-2,2'-di-sulfonic	0.87 - 35	520	[87]
PNA + Citrazinic acid	11 - 304	530	[88]
PNA+ Guaiacol	0.7 - 3.3	540	[89]
4-Nitroaniline + 1-Naphthol	0.4 - 3.0	610	[90]
PNA+EMME	11 - 348	439	[18]
PNA+ECA	4 - 391	439	[18]

* SA, sulfanimide; NEDH, N-(1-naphthyl) Ethylenediamine hydrochloride; PNA, p-nitroaniline; Eaa, ethyl acetoacetate; PAA, p aminophenylmercaptoacetic; EMME, ethoxyethylenemaleic ester; ECA, ethylcyanoacetate.

Table 2.6 – List of dye variants used in the detection of nitrite. Their typical range of detection and peak absorption is also stated [18].

The use of N.E.D. and sulphanilamide is established as a European standard method of determining nitrite concentrations in drinking water (British Standard EN ISO13395). However reagent life time is a factor that needs to be considered when determining the maximum

deployment length of an *in situ* system (as per performance parameters in Section 2.2). Other compounds or chemicals can also interfere with the production of the azo dye. Antioxidants such as ascorbate and sulfhydryl remove the nitrous oxide before it has reacted and coupled with the aromatic amine. This leads to a reduced apparent nitrite concentration [13]. Other ions such as iron, aluminium, sulphides, tin, manganese and copper can interfere with the diazonium formation and absorb light in the measured region [15,18]. This risk can be mitigated using a dual channel spectrophotometric device. Seawater samples can also be injected into a sodium citrate carrier solution before combining with the reagent to avoid the precipitation of any calcium and magnesium present [91].

The detection of nitrite (NO_2^-) in this study is facilitated by a variant reaction (illustrated in Figure 2.12) that replaces sulfanilic acid and α-napthylamine with the derivatives sulfanilamide and N-(1-naphthyl)ethylenediamine dihydrochloride (N.E.D.H). It was first presented by Bratton and Marshall in 1939 [75] and more recently used by A. Tovar [92]. In this reaction, under acidic conditions, the nitrite reacts with the amino group of sulfanilamide to form the diazonium cation, which couples to N-(1-naphthyl)ethylenediamine (N.E.D.) to form the azo dye. The molar absorption coefficient (decadic) of the azo dye is 1500000 $M^{-1}m^{-1}$ [75]. The diazotization reaction represents an electrophilic aromatic substitution reaction with the diazonium ions (sulfanilamide) being the electrophilic agent and the second aromatic amine (N.E.D.) being the nucleophilic base [24]. In this study hydrochloric acid creates the acidic conditions (pH 1-2) under which nitrite reacts with sulfanilamide. The pH must be maintained in the region 1-2 so as not to affect the N.E.D. coupling [75]. A significant decrease in the acidity will cause a decrease in absorption.
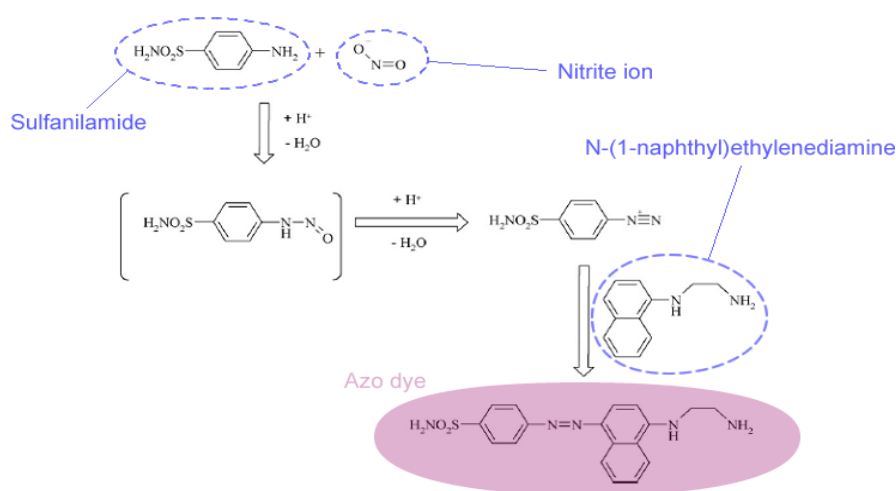
Figure 2.12 – The variant Griess reaction. Under acidic conditions nitrite reacts with the amino group of sulfanilamide to form the diazonium cation, which couples to N.E.D. [24].

In stop flow kinetic studies the production of azo dye in the griess reaction has been shown to require 60-430 seconds for 90% colour development [93]. Using a simple chicane mixer [94] it has been shown to take 144 seconds for greater than 90% colour development, as shown in Figure 2.13.
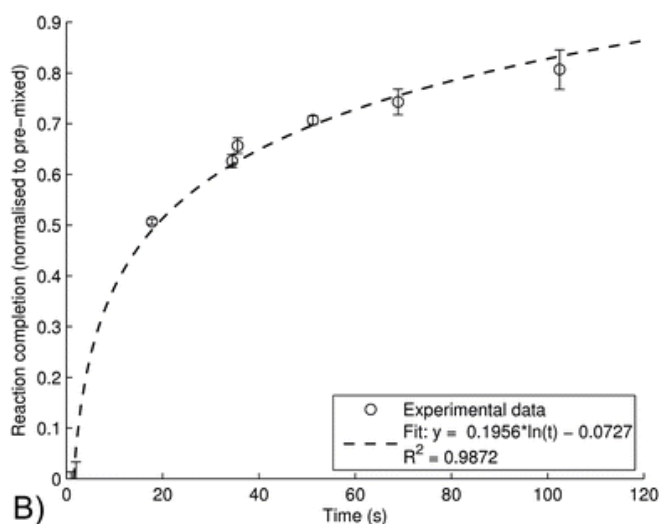
Figure 2.13 – Graph showing the Griess reaction completion against time where the absorption values are normalized to a completely mixed and developed solution [94].

It should be noted that both the stop flow and chicane mixer studies include the effects of mixing characteristics in the reaction kinetics (i.e. chicane mixer has a single diffusion boundary, see Section 2.6.2). An increase in the reaction times can be achieved through an increase in the extent of mixing.

2.4.1.1.1 Detection of ammonium and nitrate using the Griess reaction

The variant Griess reaction can also be used to detect ammonium (NH_4^+) and nitrate (NO_3^-) after their conversion to nitrite prior to diazotization [24,92]. The resulting absorption is the sum of that from nitrite and the reduced or oxidised secondary component. The concentration of the secondary component, ammonia or nitrate, is calculated by the difference between the total absorption and that of nitrite alone.

The oxidation of ammonium to nitrite was first presented by M. Berthelot in 1889. Hypochlorite and phenol in an alkaline environment was used to produce a blue dye whose absorption was proportional to the concentration of ammonium. More recently Richards [95] presented the oxidation of ammonium by its reaction with hypochlorite in the presence of potassium bromide (KBr), the product of which can be detected through the Griess reaction. Matsunaga [96] reported a modified Richards method that reduced the oxidation time of the ammonium from

3.5 hours to 1 minute. This reaction forms the basis for the detection of ammonium for future work suggested by this study. Sodium hypochlorite (NaOCl) is used to transform ammonia into monochloramine (NH$_2$Cl) at a pH> 7.5 (otherwise trichloramine, pH<4.5, or dichloraime is formed, pH 5-7) and the monochloramine in the presence of potassium bromide leads to the production of nitrite (Equation 2.11). Sodium Hydroxide (NaOH) is used as the buffer and to create the alkaline conditions. Polyvinyl alcohol (a synthetic polymer) can also be added to aid colour formation and act as a dispersing agent to prevent precipitation when sulfanilamide and sodium hypochlorite mix [97,98] during the detection of ammonium.

$$NH_4^+ + OH^- \rightarrow NH_3 + H_2O$$
$$NH_3^- + NaOCl = NH_2Cl + NaOH$$
$$NH_2Cl \xrightarrow{Br^-} NO_3^-$$

Equation 2.11
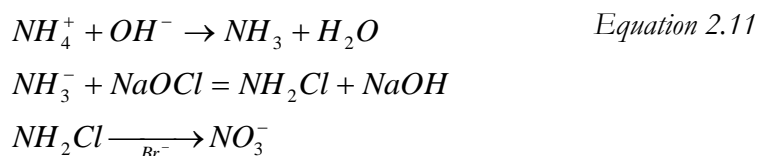
The reduction of nitrate to nitrite can be performed by chemical [24] or enzyme nitrate reductase [99] methods. Present day chemical reduction methods use cadmium (or copper coated cadmium), vanadium [100] or zinc columns as they offer a high lifetime and surface contact area. The most widely used are cadmium columns [101,102,103]. The column is designed to increase the surface contact area between the sample and the compound used in the reduction (hence increase the speed of the reaction). The simplest design is a bead packed tube. The reduction of nitrate to nitrite (Equation 2.12) can take place under acidic or alkaline conditions.

$$NO_3^- + 2H^+ + 2e^- \rightarrow NO_2^- + H_2O$$
$$Cd \rightarrow Cd^{2+} + 2e^-$$

Equation 2.12
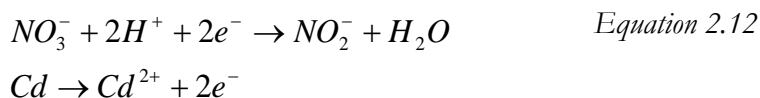
2.4.2 Luminescence

There are two luminescence methods used in the detection of nitrite; bioluminescence (B.L.) and chemiluminescence (C.L.). Bioluminescence uses the natural luminescence of a living organism, produced when chemical energy is converted to light [104,105]. Chemiluminescence is the consequence of a chemical or biochemical reaction (see Figure 2.14 for an overview of the mechanism that lead to a C.L. reaction). The reactions produce sufficient energy to induce the transition of an electron from its ground to excited state. This then decays to a lower energy state and in so doing emits a photon. No excitation light source is needed during luminescence detection so the method is highly sensitive as there is little attenuation or noise from filters. A limit of detection of 1-2nM for nitrate and nitrite (in laboratory conditions) has been achieved [106,107]. The limit of the detection is restricted in the majority of chemiluminescence sensors by the purity of the reagents used.

$$A + B + (\text{cofactor})$$

$$\downarrow \text{catalyst}$$

$$P*$$

$$P + h\nu \qquad P* + F \longrightarrow P + F* \longrightarrow F + h\nu$$
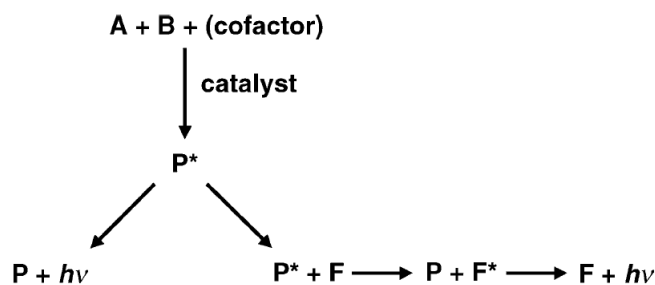
Figure 2.14 – Diagram showing the mechanisms that lead to a chemiluminescent reaction, (A) substrate, (B) oxidant, (P) Product, (P) Product in excited state, (F) fluorophore, (F*) fluorophore in the excited state, (hv) emission of radiation [**104**].*

The chemiluminescence method for the detection of nitrite and nitrate in seawater was first applied in 1982 [**108**] and can be used for other compounds or elements such as hydrogen peroxide, ammonium, chlorine, copper, oxygen, phosphate and sulphites [**109**]. The technique uses an acetic acid-potassium iodide mixture at room temperature for the reduction of nitrite to nitric oxide. The nitric oxide is then removed from solution by scrubbing with helium gas and passed through a chemiluminescence NO_x analyser.

The number of chemical reactions that produce C.L. is small, limiting the procedure to relatively few species. Some reagents can produce emissions for more than one analyte and fluids need to be pre-filtered. All are affected by temperature, pH and ionic strength [**104**]. The chemiluminescence method requires expensive equipment, intensive labour and large sample volumes. Most chemiluminescence systems also use a discontinuous method because of the production and build-up of bubbles during gas-separation [**104**].

Due to the discontinuous flow, low measurement frequency, large sample volumes, limited selectivity of reagents and effects of environmental variables a chemiluminescence method is not the first choice for use in an *in situ* sensor.

2.4.3 Fluorescence

Fluorescence is the excitation at one wavelength and the emission at another by a fluorophore. It is frequently used in the detection and classification of immunoassays, pathogens and in nucleic acid analysis. Fluorescence is the preferred laboratory method for the determination of ammonia. Using the reagent orthophthaldialdehyde (O.P.A.) it is possible to detect ammonium (in the laboratory) with a 1.5nM limit [**110**]. Fluorescence can also be used in the detection of nitrite, whereby nitrite is used as either a reagent or catalyst for chemical reactions that produce fluorescence molecules [**111**]. Nitrite levels affect the properties of the fluorescence through

development, enhancement or quenching allowing its concentration to be determined. The magnitude of the fluorescence response is a function of the nitrite concentration present. Figure 2.15 shows the fluorescence quenching caused by the addition of nitrites to Proflavine.
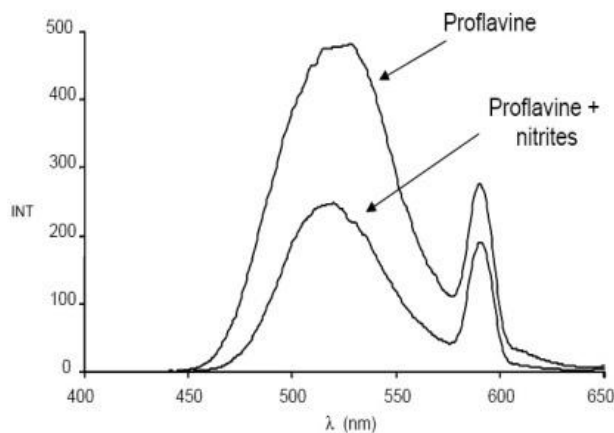
*Figure 2.15 – Quenching of the fluorescence by Proflavine and nitrites [**111**] where the intensity of the fluorescence response is reduced by the addition of nitrite.*

Optical detection systems for the measurement of fluorescence signals typically contain; a light source (for example; a mercury lamp, L.E.D, or laser), excitation filter, dichroic mirror (used in the separation of excitation and emission light), emission channels, an emission filter, detector and electronics [**112**]. Electronics are required to amplify the signal due to the low quantum yield of the fluorophores and the low emitted light strength. A weak light source must be used to excite the fluorophores to avoid bleaching. The dichroic mirror can be removed in setups where the excitation source is perpendicular to the emission detector such as in liquid waveguide capillary cells (L.W.C.C's) where the tube is illuminated transversely [**26**].

Chemicals that can be used in the fluorescence detection of nitrite include Aniline [**113**], and Proflavine [**111**]. The detection of nitrite using these chemicals relies on the reaction between nitrite and these aromatic primary amines to form a fluorescent azoic acid. Aniline reacts with nitrite to form the bezenediazonium ion ($\lambda_{ex}/\lambda_{em}$ = 220/296nm) and has been used to detect nitrite and nitrate (by prior reduction to nitrite) with concentrations as low as 4.6nM and 6.9nM respectively [**113**]. The fluid is heated (to 70°C) during the reaction to increase the yield of the diazonium. The total tubing length within a typical fluorescence instrument (capable of nanomolar detection [**113**]) is 5m and this allows a maximum throughput of 18 samples per hour (0.005 Hz), over a maximum operating time of 2 hours whilst deployed on a ship. Proflavine also reacts with nitrite, but in this case nitrite quenches the fluorescence of the diazonium ion ($\lambda_{ex}/\lambda_{em}$ = 290/519nm). It has been used with a commercial fluorometer to detect 20nM concentrations in seawater [**111**].

Fluorescence measurements suffer from background interference from dissolved organic matter & leachates in surface sea waters [114]. Reverse flow injection analysis (r.F.I.A.) can be used to correct this, whereby the sample acts as the carrier, while a fixed volume of reagent is injected.

2.4.4   Raman spectrometry

Raman spectroscopy uses a monochromatic light source to irradiate a sample (solid, liquid or gas) and measures the difference in frequency between excitation and emission [31]. The detection procedure is highly specific as it relies on the unique makeup or vibration of the particle. Nitrate and nitrite have two Raman intensity response peaks each (Figure 2.16b). Nitrate at around 1200 & 700cm^{-1} and nitrite at 1350 & 800cm^{-1} [115]. The intensity of the nitrite response is considerable smaller than nitrate (8 times) and as such the L.O.D. is higher. Therefore little research has been conducted into its use in the detection of nitrite.

The technique has been previously used for *in situ* detection of dissolved gasses [116] using the deep ocean Raman *In situ* Spectrometer (D.O.R.I.S.S.). Capable of measurements at a depth of 3600m it uses a 532nm wavelength laser and is contained within a package 1.76m long and 32cm diameter. This type of instrument can only be deployed on platforms with significant infrastructure as it has a mass of 211Kg. Fluorescence (350 to 550nm) is a problem in Raman spectroscopy, but at depths below 200m little interference has been reported (Figure 2.16a). The size and weight of Raman spectroscopy devices means they are not suitable for *in situ* deployment.
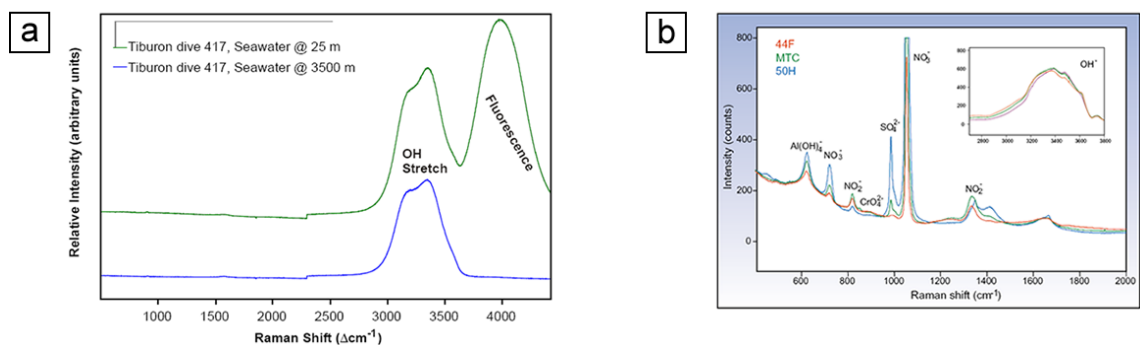
Figure 2.16a & b – a) The change in Raman intensity due to fluorescence with depth [116] and b) Raman spectrum for a variety of elements including nitrite and nitrate [115].

2.4.5   Capillary electrophoresis

Capillary electrophoresis (C.E.), first used in 1995 [117], is the separation of ionic species by their charge and frictional forces. A schematic of a typical experimental setup is shown in Figure 2.17. When a voltage is applied across electrodes in a capillary (25 to 100µm diameter) solute ions will

move towards an electrode of opposite charge. The concentration of nitrite or other relevant chemicals can then be detected using an optical method (UV–Visible or fluorometric) [118,119]. Using capillary zone electrophoresis resolutions of 0.271µM have been achieved in the detection of nitrite in natural water [120].
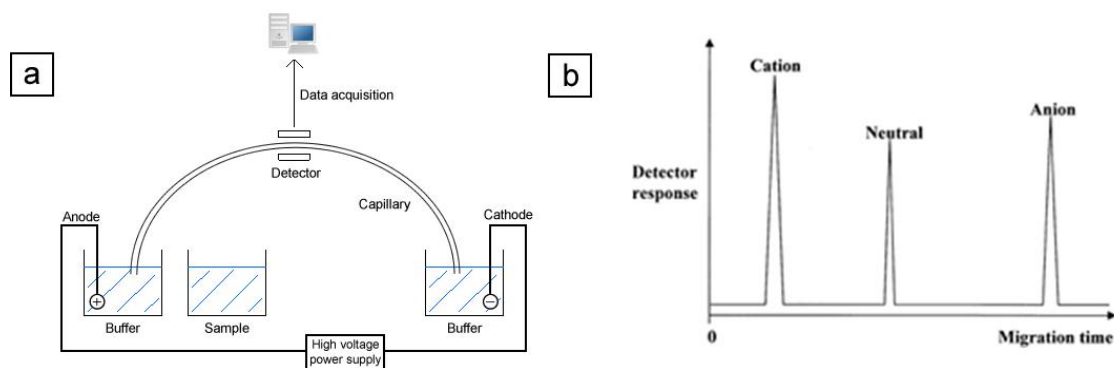
Figure 2.17a & b – a) A diagram showing the overall setup of capillary electrophoresis, b) An electropherogram showing the detector response over time with a potential applied across the electrodes [21].

The removal of proteinaceous material is necessary before any analysis and adds extra steps therefore reducing the scaling possibilities for this technique. The success of C.E. is also highly dependent on the buffer solution used and it is not easy to analyse anions in seawater [24].

2.4.6   Electrochemical

Nitrite and nitrate can be oxidised or reduced at an electrode as they are electroactive species. The concentration levels can then be detected amperometrically [121], potentiometrically [122] or voltammetrically [123]. Electrode modifications for improving sensitivity and repeatability include deposition of a fresh surface layer after each analysis (not suitable for continuous monitoring), increasing the surface area through surface and design modifications, chemical surface modifications and the use of biological catalysts. Electrochemical detection can be combined with either chromatography detection or capillary electrophoresis [124]. Significant problems including low repeatability (from passivation of the electrode) and sensitivity are encountered unless electrode modifications are carried out. The presence of other electro-active compounds in the solution can also interfere in the analysis as the potential for nitrite oxidation is high. These difficulties make electrochemistry unattractive for further development. However, with a detection limit of 0.01µM and a detection range of between 0.01µM and 10mM [13] it could provide the necessary performance (as per the performance parameters in Section 2.2).

2.4.7 Laser Induced Breakdown Spectroscopy

Laser induced breakdown spectroscopy (L.I.B.S.) or laser spark spectroscopy (L.A.S.S.) started to be used for single wavelength multi-element analysis in the 1980's. Broadband L.I.B.S. is now used to perform total spectral analysis, in gas or water, removing the need to perform thousands of measurements. Figure 2.18a shows a schematic of the process. It is the analysis of the light emission that is produced when a pulsed laser beam (>100 megawatts/cm) is directed at a sample to create high temperature micro-plasma [125]. A photosensitive detector is used to collect the spectrum of light emission and record its intensity at specific wavelengths. A high temperature (>10,000K) and high electron density plasma is produced and the sample material is broken down, vaporised, atomised and partially ionised. During the plasma formation, electrons interact and recombine with ions to release energy across a broad spectral range of 200-980nm (as shown in Figure 2.18b). Two laser pulses between 50 and 100μs apart are used. The first produces a cavitation bubble in the water while the second pulse excites the plasma within. Due to the size, power requirements and low sensitivity of the devices this L.I.B.S. detection method is unsuitable for *in situ* deployment as a low-cost and miniature sensor is required.
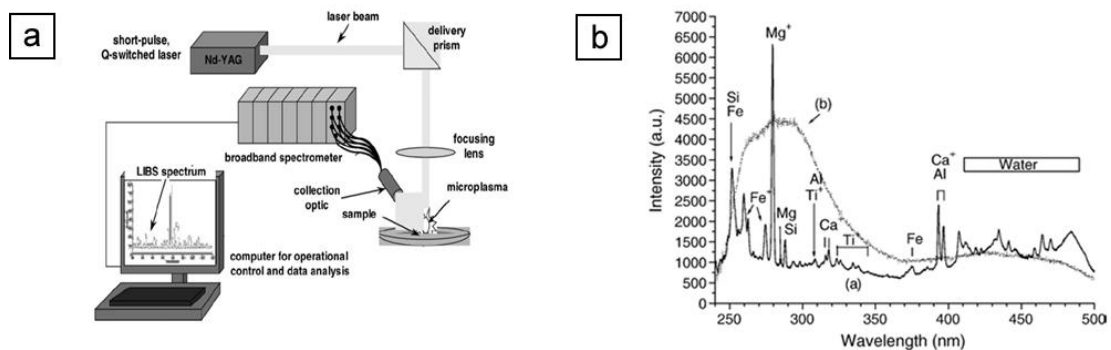
Figure 2.18a & b – a) Diagram of L.I.B.S. setup [125] and b) Graph showing the broadband spectroscopy reading from a water sample [126].

2.4.8 Mass spectrometry

Mass spectrometry is the measurement of the mass-to-charge ratio of ions, and can be used to detect multiple species in parallel [127]. It is a well known laboratory technique and the principles were discovered by Eugen Goldstein in 1886. It relies on a magnetic field to separate moving ions of different masses due to Newton's second law (e.g. lighter particles have an increased deflection). For the analysis of aqueous fluids it is normally combined with gas chromatography to enhance the separation of compounds [128]. Current *in situ* mass spectrometry instrumentation exists but measures 1.14m in length and 19cm in diameter [112] and draws 100W during

operation. Therefore this technique is unsuitable for the *in situ* deployment situations proposed in Section 2.2.1.

2.4.9   Summary

Table 2.7 provides an overview of this section indicating whether each technique fulfils the requirements of the key performance drivers described in Section 2.2. It is possible to conclude that the most suitable technique for the reliable, sensitive and precise detection of nitrite at depth is colourmetric spectrophotometry. The low power requirements (light source and photo detector) and its current use as an ISO standard are additional advantages of the method. The specific reagents used in the detection of nitrite in this study are detailed in Chapter 4. Other chemical sensing techniques covered have either high power requirements or insufficient performance for the metrology of nitrite.

Technique	Requirement					
	Size	Weight	Power	Sample volume	Sensitivity	Selectivity
Direct spectrophotometry	✓	✓	✓	✓	✓	✗
Colourmetric spectrophotometry	✓	✓	✓	✓	✓	✓
Luminescence	✗	✗	✓	✓	✓	✓
Fluorescence	✓	✓	✓	✓	✓	✗
Raman spectroscopy	✗	✗	✗	✓	✗	✓
Capillary electrophoresis	✓	✗	✓	✓	✗	✗
Electrochemical	✓	✓	✓	✓	✗	✗
L.I.B.S.	✗	✗	✗	✗	✗	✓
Mass spectrometry	✗	✗	✗	✓	✓	✓

Table 2.7 – Overview of nitrite detection techniques and their suitability for use in an in situ sensor based on key performance parameters.

2.5   Existing *in situ* systems

The majority of literature on chemical sensors refers to instrumentation that is based in a research laboratory. The demand for *in situ* sensors (produced by the need for prompt water quality analysis) has led to several commercial nutrient analysers being developed. This section reviews a number of these analysers. Table 2.8 towards the end of this section summarises those available.

The NAS-3X sensor [129], shown in Figure 2.19a, has been deployed for 6 to 12 months in the Atlantic Network of Interdisciplinary Moorings and Time-series for Europe (A.N.I.M.A.T.E.) program. When not sampling it can be put into 'sleep mode' which has a decreased power

consumption (<0.002W). It is a commercial *in situ* nutrient analyser system and is available (£25,000 each) in four different versions which measure one of the following nutrients; nitrate (0-300μM), phosphate (0-6μM), silicate (0-60μM) or ammonia (0-100μM). The sensor uses rudimentary macro scale technology along with a 2cm long optical detection cell to achieve a 0.05μM limit of detection for nitrite. For the analysis of nitrite and nitrate it relies on chemical reagents (Sulphanilamide and N.E.D.) to react with nitrite (nitrate reduced to nitrite) in the seawater forming a coloured dye (colourmetric spectrophotometry technique, Section 2.4.1.1) and then measures the light attenuation (see Figure 2.19b for a schematic of this sampling process). The nitrite version of the sensor can take 720 samples per deployment at intervals greater than 5 minutes apart [130]. It is typically *in situ* for 1 to 3 months at depths up to 250m.
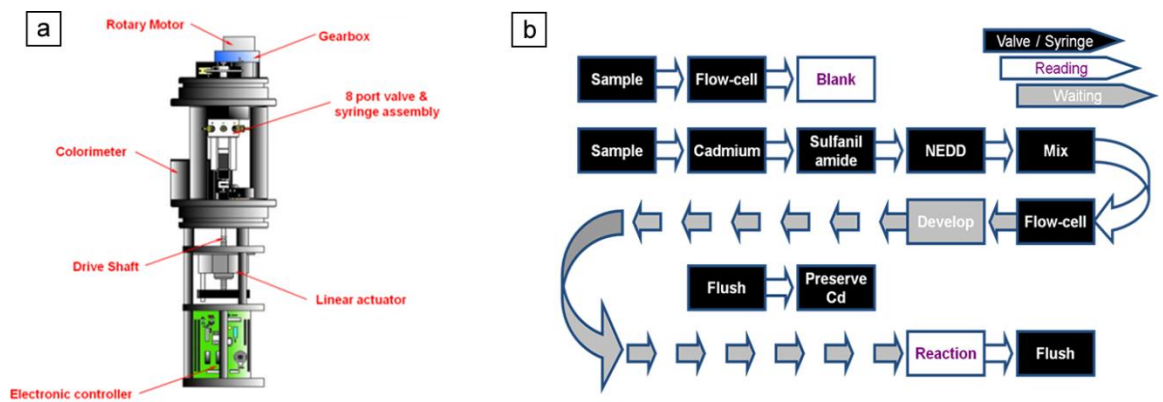
Figure 2.19a & b – a)Internal diagram of a NAS-3X and b) the automated sampling process flow used within the sensor for the detection of nitrate [129].

M. Finch et al [71] have reported a nitrate detection device based on U.V. absorption measurements (>0.21μM L.O.D.). Rather than taking an entire spectra, 6 absorption measurements are taken at; 205, 220, 235, 250, 265 and 280nm. It can be deployed to depths of 5000m and is capable of measurements every 1 second (1 Hz). A 1 Hz rate roughly translates to a 1m resolution on a hydrographic cast or 5m during towing. A second reference absorption at 300nm compensates for any particulates. Interference from chloride, bromide was removed using a constant ratio linked to salinity and each other [71].

K. Johnson et al [40] also presented an *in situ* ultraviolet spectrophotometer (I.S.U.S., Figure 2.20b) that could resolve nitrate concentrations down to 1.5μM whilst deployed on a mooring in the Pacific Ocean for 6 months (maximum depth of 2000m). The absorption of the sea-water was measured with a spectral scan between 200 and 400nm using a 3W Fiberlight® source. The resolution could be increased to 0.2 μM by averaging over 30 seconds. Averaging over a time

period lowers the temporal resolution of the system, which was stated as 1 second (limited by the time needed to integrate enough light onto the detector array to produce the desired signal to noise ratio. No degradation of performance was noted over the first 3 months but absorbance values drifted linearly higher over a longer time period. The drift was attributed to fouling of the instrument. The correction required for temperature changes (1% per degree Celsius) was reported to be considerably smaller than that needed for salinity changes.
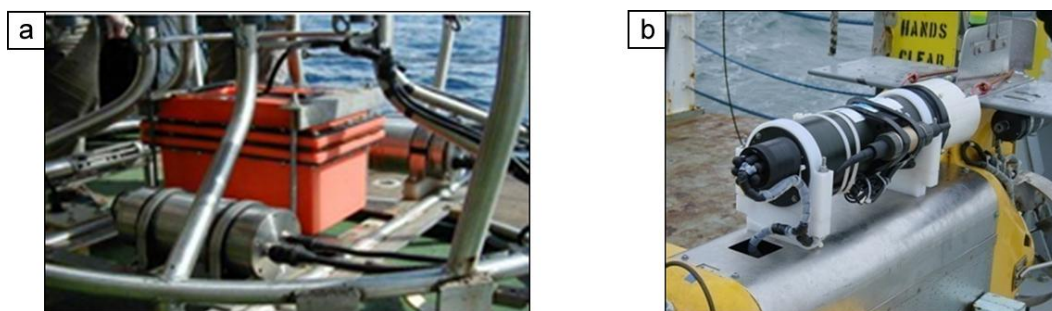
Figure 2.20a & b – a) S.U.V.6 detection system mounted on a rosette frame and b) I.S.U.S. mounted on a Chelsea technologies Seasoar.

L.W.C.C. instruments that have been deployed in the ocean (for example; S.E.A.S. [**97,91**]) report that a waveguide of 1m gives a nitrite limit of detection of 1.2-2.5nM. The S.E.A.S. or spectral analysis system operates up to a maximum depth of 500m and utilities the Griess reaction method for the detection of nitrite through colourmetric spectrophotometry. It uses a 710nm light source and measurements are taken by 5 spectral scans over 20 seconds, but only after 160 seconds of stopped flow for colour formation. The sensor (not including any chemical reservoirs) measures 11.5cm in diameter and 50cm in length and requires 6W of power during operation [**91**]. Compared with the specifications for the L.O.C. sensor to be developed by this study the sampling rates are far lower, power consumption higher, and the size of the instrument greater.

The sensors presented in this section and listed in Table 2.8 have a relatively high power consumption (>3.4W) and the batteries required to run them *in situ* need to have a high capacity (with a power consumption of 4 Watts a 10Amp hour battery would only last for 30 hours). None of the sensors utilise L.O.C. technology and many are contained within large housings to protect fragile electronics and detection setups. Using L.O.C. technology will decrease the size and increase of the deployability of an *in situ* nitrite sensor.

Sensor	Ref.	Principle	Chemical	L.O.D. (µM)	Sampling Rate (Hz)	Dimension (HxWxD)(cm)	Power (W)
I.S.U.S.	[40]	Direct UV-Vis	Nitrate	1.5	1	44xØ12.7	3-5
S.U.V.6	[71]	Direct UV-Vis	Nitrate	0.21	1	43xØ11.4	3 - 4
N.P.A./D.P.A	[131]	Colourmetric	Nitrite	0.02	0.00008	122xØ32	10
SEAS-II	[97]	Colourmetric	Nitrite	0.001	0.01	50xØ11.5	6
SubChemPak	[132]	Colourmetric	Nitrite	0.001	1	94xØ12.7	40-80
AquaSensor	[133]	Colourmetric	Nitrite	0.15	0.003	48xØ16.8	6
T.U.C.S	[134]	Raman	Nitrite	2	30	36x10x15	6
NAS-3X	[129]	Colourmetric	Nitrate/Nitrite	0.05	0.003	79.9xØ24.6	3.4

Table 2.8 – Overview of current in situ sensor types, performance, power requirements and dimensions.

2.6   L.O.C. technologies

Lab On a Chip (L.O.C.) technologies allow laboratory functions and processes to be integrated and scaled down to a miniaturized chip format [135,136]. In turn these chips can be used to form smaller, lower cost and lower power sensors than are currently commercially available. Miniaturisation brings additional benefits including lower fluid volume consumption and faster analysis [137]. A guide to the theoretical science behind the technologies and a detailed benefits analysis has been presented by H. A. Stone et al [138]. There are numerous demonstrations of L.O.C. devices in the laboratory where it is necessary to use standard bench top equipment to operate them. However there are no demonstrations of integrated L.O.C. devices *in situ* (see Section 2.5) where the benefits (i.e. lower power consumption) would be further pronounced [139].

As one of the objectives (Section 1.1) of this study was to move forward the conversion of the 'chip in the lab' to the 'lab on a chip' that can be deployed *in situ*, the first step taken was the integration of optical and micromixer L.O.C. components. These two have a big impact on the ability to miniaturise and to minimise reagent volume consumption. The development of off-chip pumps and valves is less important as they will have a smaller effect on reagent volumes. Also, miniature commercial products (hence reliable) are already in existence to provide these functions. Therefore it is proposed that a two step approach is used in the creation of a deep sea *in situ* L.O.C. sensor. The first, to integrate optical detection and mixing is covered by this study, whereas the second to integrate pumps and valves is outside the scope of the study and suggested as a next step (see Section 7).

This section reviews the two elements (optical absorption cells and micromixers, Section 2.6.1 and Section 2.6.2 respectively) that are integrated into a L.O.C. device and the state of the art in

L.O.C. systems (Section 2.6.3) that are relevant to the application and design of a nitrite sensor. This research is used as background in the design and development of the L.O.C. devices in Chapter 4. Current methods of fabrication used to manufacture low-cost robust L.O.C. systems are also reviewed in Section 2.6.4 to provide background for the novel techniques developed in this study.

2.6.1   Optical absorption cells

To provide a sufficiently long absorption cell (and hence limit of detection and sensitivity), which is not influenced by stray light, liquid core or waveguide capillary cells (L.C.W's or L.W.C.C's) are often used for spectrophotometry in macro devices [97]. Due to the long absorption cell path lengths possible (up to 5m) L.W.C.C's are used for detecting ultra low concentrations of analytes. These waveguides provide a reliable method of extending the path length of light whilst limiting internal volume of the cell and light loss with non collimated sources. This lowers the minimum absorption that may be resolved and determined. A typical L.C.W. is a hollow tube (I.D. < 1mm) constructed from a low refractive index material (~1.29) and uses total internal reflection to contain light within a fluid (with a higher refractive index than the tube ~1.33 – 1.34 [97,26]) that flows inside the tube. Figure 2.21 depicts the principle of operation of two types of L.C.W., the first depicts (Figure 2.21a) a hollow Teflon tube (Type I L.C.W.) and Figure 2.21b shows a Teflon AF clad silica tube (Type II L.C.W.).
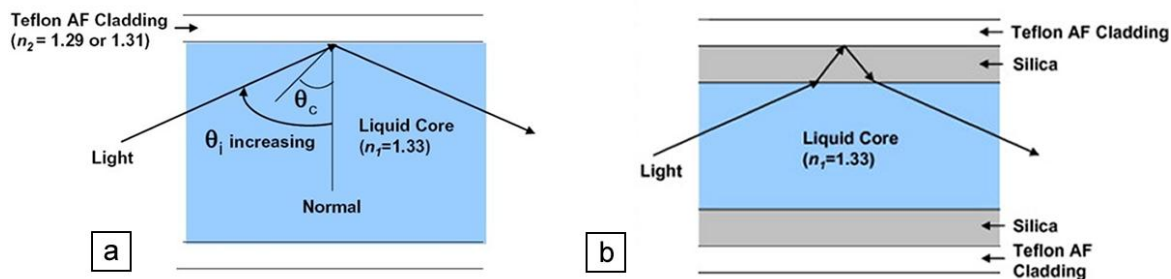
Figure 2.21a & b – a)The path length of the total internally reflected light in a type I L.C.W. and b) the light path in a type II L.C.W. where θ_i and θ_c are the incidence and critical angles [26].

The long path length (and hence physical size) of these absorption cells, their fragile construction and the fact that they would need to be externally mounted on a Lab On a Chip device makes them 'as is' unsuitable for a first prototype *in situ* sensor.

Optical absorption cells are often incorporated into L.O.C devices as sections of microfluidic channel (100μm [140] to 10mm in length [141]). Waveguides are used to direct (collimate)

excitation and emission light into and out of these cells. They are not normally used to decrease the propagation losses of light or the influence of stray light within and on the cell. It has been shown that the principle on which L.W.C's function can be integrated into microscale devices [142,143] however the situations in which materials such as Teflon AF can be used are limited due to the biofouling, bubble trapping and adsorption of surface reactive species that occurs over extended deployment periods [144,114]. Similar waveguiding absorption cells have been integrated into L.O.C. devices by either using lower refractive index (<1.34) cladding on the base and lid of the microfluidic channel [145] or by using air channels (R.I≈1) either side [146,147]. This 'two dimensional' waveguiding has a higher propagation loss than a waveguide capillary cell (25dB/m compared with 0.02dB/m [148]) and is not normally used to extend the length of the absorption cell past that of the dimensions of the L.O.C. device. The low cost and ease of integration of two dimensional waveguiding for an optical absorption cell in a L.O.C. device means that it is attractive for this study. It can be used to lower the propagation loss in a cell and reduce interference between two collocated cells (i.e. in a dual channel spectrophotometer, Section 2.4.1.1). The use of absorption cell waveguides in an L.O.C. is detailed in Section 4.3.1.3.

2.6.2 Micromixers

For quantitative reactions between differing fluid species or the even distribution of particulates, in an L.O.C. device, it is important to have rapid, effective and stable mixing [149]. Devices that measure absorption to detect chemical concentrations produce signals proportional to mixing levels. Therefore any variation in the degree of mixing during sampling will produce erroneous and unreliable results (as stated in Section 2.2.20). The size of the mixer (total internal volume as well as channel cross section) will affect the pressure drop over the L.O.C. device, the effective flushing volume, dispersion (and hence time response) and minimum resolvable volume (Section 2.2). In general a greater mixing efficiency decreases device size, weight, and improves reliability. Mixers must also be able to retain mixing efficiency and produce a constant mixing level throughout minor variations in pressure, flow rates, surface tension and fluid density.

A complication of mixing on the microfluidic scale is the inability to use turbulent flow (generated through channel geometry changes) to mix a fluid as a fluids inertia (proportional to mass) no longer has a significant effect [150]. The micromixers focused on and used within this study are specifically designed to rely on laminar flow mixing not localised high Reynolds number turbulent flows as they cannot be replicated in small channels.

Micromixers can be split into three main categories using the technique they utilise to mix fluids; serpentine, split and recombine and herringbone. The most commonly found type in L.O.C.

devices is the serpentine (otherwise known as a chicane mixer, shown in Figure 2.22a) due to its ease of fabrication (simple rectangular channels) and design. It relies on diffusion along the boundary layer of the fluids (i.e. movement of particles from a region of high concentration to a low concentration). As there is only a single boundary layer in a chicane mixer a long path length is required to achieve complete mixing and results in a high back pressure.
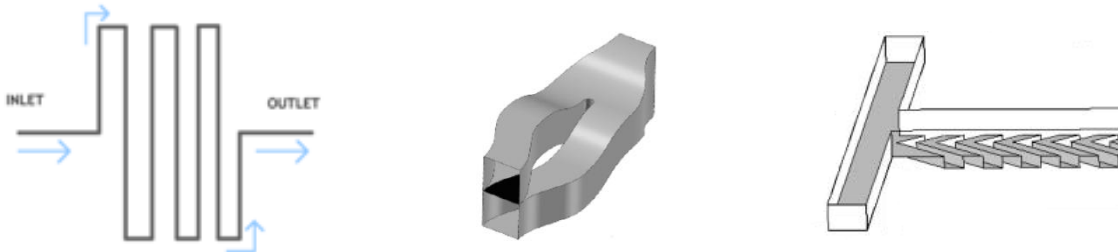
*Figure 2.22a, b & c – Illustrations of the channel shapes for the three main micromixer categories a) serpentine or chicane mixer, b) split and recombine [**151**] and c) herringbone or grooved channel [**152**].*

An improvement on the chicane mixer principle is the split and recombine micromixer [**151**] illustrated in Figure 2.22b. It is based on the principle of increasing the number of diffusion boundary layers and therefore increasing the extent of mixing over a set length. Both horizontal and vertical lamination can be used in the split and recombine (S.A.R.) technique [**153,151**]. The technique enables mixing to take place in a compact space, however the design must ensure that smearing is not increased due to offset fluid flows (i.e. longer path length for certain fluid segments). Herringbone mixers (shown in Figure 2.22c) were first introduced by Stroock et al [**154,155**]. They have been optimised in many studies since [**156,157,158,159**]. The grooves in the channel are designed to induce helical flows within the fluid (resulting in folding and stretching) and aid the underside transportation of fluid to increase the boundary layer contact area. The herringbone designs produce smearing due to the transport of fluid in the grooves and are unsuitable for use in accurate, high resolution sensors. They do however offer an opportunity to achieve a lower pressure drop. A comparison of all three of these mixer types at micro litre flow rates can be found in Table 2.9 where the key performance parameters reviewed in Section 2.2 are used to help identify the most micromixer suitable for this study.

Ref.	Mixer Type	Flow rate (μl/min)	Pressure drop (kPa)	Mixing length (mm)	Mixing level (%)
[160]	Chicane	405.0	n.p.	75	>90
[161]	Chicane	40.0	n.p	2.8	81
[162]	S.A.R. – horizontal	1.2	2.86	2.4	>90
[162]	S.A.R. – vertical	0.9	1.3	2.4	>90
[163]	S.A.R.	4.8	3	2.8	>90
[151]	S.A.R.	3500.0	n.p.	960	>90
[164]	S.A.R.	4.5	n.p.	12	>90
[154]	Herringbone	20.4	n.p	9	>90
[156]	Herringbone	1.1	n.p.	0.44	80.5

Table 2.9 – Comparison of micromixer performance across the three main categories, where n.p. indicates that the information is not provided in the reference.

Although the minimum resolvable volume is not presented in the majority of micromixer literature it is a key parameter in the selection of a micromixer type for this study (i.e. minimal dead volume and smearing). The pressure drop over the mixer is also rarely reported. However it is not expected that it will be a key parameter until pumps are integrated onto the same L.O.C. device as the mixer and optical detection cell, which is outside the scope of this study. The maximum pressure capability of the pump will then become a limiting factor. Therefore the most suitable type of micromixer for this study (i.e. to reliably mix two fluids over the shortest length possible) is a split and recombine mixer. It can operate over a range of flow rates as the principle on which it operates remains valid throughout laminar flow and can be designed to produce minimal smearing.

2.6.3   Integrated L.O.C. systems

L.O.C. devices combined in a single package with detection systems, pumps and microfluidics are few and far between. Figure 2.23 provides an overview of what a true L.O.C. device should comprise of. Several examples that do exist are examined in this section. Other micro devices that have not been fully developed into compact or continuous flow devices yet have the capability to produce rapid and accurate measurements are also presented.

Lab on a Chip

Fluid delivery system → Positive displacement pump / Centrifugal pump / Electroosmosis pump / Biological pump

Fluid handling → Micro channels / Fluid mixing

Detection mechansim → Optical detection / Electrical detection

Electronics → Electrical ciruitry for driving detection and delivery system
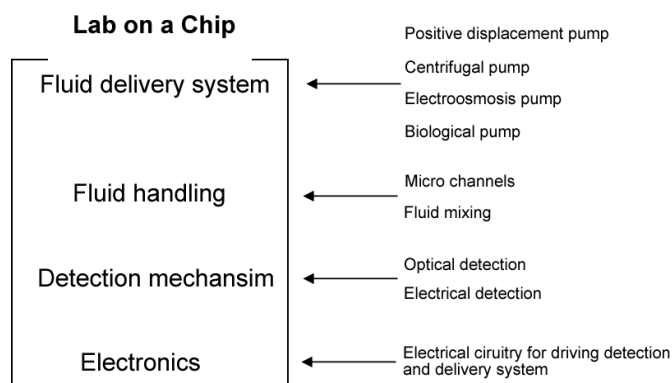
Figure 2.23 – Schematic of what makes up a Lab On a Chip chemical analyser and example components for each category.

A significant proportion of the literature available on L.O.C. spectrophotometric devices present a microfluidic cell and measure absorption of the fluid within it using bench top components (i.e. laser light sources and photomultipliers). The silicon device (35mm by 35mm) presented by Bargiel et al [141] and used in the measurement of phosphate concentrations is one such device (see Figure 2.24a). It uses a 700μm wide, 150μm deep and 10mm long dog legged microfluidic path (1.05μl) as the optical cell allowing absorption measurements to be taken using two 125μm (62.5μm core) glass fibres connected to a Ocean Optics spectrophotometer (PC200). The optical fibres are inserted into the device and sealed in place (see Figure 2.24b) using U.V. curable epoxy (Epo-Tek UVO-114).
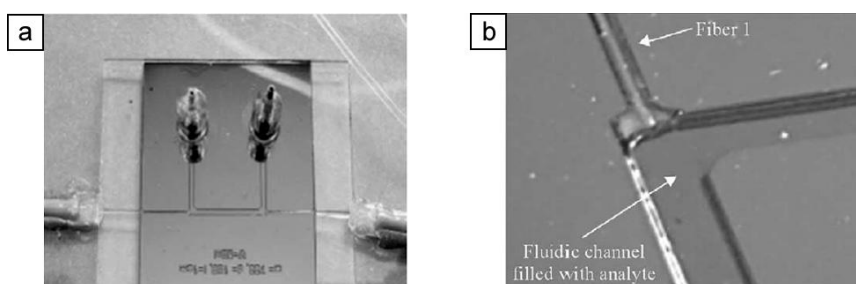
Figure 2.24a & b – Picture of, a) a silicon device incorporating an absorption cell and b) the interface between absorption cell and optical fibre for the same device [141].

The fragile nature of device and the use of bench top components renders it is unsuitable for *in situ* deployment. However the use of optical fibres to launch the light into the cell decreases propagation and coupling losses as well as L.O.C. device fabrication complexity. For use with an *in situ* sensor this method would need development as the poor finish on the epoxy seal will lead to bubble and particle trapping (leading to smearing and decreases in precision). A fluorescence detection system presented by Zhao et al [165] butt couples the optical fibres against the

P.D.M.S. channel wall to avoid penetrating into the channel (illustrated in Figure 2.25b). Additionally a L.E.D. is used as the excitation light source (UVLED365-10, Roitner) although the detection is still carried out by a Photomultiplier (Hamamatsu R928) as shown in Figure 2.25a.
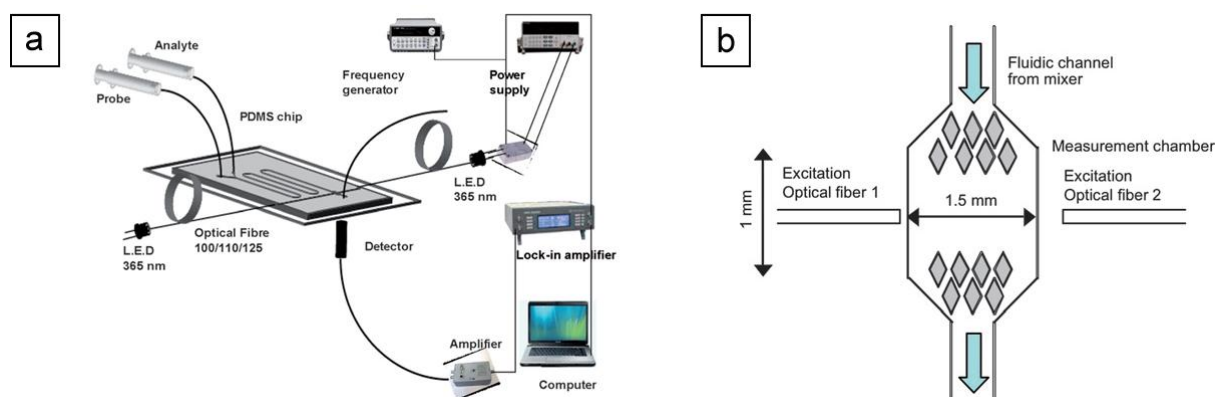
Figure 2.25a & b – a) A schematic overview of the experimental setup and b) optical detection method of the fluorescence detection system used by Zhao et al [165] to measure lead concentrations.

The two systems (modular and monolithic) described by Tiggelaar et Al. [166] and designed to detect ammonia in solution (Berthelots reaction, Section 2.4.1.1.1) have similar characteristics to that required by this study. Both use a 7mm long (200µm depth and 0.8mm width) microfluidic absorption cell constructed from a silicon substrate (which is not an ideal material for low-cost L.O.C., see Section 2.6.4) bonded to a Pyrex plate. Single channel absorption measurements (λ=590nm) [167] are carried out by a L.E.D. and photodiode (connected to a Model SR 830 Stanford Research lock-in amplifier) using 45° angle surfaces to couple the light in and out of the cell [168]. Individually the cell is capable of detecting premixed concentrations of ammonia with a limit of detection of 0.002µM (2×10^{-7} decadic absorption units).

Both systems integrate the absorption cell with four piezoelectric peristaltic micro pumps (maximum flow rate of 30µl/min and a maximum pressure of 700mbar), two mixers (T-junction) and a reaction coil (chicane mixer). The excitation source (590 nm Agilent Technologies HLMP-EL08-VY000 L.E.D.) and detector (Silonex SLSD-71N1 photodiode) are separate components. In the modular system the components are fabricated separately and all coupled to an electrical and fluidic circuit board. In the monolithic system (shown in Figure 2.26a & b) they are realised in the same combined fabrication process. Neither was capable of achieving the limit of detection of the standalone absorption cell (monolithic - 1mM over a range of 10-20mM, and the modular 0.5µM over a range 5.6 to 560µM) due to the fluctuation in solution flow rates and hence the colouration and absorbance (Section 2.6.2). The monolithic system had a limited

lifetime of approximately one day as the bond between the silicon and the Pyrex wafer failed around the pumps. This failure occurred whilst in a laboratory setting and at atmospheric pressure (i.e. not at depth).
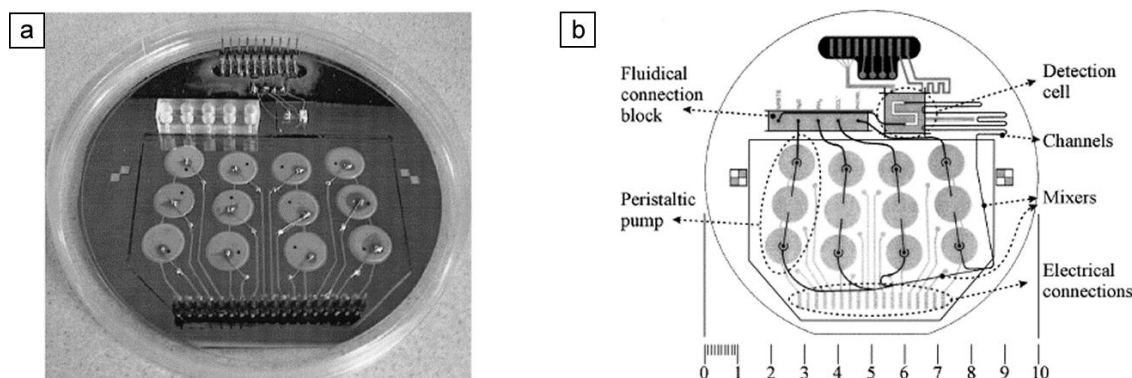
Figure 2.26a & b – a) Photograph of the monolithic device with four piezoelectric peristaltic pumps visible, b) diagram of the overall layout with a scale in centimetres [166].

The device reinforces the reasoning behind the integration of pumps and valves being outside the scope of this study. They are the only 'moving' part of the device, did not perform to the required standard and have failed. The failure of the pumps in the monolithic device renders the entire device useless. The devices also highlight the need for consistent flow rates. Therefore this study uses low cost (rapid fabrication) and proven fabrication routes, with additional design focus on the effects of inconsistent flow rates (see Section 4.3.3.1).

The total integration of light sources and detectors can be achieved using dye lasers and embedded photodiodes (selective doping) [169]. Fabricated out of SU-8 using U.V. lithography and with a footprint of 15mm by 20mm the device presented in Figure 2.27a & b is designed to detect absorption changes at a flow rate of 1μl/hr. The sensor comprises of a dye laser, multimode waveguides, a basic fluidic mixer (50μm wide and 8mm long), an optical detection cell (500μm length) and five photodiodes. Limited results were presented although a 60μM xylenol orange dye at 576nm was reported to have an absorption of 0.154A.
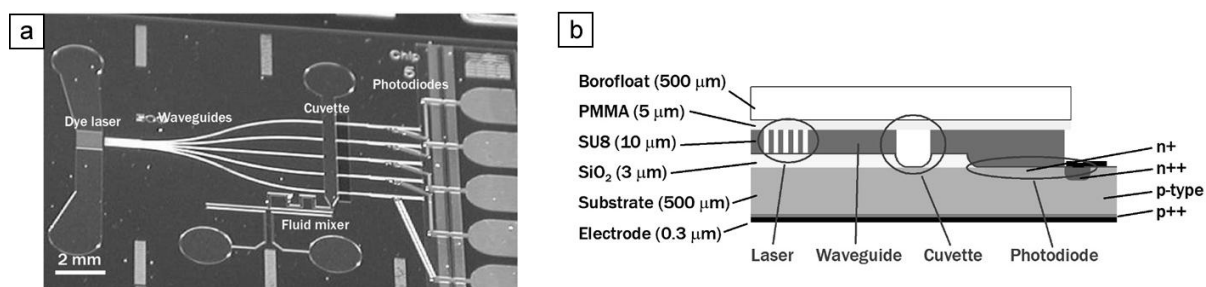
Figure 2.27a & b – a) Photograph of the L.O.C. device before the bonding of a lid, b) diagram of the cross section indicating the construction of dye laser and photodiode [169].

In this case an external light pump (≈14mW) is still required to drive the dye laser yet has introduced complex (and high cost) fabrication methods. The device is not suitable for operation *in situ* or at pressure, and would require significant reengineering to measure the absorption during continuous flow.

An example from literature of integrating the light source and detection into a small package can be found in the miniaturised system for the detection of fluorescence by L. Novak et al [112] and is shown in Figure 2.28a & b. It uses a 490nm wavelength L.E.D. driven by a lock-in amplifier to excite a fluid placed on a focusing lens and measures the emission using a silicon photodiode. The L.O.D. for a concentration of fluorescein was reported to be 1.96nM, with a maximum detectable value of 6.89mM (photodiode saturation). Although not a true L.O.C. system and not integrating continuous flow it provides a benchmark for the packaging of L.O.C. sensors.
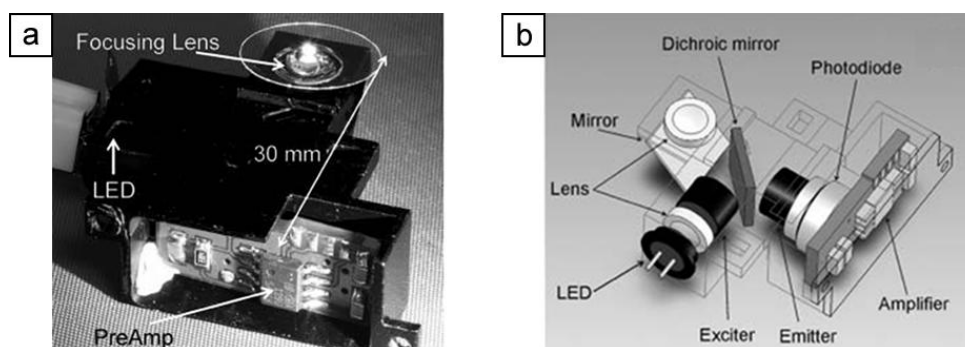
Figure 2.28a & b – a) Photograph of the integrated detection system presented by L. Novak et al, assembled in a metal housing (30x30x11mm) and b) a diagram with the key parts illustrated.

A novel solution to the problem of fluid delivery (e.g. pumping) is presented by M. J. Madou et al [170,171]. The centrifugal force on fluid within a rotating microfluidic device is used to move fluid from the inner to outer edge of a disc [172]. The compact disc (C.D.) shaped device (with

microfluidic channels of 500μm width by 250μm depth, Figure 2.29) is rotated at a range of R.P.M's (500-4200) to produce flow rates from 10nls^{-1} to greater than 100μls^{-1} with a pressure of around 20kPa (1800rpm using water) [172].
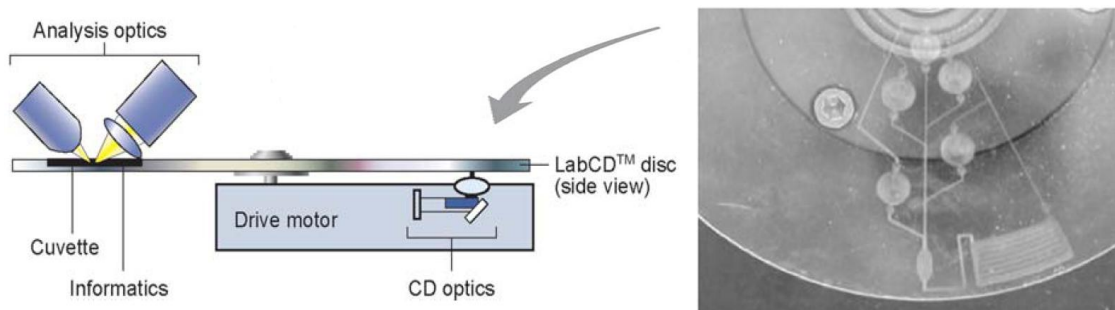
Figure 2.29 – Diagram of LabCD^{TM} instrument using reflection spectrophotometry [173] and a demonstration flow sequencing C.D. device.

Although this system has been commercialised by several companies (Tecan and Gyro) and they are disposable and cheap, the deployment of this device at depths would present numerous problems. To withstand pressure the structure needs to be contained in fluid (normally oil, as detailed in Section 4.2.1) and due to the viscosity of the fluid compared with air achieving the rotational speed necessary would require large amounts of power. The sensitivity of optical measurements is also limited by the short path lengths that can be achieved (e.g. depth of channel) unless optical gratings or mirrors are used.

The most relevant *in situ* L.O.C. based sensor example available at the time of writing is that presented by C. M. McGraw et al [1]. It is an autonomous microfluidic system for phosphate detection based on measuring the absorption of yellow vanadomolybdophosphoric acid at a wavelength of 370nm. The absorption is measured across the height of a 22mm long serpentine channel (200μm wide by 200μm high channel, see V in Figure 2.30a) using a U.V. L.E.D. (NSHU550E, Nichia Corporation) and photodiode (S1227-33BR, Hamamatsu Photonics UK Limited) directly butted against the lid and base of the chip (Figure 2.30b). The chip is fabricated from two P.M.M.A. layers sealed using pressure sensitive adhesive.
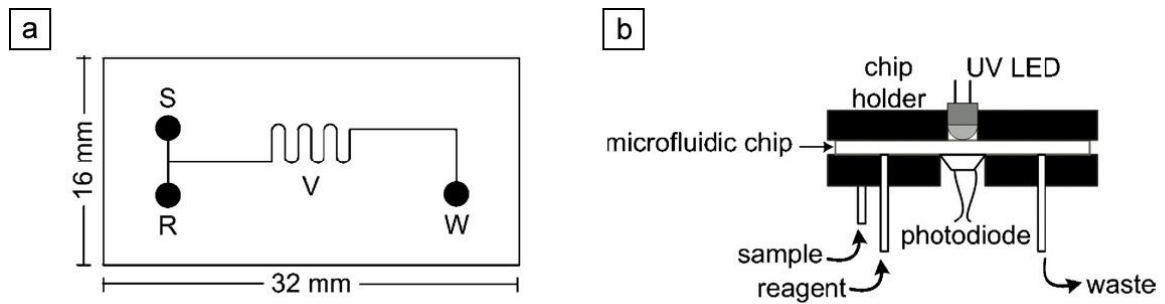
Figure 2.30a & b – a) Diagram of indicating the microfluidic paths where S and R are inlets, V is the serpentine channel and W is the outlet, b) A cross section showing the principle on which the absorption measurements are made [1].

The L.O.C. device is packaged along with a peristaltic pump (2PP10.S Eurolink Associates, Tyne and Wear), and reagent and waste bags into a waterproof polycarbonate box (see Figure 2.31 for schematic). A separate box or 'base station' contains the electronic control, data acquisition and communication components and battery. The sensor is capable of lasting 7 days (48 measurements per day) using a 12V, 7Ah battery giving a power consumption of 0.5W (or 0.25W per measurement). The limited measurement frequency is due to the stop flow measurement system that the sensor uses (to allow mixing and reaction to occur) and decreases the temporal resolution of the system.
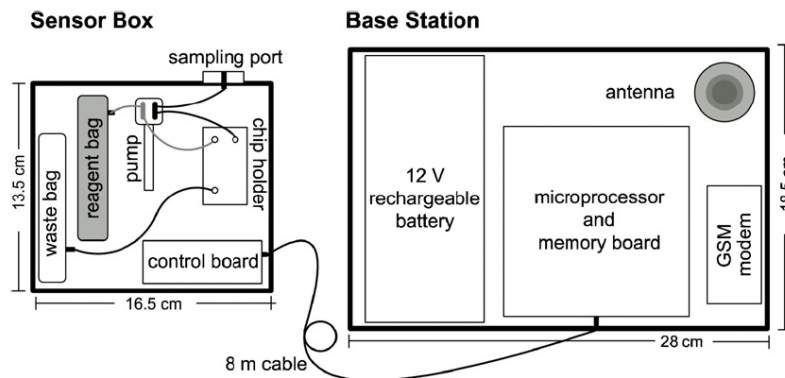
Figure 2.31 – Diagram of the phosphate sensor box (containing the L.O.C. device) and base station (containing the battery and control electronics) [1].

During bench top calibration the limit of detection was 0.000596A (decadic absorption units). For deployment over a 36 hour period (carried out in the Towns River, Ireland) a limit of detection of 0.001987A was achieved. However this is not a truly *in situ* deployment as the base

station was left on the river bank. It is also not capable of operating at depth or in a harsh ocean environment.

It was noted by C. M. McGraw et al that the change in temperature caused a variation in the brightness of the L.E.D. leading to small changes in measured intensity and hence accuracy and precision. The change in L.E.D. intensity can be counter acted through the use of a dual channel spectrometry (see Section 2.4.1) and *in situ* calibration. The change in temperature also caused a change in the reaction time (5 minutes to 30 minutes). The reaction time could be shortened using an effective micromixer rather than relying on diffusion across a single boundary in the serpentine channel (as detailed in Section 2.6.2).

2.6.4   Low-cost and robust lab on a chip fabrication

This section reviews the most widely used materials in microstructure fabrication. It compares their advantages and disadvantages for use in small batch quantity microfluidic devices. This section also provides background for the novel fabrication process using fluoropolymers described in Chapter 3.

2.6.4.1   Silicon

The most common material used in the fabrication of L.O.C. and Micro-Electro-Mechanical Systems (M.E.M.S) devices is silicon, as the same manufacturing methods used in the creation of electronic integrated circuits (I.C.) can be applied. The economies of scale mean that it is a cheap (for large volume production) and effective material, that does not suffer from fatigue and is available in a virtually pure (up to eleven nines [174]) and defect free state. In circumstances where silicon doesn't offer the optical properties and transparency required glass wafers are used as the alternative. Although the substrate material used in the creation of silicon L.O.C. devices is cheap (£25 for a six inch diameter wafer) the fabrication procedures (see Table 2.10 for an overview) are expensive. They require clean rooms, are labour intensive and the initial equipment set up costs are high. Glass is also structurally weak and prone to fracture under shock or out of plane loading.

Process	Description
Photolithography	A light pattern is used to expose a photosensitive layer. Immersion in an aqueous chemical solution dissolves away the parts that were exposed to light (positive photolithography) or those that weren't (negative photolithography)
Wet or Dry Etching	A chemical (liquid or gas) agent removes material not protected by a resist.
Reactive Ion Etching (R.I.E.)	Plasma is hit by an R.F. source forming an ion stream which is accelerated towards and reacts with the surface of the device being etched.
Deep Reactive Ion Etching (D.R.I.E.)	Similar process to R.I.E., but a polymer is deposited on the sidewalls of an etch and allows an increased etching aspect ratio.
Thin film deposition	A technique for depositing a third party material onto a substrate. Can happen via physical or chemical vapour deposition, sputtering or evaporation.
Doping	This is the intentional process of adding impurities to a semiconductor to change its electrical properties.

*Table 2.10 – An overview, including a short description, of fabrication processes available for silicon [**175,176,177**].*

L.O.C. devices constructed using a silicon substrate are typically fabricated in two halves and then bonded together to create sealed microfluidic channels. This bond is achieved through a combination of heat and pressure (i.e. fusion bonding [**178**]) or by using an intermediate adhesive layer combined with heat and pressure [**179**]. The effectiveness of the bond is vital to the successful operation of the L.O.C. device. Further details on bonding in an L.O.C. microfluidic device can be found in Section 2.6.4.4.

2.6.4.2   Polymers

Polymeric materials are also used in the construction of microfluidic devices. They can offer low-cost, high volume fabrication benefits along with optical clarity. Common polymers include; Polydimethylsiloxane (P.D.M.S), Polymethylemthacrylate (P.M.M.A.), Cyclic Olefin Copolymer (C.O.C.) and Polycarbonate (P.C.). Injection moulding can be used to fabricate devices from any of these polymers but the setup costs are restrictive in the research environment. Replica moulding or embossing is normally used instead and offers a cheap, rapid fabrication route without requiring a clean room environment. Using this method microfluidic devices are constructed in two halves which are sealed or bonded together (see Section 2.6.4.4).

Other alternative polymers including fluoropolymers (e.g. Polytetrafluoroethlyene (P.T.F.E.), Fluorinated Ethylene Propylene Copolymer (F.E.P.) and Polychlorotetrafluoroethlyene (P.C.T.F.E.), also offer advantages over hard silicates and other polymeric materials. More details on the use of each of these polymers is presented below.

2.6.4.2.1 Polydimethylsiloxane

In recent years P.D.M.S. has become the material of choice for the rapid prototyping of microsystems [177] in the research laboratory. It has been used to create a wide variety of structures (minimum resolution of 20 - 100μm [180]) including micro-valves and micro-pumps. First proposed in 1998 [181] the fabrication procedure (soft lithography) for this elastomer involves mixing a pre-polymer and curing agent (10:1 weight ratio) together. Then pouring over a mould and curing at 60°C. The moulds or 'masters' are fabricated using silicon or glass micromachining techniques and then electroplated to increase their lifetime. A cheaper option, that requires significantly less capital investment and time, is the creation of masters using negative photoresists (see Section 2.6.4.3). Upon curing or cross linking the P.D.M.S. becomes an elastomeric material with a low young's modulus of 750kPa [182] that enables it to conform to surfaces and form reversible seals. The network structure of P.D.M.S. makes it highly permeable relative to other materials. This permeability means it can absorb molecules, organic solvents and fluorescent dyes (see Figure 2.32 for an example) causing it to swell [177], dissolve or cause interference in measurements. P.D.M.S is optically transparent (420 to 1100nm) [183], flexible, low cost and doesn't require a full scale clean room fabrication facility.
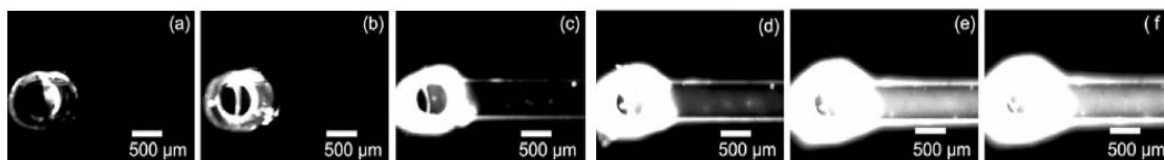
Figure 2.32 – Fluorescence images of Nile red being absorbed into a PDMS channel after repetitive fillings [184].

2.6.4.2.2 Polymethylemthacrylate, Cyclic Olefin Copolymer, Polycarbonate

L.O.C. devices comprised of these three materials are normally fabricated through hot embossing [185,186,187] or injection moulding [188,189,190]. The fabrication steps for devices are similar, although there are some key differences in the material properties. Table 2.11 provides an overview of both the general and optical properties of each of the materials.

Polymethylemthacrylate (P.M.M.A.), a synthetic polymer of methyl meth-acrylate, is a thermoplastic. It has a low viscosity prior to curing (activated by the methyl ether-ketone peroxide (M.E.K.P.) catalyst), rigid after and can withstand moderate amounts of pressure (Young's modulus of 200GPa) and temperature (T_g = 106°C). Microfluidic channels are shaped using hot embossing (2MPa pressure at 120°C) with a master stamp constructed using silicon

micromachining or the lithography, electroplating, and mould process (L.I.G.A.). P.M.M.A. has a higher impact strength than glass, and is more resistant to deformation than P.D.M.S.

	P.M.M.A.	C.O.C.	P.C.
General Properties			
Density (g/cm³)	1.2	1.02	1.2
Flexural modulus (Msi)	0.45	0.5	0.34
Tensile strength (ksi)	10	9	9
Elongation (%)	5	3-10	80
Notched Izod (ft-lb/in)	0.3	0.4	5-16
Heat distortion temperature, (ºC)	92	75-170	142
Shore (D)	100	89	85
Water absorption (%)	0.1	0.01	0.04
Optical Properties			
Luminous transmission (%)	92	92	88
Haze (%)	1	1	1
Index of refraction	1.491	1.53	1.586
Abbe Number	61	56	34
Birefringence	Low	Low	Variable
Stress-optical coeff. (10^{12} Pa/s)	-4.6	4.0	68

Table 2.11 – General and optical property comparison between Polymethylemthacrylate, Cyclic Olefin Copolymer, and Polycarbonate [191].

The optical properties (light transmittance extends through the visible spectrum into the near U.V.) of C.O.Cs are similar those of P.M.M.A, but it has one tenth of its moisture absorption. C.O.C.'s are also approximately 75% stiffer than P.C, and have about the same resistance to crack propagation as P.M.M.A. These factors, as well as their low birefringence, excellent surface replication, and transparency to blue-green light, make them a candidate for colourmetric absorption spectrophotometry.

2.6.4.2.3 Fluoropolymers

There is limited prior art in the fabrication of L.O.C. devices using fluoropolymers [192,193] although trenches and other structures can be embossed [194] into them. This is due to difficulties in achieving good adhesion due to their low wettability and bonding substrates (see Section 2.6.4.4) together to form enclosed microfluidic channels. However they have excellent chemical resistance and as such are more commonly used for inert coatings [195].

The properties of eleven common fluoropolymers can be found in Table 2.12. The mechanical properties of the materials can be tailored to particular applications by varying the composition of the precursor chemicals.

Acronym	Full Name	Colour	Main properties	Common Uses
F.E.P.	Fluoroethylene propylene	Transparent in thin sheets (up to ≈2-3mm)	Chemical resistance, low dielectric constant, good dimensional stability and U.V. and visible transmittance	Cable Sheathing Chemical resistant coatings and films.
E.C.T.F.E.*	Ethlene-chlorotrifluorethylene	Naturally beige, but in clear as thin film	Excellent mechanical properties, abrasion and chemical resistance.	Electrical insulation, tank linings, pipes and pumps.
P.C.T.F.E.	Polychloro-trifluoroethylene	Transparent in thin sheets (up to ≈2-3mm)	Highly transparent, chemical resistance, low creep	Non permeable packaging and refrigeration components.
P.T.F.E.	Polytetrafluoroethylene	White	Low coefficient of friction, chemical resistance, low dielectric constant, good dimensional stability	Tubing, Chemical pump diaphragms and non stick saucepans.
E.T.F.E.	Ethylene-tetrafluoroethylene copolymer	Transparent as film, opaque as sheet	High impact resistance and tensile strength, chemical resistance	Valves, cryogenic applications, bearings and windows.
P.F.A.	perfluoralkoxy	Amorphous grades highly transparent	Low resistance to abrasion, excellent chemical resistance and melt processable	Hostile environment and extended lifetime pumps and pipes.
P.V.F.*	Polyvinyl-fluoride	Transparent as film	Excellent abrasion resistance	Raincoats, solar panels and gas sampling bags.
P.V.D.F.	Polyvinylidine DiFluoride	Transparent solid	Ferroelectric polymer, excellent strength and resistance to solvents, acids and heat. Expensive	Piping, semiconductors
F.P.M.	Fluoropolyer (Viton)	Black	Chemical resistance	Seals, grommets
C.T.F.E.	Chlorotrifluoroethylene	Transparent	Good electrical properties, hard resistant to creep. Lowest permeability to moisture	Seals, wire insulation and components for handling corrosive liquids.
F.F.K.M.	Fully Fluorinated Perfluoroelastomers	Opaque	Chemical resistance and high service temperatures	Seals and gaskets

*Table 2.12 – Table of fluoropolymer properties describing their natural colour, main properties and common uses where * indicates a partially fluorinated polymer.*

P.T.F.E (Teflon™) is the most known of fluoropolymers (thermoplastic) and has remarkable properties; mechanical resistance, chemical inertness, temperature stability, low dielectric loss, negligible moisture absorption (<0.01% over 24hrs - lowest of nearly all polymers), thermal stability, and biocompatibility. P.T.F.E., whose non-stick nature has been widely exploited, is also often chosen for circuits that operate at frequencies above 30Mhz or require closely-spaced circuit elements with their associated capacitive coupling problems [196]. P.T.F.E. is opaque but transparent fluoropolymers such as P.C.T.F.E. and F.E.P. are also available.

Thin P.T.F.E. sheets are produced by skiving from large cylinders of P.T.F.E. It is a process in which thin sheets are sliced off from a rotating cylinder. The thin sheets have a natural curl, reflecting their method of formation and long macroscopic scratches which are the result of imperfections in the knife blade. Skiving is also likely to leave residual mechanical stresses in the P.T.F.E. sheet parallel to the knife blade edge. This also results in fabrication issues (i.e. bonding).

2.6.4.3 Dry film and liquid resists

Dry film resists are thin layers (<100µm) of a photosensitive or definable material (e.g. acrylic, epoxy) that can be laminated [145] onto a substrate. Liquid resists are photosensitive fluids (e.g. SU-8) that are spun onto a substrate (using centripetal force to distribute it evenly, Figure 2.33a) to achieve even thicknesses of between 1µm and 2mm [197]. Micro structures, see Figure 2.33b for an example, within both are created using photolithography, followed by immersion in an etching solution and curing. A negative resist is rendered insoluble to the etching solution when exposed to U.V. light where as a positive resist is rendered soluble. The pattern of exposure is created using either a light or dark field image on a transparency (>20µm feature definition), a chrome mask (≈500nm feature definition but at increased cost [181]), direct write masks (feature sizes <50nm [198]), or electron beam lithography (focused electron beam to write ultra fine patterns). The properties of the photosensitive material also limit the minimum feature size (dry film ≈ 40µm, liquid resists ≈ 10µm). Dry film or liquid resist L.O.C. devices are then created by bonding (see Section 2.6.4.4) a lid onto the pattern resist layer to create enclosed microfluidic channels. This lid can also be patterned.
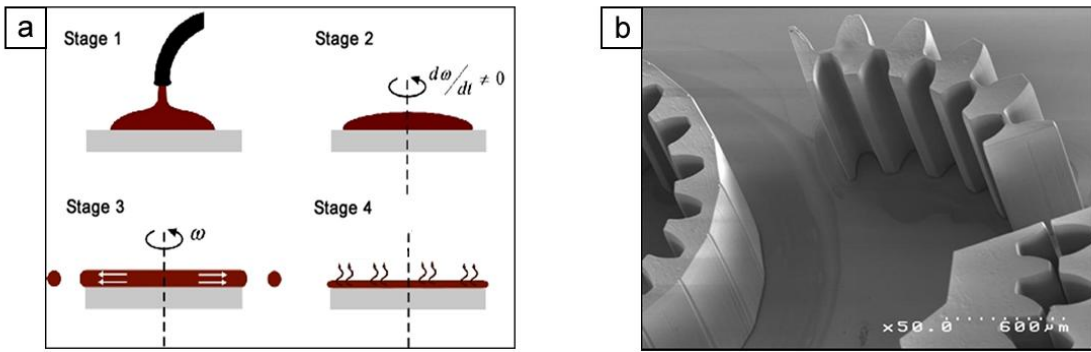
Figure 2.33a & b – a) SU 8 spin on process where the resin is deposited on the substrate in stage 1, spun up to an angular velocity of ω in stage 2 and 3 to distribute the resin across the substrate, and then heated b) SU-8 structure produced by lithography [197].

Dry film and liquid resists offer the opportunity to fabricate microfluidic structures accurately outside a clean room environment. The minimal setup costs and robustness of the structures created make the fabrication process ideal for this study. The combination of dry film resists and fluoropolymers substrates to produce robust and chemically inert L.O.C. devices is investigated in Chapter 3.

2.6.4.4   Bonding

A poor bond or seal between two halves of a microfluidic device results in fluid leakage from and between microfluidic channels. It also decreases the maximum fluidic pressure and hence flow rate. For each material substrate used in the construction of a L.O.C. device a surface treatment can often be used to increase the bond strength. Surface treatment to improve adhesion can be achieved by; increasing the surface energy (wettability) of substrate surface; improving surface topography to enhance mechanical adhesion; increasing surface roughness; and changing the surface composition.

A measure of the expected bond strength can be gained through examining the wettability of a substrate or resist. Wetting describes the stability of a drop on the surface of a material. If a droplet, when placed on a surface, maintains its round shape then it can be said to have a low wettability or high contact angle. A surface on which the droplet spreads has a high wettability or low contact angle. Highly wettable surfaces are termed hydrophilic and non-wettable surface, hydrophobic. The contact angle provides a correlation between the surface energy of the substrate and the magnitude of the bond strength (i.e. the contact angle between a fluoropolymer and a liquid provides a measure of the bond strength of the material to a laminated epoxy, as presented in Section 3.4.2).

The contact angle between a surface and droplet depends on the surface tension/energy of both the solid (σ_G) and the liquid (σ_L) (see Figure 2.34a & b). The surface energy of a solid describes its reactivity towards the liquid and vice versa. It quantifies the disruption of the chemical bonds that occurs when a surface is created.
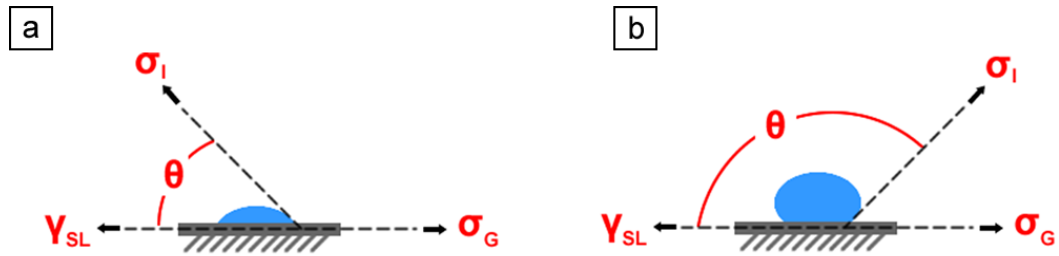
Figure 2.34a & b – a)A surface with a high wettability or low contact angle, b) A surface with a low wettability and high contact angle.

The interfacial tension (Y_{SL}) and its relationship to the contact angle (θ) is given by Young's equation (Equation 2.13). If a solid has a high surface energy or high wettability then the forces between molecules in the solid and liquid are stronger than those inside the liquid. Therefore force overcomes the surface tension and causes the droplet to spread out [199].

$$\sigma_s = \left(Y_{SL} + \sigma_l\right)\cos\theta \qquad \textit{Equation 2.13}$$

The contact angle of a water droplet on a solid can provide an indication of the adhesive strength. In the case of dry film fabrication any increases in the surface energy of a substrate will result in better film to substrate adhesion [200,201]. The increase in surface area contact between the two materials caused by the increased wetting improves the mechanical, chemical and dispersive adhesion [202]. Surface treatment, by plasma oxidisation, is also commonly used to improve the bond strength of P.D.M.S. devices by creating a hydrophilic surface. Section 2.6.4.4.1 below details common surface treatments for fluoropolymers.

2.6.4.4.1   Surface treatment of fluoropolymers

The main processes used to modify the surface of a fluoropolymer increase the adhesion through a change in the surface composition which leads to an increase in the surface energy and wettability. Common methods for this process are chemical treatment, plasma treatment, irradiation treatment, corona discharge, flame treatment and ozone treatment. A description of each is provided in this section and a summary of the advantages and disadvantages of each surface modification method for fluoropolymers is shown in Table 2.13. It should be noted that some treatments are only suitable for partially fluorinated polymers.

Chemical treatment is the most widely used method in the surface treatment of fluoropolymers. It involves a transformation in the chemistry and morphology of the polymer surface to improve adhesion characteristics or environmental durability. Several chemical etchants are available; sodium liquid ammonia [203], sodium hydride [204], sodium naphthalenide (also known as sodium naphthalide) [205], benzion dianion [206] and other liquid alkali metal (Li, K, Mg e.t.c.) amalgams [207]. Most rely on the production of carbonyl and carboxylic functional groups on the polymer surface (carbonisation) and it's defluorination to increase the surface energy [208]. The alkali metals reactions are fast (≈30-60 seconds [196]) but are hard to control (difficult to monitor depth profile) and the etched surface degrades with heat (loss of improved adhesion). Milder reactants such as benzion dianion take several hours to carbonise the surface [203]. Heavy carbonisation (causing a dark brown colourisation of the surface) can lead to the creation of porous surfaces [196]. Magnesium solutions in liquid ammonia do not carbonise the surface and as such don't destroy the surface properties (i.e. hydrophobicity, environmental resistance) [207]. Sodium naphthalenide (or a sodium naphthalene complex) is often used to enhance the adhesion of Copper (Cu) to Teflon in the fabrication of circuit boards and can provide an etch depth of 3,000 Angstroms [196]. The Teflon is exposed to the sodium naphthalene which introduces unsaturated bonds, hydroxyl, carbonyl and carboxylic groups to the substrate surface, increasing the substrates reactivity and wettability. The chemical functionality of the surface produced by this treatment doesn't vary greatly between fluoropolymer types but the etch depth (F.E.P. ≈ few hundred angstroms, P.T.F.E. etch ≈ 3000A) depends on the material and surface topology [205]. The surface topology controls the extent of contact to the etchant. Hence skived P.T.F.E., which has surface damage (chain scission and void formation) and an increased surface area, etches to a greater depth than laminated or smooth P.T.F.E. samples. Chemical etching can also relieve the stress induced in skived P.T.F.E. during processing [196]. Side effects of this process are the discolouration and increase in porosity of the material's surface due to defluorination.

Adhesion of etched surfaces to epoxy resins (i.e. in the building industry) is so large that cohesive failure usually occurs in the P.T.F.E. and not the boundary layer [209,208]. The adhesion of chemically etched fluoropolymers to photosensitive epoxy thin films and the subsequent development of fluoropolymers L.O.C. devices is detailed in Chapter 3.

Corona, flame and plasma surface treatments all rely on the creation of plasma but the method of plasma creation and the conditions under which it is produced varies. In these treatments ionised gas molecules penetrate into the molecular structure of a polymer and break the molecular bonds on the surface creating free radicals that rapidly react with oxygen to form polar chemical groups

[203,210]. **Corona treatment** (see Figure 2.35a for a typical industrial setup) ionises the atmospheric air (creating plasma) between an electrode and a dielectrically insulated and earthed roller. The electric field used to ionise the air is created by a high potential, typically in the region of 20kV, driven at a frequency of 10-20 kHz. The corona discharge technique is suited to the processing of thin films (<1mm sheet) and is used in wire insulation bonding. Although corona treatment is stable in air exposure to solvent and mechanical abrasion will render the treatment ineffective [211]. **Flame treatment** uses the combustion of oxygen and natural gas (methane, propane or butane) to create an oxygen rich flame plasma. This introduces radicals and creates chain scission in the fluoropolymer surface. The radicals subsequently react with oxygen and/or nitrogen leading to hydroxyl, carbonyl, amide and carboxylic groups [212]. **Plasma treatment** (see Figure 2.35b for a schematic of the treatment process) is very similar to corona treatment with the exception that gases (O_2, H_2, N_2, He, Ne, Ar, CF_4, NH_3 or CH_4) are injected into the corona discharge to modify the reaction with the polymer. The free electrons in this discharge are accelerated by the electric field and collide with neutral gas molecules or atoms. Due to these collision metastable positive ions, electrons and free radicals are generated. During each plasma process a competition between an etching process (sputtering or chemical etching) and a (re)deposition process exists. Plasma treatment has four major effects; surface ablation or etching, cross linking and modification of the chemical structure. It can be used to modify the surface from hundreds to thousands of angstroms deep [213].
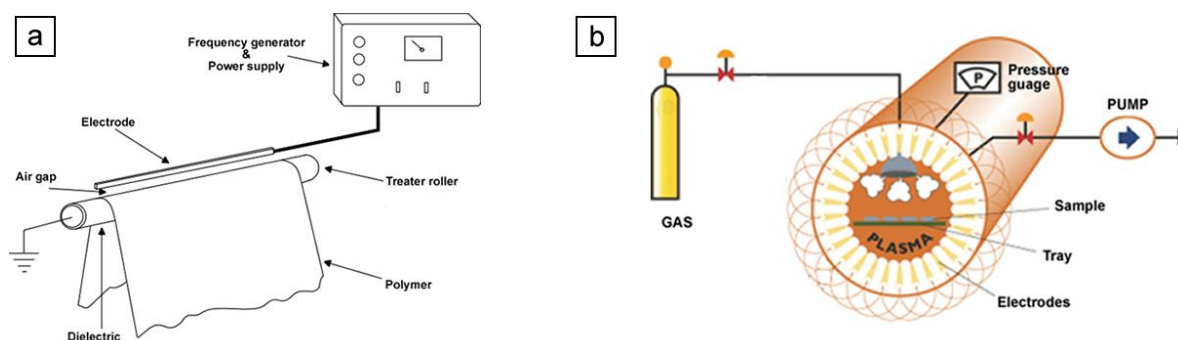
Figure 2.35a & b – Schematic diagram of an example a) corona discharge treatment setup and b) plasma treatment setup [214].

Irradiation treatments (using X-ray, γ-ray, U.V, laser, electron beam or ion beam sources) produce alkyl-type radicals and carbon-carbon double bonds on the surface of the polymer and cause defluorination, oxidation, cross-linking and chain scission [209,205]. Chain scission leads to a reduction in tensile strength and elongation whereas as cross linking increases tensile strength but reduces elongation [215]. This type of treatment has been shown to improve wettability,

crystallisability and lubrication properties. **Ozonation** of fluoropolymers (using ozone gas O_3) leads to the creation of alkylperoide and hydroperoxide groups. The concentration of peroxides increases with ozonation time and temperature up to a point when the polymer starts to degrade. It is only fully effective on partially fluorinated polymers and the treatment has a lifetime of between 6 – 24hrs.

Type	Advantages	Disadvantages	Current uses
Chemical	Simple Low capital cost	Wet methods Waste products hazardous Hard to control	Adhesion to metals Frying pans Rollers Copper patterning and circuit fabrication
Plasma	Uniform and stable oxide layer Insensitive to surface contamination Long shelf life prior to bonding Low processing costs Environmentally friendly Treat hard to reach area's	Elevated temperatures or moisture will comprise treatment High capital cost Short lifetime of 1-2 weeks	Car bumpers PDMS bonding
Flame	Insensitive to contaminants Can be used on 3d shapes Suitable for inline processing High speed No backside treatment Short processing time	Careful control to avoid thermal damage Short lifetime of 1-2 weeks	Plastic bottles
Corona	Low capital cost Clean Suitable for inline processing Short processing time	Solvent wiping renders treatment ineffective Ozone creation Short lifetime of 1-2 weeks Thin surface treatment layer (few hundred angstroms) Static build up	Paint adhesion replacement for primers
Ozone*	Simple Can be used on complex shapes	Ozone creation	Reduce the risk of microbial contamination for food packaging
Irradiation	No changes in surface topology	Health and safety risks Can bulk mechanical properties	Sterilizing in the medical industry

*Table 2.13 – Advantages and disadvantages of surface treatment processes and their current use. * indicates treatments that only work on partially fluorinated polymers.*

Chemical treatment has the advantage over other techniques such plasma treatment, corona discharge or oxidation by flame and U.V. treatment [9; 10; 11] that it does not require any costly equipment and is fast and effective. The adhesion strength of P.T.F.E. is also greatest when a sodium naphthalene treatment is used [12].

2.6.4.5   Fluorescence

Fluorescence is the absorption at one wavelength and the emission at another. The difference between the absorption and emission bands of a material is referred to as the Stokes shift and is normally 10 – 150nm for polymers (illustrated in Figure 2.36a). It arises in polymers through additives and impurities added during its manufacture, or because of the materials intrinsic nature. The majority of polymers show significant fluorescence background when excited by near U.V. or visible radiation [216] specifically blue or green light [217], see Figure 2.36b.
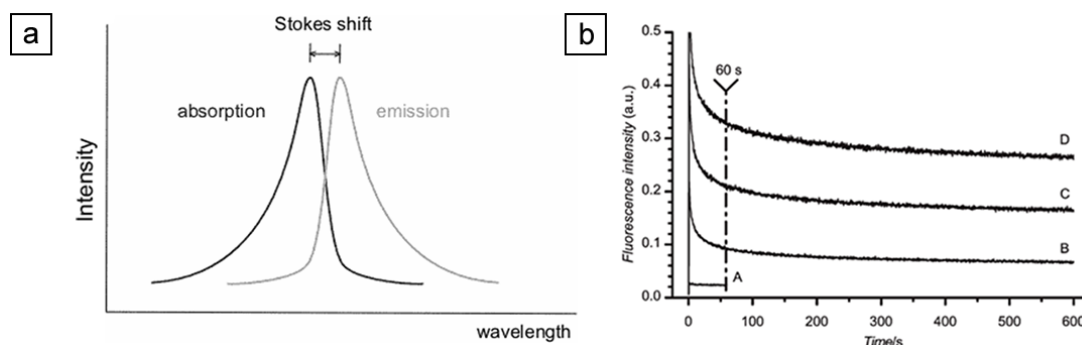
Figure 2.36a & b – a) A graph of intensity against wavelength showing the difference between the absorption and emission peaks referred to as Stokes shift [31] and, b) decrease in fluorescence with time [216].

The fluorescence of materials is primarily non linear with complex kinetics [216]. It decreases over time with continuous illumination from either a monochromatic or non monochromatic light source (Figure 2.36b). Constant illumination of the material causes photo-bleaching or photo-chemical destruction of the fluorophores and depends on light intensity, exposure time and material type. The photon induced chemical damage and irreversible covalent modification of the fluorophore happens upon transition from its excited singlet state to excited triplet state [218]. Auto-fluorescence recovery can take place after exposure to a light source but is limited to 15-20% over a 24hr period. The change in auto-fluorescence predominately affects those experiments utilising long reactant and signal interaction times or if the fluorescence signal is low (for example; in the fluorescence based determination of ammonia). Absorption measurements rely on specific wavelength (or monochromatic) light and Stokes shift will cause an offset in the maxima wavelength and intensity values. Therefore material fluorescence will manifest in increased L.O.D. (i.e. the signal to noise ratio and sensitivity will decrease) and noise during optically sensitivity spectroscopy measurements. It will also decrease the time required between calibrations.

2.7   Summary

Colourmetic spectrophotometry was identified as the most suitable nitrite detection method in Section 2.4. This chapter has also looked at the technologies that could be used to deliver such a miniature *in situ* spectrophotometric device. To fulfil the key performance drivers identified in Section 2.2 it is necessary to use L.O.C. technologies to achieve a low cost, miniature, low power, small sample volume, high sensitivity sensor. There is no consideration for the use of most L.O.C. devices or others reviewed in this section outside the laboratory environment. The fragile nature of construction and fundamental design principles prevent their operation *in situ*. In summary there is no *in situ* sensor available or presented to date that would fulfil the requirements of this study. This highlights the reason for this study to develop a Deep Sea Lab On a Chip chemical sensor.

To use L.O.C. technologies it is of key importance that a micromixer is capable of producing rapid, effective and stable mixing with minimal back pressure and dispersion. The mixer and optical absorption elements must be integrated to minimise dead volumes and therefore the minimum resolvable volume. All L.O.C. elements must be able to resist pressure. Off chip pumps and valves can be used without significantly degrading performance and reduce the development time required to achieve a first prototype. To demonstrate this technology a functional prototype that can operate submerged in seawater was required and is presented within this study (see Chapter 4 and 5).

Table 2.14 summarises the materials and fabrication techniques reviewed in this section. All are capable of producing a L.O.C. device but those with limited chemical resistance cannot be used as the proposed detection system relies on several aggressive chemicals (hydrochloric acid, polyvinyl alcohol & sodium hydroxide). P.D.M.S. and acrylic dry film resists are not resistant to these chemicals [**219**].

Manufacturing Material	Advantages & Disadvantages
Silicon	Batch processed Proven Long lead time Expensive High resolution High accuracy
P.D.M.S.	Easy sealing Low-cost Non clean room environment Fast processing Non-toxic Reversibly deformed Limited resolution Requires 'masters' Swells in contact with organic solvents High elasticity
P.M.M.A. – soft lithography route	Requires embossing 'masters' Fast processing Low-cost Ideal for large batch numbers High impact strength
C.O.C.	Low moisture absorption Good optical properties Requires embossing 'masters' Fast processing Low-cost Chemically resistant
P.C	Good optical properties Ideal for large batch number Low-cost Machinable Poor chemical resistance
Fluoropolymers	Chemically and biologically inert Low dielectric constant Low refractive index Robust (good mechanical properties) Low-cost
Acrylic or epoxy dry film resists	Limited resolution Limited batch production Fast processing Good solvent resistance Limited resolution Limited thicknesses
SU-8 polymer resin	Expensive basic material Relatively fast processing Variable thickness

Table 2.14 – Overview of possible fabrication routes for microfluidic devices detailing the advantages and disadvantages for each.

The cost of silicon devices and the complexity of their fabrication makes them too costly for prototyping in this study. If they were to be used for *in situ* devices (at a later stage when mass

production reduces the cost) packaging them (to avoid damage) would increase sensor size and weight. This study uses epoxy thin film fabrication methods to create the first generation of microscale L.O.C. prototypes (Section 4.2) due to their low cost, rapid turnaround (in-house fabrication) and chemical resistance. The second generation of devices used in benchtop testing (Section 4.3) and *in situ* deployment (Chapter 5) utilise a liquid (SU8) photosensitive resist and P.M.M.A. substrate (outsourced fabrication).

In parallel research, novel fabrication techniques using dry film resists and fluoropolymer substrates were developed in an attempt to provide an even more robust low-cost solution. This low-cost fabrication technique is described in Chapter 3.

3. FABRICATION USING FLUOROPOLYMERS

To increase the durability and deployment opportunities for a L.O.C. device, fabricated using the low cost and rapid dry film lamination process (Section 2.6.4.3), experiments were conducted to replace the commonly used glass substrate with a fluoropolymer substrate (Section 2.6.4.2.3). This chapter describes the novel process developed for achieving reliable and repeatable dry film fabrication using fluoropolymers. As demonstrators, micro-channels were fabricated using three different compound structures: 1) fluoropolymer/epoxy laminate/fluoropolymer structures, 2) fluoropolymer/fluoropolymer structures and 3) fluoropolymer/epoxy laminate/glass structures.

The chapter also evaluates three types of fluoropolymer (P.T.F.E, P.C.T.F.E. and F.E.P.) substrate for use in µ.T.A.S. devices with integrated optics. The fluoropolymers are hydrophobic in their untreated state and therefore the adhesion and bond strength of the fluoropolymer to laminated epoxy film has been a major technical hurdle to date. Surface modification with sodium naphthalene treatment has the potential to improve adhesion and bond strength (Section 2.6.4.4). Details of this etching process and the bonding & curing of fluoropolymer / epoxy laminate structures is covered in Section 3.3.2 to 3.3.4. Surface wetting, contact angles, and bond strengths tests used to characterise the success of the etching and bonding are described in Section 3.4. As the intended application, although not limited to, of the fabricated devices is the measurement of the absorption of a fluid the optical properties of fluoropolymers are also examined (Section 3.2) to analyse the possible interference from natural fluorescence in spectrophotometry, as described in Section 2.6.4.4.

3.1 Mask design

This section provides details of the mask (shown in Figure 3.1) used in creation of microfluidic channels for the demonstration devices. The dark field mask (designed as a single channel absorption measurement device with an integrated mixer). comprised of two fluid inlets, a simple chicane mixer (250µm wide) channels, a dog legged detection path (500µm wide) and two fibre insertion channels.
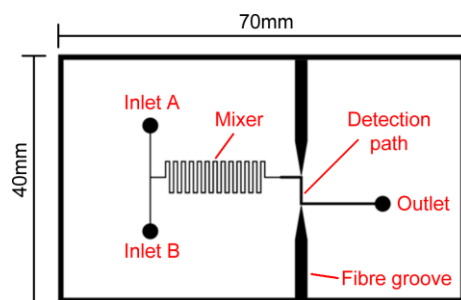
Figure 3.1- Annotated diagram of the dark field mask, designed as a single channel spectrophotometric device, used in the exposure of the photosensitive dry film laminate.

3.2   Optical waveguides

μ.T.A.S. and L.O.C. devices are frequently fabricated with intrinsic waveguides, to enable compact on-chip optical analysis and connection to light sources and detectors [3; 7]. These planar wave guiding structures use a high refractive index (R.I.) core (e.g. epoxies) clad with a lower refractive index material (often air) to enable total internal reflection (T.I.R.). To incorporate intrinsic waveguides on fluoropolymer (R.I. = 1.34-1.44) devices, a thin dry film resist (R.I. ≈ 1.5) is laminated on the substrate. This would not be possible with P.M.M.A., P.D.M.S, P.C. and glass due to their high refractive indices see Table 3.1.

Material	Glass transition temperature (°C)	Melting point (°C)	Young's modulus (GPa)	Refractive Index (@598nm)	Linear thermal expansion coefficient (K^{-1})
Soda Glass	520-600	1000	72	1.5	8.5×10^{-6}
P.M.M.A.	100	135	2.4-3.3	1.5	4.4×10^{-4}
P.D.M.S.	-125	-50	0.4-0.9	1.45	3.1×10^{-4}
P.C.	150	267	2.3-2.4	1.55	3.7×10^{-5}
P.T.F.E.	120	327	0.3-0.8	1.35	13×10^{-5}
P.C.T.F.E.	52	220	1.3-1.8	1.435	70×10^{-6}
F.E.P.	103	275	0.5-0.6	1.344	104×10^{-7}

Table 3.1 - Properties of materials commonly used in the fabrication of L.O.C. devices [8].

Fluoropolymers have a low R.I. (~1.34-1.44) and offer an alternative cladding material for applications (e.g. deep water or high vacuum) where using air (R.I. ≈ 1.003) is not feasible. When compared to using glass substrates (R.I. ≈ 1.5) for the lid and base of a device constructed from epoxy (R.I. ≈ 1.5-1.6) fluoropolymer cladding provides improved wave guiding and reduced light loss. The low R.I of some fluoropolymers means they are commonly used in the cladding of polymer optical fibres (P.M.M.A. core with fluorinated acrylate or methacrylate cladding).

The R.I. of most materials varies with wavelength, and Table 3.1 also details the R.I of the fluoropolymers at a wavelength of 589nm. This data was used to calculate the critical angles (θ_{crit}) using Snell's law (Equation 3.1) for total internal reflection of the structures shown in Figure 3.2 where the refractive indices of the two mediums are given by n_1 (core) and n_2 (cladding).

$$\theta_{crit} = \sin^{-1}\left(\frac{n_2}{n_1}\right)$$

Equation 3.1

Figure 3.2a shows an epoxy laminate film bonded to a fluoropolymer base and lid. The waveguide is formed by etching channels into the epoxy. Air in these channels acts as the cladding. The lid and base also as act as a cladding as they have a lower R.I. than epoxy laminate. Higher propagation loss is observed when a glass lid is used (Figure 3.2b) as this reduces the numerical aperture and therefore total internal reflection. For applications where using air as a waveguide cladding is not acceptable then fluoropolymers can be embossed and a U.V. curable polymer spin coated on to substrate, as shown in Figure 3.2c. Whilst an epoxy/air structure has a 39º acceptance angle the epoxy/glass structure is only 70º. For epoxy/FEP this decreases to 57º, providing a higher coupling efficiency to external light sources due to the larger numerical aperture possible than with glass devices.
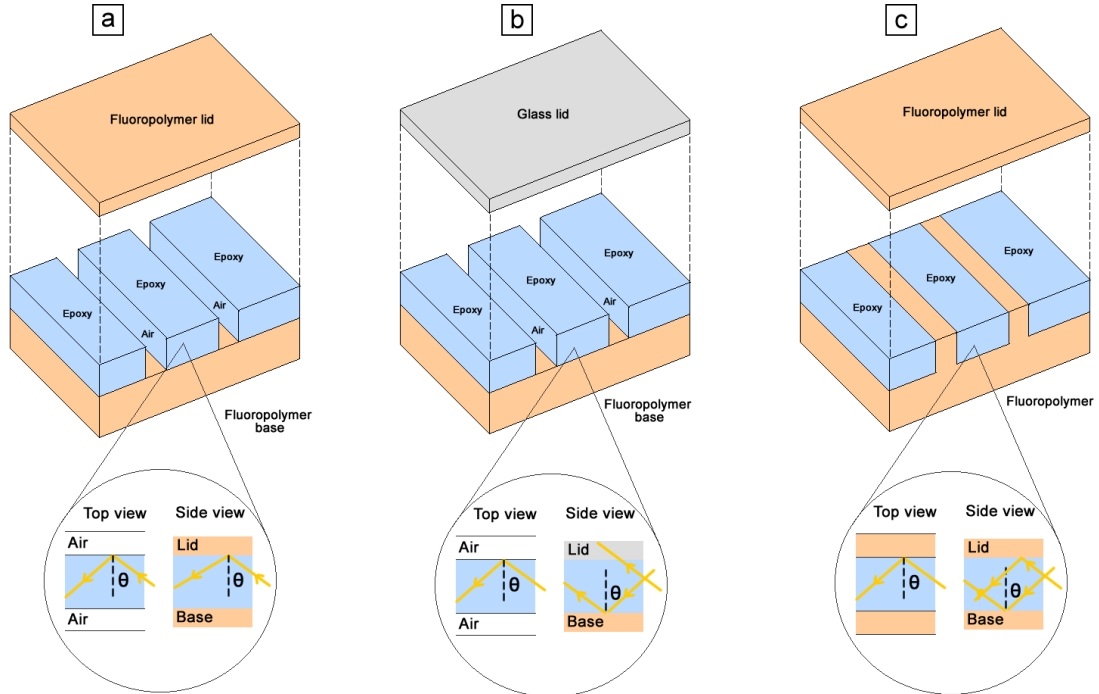
Figure 3.2a, b & c – Cross section of three different waveguides structures and their wave guiding principles (where the acceptance angle is equal to θ), a) fluoropolymer / epoxy / fluoropolymer b) fluoropolymers /epoxy /glass c) fluoropolymers /fluoropolymer.

The limited depth of the colouration caused by the chemical etching process means that only the transmission of transparent materials is decreased. The bulk refractive index of the material is unaffected and any localised refractive index changes caused by the treatment do not affect the overall wave guiding properties of the structure. The porosity of the treated material relates to the amount of chemical etch that has taken place [13].

3.3   Fabrication process

Untreated fluoropolymers, P.T.F.E, P.C.T.F.E. and F.E.P. were purchased from Goodfellow Cambridge Ltd as thick films (1mm). P.C.T.F.E. and F.E.P. offered optical transparency. Sodium pre–treated P.T.F.E. samples were obtained from Davis Industrial Plastics Ltd. For the epoxy resist, Ordyl SY335 (50μm thickness) and SY320 (20μm thickness) laminates (provided on a roll) from Elga were used. These epoxies have excellent chemical resistance, and can be cured to provide sufficient mechanical strength to create masters for the embossing of fluoropolymers.

3.3.1   Material preparation

Unprocessed P.T.F.E, F.E.P. and P.C.T.F.E. materials exhibit significant surface roughness and thickness variation due to the techniques used for their manufacture (see Section 2.6.4.2.3). When constructing laminated microfluidic devices, any variation in the base and lid thickness leads to uneven pressure points during bonding. The epoxy laminate is compressed at the high pressure zones and distortion of channel geometry occurs as shown in a picture of an F.E.P. epoxy device in Figure 3.3. The variation in polymer thickness over a 0.25mm^2 substrate area was measured using a KLA Tencor P16 Surface profiler and a vacuum chuck. The profiles were performed with a stylus speed of 200 μm per second and a 200Hz sampling rate with a 10μm Y spacing. To analyse the results Scanning Probe Imaging Processor (S.P.I.P.) software by Image Metrology was used.
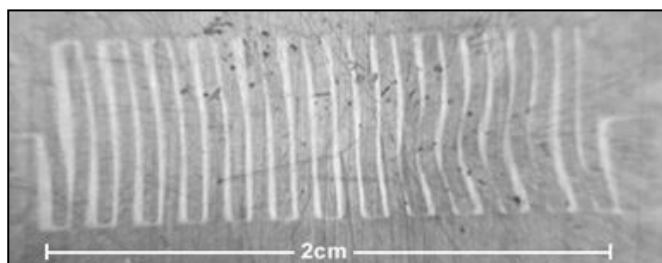
Figure 3.3 - Channel deformation for an FEP-epoxy device caused by variation in substrate thickness.

The surfaces were found to vary by up to ±10% (100μm for a 1mm thick sheet) (Appendix 8.1.2). To resolve this problem the polymer was flattened by pressing the plastic substrates at

elevated temperatures (200ºC) between heated press plates (depicted as stage 1 in Figure 3.4). This decreased the roughness significantly for F.E.P. (>5000%) – see Table 3.2. As F.E.P. and P.C.T.F.E. have a lower glass transition point they see more viscoeleastic flow and hence a larger decrease in thickness variation than in P.T.F.E.

Material	Roughness average (nm)	Minimum feature height (nm)	Maximum feature height (nm)
Glass microscope slide	0.872	-8.32	5.96
F.E.P.	20748	-41102	113000
F.E.P. etched & compressed	3.54	-28.4	3.80
P.T.F.E.	888	-4212	6241
P.T.F.E. etched	387	-3072	1578
P.T.F.E. etched and compressed	270	-1951	3937

Table 3.2 – Average roughness, minimum feature height and maximum feature height of substrates before and after compressing at an elevated temperature (200ºC).

All three fluoropolymers were manually cut to size (70 by 40mm) and connections for fluid inlets and outlets were made by punching holes with a bevel edged hypodermic needle through a milled acrylic two part template (as shown in Figure 3.5). Alignment is achieved using a recess in the lower template part. This process step is depicted as stage 2 in Figure 3.4. Prior to surface processing, the fluoropolymers were cleaned by ultra-sonicating in detergent solution, followed by successive washes (1 minute) in Acetone, Methanol and Isopropanol, then dried using compressed N_2 gas. Dehydration of the samples was performed in an oven for 30 minutes at 60ºC. Temperatures higher than this lead to deformation of the material.
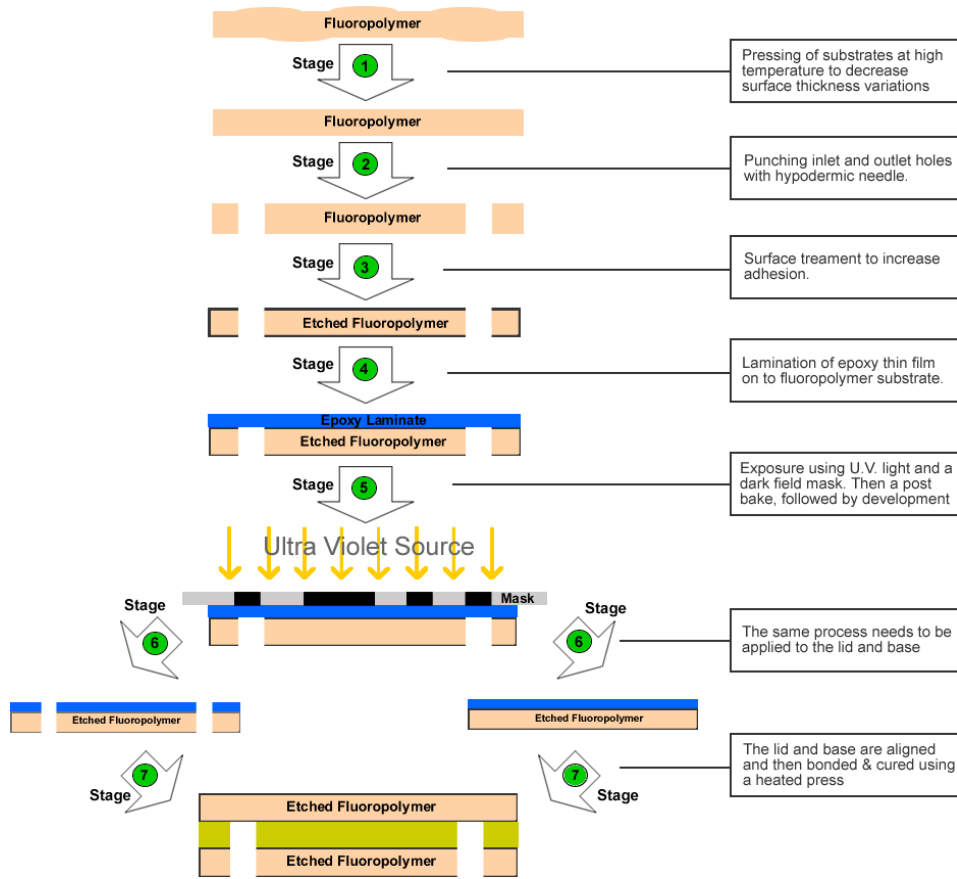
Figure 3.4 – Process flow diagram with stages 1 to 7 of the fluoropolymer device manufacturing indicated.
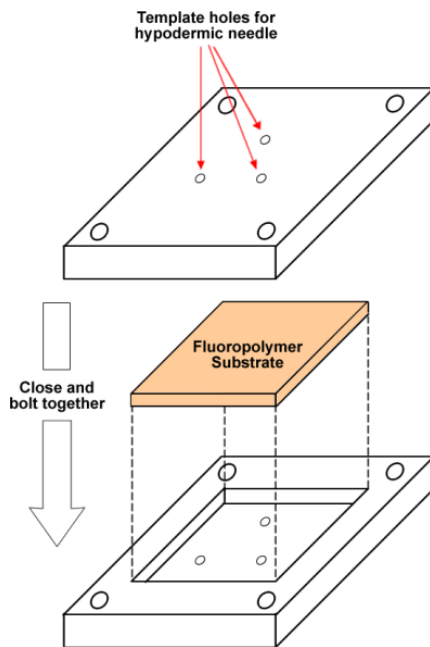
Figure 3.5 – Diagram of the template used to punch holes in the fluoropolymer substrate. Once fitted together the hypodermic needle is inserted into each hole and punched through the substrate producing a non burred hole.

3.3.2 Surface treatment

Sodium treatment of the fluoropolymers consists of three steps: 1) immersion into a bath of proprietary Sodium Naphthalene for 15 seconds. During which, the solution was ultra-sonicated to ensure mixing. 2) After draining excess solution (≈10 seconds), the sample was placed in a de-activation solution (Propan-2-ol) and 3) immersed in a pH neutralising solution (Citric Acid, pH of 2.2 at 20% w/w in water), both for 15 seconds. All treatment solutions were obtained from A.P.C. Ltd, UK with process timings developed based on achieving a 'Nut Brown' colour post surface treatment. After washing under distilled water and drying, the sample was placed in an oven at 60°C for 1hr. The surface treatment process is depicted as Stage 3 in Figure 3.4. For certain applications it may be required to selectively treat the surface, for example if channel regions are to be created that should remain hydrophobic. This was achieved by masking the polymer using adhesive tape or, for fine patterning, a dry film laminate resist. However, the low adhesion of the laminate to the untreated polymer makes fine patterning difficult. Careful handling and low development times (<1 minute) are required to prevent undercutting and the laminate peeling from the surface. Figure 3.6 shows the effect of surface treatment on a P.T.F.E. substrate, where the darker regions indicate treated surface areas. The over treated area's have a higher porosity and lower mechanical strength compared to the ideal areas.
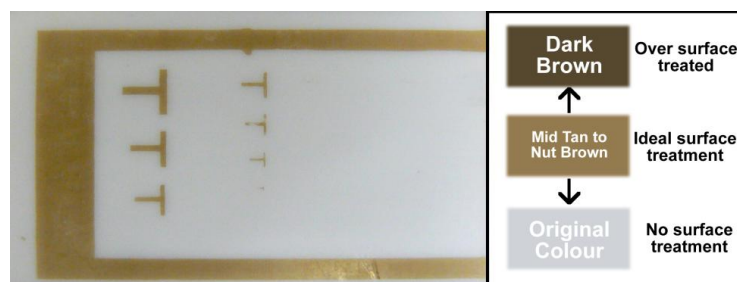
Figure 3.6 – Selectively surface treated P.T.F.E. after using an epoxy laminate mask. The colour guide shows that the white areas are the un-treated regions and the darker areas the treated.

3.3.3 Dry film lamination

The photosensitive dry film epoxy resists, Ordyl SY355 (50μm) and SY320 (20μm) were laminated on the fluoropolymers using a Photonex 235LSI laminator at 110°C and a speed of 5.6 millimetres per second. Multiple layers (up to 200μm) were laminated to increase the film thickness, at a reduced temperature of 100°C which prevented periodic undulations appearing in the laminate.

The laminate is a negative resist, and a dark field, low resolution mask (see Section 3.1 for the design), printed on acetate sheet was used in the exposure of the laminate material. Exposure was

performed using a light box (Mega Electronics AY315) and the time was optimised for different thickness of material (27 seconds for 2x50µm layers, 20.496 kJ/m^2; 24 seconds for one layer, 18.219 kJ/m^2). A post-exposure bake was performed at 85°C for 4 minutes. After cooling the sample was developed in Elga BMR C-3 developer (in an ultrasonic bath), for 3 minutes using a Pasteur pipette to spray and agitate the solution. The sample was immersed in the BMR F-5 rinse solution for a further 90 seconds, finally gently rinsing in D.I. water then drying with nitrogen. Figure 3.7(a, b & c) show device details after this stage, and these processes are depicted as stage 4 and 5 in Figure 3.4.
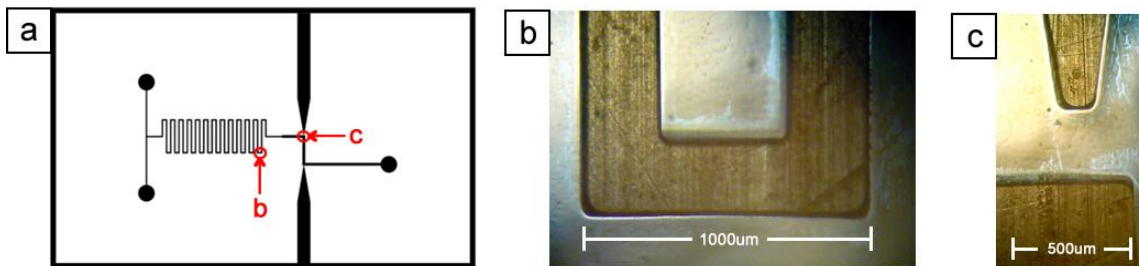
Figure 3.7a, b & c – a)Positive film transparency mask with the location of the images included in b and c indicated, where b) is part of a simple chicane mixer fabricated in a P.T.F.E. / epoxy structure before curing and c) a dog leg with a fibre insertion groove.

3.3.4 Bonding and curing

Two pieces of material were processed in the same way to form the bottom and top halves of a chip. The two halves were aligned by hand and placed in a hot-press (Specac 15 Ton press with heated platens) for bonding. F.E.P. & P.C.T.F.E. exhibited instability at elevated temperatures (thermal expansion coefficients up to 15x that of glass) and pressure, where creep or viscoelastic flow of the substrates into the channels was observed. In preliminary experiments the channel height decreased from the original value of 100µm to 20µm (for F.E.P. & P.C.T.F.E. devices) and from 100µm to 80µm for the P.T.F.E. devices. P.T.F.E. has a higher working temperature and melting point (327°C) compared to P.C.T.F.E. (212°C) and F.E.P. (279°C) and hence is less prone to creep at elevated temperatures. The changes in channel height were resolved by reducing the pressures initially required to ensure complete bonding.

For the improved protocol the sample was clamped between two metal plates at 24.5kN/m^2 and heated from room temperature (22°C) to 150°C at a rate of 300°C per hour. When the sample temperature reached 150°C a pressure of 294kN/m^2 was applied for 30 minutes before ramping the temperature up to 200°C (at a rate of 300°C per hour) for a further 90 minutes. The sample was then cooled to room temperature at a rate of 120°C per hour, with the pressure maintained.

3.4 Experimental results

This section characterises the performance of the fabrication of fluoropolymer laminate devices (through wetting and bond strength measurements) and highlights some of the difficulties associated with using these novel materials (expansion during curing and fluorescence).

3.4.1 Expansion during curing

Initial experiments to fabricate fluoropolymer devices resulted in substrate failures (particularly glass) due to expansion and contraction mismatches. During heating the energy stored in and the length of intermolecular bonds changes. This results in an increase in length, width and height of an object and can be described by Equation 3.2.

$$\alpha = \frac{1}{L}\left(\frac{\partial L}{\partial T}\right)$$

Equation 3.2

Where α is the linear thermal expansion coefficient (K^{-1}), L is the length before heating (m), ∂L is the change in length (m) and ∂T is the change in temperature (K). Figure 3.8 shows an example of this failure caused by expansion and contraction of the materials.

Figure 3.8 – Picture of a glass, epoxy and treated P.T.F.E. construct that has shattered during cooling.

The expansion of the four materials used in construction of the L.O.C. devices is calculated in Table 3.3. The values are based on a sample size of 70x40x1mm (LxWxH, 2.8e-6m^3), and a ∂T=180.

Material	Linear thermal expansion coefficient (K^{-1})	ΔLength (mm)	ΔWidth (mm)	ΔHeight (mm)
Glass	8.5×10^{-6}	0.107	0.00006	0.000001
Epoxy	10×10^{-5}	1.260	0.720	0.018
P.T.F.E.	13×10^{-5}	1.638	0.936	0.023
P.C.T.F.E.	70×10^{-6}	0.800	0.504	0.126
F.E.P.	104×10^{-7}	0.130	0.074	0.002

Table 3.3 – Calculated expansions in length, width and height of materials using the linear thermal coefficient listed.

These calculations do not take into account the restriction in the z direction caused by the press, although the changes in height are negligible compared to change in length. To overcome the mismatch in expansion (≈1mm in width between glass and P.T.F.E.) the rate of temperature change was decreased to allow creep and hence reduce thermal stress.

3.4.2   Bond strength

The bond strength of the fluoropolymer-laminate devices were characterised by a 180 degree T peel test for flexible assemblies (similar to ISO 11339:2003) on an Instron 1195 tensile testing machine. Two substrates (1-1.2mm thick, 75mm in length and 10mm wide) each with a 20μm layer of epoxy (20x10mm) were bonded together to form the samples. The average value over three samples for each fluoropolymer is shown in Table 3.4. The difference between the untreated and treated fluoropolymer bond strengths was 2.96kN/m for P.T.F.E., 0.39kN/m for P.C.T.F.E. and 2.0kN/m for F.E.P. Due to the negligible adhesion of the laminate to untreated P.T.F.E. and F.E.P. it was impossible to test the bond strength for these constructs. The P.T.F.E/epoxy/P.T.F.E. bond strength was the greatest (2.96kN/m); this data concurs with the contact angle measurements and its indication of bond strength. Samples of surface treated P.T.F.E. that had undergone heat treatment at 200ºC showed a bond strength of 0.94kN/m, a decrease of 69% over the bond strength for non heat treated P.T.F.E.

Substrate	Bond strength (kN/m)	Failure type
Plain P.T.F.E.	≈ 0	Laminate/substrate
Treated P.T.F.E.	2.96	Inter-laminate and laminate/substrate boundary
Treated and heated PTFE	0.94	Laminate/substrate boundary
Plain P.C.T.F.E.	0.16	Laminate/substrate
Treated P.C.T.F.E.	0.55	Inter-laminate and laminate/substrate
Plain F.E.P.	≈ 0	Laminate/substrate
Treated F.E.P.	2.00	Inter-laminate

Table 3.4 – Bond strengths and failure type for the fluoropolymers used, measured using a 180 degree T peel test.

After failure, epoxy layers remained on both the base and lid of all the devices fabricated using surface treated substrates. This and the 'rolling hills', created by shear forces seen on visual inspection of the fracture surfaces (Figure 3.9a) provides evidence that the strength of the fluoropolymer-epoxy laminate bond is greater than that of the bulk epoxy [220].
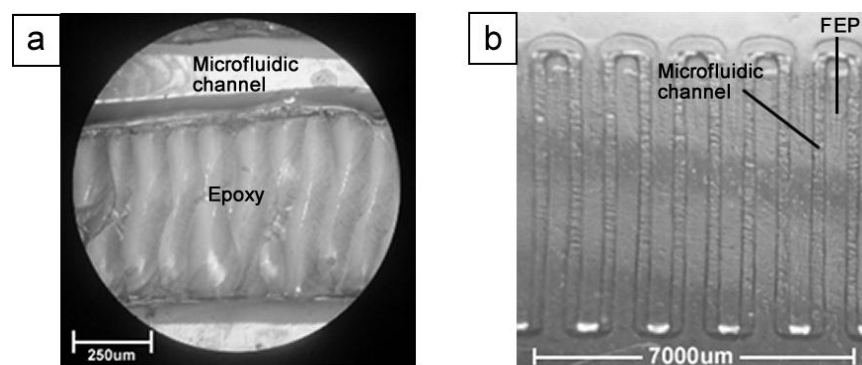
Figure 3.9a & b – a)Picture of ductile fracture plane in the epoxy laminate and b)fully cured and bonded F.E.P. chip showing the microfluidic channel

Examples of microfluidic structures manufactured in this study from P.T.F.E./epoxy/glass are shown in (Figure 3.10a & b). Figure 3.10b shows fluorescein in a buffer solution flowing through part of the chicane mixer of the device shown in Figure 3.10a. Similar structures were made from P.C.T.F.E. & F.E.P. (Figure 3.9b) although fabrication of devices using P.T.F.E. substrates (Figure 3.10c) proved the most reliable. P.T.F.E's stability at the temperatures required during bonding (up to 200°C) and its adhesion strength to the laminate are key factors in its suitability. Successful P.T.F.E./epoxy/glass constructs require the rate of cooling to be decreased from 120°C to 60°C per hour to prevent glass fracture due to thermal expansion mismatches.
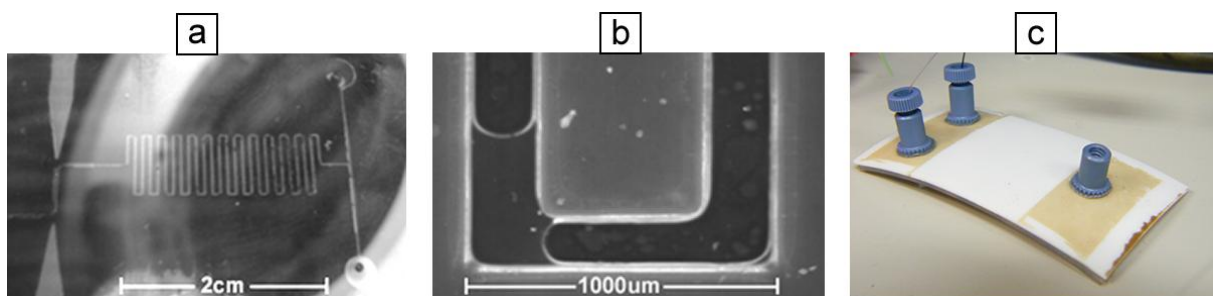
Figure 3.10a, b & c – a) A P.T.F.E. substrate with a glass lid used for absorption measurements b) Fluid flowing through a P.T.F.E.-glass microfluidic device and c) A P.T.F.E./epoxy/P.T.F.E. device with nanoport fluid inlets and outlet attached (curved due to incorrect cooling during fabrication).

3.4.2.1   Wetting

The contact angle between a fluoropolymer and a liquid also provides a measure of the bond strength of the material to a laminated epoxy (see Section 2.6.4.4). For comparative purposes the contact angles of the untreated and surface treated fluoropolymers (laboratory treated and commercially pre-treated), and of glass were measured with a 0.5µl water droplet placed using a

micro-mechanical stage, as shown in Figure 3.11. The angle (α) between the drop and the sample surface was measured and the average data from three readings is shown in Table 3.5.
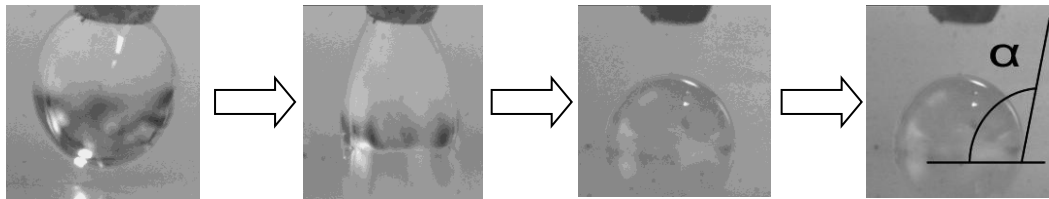
Figure 3.11 – A substrate being raised up to the droplet and then lowered to detach the droplet from the dispenser.

A change in contact angle confirms that fluoropolymer treatment has occurred [**221**]. The change of contact angle due to laboratory fluoropolymer surface treatment was 53° for P.T.F.E, 34° for P.C.T.F.E. and 46° for F.E.P. The lab treated samples showed a contact angle 15% higher than commercially treated samples. The contact angle can be assumed to be a function of the amount of etch as the surface properties (roughness, interfacial energy e.t.c.) determine the surface energy of the material and hence the contact angle [**222**].

Description	Measured Contact angle (°)	Droplet image
Glass slide	16	
Plain P.T.F.E.	105	
Lab treated P.T.F.E.	52	
Pre-treated P.T.F.E.	43	
Pre-treated and heated PTFE	72	
Plain P.C.T.F.E.	98	
Lab treated P.C.T.F.E.	64	
Plain F.E.P.	112	
Lab treated F.E.P.	66	
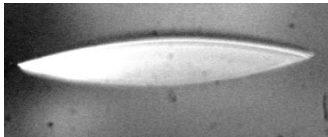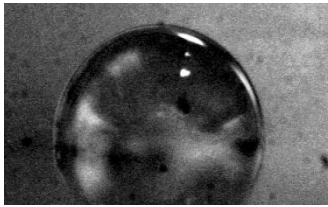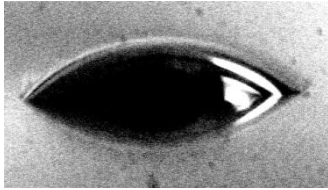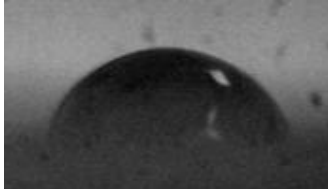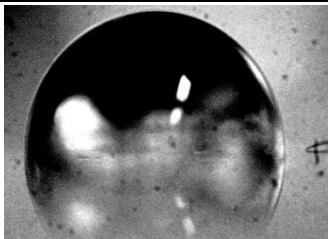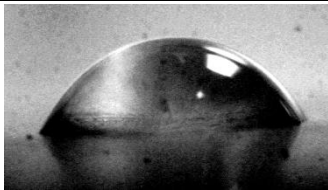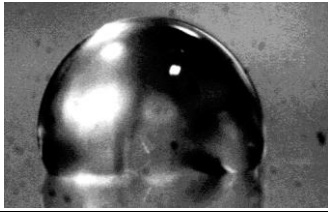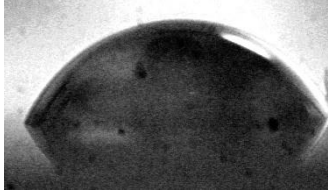
Table 3.5 – Contact angles for the treated and untreated fluoropolymers used within this study.

After chemical treatment, further exposure of un-bonded materials to heat (150 – 200°C for 2hrs), in air changes the contact angles back to near their original values. The colour of the chemically treated regions also lightens during heat treatment. The contact angle for pre-treated P.T.F.E. returns to 72° from 43°, 70% of the original value for untreated P.T.F.E. This process provides a mechanism for producing hydrophobic channels within microfluidic devices thus allowing the creation of bubble traps [223,224].

3.4.3   Material fluorescence

The fluorescence intensity of the P.T.F.E., P.C.T.F.E. and F.E.P. with and without the epoxy thin film was measured at 5nm intervals using a Tecan Safire[2] surface plate reader [225] with a 230-830nm excitation and 280-850nm and emission range. The average result of 5 reads per sample was taken. Emission measurements near the excitation wavelength were removed from the data due to saturation of the detector.

The Safire[2] reader is designed to measure the fluorescence of liquid samples and takes a 96 well surface plate. To enable solid substrates to be read, platforms were machined out of the plastic plate (Table 3.6). All these platforms are required to be the same height otherwise the fluorescence values measured are not relative. Substrates were washed consecutively with Acetone, I.P.A. and methanol to remove any foreign particles.

Parameter	Value
Excitation wavelength start	230nm
Excitation wavelength end	850nm
Emission wavelength start	280nm
Emission wavelength end	850nm
Excitation and emission wavelength step size	10nm
Excitation and emission bandwidth	5nm
Gain (manual)	170
Lag time	40μs
No. of reads per measurement	5
Target temperature	25°C
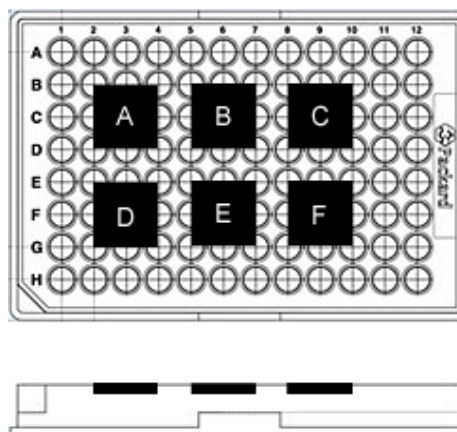
Table 3.6 – Table of setup parameters for the surface plate reader and diagram of modified surface plate and substrate positions.

The surface plate reader was setup to measure the entire emission wavelength (280 to 850nm) intensity. This causes problems when the excitation wavelength (5nm bandwidth) nears the measured emission wavelength as the intensity can peak above the maximum measurable (e.g. saturation of detection mechanism). The intensity measured includes a small contribution from

short stokes shift fluorescence but is dominated by reflected and refracted excitation light. Therefore it is necessary to remove data points from these regions. As emission wavelengths are normally longer than the excitation wavelength data up to 15nm below the excitation wavelength was removed. Additionally if any data within 20nm of the peak exhibited a step change of over 200% it was removed.

The fluorescence intensity of the samples were normalised to the peak emission intensity of a 318M fluorescein solution (Fluorescein m.p. 320oC, Fisher Scientific Ltd) at 535nm with an excitation wavelength of 500nm. However at wavelengths above 400nm the emission of the three polymers is low (<1.8% for P.C.T.F.E, <0.8% for P.T.F.E. and <0.8% for F.E.P.) See appendix 8.1.1 for further emission and excitation data. The intensity spectrum (relative to the fluorescein, as above) for treated P.C.T.F.E. with a laminate layer is shown in Figure 3.12. It can be observed that below an excitation wavelength of 280nm there is a peak in the relative fluorescence intensity (maximum of 0.350). Above 400nm the relative fluorescence intensity is minimal and therefore the material fluorescence will have minimal effect on L.O.D. and noise during optically sensitivity spectroscopy measurements (Section 2.4.3).
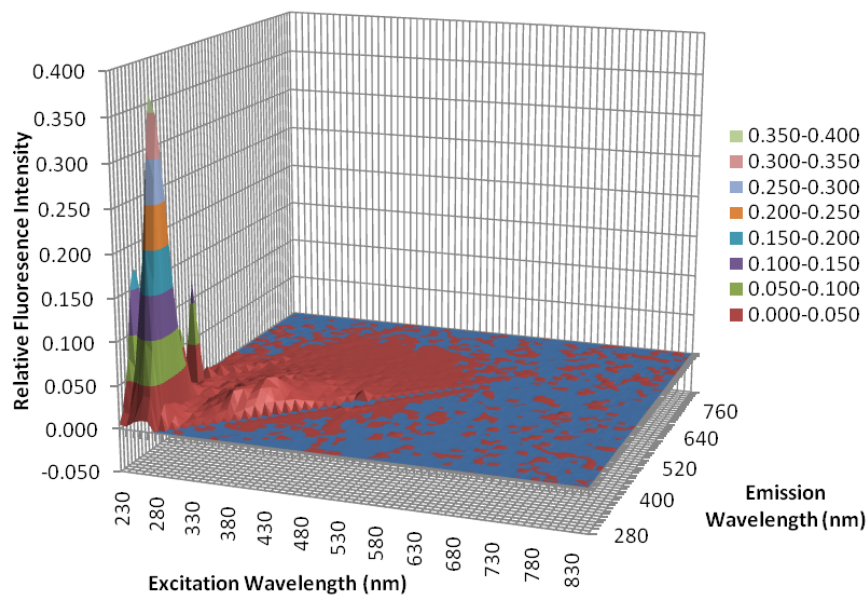
Figure 3.12 – Fluorescence intensity plot for treated P.C.T.F.E. with an epoxy laminate thin film layer.

3.5   Summary

A novel fabrication route for epoxy thin film laminate devices using fluoropolymer substrates has been described in this chapter. The most successful fabrication was achieved using surface treated P.T.F.E. substrates with low thickness variations. Surface treated P.T.F.E. devices also

provided the highest peel strength (2.96kN/m) in 180 degree peel tests. Both contact angle measurements and peel tests confirmed the increase in adhesion of the P.T.F.E, P.C.T.F.E. and F.E.P. fluoropolymers to the thin film laminate caused by chemical surface treatment. All of the fluoropolymer substrates offer significant advantages over glass and Si, providing cheap (£0.10 per cm^2), simple and robust platforms. The inherent fluorescence of these fluoropolymers is minimal in the wavelength range between 400-700nm, and their low refractive indices are ideal for use in creating integrated waveguides and use in a large variety of sensors. Sensors that rely on optical measurements below 400nm may be affected but the effect of fluorescence on the results (Section 2.6.4.4) can be minimised by the use of a lock in amplifier and a reference signal that cancels out the auto-fluorescence background and decay effects.

The bond strength of the thin film to the substrates was high enough to maintain a watertight seal during experimentation (500µM wide by 100µM high channels at 7.5kPa) and prevent delamination. The production of polymer only constructs which are resilient to shock increases the number of deployment scenarios and decreases the packaging costs over traditional glass L.O.C. systems. The work conducted and presented should help the devices shift from "chip in lab" to "Lab On a Chip" and allow robust sensors to be developed. However this fabrication route was not used for developing nitrite sensors in this study as the technology requires further development. Achieving the same level of knowledge and understanding (i.e. lifetime, fabrication failure rates, minimum feature size) of other mainstream fabrication routes (i.e. glass and epoxy thin film or PMMA & SU8) is outside the scope of this study. At the time of writing this other tried and tested methods provided a better platform for nitrite sensor development.

4. NITRITE DETECTION

This chapter focuses on the detection of nitrite using L.O.C. technology. A three stage iterative process was used by this study to develop an *in situ* prototype L.O.C. sensor to perform this task. This iteration was required as minimal literature and prior art was available on deep sea L.O.C. sensors. Each stage provided key information on the performance characteristics and technical obstacles, feeding into the each subsequent iteration of the sensor. The why, what and lessons learnt from each stage are detailed in the summary below:

- **Stage I – Macro and microscale sensor** (Section 4.1) – A combination of macro and microscale components where used for proof of principle experiments to determine the suitability of the variant Griess reaction (as described in Section 2.4.1.1) for the colourmetric spectrophotometric detection of nitrite in seawater. This chemical reaction had previously only been tested in large flow analysis systems [92] not in the type of miniaturised system proposed by this study. The components used had minimal fabrication lead times and offered a rapid way of identifying design and interface issues. Microscale elements were also used to determine the viability of low Reynolds number mixing (Section 2.6.2).

  While it was possible to successfully detect concentrations of nitrite in seawater (L.O.D. of 0.104μM), this preliminary work identified repeatability issues linked to the fluid delivery system (i.e. oscillating flow and air bubbles) and identified the benefits of a more compact mixing and detection system (i.e. minimal fluid path length). It was also confirmed that coloured dye could be used as a non toxic replacement for azo dye during testing.

- **Stage II – Microscale L.O.C. sensor** (Section 4.2) – Covers the 'in house' fabrication of a glass substrate epoxy thin film L.O.C. device (photo patterned and etched) L.O.C. device. The creation of a compact package combining mixing and optical detection (dual channel) enabled a reduction in fluidic path lengths reducing response times. The introduction of a three dimensional f-shaped mixer also provided a greater mixing efficiency than the chicane mixer used in stage I.

  The ability to detect nitrite concentrations using a low cost L.O.C. optical detection system was confirmed. It was noted that to provide head room for future system performance (i.e. higher measurement range and lower L.O.D.) that the coupling efficiency would need to be increased from that measured (0.11%). The combination of an improved extent of mixing and a differential absorption system provided a limit of detection for nitrite in seawater of

0.838μM with a precision of 7.801μM at 12.5μM. The poor precision was associated with incomplete mixing, and backed up by a comparison with pre mixed samples and visualisation of the mixing. The consolidation of components also led to a reduction in the number of faulty (i.e. leaking) interconnections.

- **Stage III – Bench top prototype sensor** (Section 4.3) – Due to compressed timescales the L.O.C. device designed by this study was manufactured by a third party. It presents the dark field mask design of the device, the calibration of ancillary components (e.g. pump and flow sensors) and the fabrication of the optics used to measure absorption. A qualitative investigation into the performance of the on board micromixer is also included. Results are presented for the detection of nitrite in the laboratory. A characterisation of a particulate filter is also included.

  Once again the device was able to detect nitrite concentrations through the change in absorption of an azo dye. The L.O.D. decreased to sub 100nM with a significant improvement in the precision (now sub μM) compared in stage II. This was enabled by an increase in the coupling efficiency between the L.E.D. and optical fibre (0.11% to 6%) and an improved extent of mixing (achieved through increasing the number of mixing segment from 4 in stage II to 16 in stage III).

The design and development of a L.O.C. device through this iterative process led to the production of a fully packaged *in situ* sensor. Chapter 5 details the construction and deployment of an *in situ* nitrite and nitrate sensor based on the same L.O.C. device that is reported in stage III. Sea trials (in the Atlantic Ocean) provided diagnostic and initial sensor performance data and proved the resilience of the sensors and its operation at depth.

4.1   Stage I – Macro and microscale sensor

In this section both macro and microscale components are used to provide absorption measurements as a proof of principle for the colourimetric spectrophotometric detection of nitrite in seawater using the variant Griess reaction. To minimise the limit of detection of nitrite (a key performance parameter, see Section 2.2.12) the peak wavelength of the light source used for absorption measurements needs to closely match the peak absorption wavelength of the azo dye. The peak absorption of the azo dye over a range of nitrite concentrations (measured using a Cary 1 Bio spectrophotometer) is shown in Table 4.1 where the reagents used in the variant Griess reaction are described in Section 4.1.3.

Nitrite Concentration (μM)	Peak Wavelength (nm)	Max change in absorption (%)
50	540	0.31
45	540	0.26
40	541	0.36
35	540	0.50
30	540	0.39
25	541	0.36
20	543	0.59
15	542	0.35
10	543	0.54
5	543	0.45

Table 4.1 – The change in peak absorption wavelength with nitrite concentration and its effect on absorption.

The azo dye absorption peak has a width of 213nm and rise width (10 to 90%) of approximately 52nm. The maximum absorbance wavelength of the azo dye is at 543nm for low concentrations (<20μM) and reduces to 540nm at 50 μM. The change in peak position (3nm over 45uM) accounts for an average error in absorption of 0.411% assuming a 3nm wavelength offset (i.e. a 1% variation in the peak absorption wavelength accounts for a change in absorption of approximately 1.8%). This drift in peak wavelength with concentration is caused by the change in composition of the solution at high concentrations [60]. The drift will affect the sensors accuracy (see Section 2.2.10) although the drift can be calibrated for as long as the sensor is precise (see Section 2.2.11).

Although the optimum peak intensity of a light source is 543nm (measuring the absorption at this wavelength would enable the lowest L.O.D. to be achieved) it is not always possible as L.E.D.'s are provided in set bands. As a compromise the light sources in this study have a peak intensity between 523-563nm.

Coloured dye was also used in the macro and microscale system (see Section 4.1.3). It provided a non-toxic method of testing the detection setup and identifying problems (i.e. leaks) and has significant absorption in the 543nm wavelength. The difference in peak absorption (and therefore L.O.D.) between the azo dye and the coloured dye was measured (≈38%) to provide information to enable a comparison of the sensor effectiveness. The absorption spectrum of a solution of 0.04% coloured dye (diluted using D.I. water from a base concentration of 100%) was measured (Figure 4.1, blue line) using a spectrophotometer (Cary 1 Bio). Plotting the absorption spectrum of the azo dye (100μM nitrite, prepared as per Section 4.1.3) alongside it (Figure 4.1, red line) shows that the wavelength of peak absorption of the coloured dye (506nm) is lower than that of the azo dye (537nm at 100μM).
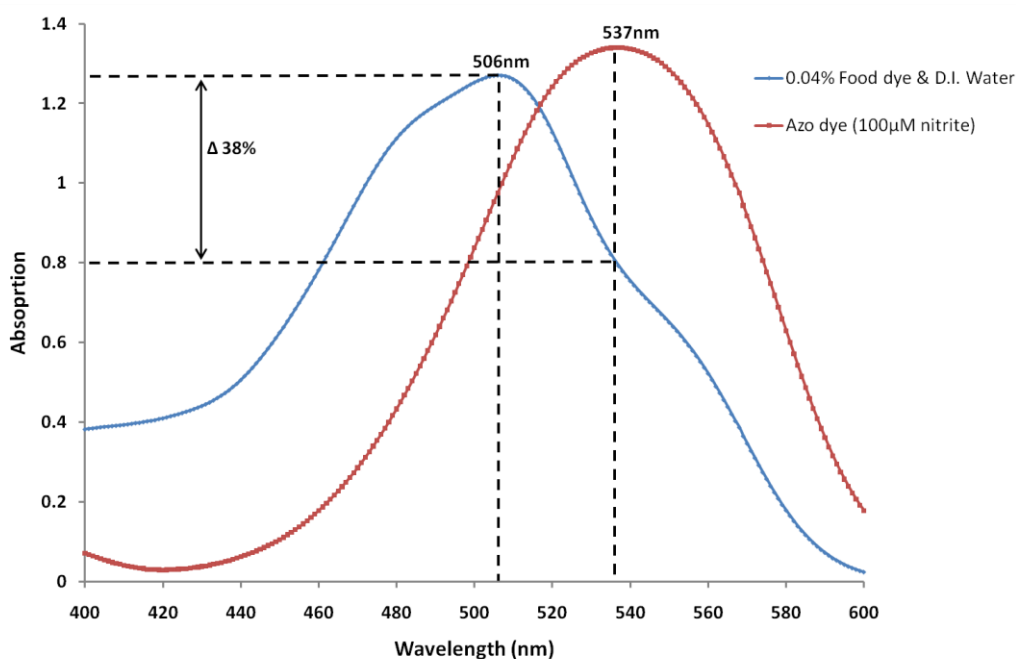
Figure 4.1 – Graph of absorption versus wavelength for coloured food dye and azo dye, with the wavelength of peak absorption indicated at 506nm and 537nm respectively.

The mixing of fluids (reagent and sample for the detection of nitrite or coloured dye and Milli-Q (M.Q.) water) was conducted with prefabricated commercial microfluidic technology, manufactured by Epigem Ltd, comprising of microfluidic modules and an interconnecting base. The modules connect to the baseboard using P.T.F.E. compression ferrules. Both modules and base are constructed using epoxy with a P.M.M.A. outer shell. They are chemically resistant to a variety of liquids including alcohols, weak/strong base, weak acid and chlorinated solvents at room temperature [226] which makes them ideal for the fluids involved in the variant Griess

reaction (which are pH 1-2), therefore fulfilling the material compatibility key performance parameter in Section 2.2.15. The technology provided a rapid, effective and consistent tool for prototyping allowing data to be gathered quickly without long fabrication lead times and design or interface issues to be identified early on.
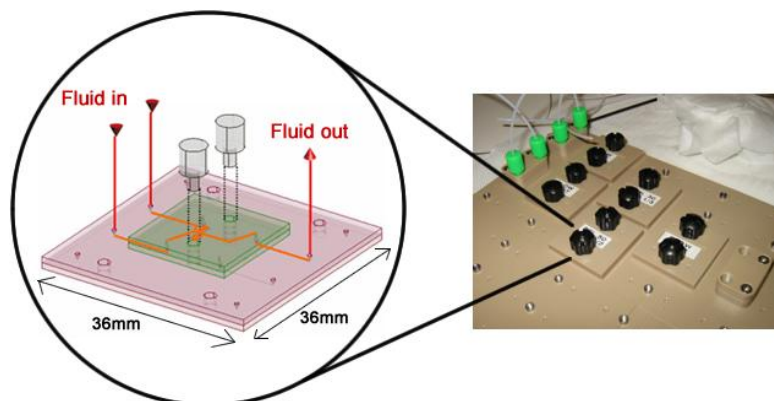
*Figure 4.2 – Illustration of a micro module manufactured by Epigem Ltd [**227**] with the fluid paths highlighted and a photograph of the Epigem microfluidic component system.*

No absorption cell or module was available from Epigem to integrate with the baseboard so a custom macroscale optical detection block or 'Optoblock' was designed and manufactured. The level of accuracy required was on the edge of traditional manufacturing equipment's performance envelope. Therefore fluid channels were designed so tolerances and dead volumes could be reduced after the main manufacturing stage and to ensure the channels were joined together to allow fluid flow. Further details on the 'Optoblock' can be found in Section 4.1.1.1.

4.1.1 Fluid delivery

The choice of pump was limited by the chemical resistance (key performance parameter, see Section 2.2.15) of the materials used in their construction (e.g. seals). The only pump available that fulfilled the performance criteria was a solenoid pump provided by the Lee Company (LPLA1210050L, 50µl per actuation with an actuation frequency of 2Hz and maximum pressure of 0.3bar) (pressure resistant and proven at depth [**228**]). An illustrated cross section of the pump is shown in Figure 4.7a. However the principle on which the pump functions creates pressure and flow rate variability over time. Additionally the maximum pressure it can produce (0.3bar) at low flow rates is relatively low before it ceases to operate. This is not ideal as changes in flow rate result in changes of absorption measurements due to variance in the extent of mixing and fluidic delay.

The flow profile for the Lee pump was measured using Sensiron LG16-1000A flow sensors (Figure 4.3). The sensors are the only miniature, low power (7.8μW) and highly sensitive (0.03μl/min) sensors commercially available whose wettable components are fabricated from inert materials. The inert materials used allow the reliable flow rate measurement of the harsh chemicals used in the detection of nitrite. In addition the material does not distort the chemical concentration of a species of interest through absorption or adsorption.

Parameter	Value
Total mass	6g
Physical dimensions	35x22x9mm
Power requirements	7.8μW
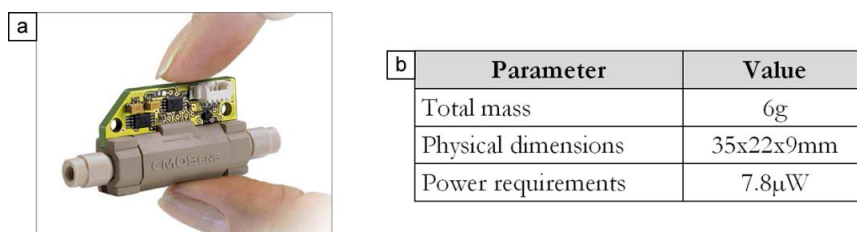
Figure 4.3a & b – a) A picture of the Sensiron LG16-1000A flow sensor and b) an overview of their specification.

Each flow sensors was calibrated by recording the voltage output for thirty seconds over a series of reference flow rates (see Appendix 8.2.1.1). The reference flow rate (up to a maximum of 1500 μl/min) was provided by a syringe pump (Nanomite, Harvard Apparatus) and the voltage output of the flow sensor logged by a data acquisition card. The flow rate is linearly proportional to the voltage and as such the equations that represent the voltage to flow rate calculation are shown in Equation 4.1 and Equation 4.2.

$$y = 0.0005x + 2.5015$$ *Equation 4.1*

$$y = 0.0005x + 2.4976$$ *Equation 4.2*

The flow profile (Figure 4.4a) for the Lee pump is a rapid increase in flow rate (>5000μl/min) followed by a period of reverse flow (>-3500μl/min). When a pressure drop (i.e. a microfluidic channel) is introduced before the pump the flow profile is altered (Figure 4.4b) and there is no longer any reverse flow. However the stoke volume (calculated from the area under the graph in Figure 4.4b) has reduced from 50μl to 29.63μl.
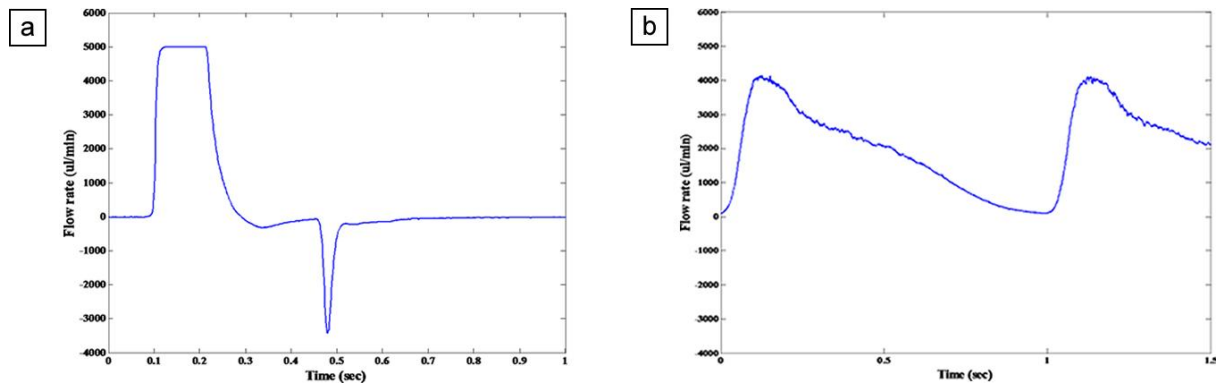
Figure 4.4a & b – Graph showing a) flow rate against time for the lee solenoid pump operating at 1Hz and b) pumping through the L.O.C. device

An example of the variation in an absorption channel signal using the Lee solenoid pump is shown in Figure 4.5 where the Lee pump is operating at a frequency of 1.571Hz. It causes a variation (ΔV) of 0.1041V at a frequency of 1.369Hz. For example this would which relates to a 7.44μM change in concentration (based on the results presented Section 4.2.10). This would mean that the sensor performance would be restricted to outside the precision, resolution and L.O.D. performance parameters sought (as presented in Section 2.2).
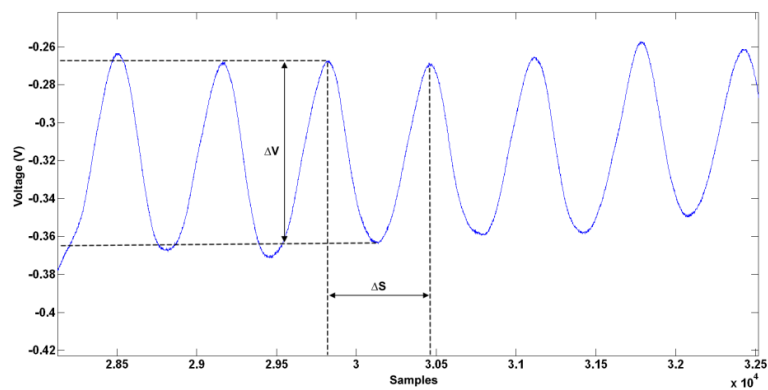
Figure 4.5 – Filtered signal showing the influence of the Lee pump operation at 1.571Hz on the voltage, and consequently the measured absorption.

The requirement for the flow to be consistent and smooth led to the investigation of the flow rate profiles of pumps for *in situ* deployment. Other solenoid pumps are available (e.g. Burkett diaphragm Type 7604 pump) that operate at a higher frequency (20Hz) however the pump profile is still cyclic and they have not been proven at depth. By adding hydraulic capacitance to a system including the Lee pump it is possible to smooth the profile of the flow, remove the negative flow and increase the period of time that the flow rate is constant. Figure 4.6 shows the

flow profile (measured at the inlet) of the Lee pump connected to the L.O.C. device via a 1ml glass syringe (Hamilton 1700 series) half filled with water. The syringe acts as a capacitor and dampens the initial high flow rate. The constant flow allows a consistent mixing ratio.
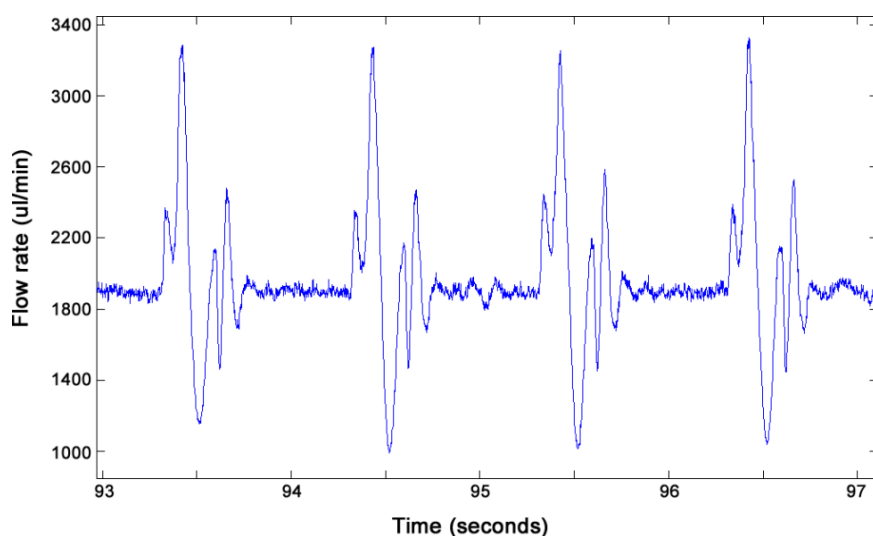
Figure 4.6 – Graph of the flow rate against time for a Lee pump operating at 1Hz with a 1ml syringe between the pump and the L.O.C. device.

To overcome the problem posed by flow rate fluctuations (both from the solenoid principle of operation and when it ceases to function) a temporary solution was constructed and is shown in Figure 4.7b. It allowed the fluid to be isolated from the oscillating pressure waves of the pump by using air to pressurise fluid containers (resulting in a ±10mbar pressure oscillation). The air acts as a capacitor and dampens the initial high flow rate. Whilst not suitable for *in situ* deployment this setup provided a rapid interim solution.
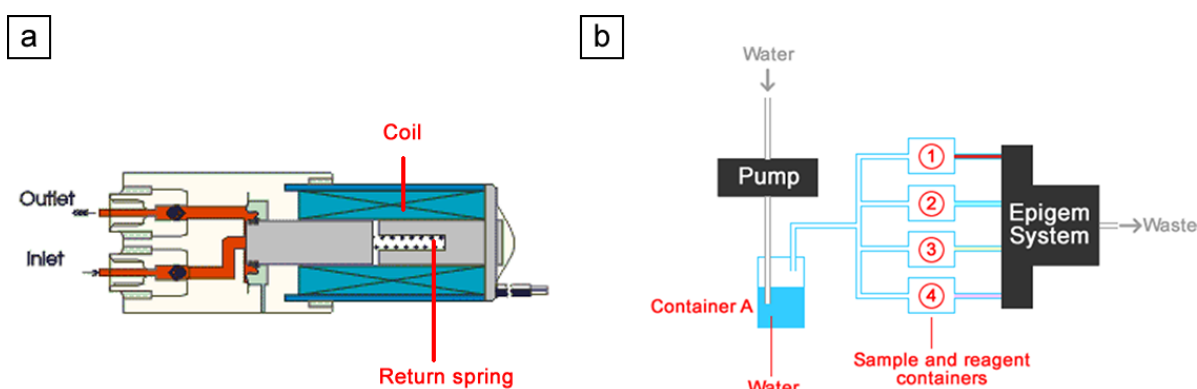
Figure 4.7a & b – a) Illustrated cross section of the Lee Company solenoid pump and b) the pumping set up used with the stage I system where the solenoid pump fills container A with water forcing air into the sample and reagent containers. The pressurised sample and reagent then flow through the Epigem system and 'Optoblock'.

4.1.1.1   Air bubbles

Bubbles present within the fluid and flow oscillations due to the pump increase noise in the L.O.C. device as the ratio of reagent and sample varies, as does the mixing level, and consequently the development of the azo dye is not stable. The trapping of air bubbles within a L.O.C. device is a serious issue in the design and operation of a sensor. Bubbles within a fluid can cause channel blockage, flow rate changes (which then affects the concentration of reagents), and interfere with the optics by presenting a volume in the light path with a different refractive index (causing light scattering and path changes hence signal changes, Figure 4.9). The bubbles within the fluid are created by air being drawn in through sample inlets, incomplete sealing of connections (as in the case of the Epigem system bread board system, Section 4.1), and through bubble initiation or micro bubble growth. Examples of bubble formation from an increase in temperature can be seen in P.C.R. chips [229]. Bubble initiation is produced by the diffusion of a gas out of a fluid. The gas most likely to reach a saturation level (that causes bubbles to form) is oxygen [230] . The saturation level of oxygen in water is related to the temperature, pressure and salinity levels by Henry's law (Equation 4.3), where P is the partial pressure of solute above solution, C is the concentration of solute in solution and K is henrys law constant [31].

$$e^p = e^{kc} \rightarrow p = kc \qquad\qquad \textit{Equation 4.3}$$

$$C_p = C^* \times P \left[\frac{(1 - P_{wv})(1 - \theta P)}{(1 - P_{wv})(1 - \theta)} \right] \qquad \textit{Equation 4.4}$$

$$\%Saturation \times \frac{(DO)}{C_p} \qquad\qquad \textit{Equation 4.5}$$

The equilibrium concentration of oxygen that water is able to hold at a depth is given by Equation 4.4, where C_P=Equilibrium oxygen concentration at non standard pressure (mg/L), C^*=equilibrium oxygen concentration at standard pressure (mg/L), θ=temperature dependence, P=non standard pressure (atm), P_{WV}=partial pressure of water vapour (atm). The level of oxygen in the water required to produce saturation (%) can be calculated using Equation 4.5 where D.O. is dissolved oxygen (mg/L) [231].

A draw through pump system decreases the pressure in the fluid and therefore decreases the equilibrium oxygen concentration saturation level. If the level of oxygen concentration in the water is near the equilibrium level before the fluid enters the sensor and the pressure is reduced then oxygen will come out of solution to create new bubbles or cause bubble growth.

Pressure (kPa)	Temperature (°C)	Equilibrium oxygen concentration (mg/L)	Salinity corrected oxygen concentration (mg/L)
131.32 (1.296atm)	20	11.785	9.923
131.32 (1.296atm)	10	14.628	12.156
101.32 (1 atm)	20	9.095	7.658
101.32 (1 atm)	10	11.290	9.382
71.32 (0.704atm)	20	6.404	5.392
71.32 (0.704atm)	10	7.950	6.606

Table 4.2 – Equilibrium oxygen concentrations for various pressures and at either 10 or 20 degrees Celsius.

Oxygen solubility is also inversely proportional to salinity so values taking this into account are also included in Table 4.2 (based on a conductivity of 4.500milli-Siemens [232]). Values for a pressure of 71.32kPa represent those that could be seen when using a micro-pump to draw water through the sensor on the surface, and 131.32kPa is for 2.96m under water (depth value chosen due to reference information availability).
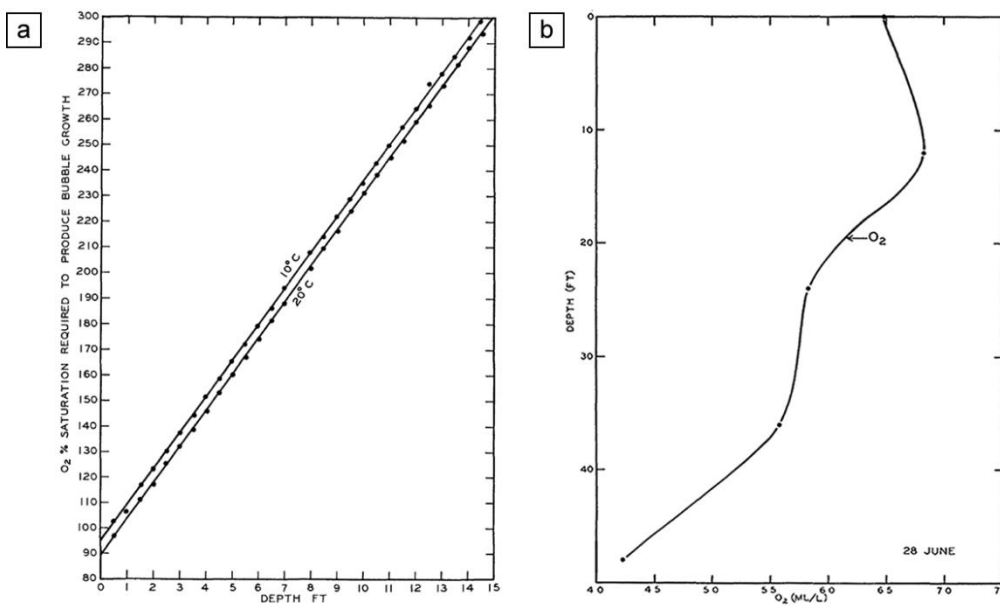
Figure 4.8a & b – a) Oxygen super-saturation necessary to produce bubble growth and an example of the vertical distribution of oxygen [230].

The equilibrium oxygen concentration increases with depth (Table 4.2) in the ocean (gas solubility increases with pressure, Figure 4.8a) so when the sensor is a few metres below the sea bubble growth and nucleation would be prohibited. The amount of dissolved oxygen at the sea surface varies between 5.13 and 9.9932mg/L [230] and the level for saturation to cause bubble growth only occurs in the first few metres. Therefore any problem in bubble formation would be restricted to near surface and laboratory based measurements.

A decrease in pressure can also cause an expansion of micro-bubbles already present within the water. In equilibrium the internal pressure in a bubble is equal to the sum of ambient pressure and the skin pressure due to the surface tension (Equation 4.6) [233,234]. Where P_{in} is pressure inside the bubble (N/m^2), P_{amb} is the ambient pressure outside (N/m^2), γ is the surface tension (Nm) and r is the radius of the bubble (m). A change in the ambient pressure means the bubble has to expand to remain in equilibrium.

$$P_{in} = P_{amb} + \frac{2\gamma}{r}$$

Equation 4.6

The bubbles may not be visible within fluid inputs but with a draw through pump system they can expand and coalesce with other bubbles already present within the system to a size that becomes noticeable (>5μm). The primary reason for operating a draw through pumping system (rather than a push through) is to reduce the number of pumps required. It allows the flow rates of reagents and samples to be controlled by either valves or different size channels. If only one pump is required power consumption and production costs are kept to a minimum.

Whilst the device is being tested in the laboratory the effects of bubbles can be removed or decreased by 'degassing' the reagents and samples in a vacuum desiccator ($\approx 2\times 10^{-3}$ mbar). The effects are short term as the fluids will reabsorb gases through diffusion [235]. During *in situ* deployment degassed reagents could be stored in hermetically sealed containers and be relied on to counter act any air introduced from the seawater sample as is not possible to degas continuous fluid samples without consuming large amounts of power (>100W). Alternatively a push through pump system can be utilised, as is the case for the stage I experiments presented.
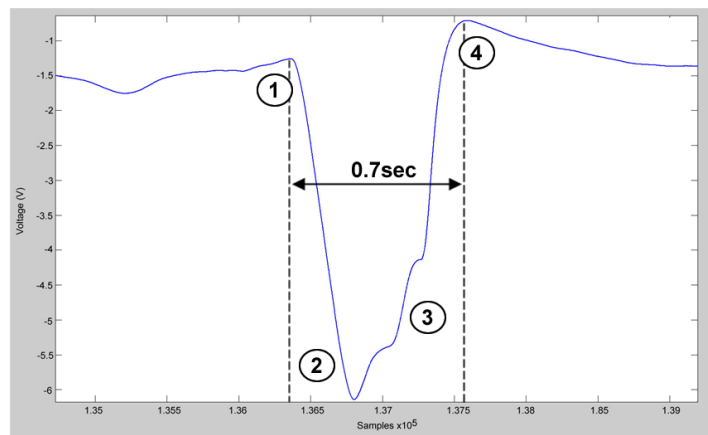
Figure 4.9 – Change in voltage caused by a bubble passing through the optical detection path where 1) indicates the bubble entering the optical cell, 2) and 3) the bubble causing a large decrease in the light reaching the photodiode and 4) the bubble exiting the absorption cell.

4.1.2   Experimental setup

The pumping setup (as per Figure 4.7b) was connected to the Epigem modules via microbore tubing (Ø0.8mm). The total path length of fluid between each sample and reagent container and the Epigem system inlets was 250mm. The pressure generated by the pump inside container A (see Figure 4.7b) was monitored on the inlet using a digital differential pressure meter (Digitron 2002P). Two configurations of Epigem modules (each 36 by 36mm with 100μm wide by 100μm high channels) were used. Figure 4.10a shows the setup for coloured dye experiment (presented in Section 4.1.4) where the two fluid inlets (sample and D.I. water) are brought together in a 200mm path length chicane mixer module before entering the optical detection module. Figure 4.10b shows the setup for the detection of nitrite experiment (presented in Section 4.1.5) where the sample and sodium citrate are brought together in a 50mm path length chicane mixer and then mixed together with a reagent in 100 and 500mm path length chicane mixers. The fluid output from the final chicane mixer passes into the optical detection module.
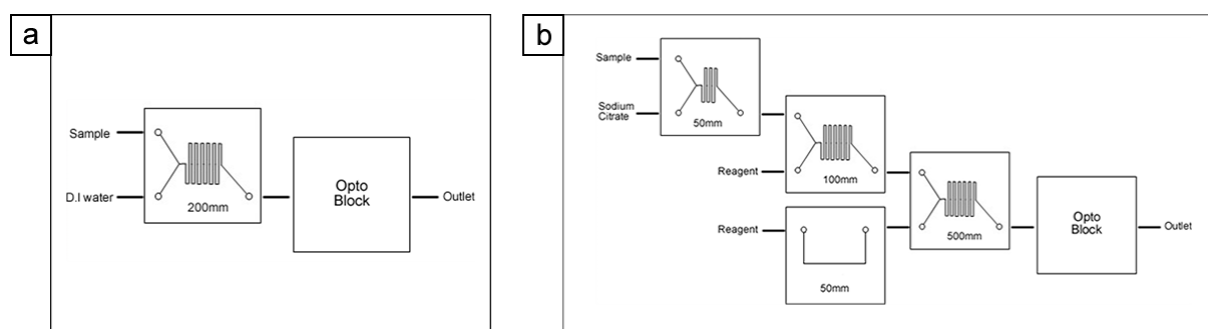
Figure 4.10a & b – Diagram of the Epigem system setup used for a) coloured dye detection and b) nitrite detection where the microfluidic path lengths are indicated on each module.

The optical detection block (illustrated in Figure 4.11a) or 'Optoblock' was manufactured in acrylic and its dimensions are shown in Figure 4.11b. The light source was a green led (Toyoda Gosei E1L31-AG0A-02) with peak intensity in the 532nm region (Δλ=35nm) driven at 2.8V (834mcd). Although the peak wavelength of the L.E.D. ($\lambda_{max}\approx532$nm) is higher than 506nm absorption peak of the coloured dye, light will still be absorbed (68% of maximum). A photodiode (Taos TSLG257) with an integrated green filter lens and trans-impedance amplifier was used to detect the intensity of light after a 12mm path length, 1mm diameter channel (with a total volume of 9.42μl). A diagram of the absorption cell is shown in Figure 4.11c.
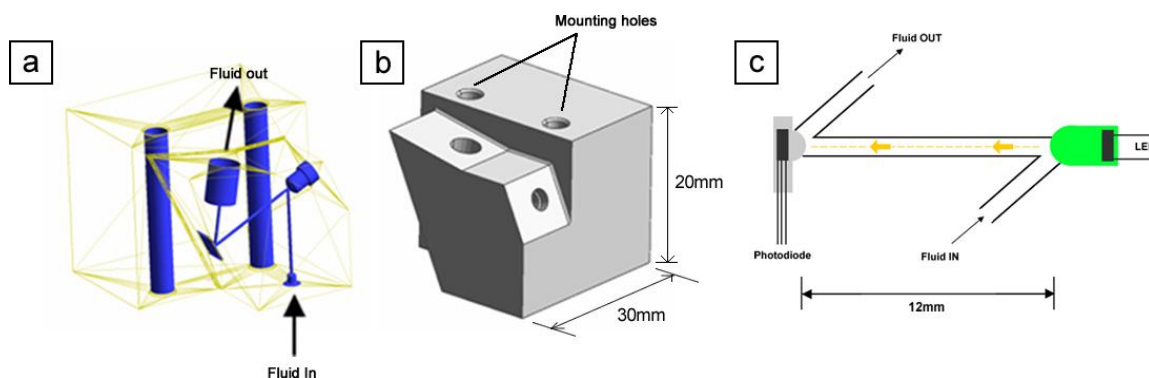
Figure 4.11a, b & c – a) a semi-transparent and b) opaque view of the 20 by 30mm acrylic optical block c) Optical setup of the macroscale detection block where the absorption of the fluid is measured using a L.E.D. and photodiode.

The photodiode and L.E.D. were connected via a digital to analogue converter (D.A.C. - NI-DAQ e-series 6036E) to a laptop. National Instruments LabView software allowed the L.E.D. driving voltage to be changed and the photodiode voltage output to be recorded.

4.1.3   Reagent and standard preparation

This section details the preparation of the samples, coloured dye and reagents used to test and characterise the stage I macroscale and microscale detection system.

- A stock solution of 0.1% coloured dye was prepared by diluting red food dye (Superfoods Ltd) with deionised water. A range of concentrations between 0 and 0.1% were subsequently prepared through dilution of the stock solution with deionised water.

- Nitrite samples were prepared from a standard seawater and 100µM nitrite solution (O.S.I.L. Uk Ltd) mixed with 2.5% v/v sodium citrate.

- The reagent used for the detection of nitrite (based on the Tovar et al [92] variant Griess reaction, presented in Section 2.4.1.1) was comprised of 0.06M sulfanilamide, 2M HCl, 0.5% polyvinyl alcohol and 0.05% N-(1-napthyl)ethlenediamine dihydrochloride, all sourced from Fisher Scientific Uk. It was prepared in 200ml batches by mixing together; 2 grams of sulfanilamide and 1 gram of P.V.A. dissolved in 35ml of concentrated HCl and 65ml of deionised water; and 0.1 gram of N.E.D. dissolved in 100ml of deionised water.

4.1.4   Detection of coloured dye

A series of coloured dye samples (between 0 & 0.1% concentration) were mixed with D.I. water inside the Epigem system (setup shown in Figure 4.10a) and the absorption measured as the fluid flowed through the 'Optoblock' at 101μl/min (1:1 ratio of coloured dye samples and D.I. water). The voltage output of the photodiode was recorded after 40, 41 and 42 minutes (full results are presented in Appendix 8.2.1.1). The delay in taking a measurement allowed any resident dye from previous samples to be flushed out and to remove any smearing effects. The fluid output for each sample concentration was also collected in a cuvette and the absorption measured using a commercial spectrophotometer (Appendix 8.2.1.2.1). Figure 4.12 shows a graph of absorption versus concentration for the series of coloured dye samples. Two measurements were taken for the 0.02 and 0.03% concentrations because of uncertainty in the sample dilution.
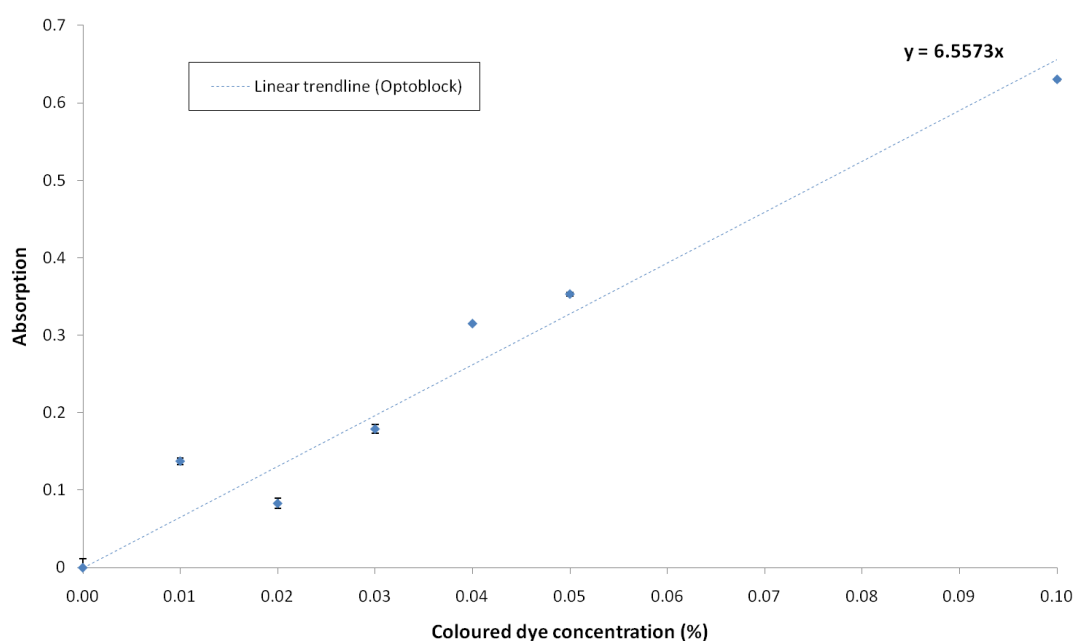
Figure 4.12 – Graph showing absorption measured in the 'Optoblock' against dye concentration where the error bars are the positive and negative standard deviation (resolution). The linear trendline for the plot and the equation of the line are also shown.

The results show an increase in measured absorption with an increase in concentration. The average standard deviation of all measurement points (and thereby resolution, Section 2.2.9) is 0.00497A (0.00076% dye concentration). Using the equation for the limit of detection presented in Section 2.2.12, and with k=3, the run has a L.O.D. of 0.0045% (or 0.0295A).

The equivalent nitrite concentration in seawater for an absorption of 0.845 would be 56.56μM. Using this it is possible to calculate the equivalent minimum concentration of nitrite that the device would be able to detect (i.e. L.O.D.). This is achieved using Equation 4.28 below where A_n is the absorption of the nitrite sample of concentration C_n, A_d is the dye L.O.D. and the equivalent nitrite concentration is E_d. The respective limit of detection for a 0.0045% concentration would be 1.975μM. This provides a comparison of sensor effectiveness.

$$\frac{C_n}{(A_n/A_d)} = E_d \qquad \text{\textit{Equation 4.7}}$$

$$\frac{56.56}{(0.845/0.0295)} = 1.975μM \qquad \text{\textit{Equation 4.8}}$$

Figure 4.13 shows the commercial spectrophotometer absorption measurements of the fluid output against the absorption measured in the 'Optoblock'. The absorption readings from the commercial spectrophotometer are consistently higher than those of the 'Optoclock'. Although, the accuracy given by the deviation from the linear trend line on the graph, is inconsistent.
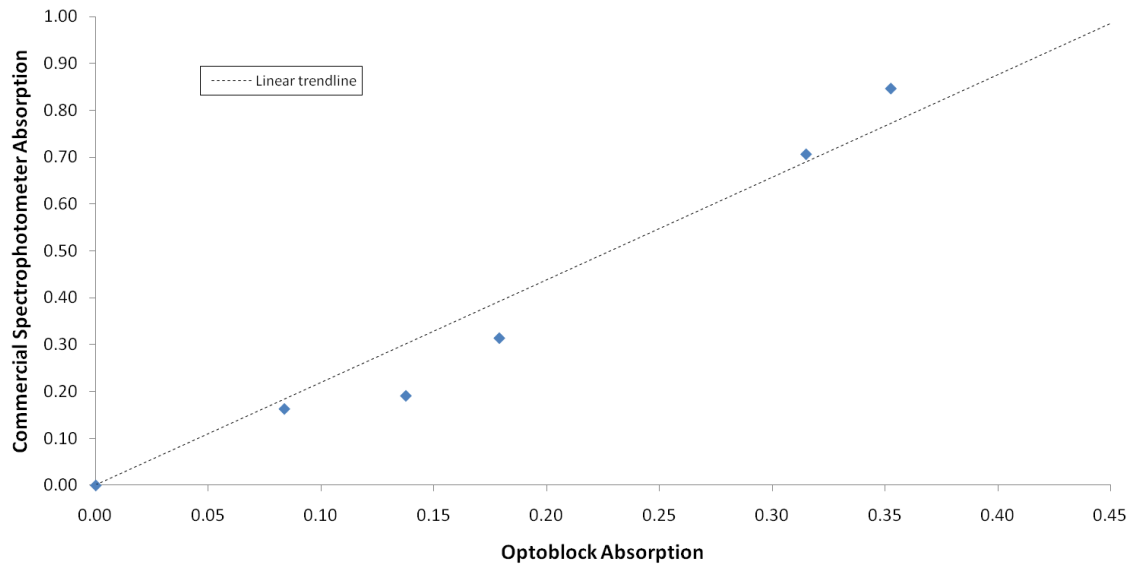
Figure 4.13 - Graph showing the absorption measured in the Cary 1 Bio commercial spectrophotometer against the absorption measured in the 'Optoblock' for coloured dye and deionised water concentrations between 0 and 0.1%.

After each concentration a blank sample was run to gain a baseline reading. It showed a decrease in the voltage recorded with run number and a decrease in concentration.

4.1.5   Detection of nitrite

Differing concentrations of nitrite in sea water (0, 5, 7 and 10μM) and a reagent (see Section 4.1.3 for details) were mixed together inside the Epigem board. No change in the absorption with change in concentration was detected with the setup used in the coloured dye experiments so the Epigem module setup was modified to increase the mixing level. The revised setup (see Figure 4.10b) used the longest path length chicane mixer available (total path length of 500mm). The voltage output of the 'Optoblock' photodiode was recorded after 20 minutes of continuous flow. Results are presented in Figure 4.14 for two separate runs of the four nitrite concentrations (0,5,7 and 10μM).
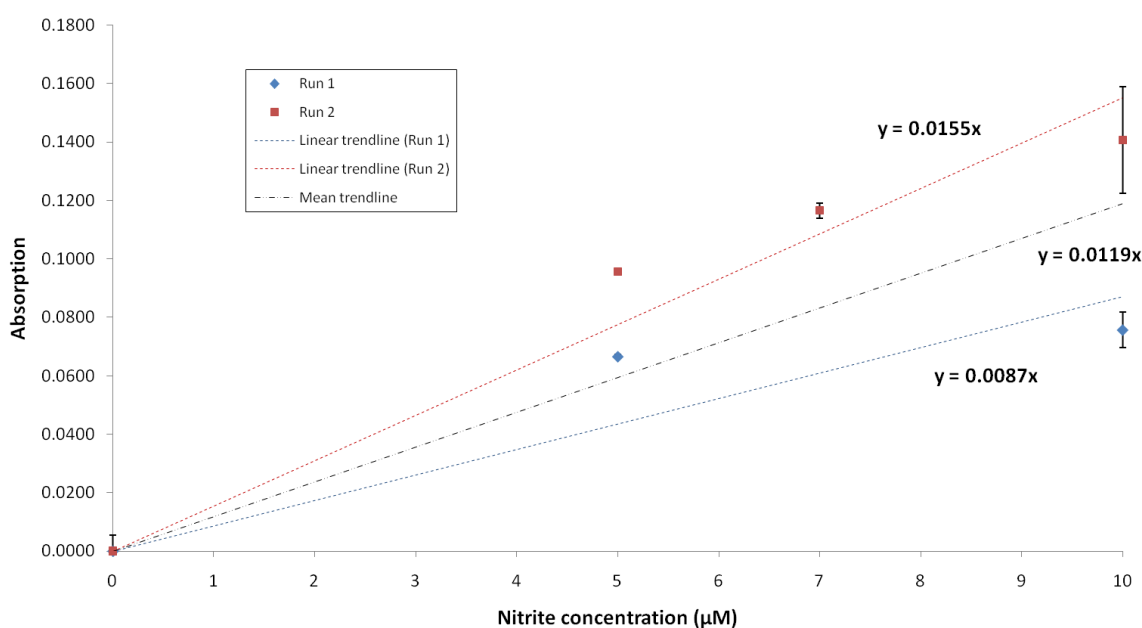
Figure 4.14 – Graph showing absorption against nitrite concentration for two runs where the error bars are the positive and negative standard deviation (resolution). The trend lines and representative equation for the two runs are also shown.

Once again the results show an increase in measured absorption with concentration. The average standard deviation (resolution) of the absorption measurements for each of the two runs was 0.0041A (0.47μM) and 0.0055A (0.35μM). Using the equation for the limit of detection presented in Section 2.2.12, and with k=3, the two runs have a L.O.D. of 1.5μM and 0.104μM respectively. The precision, given by the standard deviation of absorption values measured at 10μM across the two runs (as per Section 2.2.11), was 0.037A (3.11μM).

4.1.6   Discussion

Coloured dye was used as a non toxic, rapid method to test the detection setup and identify any early issues. Absorption measurements recorded for the detection of coloured dye resulted in an equivalent nitrite concentration L.O.D. of 5.09µM. The stage I microscale and macroscale sensor was also successfully used in the detection of nitrite in seawater with an average L.O.D. of 0.802µM. The differences between values for subsequent runs in the detection nitrite show that there are repeatability problems associated with the experiment. Initial conclusions as to the cause of these problems focused around incomplete mixing, oscillating flow and the presence of air bubbles. These three issues are covered during the design and development of the next iteration, the stage II sensor.

These experimental L.O.D. values compare to the theoretical limit of 4.825nM, based on the 12mm path length of the 'Optoblock', 200µV minimum response of the photodiode [236], and calculated using the Beer-Lambert-Bouger law (Equation 4.9). Where P_T is equal to one, P_0 is P_T plus the minimum sensitivity of the photodiode as per Equation 4.10 and Equation 4.11. The maximum limit based on a maximum response of the photodiode of 4.5V is 41.11µM

$$-log_{10}\left(\frac{P_T}{P_0}\right) = \varepsilon bc \qquad \textit{Equation 4.9}$$

$$-log_{10}\left(\frac{1}{1 + (200 \times 10^{-6})}\right) = \varepsilon bc \qquad \textit{Equation 4.10}$$

$$\frac{8.685 \times 10^{-5}}{(1.5 \times 10^{6} \times 0.012)} = c = 4.825 \times 10^{-9}\text{M or 4.825nM} \qquad \textit{Equation 4.11}$$

The difference between the theoretical and actual detection limits could have occurred because of incomplete mixing and noise. The comparison of the commercial spectrophotometer and 'Optoblock' absorption measurements indicate mixing levels are part of the reason as the absorption values in the commercial spectrophotometer (10mm path length) are higher than in the 'Optoblock' (12mm path length).

Long fluidic path lengths (≈500mm) were necessary in the detection of nitrite to provide a degree of mixing required for the Griess reaction however they increase the amount of dispersion, fluidic delay and smearing from dead volumes and channel residue (as discussed in Section 2.2.13, 2.2.19 and 2.2.21). They also increase the fluidic resistance and hence the power requirements of the pump. The fluidic resistance of the Epigem system can be calculated using the difference in flow rate of the pumping setup with and without the system attached. The flow rate of the fluid

through the Epigem system was 101μl/min. Without the Epigem system attached the pumping setup was capable of 5500μl/min. The difference in flow rates is due to the pressure drop of the fluid through the long path lengths and narrow channels. The fluid resistance of the Epigem system is given by Equation 4.12 and Equation 4.13 where ΔP is the pressure difference (N/m^2) and Q_v is the volumetric flow rate (m^3/sec).

$$R_F = \frac{\Delta P}{Q_v}$$ *Equation 4.12*

$$\frac{30000}{1.01 \times 10^{-4}} = 1.782 \times 10^{10}$$ *Equation 4.13*

An increase in the dispersion and smearing will increase the minimum resolvable volume, time response leading to a decrease in achievable sampling frequency. This reduces the temporal and spatial resolution of an *in situ* sensor. In the next iteration of design (stage II, Section 4.2) the fluidic path lengths are minimised through component integration and improvements in mixer efficiency.

Although the development and integration of the pumping system is outside the scope of the study (Section 1.1) the requirement for a robust and reliable system that can be deployed during *in situ* trials in this study must be considered. An *in situ* version of the pumping system used in this section could be built to provide a stable reagent and sample delivery system, making use of two micro-pumps. One pump to pressurise the reagent containers and another to pump through the sample, enabling control of mixing percentages. However the size requirements of the final packaged sensor would inhibit this. Further investigation into a simple, suitable, pumping solution was needed. A temporary gravity fed solution was used during stage II (next section) and further investigations into an *in situ* delivery system are covered in the design of the stage III sensor (Section 4.3).

4.2 Stage II – Microscale L.O.C. sensor

Following the testing of the stage I prototype (Section 4.1) it was identified that the long fluidic path length caused dispersion and smearing of the sample. The stage II prototype, reported in this section, significantly decreases the path length by combining mixing and optical detection onto a single platform. Not only did this allow the reduction in smearing but decreased the package size of the sensor. The compact package was achieved by using dry, thin film, photosensitive epoxy (Section 4.2.5) to create a L.O.C. device that could be fabricated quickly, is low cost and has the necessary chemical resistance. The packaging of the mixer and optical absorption cell into one platform also reduced the number of potentially faulty interfaces (i.e. fluidic connections). The design of the package also considered the pressure effects of operating at depth in the ocean (Section 4.2.1).

To decrease the fluidic path length a three dimensional micromixer was also used to increase the mixing efficiency (higher percentage mixed over a shorter path length). Additionally it was used to improve the extent of mixing and decrease the L.O.D. of the sensor. The stage I sensor presented previously did not rely upon anything other than a simple chicane L.O.C. micromixer. As the micromixer enables the device to continuously sample and measure absorption *in situ* it was vital that confirmation of its operational effectiveness in the mixing of nitrite samples and the reagent was gained. The improvement in the extent of mixing was measured by a comparison of commercial spectrophotometer and L.O.C. measured absorption readings. This was further backed up by the comparison of the absorption of premixed nitrite and reagent samples and on device mixed concentrations. Visualisation of the mixing was also conducted (Section 4.2.14).

A differential or dual channel measurement technique was also introduced to increase resolution, precision and accuracy (as suggested in 2.4.1.1) in future *in situ* environments. The difference in fabrication technique also necessitated a change to the optical design (see Section 4.2.7.2) but low power optical sources (0.1W) and detectors were still utilised. These low powered components were combined with low power electronics to increase deployment opportunities and running times.

As in stage I, the absorption of a series of coloured food dye dilutions were initially used to test the functionality of the device. A gravity feed fluid delivery setup was used to isolate the flow rate variations from sensor performance. Presented in Section 4.2.7.1 it was to show that the new optical design was able to detect changes in absorption with dye concentration. Further tests were performed in Section 4.2.9 using a series of premixed nitrite and reagent samples to isolate the

absorption measurements from mixer performance. Finally nitrite concentrations in seawater and the reagent were injected separately into the L.O.C. in Section 4.2.10 and the microfluidic mixer used to mix the two fluids. Section 4.2.7 covers the preparation of all reagents and samples for the stage II prototype.

4.2.1 Pressure resistance

There are two ways of ensuring the sensor is pressure resistant. The first is to encase the working components (surrounded by air) within a structure capable of withstanding the pressure (e.g. a titanium case [116]). This adds weight, increases the overall size and adds complexity due to fluidic seals and the need for pressure resistant fluidic pathways. However it does separate the components from the harsh seawater environment. The alternative is to ensure each component is pressure resistant and to protect them from the environment using a thin casing filled with a pressure transmitting medium (otherwise known as a pressure compensated case [237]). This allows the size and weight of the casing to be kept to a minimum but each component must be pressure tolerant (this often means no air or vacuum can be present). For the sensor to be low cost and miniature it was necessary to adopt a pressure compensated case design. Therefore during the design of L.O.C. device (specifically that of the dark field mask used in the fabrication) and optical detection setup any pockets of air were minimised.

4.2.2 L.O.C. absorption measurements

The integration of the absorption cell into a thin film L.O.C. device meant that the use of an L.E.D. in the same manner as stage I was no longer possible. This is due to the restricted substrate shape and height of the micro channel. Laboratory based L.O.C. devices that integrate optical absorption cells (as presented in the example by Bargiel et al [141] in Section 2.6.3) often couple a laser light source into an optical fibre and insert the fibre into the L.O.C. device to resolve this issue. Due to the power limitations and pressure resistance requirements of an *in situ* sensor the use of a laser is not possible. As an alternative this section focuses on the coupling of an L.E.D. to an optical fibre. Section 4.2.2.1 identifies whether the L.E.D. can provide sufficient optical power and the coupling losses associated with launching light using this technique. The optimum length for maximum sensitivity during absorption measurements is also presented in Section 4.2.2.2.

While the addition of a another absorption cell adds to the complexity of a L.O.C. design, and increases the number of optical detection components it provides a degree of immunity to signal interference and offsets from changes in turbidity and pressure as well as interference from stray light. Even with the use of an inlet filter foreign particles are present within any seawater sample

(see Section 2.2.17). These particles cause scattering and reflectance during absorption measurements and decrease precision and resolution. Stray light (i.e. natural sunlight in near sea surface or land based deployments) can also cause a deviation from the Beer-Lambert-Bouger law as described in Section 2.4.1.1. The change in absorption from stray light and the scattering and reflectance of a medium can be factored out by using a reference medium (i.e. one without any absorbing molecules) and a differential absorption measuring system. Differential or ratio measurements can also reduce the common noise in the light source, detectors and relevant electronics [238]. To prevent variance between channels in changing environmental conditions (i.e. temperature), both channels should have the same light source. Based on this the stage II prototype uses a differential measurement system to increase accuracy and precision. As such a single L.E.D. is required to launch light into both channels to remove any unbalanced variation.

4.2.2.1   Light intensity reduction due to coupling inefficiencies

Coupling the light into and out from optical fibres results in a reduction of light intensity. Geometrical mismatch, angular losses and Fresnel losses all contribute to decreasing coupling efficiency. Geometrical mismatch is a problem coupling light into a fibre as an L.E.D. emitter area (>500 x 500μm) is normally larger than a fibre core. Coupling the light from a fibre to a detector normally results in small or no geometrical loss as the fibre is smaller than the active area of the detector. Fresnel losses are those caused when a portion of the light is reflected at the interface of two different refractive index mediums (i.e. from the L.E.D. to fibre). Angular losses are caused by the non uniform emission pattern of the L.E.D. (an example of which is shown in Figure 4.15) and the finite acceptance cone of the fibre. To provide an estimate on the losses experienced in coupling an L.E.D. to a fibre both theoretical calculations and experimental results are presented. This determines whether the selected L.E.D. is a suitable replacement for a laser.
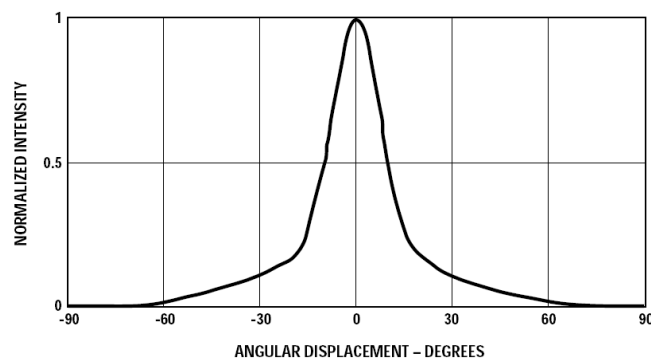
Figure 4.15 – Non uniform emission characteristics of an Agilent HLMP light emitting diode, with normalised intensity against angular displacement.

The theoretical calculation of efficiency [239] assumes the fibre (Ø240µM core) is directly butted against the active area of the L.E.D. (Agilent HLMP-CM11-Y2000) and the active area is bigger than the fibre core diameter. The fibre coupling efficiency (η) is given by Equation 4.12 where η_{geo} is the geometrical losses factor, $\eta_{Fresnel}$ is the Fresnel losses factor and η_{ang} is the angular losses factor.

$$\eta = \eta_{geo} \times \eta_{Fresnel} \times \eta_{ang} \qquad \text{Equation 4.14}$$

The geometrical loss factor is given by Equation 4.15 and Equation 4.16 where r is the radius of the fibre core (0.120mm), w is the width of the L.E.D. active area (1mm) and ℓ is the length of the active area (1mm).

$$\eta_{geo} = \left(\frac{\pi r^2}{w \times l} \right) \qquad \text{Equation 4.15}$$

$$\eta_{geo} = \frac{\left(\pi \times 0.120^2 \right)}{1 \times 1} = 0.04524 \qquad \text{Equation 4.16}$$

The Fresnel loss factor is given by Equation 4.17 and Equation 4.18 where n_f is the refractive index of the fibre (≈ 1.59) and n_i is the refractive index of the medium surrounding the active area (≈ 1.50).

$$\eta_{Fresnel} = 1 - \left(\frac{\left(n_f - n_i \right)^2}{\left(n_f + n_i \right)^2} \right) \qquad \text{Equation 4.17}$$

$$\eta_{Fresnel} = 1 - \left(\frac{\left(1.59 - 1.5 \right)^2}{\left(1.59 + 1.5 \right)^2} \right) = 0.99915 \qquad \text{Equation 4.18}$$

If the fibre butted right against the emitter area then, assuming the L.E.D. source has a cosinusoidal power angular distribution, the angular coupling efficiency (η_{ang}) can be given by Equation 4.19 where θ_{fibre} is the fibre acceptance angle and m is source angular distribution.

$$\eta_{ang} = 1 - \left(\cos \theta_{fibre} \right)^{m+1} \qquad \text{Equation 4.19}$$

The acceptance angle is given by Equation 4.20 where N.A. is the numerical aperture of the fibre (0.5) and the source angular distribution is given by Equation 4.21 where θ_{FWHM} is the full width half maximum value (30º).

$$\theta_{fibre} = \sin^{-1}(NA) = 30 \qquad \textit{Equation 4.20}$$

$$m = \frac{\log(0.5)}{\log\left(\cos\left(\dfrac{\theta_{FWHM}}{2}\right)\right)} = 19.994 \qquad \textit{Equation 4.21}$$

Therefore the maximum theoretical total coupling efficiency is 0.0429 or 4% (Equation 4.22) or (-)13.675dB (loss in dB is given by Equation 4.23). It can be seen that the main coupling loss is in the geometrical mismatch between the active area of the L.E.D. and the fibre core diameter.

$$\eta_{ang} = 1 - (\cos 30)^{19.994+1} = 0.95119 \qquad \textit{Equation 4.22}$$

$$Loss(dB) = 10\log_{10}(\eta) \qquad \textit{Equation 4.23}$$

The theoretical value of 4% was compared with an experimental value by measuring the intensity of light coupled from an Agilent HLMP-CM11-Y2000 side emitting L.E.D. (@3V) into a glass and a polymer fibre (OMC-UK Ltd, Ø240µM core). Using a power meter (Lasercheck Handheld Power Meter, Coherent Inc.) the light intensity output of a polished and flattened L.E.D. (4.52mW @3V) and the output coupled to a polymer fibre was measured (at 532nm). Table 4.3 shows the average of three optical power measurements for each.

	Average optical power output (µW)
L.E.D.	4520.00
L.E.D coupled to a polymer fibre	4.97

Table 4.3 – Measured optical power output levels for an L.E.D., and an Agilent HLMP L.E.D. coupled to a polymer fibre with a 240µM diameter core.

Using an L.E.D. power output of 4.52mW the theoretical predications for fibre coupling give a fibre output (assuming fibre attenuation is equal to zero) of 0.193mW. The experimental values give 4.97µW (0.11% or -29.59dB). The reason behind this large difference is the offset of the fibre from the L.E.D. active area. This is related to the type of L.E.D. (side or surface emitting) that was used and coupling technique. An offset from the L.E.D. active area (normally the case due to high junction temperatures (>100°C) and manufacturing constraints) increases the geometrical and angular losses whilst the Fresnel losses remain constant. The three separate

experiments presented within the stage II section are also used to confirm whether 4.97µW at 532nm is sufficient power to detect concentrations of nitrite is seawater.

4.2.2.2 Absorption cell path length

The path length of the absorption cell is a variable that directly relates to the sensitivity and limit of detection of the L.O.C. device for specific chemical species. The maximum sensitivity of an spectrophotometric absorption cell can be calculated by differentiating the Beer-Lambert Bouger law equation and finding the point of inflection of the first derivative (i.e. when the second derivative is equal to zero) as per Equation 4.24 to Equation 4.27 (Naperian version).

$$I_{OUT} = I_{IN}e^{(-kdc)}$$

Equation 4.24

$$\frac{dI_{OUT}}{dc} = -kdI_{IN}e^{(-kdc)}$$

Equation 4.25

$$\frac{d\left(\frac{dI_{OUT}}{dc}\right)}{dl} = -kdcI_{IN}e^{(-\varepsilon dc)} + kI_{IN}e^{(-kdc)}$$

Equation 4.26

$$\frac{d\left(\frac{dI_{OUT}}{dc}\right)}{dl} = 0 \; \rightarrow \; k = k^2dc \rightarrow 1 = kdc$$

Equation 4.27

The point of inflection of the first derivative occurs when kdc is set to 1 [240]. Therefore the maximum sensitivity is dependent on the length of the absorption cell, the molar absorptivity of the solution and the concentration of the species being detected. For a given molar absorptivity and a known chemical concentration of interest it is possible to calculate the length of absorption cell that will provide the maximum sensitivity. As an example, Figure 4.16 shows a 5.8mm absorption cell will provide the maximum sensitivity peak for the detection of nitrite (*k*=2.303*ε where ε=1.5x10^6 M^{-1}m^{-1}) at 50µM.
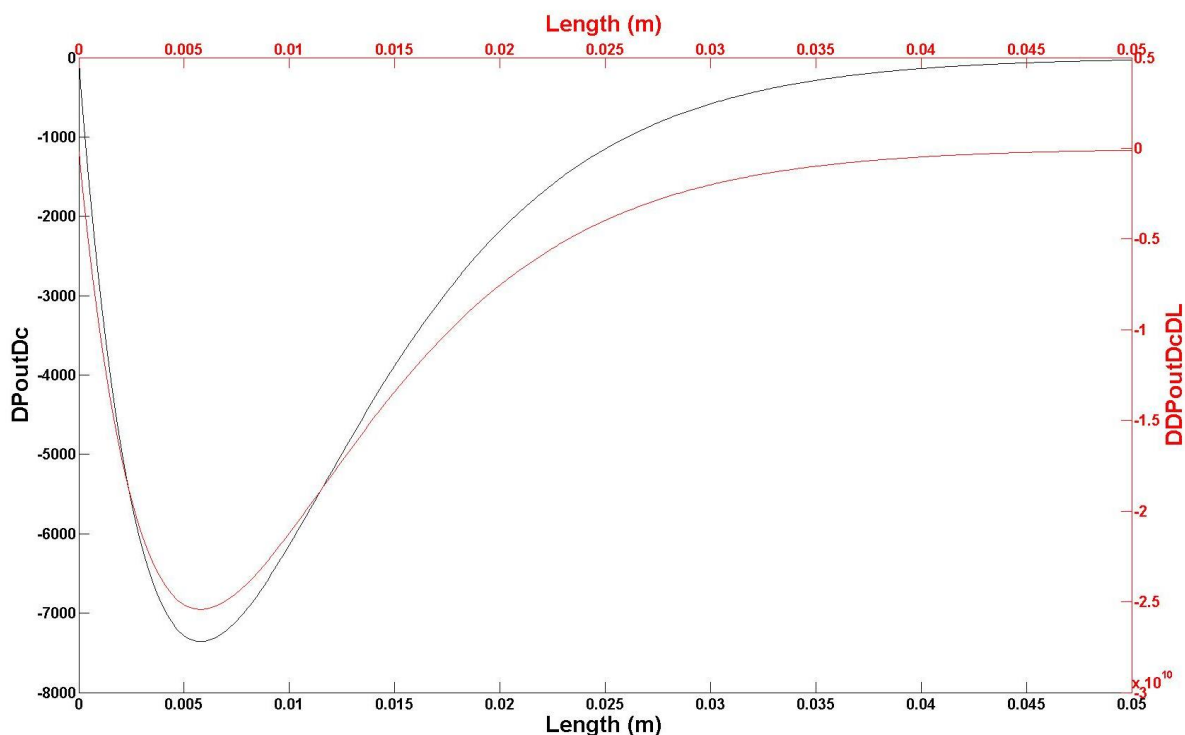
Figure 4.16 – Graph showing the first (black) and second (red) derivatives of the Beer-Lambert Bouger law for a 50μM concentration of nitrite. The maximum sensitivity occurs at the lowest point of the minima which correspond to a absorption cell length of 5.8mm.

As the average concentration found in the natural environment varies for each chemical species, and the concentration range of interest depends on the science being conducted it is not possible to have the maximum sensitivity at all times. Table 4.4 provides an example of the absorption coefficient of potential chemicals of interest and the respective optimal length of the absorption cell for maximum sensitivity.

Chemical	Absorption coefficient $(M^{-1}m^{-1})$	Concentration (μM)	Length for maximum sensitivity (m)
Nitrite	1500000	50	0.0058
	1500000	0.1	2.89
	1500000	0.001	28.95
Nitrate	2950000	0.1	0.34
Manganese	4400000	0.001	230
Phosphate	1100000	0.01	9.09
Silicate	2790000	0.001	358

Table 4.4 – Absorption path cell length required for maximum sensitivity at a typical natural environment concentration for a range of potential chemical species of interest.

The table indicates that the absorption cell for nitrite needs to be between 5mm and 30m long. For both stage II and III prototypes the fabrication techniques limited the cell length to 10 and 20mm respectively. As such the nitrite concentration at which maximum sensitivity occurs was 29 and 14.5μM respectively.

4.2.3   F-shaped micromixer

In Section 2.6.2 the split and recombine mixer was highlighted as the most suitable micromixer as it operates over a range of flow rates and is capable of mixing fluids over a short distance with minimal smearing. As such the 'on chip' mixing of the reagent and sample in the stage II prototype was performed using an F-shaped mixer design. The F shaped mixer shown in Figure 4.17b redirects the bottom half of the flow, on entrance to the first mixer element, and recombines it to the side of the remaining flow. The equal path length of each segment ensures no offset fluid flow (see Section 2.6.2). In the stage II prototype it is a three dimensional structure fabricated using two 150μm thin film layers which are then bonded together. Figure 4.17a illustrates the two dark field mask designs used in the creation of an F-shaped micromixer element. The stage II device uses four of these mixer elements to ensure mixing of the reagent and sample. The amount of mixing that took place over these 4 elements was measured (see Section 4.2.14) and fed into the Stage III prototype design.
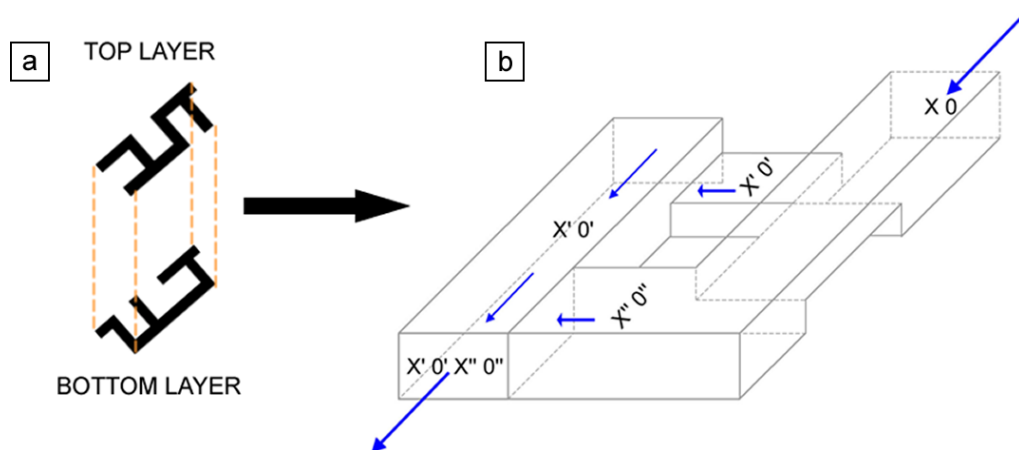
Figure 4.17a & b – a) Two layers of laminate are combined to create the mixer, b) Operational schematic of the F-shape mixer principle, with the arrows indicating the fluid direction and X and 0 indicating different flow streams.

4.2.4   Mask design

A dark field, low resolution mask (3386dpi) printed on acetate sheet (printed and supplied by JD Phototools) was used to mask the epoxy laminate material (negative resist) during exposure. The mask design (75 by 25mm) incorporated 500μm wide microfluidic channels (within the minimum

reliable feature size for dry film fabrication, Section 2.6.4.3) which are shown in black in Figure 4.18 and optical fibre grooves to enable the launching and collecting of light from the absorption cells.
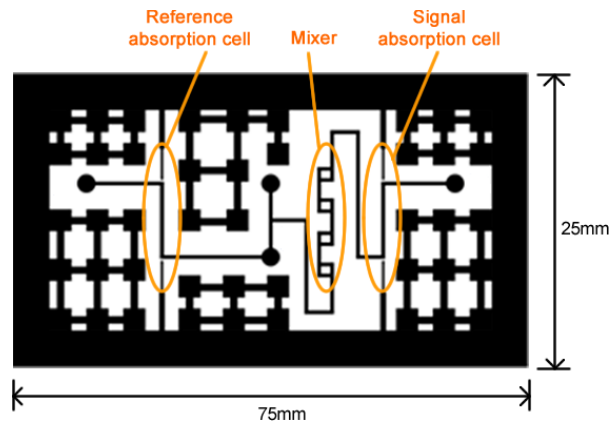
Figure 4.18- Diagram of the dark field mask measuring 75 by 25mm with the reference and signal absorption cells indicated.

The sample and reagent are mixed in four F-shaped mixer elements (as presented in Section 4.2.3) before entering the signal absorption cell (10 mm). Only the sample flows through the reference absorption cell and facilitates a differential absorption measurement. Further details on the optical absorption cell can be found in Section 4.2.7.2. To reduce dead fluid volume (and smearing effects, see Section 2.2.19) the diameter of the inlet and outlet holes and chamber should ideally match the channel width (500µm). However as it was necessary to align the lithography masks to the inlet and outlet holes by eye the mask was designed with a large inlet and outlet area 4mm in diameter.

The channel heights created by the thin film process needed to be sufficient to allow optical fibres (as reported in Section 4.2.7.2) to be inserted. A surface profiler (stylus profiler KLA-Tenor P.16+) was used to measure the thickness of cured (overnight in the oven at 190ºC to ensure complete bake) and uncured samples.

- Uncured single layer SY355 laminate measured at 49.94µm.
- Cured single layer SY355 laminate measured at 46.95µm.
- Two cured layers of SY355 laminate measured at 92.31µm.

There is a decrease in thickness of 3.05µm (6.1%) in the single layer laminate and 7.69µm (7.7%) in the double layer. The extra shrinkage (0.59µm) of two laminate layers could be accounted for in the laminating process (i.e. roller pressure) due to an extra 50µm height. Therefore L.O.C.

devices designed to accommodate fibres in this study were fabricated with a thickness of 300µm, 50µm greater than that of the fibre diameter (250µm).

4.2.5   L.O.C. device fabrication

The device was fabricated using an epoxy thin film photoresist (Elga Europe SY355) with a glass microscope slide (75 by 25 by 1-1.2mm) as a substrate. Microchannels (height of 300µM and a width of 500µM) were created by photopatterning layers (50µm each) of photosensitive dry film epoxy resist.

Prior to fabrication, the glass substrate was cleaned by ultra-sonicating in detergent solution (Cecon 90), followed by successive washes (1 minute) in Acetone, Methanol and Isopropanol, then dried using compressed N_2 gas. Dehydration of the glass was performed in an oven for 30min at 60°C. The epoxy thin film photoresist was laminated to the glass substrate, exposed and developed as per the process developed and described in Section 3.3.3. Two pieces of material were processed in a similar manner to form the bottom and top halves of the L.O.C. device. The two halves were aligned and heated from room temperature (22°C) to 200°C for 2.5 hours at a rate of 300°C per hour. The sample was then cooled to room temperature at a rate of 120°C per hour

The two methods available for creating inlet and outlet holes in the glass substrate were drilling or sandblasting. Drilling is a convenient, cheap and relatively quick (10min for 1.2mm thickness) method, but the hole size is limited to 400µm and above. Sandblasting (S.S. White Technologies Inc., Airbrasive Model K Series II) can be used to create smaller holes (minimum ≈180µm) but the damage to the glass caused by the sandblasting process and its inflexibility (hole has to be made prior to lamination and cleaning) mean it is not suitable. Adding additional steps (i.e. masking the glass with Ordyl BF400 laminate) adds process steps and time, therefore the holes were produced by drilling. The inlet and outlet holes (400µm) were drilled into the glass substrate after lamination and bonding. Silicon carbide tipped spear point drill bits (Ø400µm, Eternal Tools Ltd) revolving at low R.P.M. (<100) were used to drill holes in glass. Water was used to cool the drill bit during operation and prevent fractures in the glass due to localised heating.

4.2.6   Reagent and standard preparation

In Section 4.2.7.1 the stock (100% concentration) dye solution (coloured dye solution A) comprised of 12.5µl of red dye (Superfoods) and 20ml methanol (Sigma Aldrich, UK). The average absorption of a 200% concentration, measured over 520-540nm wavelength using a

commercial spectrophotometer, was 0.578776. To provide a range of concentrations the stock solution was diluted with methanol to achieve the desired concentration.

For the detection of nitrite, with either premixed solutions (see Section 4.2.9) or using on chip mixing (see Section 4.2.10), a series of samples were prepared from a standard seawater and 100µM nitrite solution (O.S.I.L. Uk Ltd) mixed with sodium citrate. The reagent for both (based on the variant Griess reaction, Section 2.4.1.1) was the same as that reported in Section 4.1.3 Premixed samples were prepared by mixing the sample and reagent on a vortex shaker for 30 seconds.

4.2.7   Experimental setup

The L.O.C. device, pictured in Figure 4.19a, has two inlets (A & B) and two outlets (C & D). These are indicated on the dark field mask design in Figure 4.19b. Fluid was gravity fed (using Parafilm covered 10ml plastic containers to minimize evaporation) into the fabricated device through 0.9m of tubing (0.508mm I.D., Tygon-R3603) and nanoport inlets (N-124S, Upchurch Scientific) (used to minimise dead volume). The outlets were connected to a waster container by 1m of Tygon tubing.
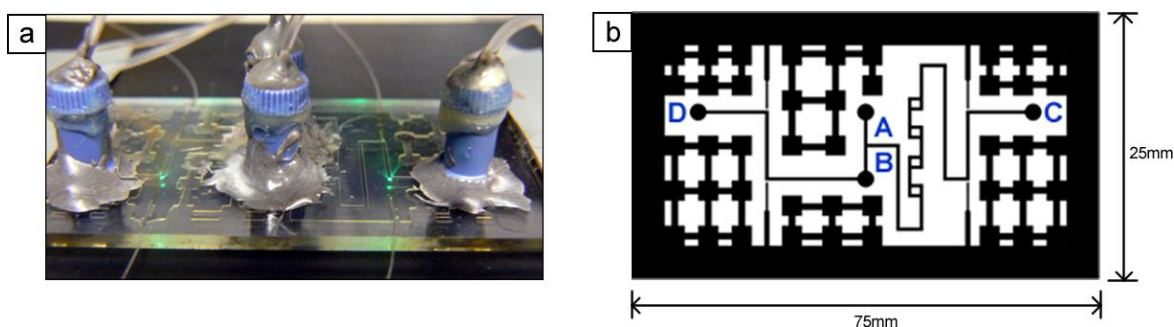
Figure 4.19a & b – a) Picture of microscale epoxy thin film device showing the four nanoport inlets, b) design used as the dark field mask in the exposure of the epoxy thin film with the inlets (A&B) and outlets (C&D) indicated.

4.2.7.1   Electronics

Electronics developed in another doctoral study [241] were utilised in conjunction with the stage II prototype to provide a voltage output directly proportional to absorbance. A square wave modulated constant current source was used to drive the L.E.D. light source. The light out of the detection path was coupled to a photodiode and the voltage signal demodulated by two lock-in amplifiers. The use of a lock-in amplifier (acts as a band pass filter [242,243]) helps to remove the effects of ambient light interference and to reduce D.C. and low frequency (flicker noise from

preamplifiers [**241**]) circuit noise. A log ratio amplifier was used as the output stage, this processes the reference and detection signals simultaneous giving an absorbance value directly. The reference signal compensates for the changes in the L.E.D. emission properties (e.g. temperature, pressure) as well as those within the fluid medium and stray light. The power required by the circuit is supplied from two 15V supplies (drawing 0.03 and 0.05 amps) with a total power consumption of 1.2W. This is with the L.E.D. being driven at 12mA pulse current with a duty cycle of 50% [**241**]. The theoretical noise limit from a P-Spice analysis of the circuit is 1.672×10^{-8} V per $\sqrt{Hz}$ at the bandwidth of 1kHz [**241**]. The performance parameters are summarised in Table 4.5.

Variable	Value
Voltage required	2 x 15V
Power consumption	1.2W
Size	150 x 120mm
L.E.D. driving current	12mA (Max)
L.E.D. driving voltage	3.0V
Frequency cut off	2.1Hz
Theoretical noise limit	1.672e-8 V/($\sqrt{Hz}$)

*Table 4.5 – Specification and performance of the electronics used in conjunction with the stage II prototype [**241**].*

Voltage outputs were recorded by either a digital multimeter (Agilent 34410A) to 5 decimal places or by a National Instruments Digital Acquisition Device (6036E) connected to a personal computer. In the latter, measurements were recorded over a 60 second period at a sampling rate of 1024Hz (greater than twice the 2.1Hz output of the electronics thereby satisfying the Nyquist condition and avoiding aliasing) and 16bit resolution (minimum sampling rate due to buffer characteristics of card). The signal was filtered using a software filter (presented in Appendix 8.5.2.1) to remove any components above 5Hz and improve the signal to noise ratio. An average voltage over 60 seconds (61440 samples & 1024Hz) of the filtered signal was used to obtain each result.

4.2.7.2   Optical detection

Optical absorption measurements were performed using pigtailed optical fibres (multimode step index polymer fibre, OMC UK Ltd). These multimode non jacketed polymer fibres (P.M.M.A. core, η=1.59, Fluorinated polymer cladding, η=1.51) have a low propagation loss in the 542nm wavelength region (0.18db/m) and a minimum bend radius of 17mm. The large acceptance angle (60° at 650nm, numerical aperture of 0.5) allows a high coupling efficiency. They are inserted between the two glass substrates through spaces etched in the laminate and butted against the

channel wall. They launch and collect the light from a 10mm long dog legged microfluidic channel. Figure 4.20a illustrates the optical setup and the positioning of the optical fibres. Index matching U.V. curable glue (Norland Optical Adhesive NOA61) was used to minimise the mismatch in refractive indices (to reduce light refracted, or reflected) between the fibre (η=1.49) and the epoxy laminate (η=1.5). The glue was pipetted into the insertion groove, along with the fibre, and cured for 30 seconds in a Mega Electronics AY315 U.V. light box.
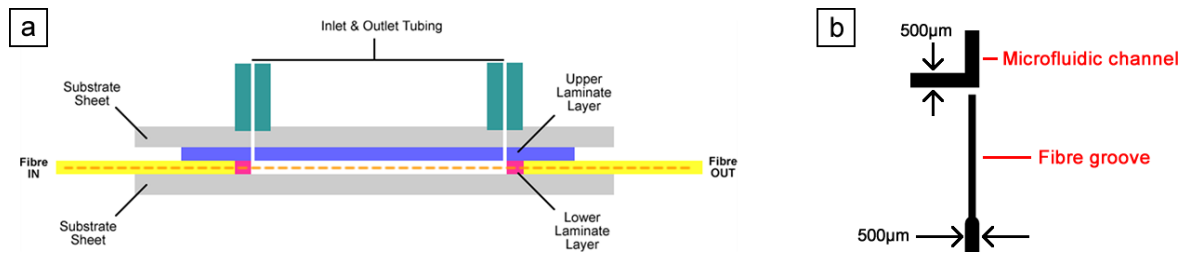
Figure 4.20a & b – a) Cross sectional diagram of device construction illustrating the optical setup and the positioning of the optical fibre, b) dark field mask design of fibre insert showing the tapered fibre groove.

To prevent lateral instability of the multimode step index polymer fibre (Ø250μm), whilst maintaining ease of assembly, the insertion groove is tapered over a short section (see Figure 4.20b). The decrease in width provides a method of aligning the fibre to the absorption cell. The minimal thickness of cladding (5μm) on the core of the polymer fibre (240μm) allows a greater coupling efficiency between the fibre and light source (as per Section 4.2.1) than would be possible with a glass fibre of a similar external diameter and numerical aperture (15μm cladding, BFH48-200, Thorlabs).

An Agilent (HLMP-CM11-Y2000) side emitting L.E.D. integrated into a S.M.A. connector was used as the light source (spectral half width of 32nm). The light was split using a SMA terminated 50-50 glass fibre splitter (Custom part, OMC-UK Ltd, 150mm tails) and two 240μm core polymer fibres used to guide the light to the detection paths (each 1cm in length). Figure 4.21a, b and c show the coupling of the light into the absorption cell. Similar fibres were used to couple the light out to two photodiodes (Taos TSLG257) mounted and aligned in a S.M.A. receptacle.
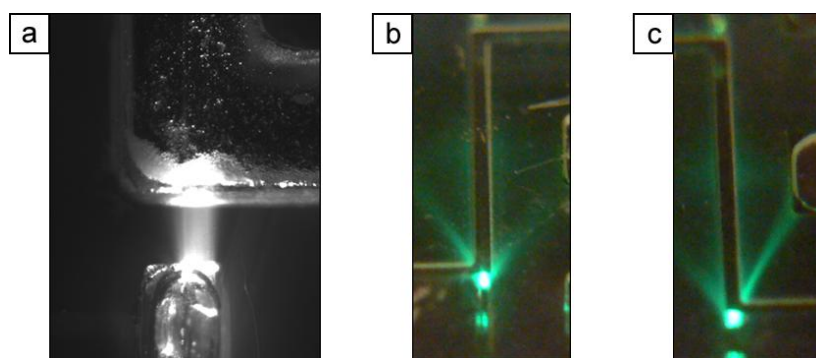
Figure 4.21a, b & c – a) OMC-UK Ltd optical fibres coupled into device, b) launching of light from the Agilent L.E.D. into reference and c) detection channel absorption cells.

4.2.8   Detection of dye and methanol

A series of coloured dye concentrations (prepared from the stock solution A in Section 4.2.6) between 0 and 100% were fed into inlet A at 7.75μl/sec and methanol in inlet B at 2.00μl/sec (see mask design in Figure 4.19b for inlet and outlet layout). The absorption signal over 60 seconds was recorded using a D.A.Q. device (N.I. 6036E) and a Matlab$^{©}$ script (Appendix 8.5.2.2). The absorption of the mixed fluids, measured across the 10mm optical cell, is shown in Figure 4.22.
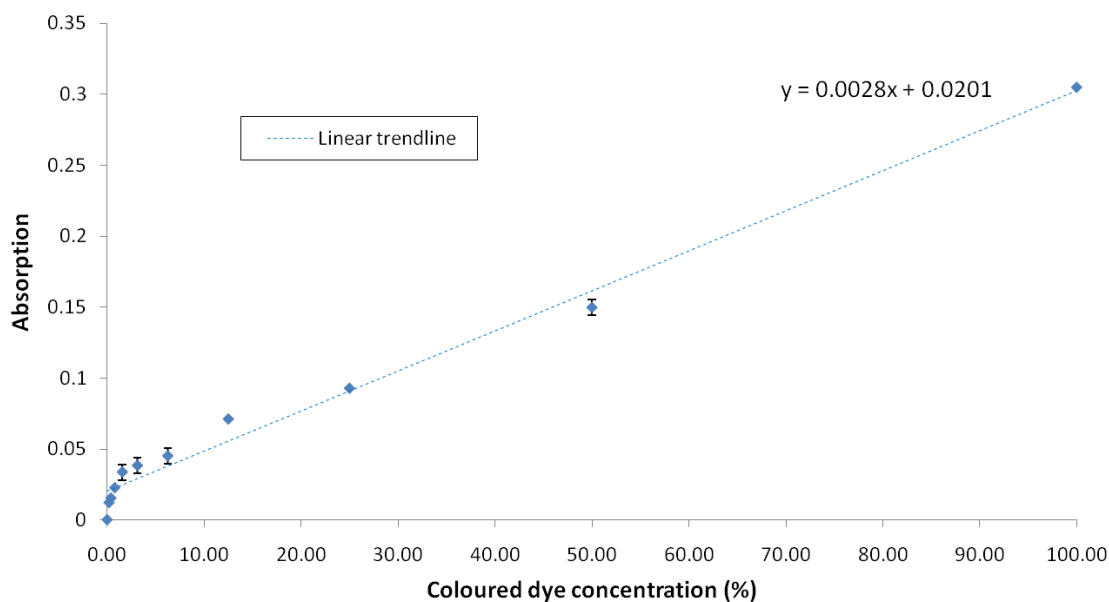
Figure 4.22 – Graph of the absorption (measured across a 10mm L.O.C. absorption cell) of an on device mixed solution of coloured dye and methanol. Results for a range of coloured dye samples (between 0 and 100% of the dye stock solution) fed into the L.O.C. device are plotted where the dashed blue line is a linear trend line and the error bars give the positive and negative standard deviation (resolution) of each measurement point.

The experiment showed an increase in absorption with an increase in dye concentration. A linear trend is seen until the 1.5625% concentration, below which the positive gradient of the slope increases. The deviation of the data from the linear trend line at low concentrations can be attributed to inaccurate dilutions. Minimal deviation from the linear trend line at high concentrations is seen. The average standard deviation (resolution) for the entire run was 0.001517A. Using the equation for the limit of detection presented in Section 2.2.12, and with k=3, the L.O.D. was 0.45% (or 0.0214A).

The absorption of a 38.72µM nitrite sample combined with reagent over the same cell path length (10mm) is 0.578776. Using this it is possible to calculate the equivalent minimum concentration of nitrite that the device would be able to detect (i.e. L.O.D.). This is achieved using Equation 4.28 below where A_n is the absorption of the nitrite sample of concentration C_n, and A_d is the dye L.O.D. and the equivalent nitrite concentration is E_d. As such, the equivalent L.O.D. (given by Equation 4.29) for nitrite would be 1.432µM.

$$\frac{C_n}{(A_n/A_d)} = E_d \qquad \qquad \textit{Equation 4.28}$$

$$\frac{38.72}{(0.578776/0.0214)} = 1.432\mu M \qquad \qquad \textit{Equation 4.29}$$

4.2.9   Detection of premixed nitrite samples

A series of premixed nitrite samples (see Section 4.2.6 for details on sample and reagent preparation) between 0 and 50µM were fed into inlet A (indicated in Figure 4.19b) at 10µl/min. Inlet B and outlet D where blocked off. These premixed nitrite samples were created by combining a known concentration of nitrite in a seawater solution with the reagent (see Section 4.2.6). For each measurement voltages were recorded at 0.5Hz over 20 seconds, after 5 minutes of stable flow, using a digital multimeter (Agilent 34410A). The voltage was zeroed after 12 minutes of flow with a blank (0µM concentration) for each run. A higher magnification on the electronics (x5 amplification) was used and has been accounted for in the absorption measurements shown in Figure 4.23. The absorption of each premixed sample was also measured in a commercial spectrophotometer (Cary 1 Bio) and is plotted on the graph to provide corroboration of sample dilution and accuracy.
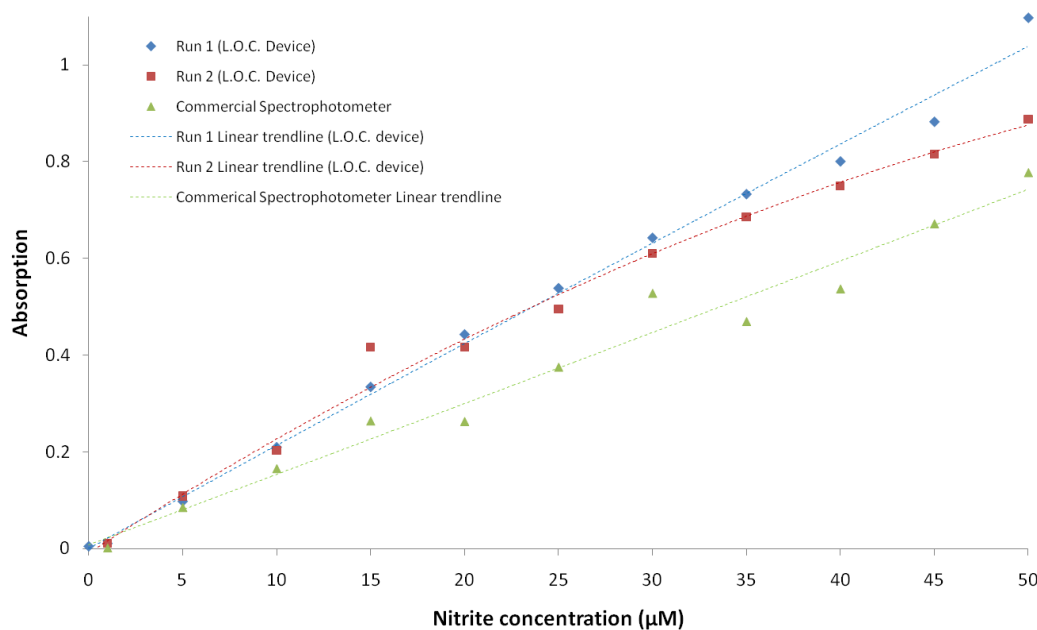
Figure 4.23 – Graph showing absorption, over a 10mm path length, against the concentration of nitrite in seawater for the two runs using a premixed and reagent sample. The absorption of the premixed samples, measured in a commercial spectrophotometer, are also shown in green.

The average standard deviation (resolution) for run one and two was 0.00096 and 0.00069A respectively. Using the equation for the limit of detection presented in Section 2.2.12, and with k=3, the L.O.D. for run one was 0.083μM and 0.102μM for run two. The precision, given by the standard deviation of absorption values measured at 10μM across the two runs (as per Section 2.2.11), was 0.00397A (0.192μM).

Both the first and second runs conducted using the L.OC. device in Figure 4.23 have a different trend line gradients although if the 50μM data point in run one and the 15μM data point in run two outliers are removed the trends would match more closely (i.e. the sensor would have a greater precision). The trend lines agree at low concentrations, but diverge non linearly at high concentrations. It is hypothesised that the difference was due to the experiment starting with an inaccurate initial concentration, which is then diluted. The inaccuracy of the initial sample can be attributed to contamination or error during sample. Alternatively stray light introduced by background illumination (i.e. natural light) could have been the cause, as described in Section 2.4.1.1.

4.2.10 On-chip-mixing and detection of Nitrite

In this section seawater samples containing nitrite concentrations (0 to 12.5μM) and the reagent were mixed using the micromixer on board the L.O.C. device. The absorption signal over 60

seconds was recorded using a D.A.Q. device (N.I. 6036E) and a Matlab© script (Appendix 8.5.2.2). Three runs were conducted over three days and the results are shown in Figure 4.24 below.
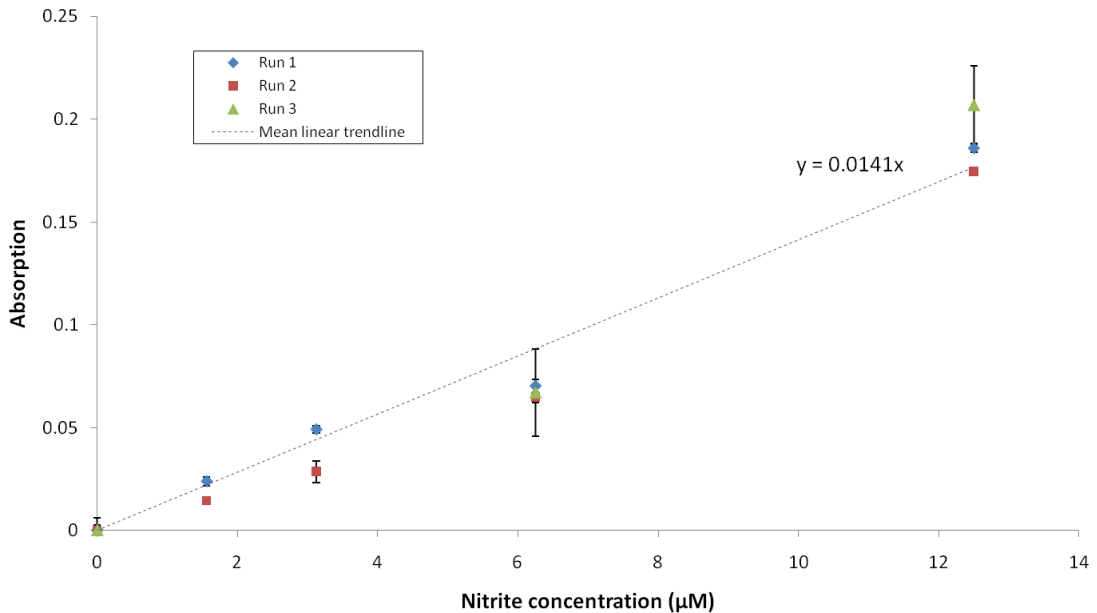
Figure 4.24 – Graph showing absorption against nitrite concentration for three consecutive runs (over three days) using gravity fed 'on device' mixed reagent and samples. The positive and negative standard deviation (resolution) for each data point is plotted along with the mean trend line of the three runs.

The average standard deviation (resolution) for run one, two and three was 0.00224, 0.00262 and 0.01553A respectively. Using the equation for the limit of detection presented in Section 2.2.12, and with k=3, the L.O.D. for run one was 0.399µM, run two 0.730µM, and run three 1.386µM. The precision, given by the standard deviation of absorption values measured at 12.5µM across the three runs (as per Section 2.2.11), was 0.110A (7.801µM).

An alternative reagent delivery system was also tested using the on device mixing of nitrite concentrations in seawater and reagent (Appendix 8.2.2.8). Instead of using a gravity feed system fluids were pumped through into the microfluidic device using a Lee solenoid pump. This increased the limit of detection to 2µM.

4.2.11   Noise

The noise level within the system (along with sensitivity, see Equation 2.3) determines the limit of detection for absorption measurements. It can arise from interference (radio frequency, mains), circuitry noise (Johnson, amplifier and flicker) or chemical noise. A frequency spectrum of the

signal sampled at 1kHz (without the 5Hz software filter) during the on chip mixing and detection of nitrite experiment (see Section 4.2.10) provided a power spectral density profile, allowing analysis of the electronic noise.

As the output of the electronic circuitry (described in Section 4.2.7.1) has a frequency cut off above 2.1Hz then no obvious peaks should be seen above this value in the power spectral density profile. However Figure 4.25a, a Fast Fourier Transform (F.F.T.) of the signal, shows that a peak is observed between 49.94 and 50.03Hz when using mains driven electronics. Noise around the 50Hz region (or multiple of) can be attributed to mains noise. This assumption is verified by switching between mains driven (Figure 4.25a) and battery driven (Figure 4.25b) electronics. Although there is still a peak present its amplitude is 3 orders of magnitude less (1.8e-2 compared with 1.02).
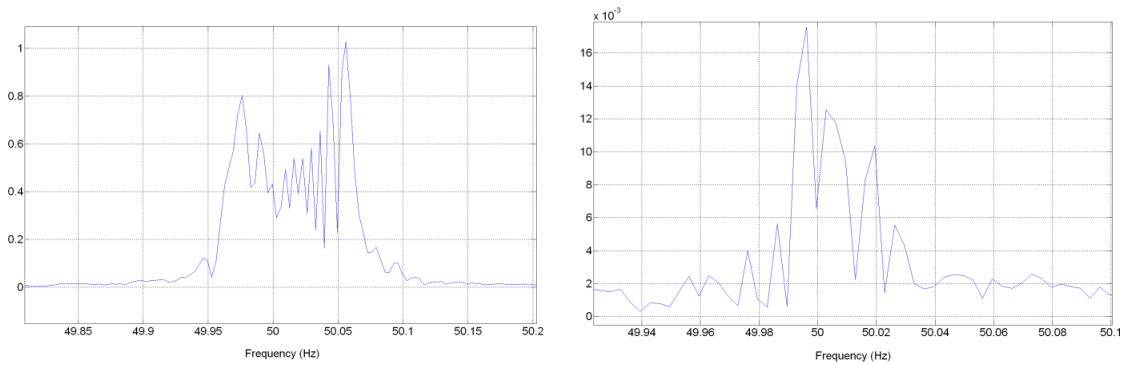
Figure 4.25a & b – Graph of the 50Hz noise signal at the output of the electronics around when the computer and electronics a) are connected to 240v mains and b) connected to a battery.

To isolate sources of noise in the electronics signals were analysed with different components either on or off. Table 4.6 lists the standard deviation of a steady state signal for the different combinations. The largest source of interference is from the laptop (used to store the data) power supply. The electronic noise with both the computer and electronics running from battery is ±0.0034V (±1σ). This compares with the NI-DAQ e-series 6036E D.A.C. that has a 1.5mV noise level with a 0.0549% measurement inaccuracy.

Computer (mains or battery)	Electronics (mains, battery or OFF)	Average Voltage (V)	Standard deviation
Mains	OFF	-0.0015	5.0928×10^{-4}
Battery	Mains	-0.091	3.6×10^{-3}
Mains	Battery	-0.2455	6×10^{-2}
Battery	Battery	-0.1097	3.4×10^{-3}

Table 4.6 – List of standard deviation and average voltage of the constant signal in a variety of different experiment setups.

Spikes in filtered data were also noticed during electrical switching (e.g. fluorescent tubes, power supplies). These large amplitude (>1V) low frequency spikes (<1Hz) are not removed by filtering as they occur at a frequency below that filtered.

An *in situ* sensor will be isolated form most R.F. interference and mains noise during deployment so the important noise floor is that produced by the electronics themselves (e.g. amplifier noise) and this is minimal. The noise level in an *in situ* scenario (i.e. computer and electronics running on battery) will affect the theoretical minimum sensitivity.

4.2.12 Dripping outlet

Both stage I and II sensors were sensitive to flow rate changes and pressure drops. This can be seen in Figure 4.26a when fluid from a L.O.C. device (presented in Section 4.2.5) outlet is allowed to drip into the waste container rather than the tubing being submersed (as per Figure 4.26b). The signal from the mixing of nitrite sample and reagent increases by 0.0026V (ΔV) as the droplet starts to form, then decreases on droplet release. The total time for drop formation and release was 50.78 (ΔS) seconds and is related to the flow rate.
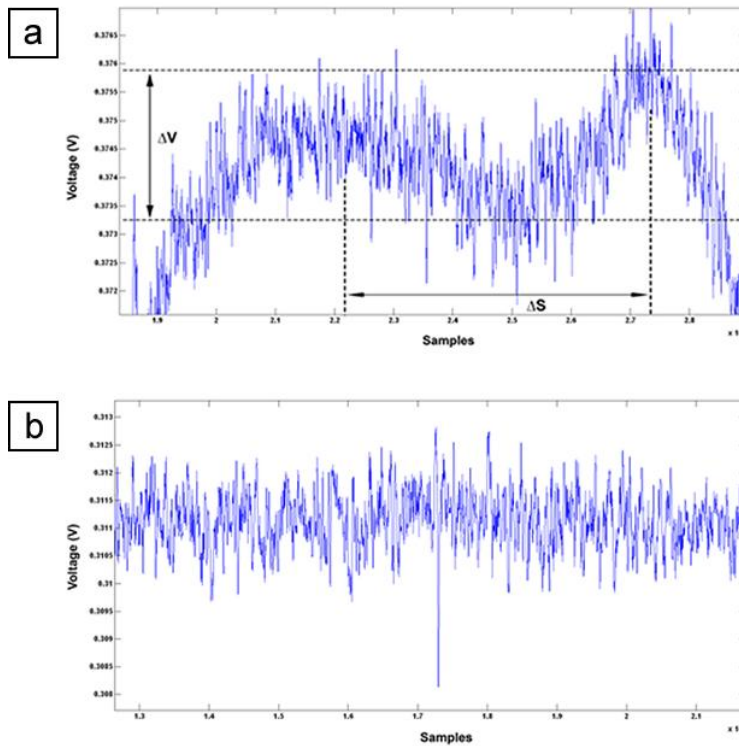
Figure 4.26a & b – a) Graph showing the oscillation and b) no oscillation in absorption signal due to droplet formation and detachment from the waste output. The change in voltage is given by ΔV.

The energy required to overcome the surface tension of the droplet causes an increase in the back pressure in the tube. The pressure difference between the fluid and atmosphere is given by the Laplace-Young equation (Equation 4.30) where R_x and R_y are the radius of curvature, λ is the surface tension of the fluid, and ΔP is the pressure difference between the air and the fluid [31,244]. Assuming a spherical droplet this can be simplified to Equation 4.31 where R is the radius of curvature of the droplet and P_{atm} is atmospheric pressure and P_{fluid} is the pressure in the fluid [244].

$$\Delta P = \gamma \left(\frac{1}{R_x} + \frac{1}{R_y} \right) \qquad \text{\textit{Equation 4.30}}$$

$$P_{fluid} - P_{atm} = \frac{2\gamma}{R} \qquad \text{\textit{Equation 4.31}}$$

The subsequent decrease the flow rate increases the time that the azo dye has to develop (measured as an increase in absorption). Following the detachment of the droplet the back pressure decreases as the radius of curvature at the water, air surface layer of the droplet is smaller. This causes an increase in flow rate and hence a signal change (voltage drop). Therefore whilst in a laboratory setting the outlet of the prototypes were submersed in partial filled waste

container to prevent this signal variation and an increase in resolution and L.O.D. In an *in situ* environment the waste outlet would be similarly designed or vent directly into the ocean.

4.2.13 Response times

A key performance characteristic of a sensor is the response time (as reported in Section 2.2). It is the time delay (ΔS) between the concentration changing and the voltage output responding (i.e. how quickly measurements will change to reflect current concentrations). A shorter time means a smaller fluidic volume before the detection chamber and that less smearing or dispersion (see Section 2.2.19) between fluid samples has occurred.

Two different fluidic setups were used to investigate smearing within the stage II sensor and are presented in this section. Both used 0 and 50μM nitrite concentration in seawater samples, and reagent to detect the nitrite concentration (see Section 4.2.6 for details on standards and reagent preparation). These were mixed on chip and the absorption measured at a total outlet flow rate of 8.3μl/sec. The first had a 30cm (150.8μl) sample inlet path length (as per Figure 4.27a) after the sample switch (Omnifit 1126 5 way valve) but before the L.O.C. device and the second a 1cm (5μl) sample inlet path length (as per Figure 4.27b).
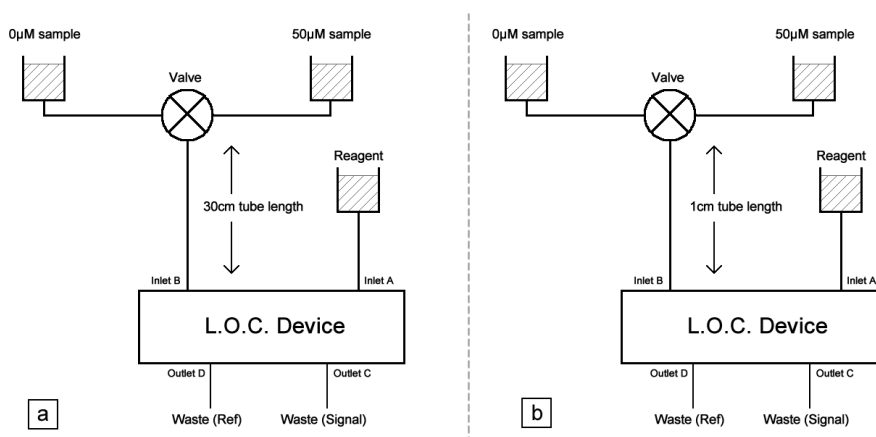
Figure 4.27a & b - Diagrams illustrating a high level schematic of the fluidic setup for a) the 30cm and b) 1cm inlet path length after the sample switch.

Figure 4.28a and Figure 4.28b show the voltage output against time following a switch between 0 and 50μM samples in the two setups. Upon sample change the absorption has two peaks, a maxima and minima, in both setups. They indicate the change in absorption caused by an interruption in the sample fluid flow. The minima is caused when fluid is temporarily stopped during sample switching. The maxima is caused when the fluid stream is started again. While the

time period for these peaks is similar (1×10^4 samples) for the two setups the settling time is greater for the first fluidic setup.
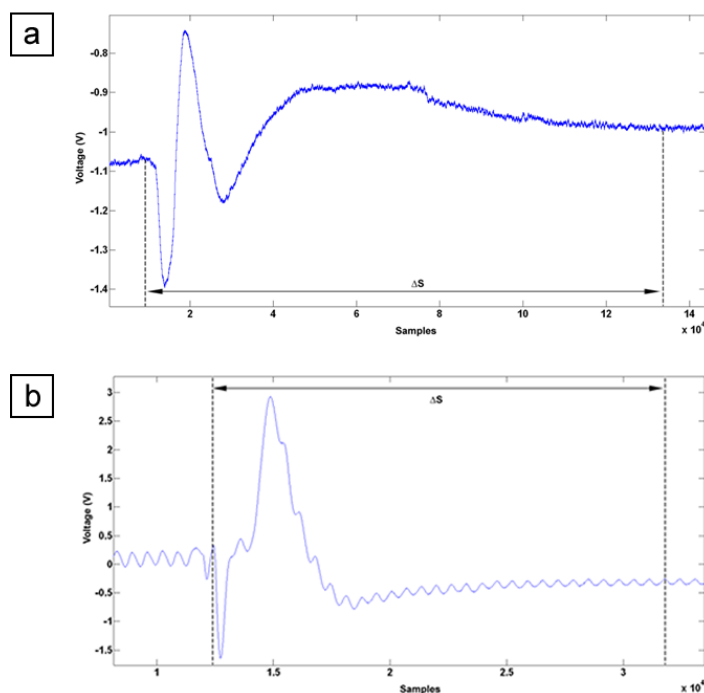
Figure 4.28a & b – a) The non filtered signal response after a change in concentration for the 30cm inlet path length and b) the non filtered signal response after a change in concentration for a 1cm inlet path length.

The response time was calculated as the time required from the change in concentration of nitrite till the output voltage had reached a final steady state value. The results are presented in Table 4.7 below.

Measurement	Setup 1 (30cm)		Setup 2 (1cm)	
	Response time (seconds)	Total volume (µl)	Response time (seconds)	Total volume (µl)
10% of final value	27.46	227.92	11.85	98.36
1% of final value	57.27	475.34	15.64	129.81
1 S.D.	71.63	596.68	14.41	119.60

Table 4.7 – Response times for a sample change in the two fluid setups with an L.O.C. device inlet path length of 30cm and 1cm. The volume of fluid that each of the response times represents is also reported.

The flow rates and time over which the sample and reagent are mixed are similar in both setups so any difference in kinetic effects (i.e. azo dye production) are minimal. Therefore the time delay can be attributed to the time taken to fill the valve (26µl), inlet path length (150.8 or 5µl), on chip microfluidic channels (13.1µl), the detection chamber (1.5µl), flush away any residue on channels surfaces and in dead volumes, and dispersion. The total volume of the fluidic path from sample

valve to detection chamber is 191.3µl and 45.6µl for setup one and two respectively. The remainder of the total volume of fluid needed, following sample switch, before the output voltage reaches 99% of its final value, is that required to flush away residue from surfaces and dead volumes, and smearing caused by dispersion. This is 284.04µl for setup one and 84.21µl for setup two. Interpolating these results for an inlet path length of zero gives the L.O.C. device a minimum resolvable volume of 77.3µl.

As the dead volume is the same in both setups it is evident that more smearing from residue on channel surfaces and dispersion has occurred in the longer path length inlet. The amount caused by the individual components of the L.O.C. device is uncertain but to reduce response times the fluidic volume between the sample inlet and absorption cell should continue to be minimised (i.e. ensure a short path length).

4.2.14 Mixer characterisation

To confirm the operational effectiveness of the mixer, investigate flow effects and determine the percentage mixing per element the visualisation of the mixing between a fluorescein solution (pH 9, Acros Organics Fluoroscein $C_{20}H_{12}O_5$) and buffer was used. The analyses of the results were used to identify improvements and guide the design of the stage III prototype to ensure complete mixing, lower the L.O.D. and increase precision.

The L.O.C. device was illuminated with a blue light source ($\lambda \approx 465$-495nm) and viewed under a microscope with a F.I.T.C. (fluorescein isothiocyanate) filter (bandpass $\lambda \approx 515$-555nm). Images were captured using a high resolution, high frame rate camera (Hamamatsu Ocra ER C4742-95) mounted on a Carl Ziess Axiovert 200 inverted microscope using a Zeiss Fluar X20 0.75NA lens in an epi-illumination setup. The device was gravity (0.6m head) fed through 0.508mm I.D. Tygon tubing at a combined flow rate of 11.15µl/sec. Pictures taken during fluid flow (greyscale 672 x 512 pixels) were analysed using a Matlab© G.U.I program (see Appendix 8.5.2.3 for code). A 20 pixel wide cross section in either the horizontal or vertical direction was taken and the intensity averaged over these 20 pixels. The whole cross section intensity values where then corrected and normalised to a scale between 1 and 0 to provide intensity cross section profiles. The intensity profile provides a clear indication as to the state of mixing as the intensity of each pixel is linearly proportional to the concentration of fluorescein within imaged by each pixel [245]. If the normalised intensity over the width of the channel is constant then it can be assumed that there is complete mixing in the x (width of the channel) & y (parallel to the channel) planes. Although not necessarily in the z direction due to the top layer of fluid being the only one visible.

Figure 4.29a shows the two fluids combining at the T junction (black indicates buffer and grey/white is the fluorescein). The buffer has a normalised intensity below 0.1 and the fluorescein a normalised intensity above 0.5. There is no or very limited mixing at the interface and no cross contamination of the different fluid streams. By the first mixer element finger (Figure 4.29b) the sharp drop in intensity between fluid streams has disappeared. The laminating of the flow can be seen in Figure 4.29c & d.
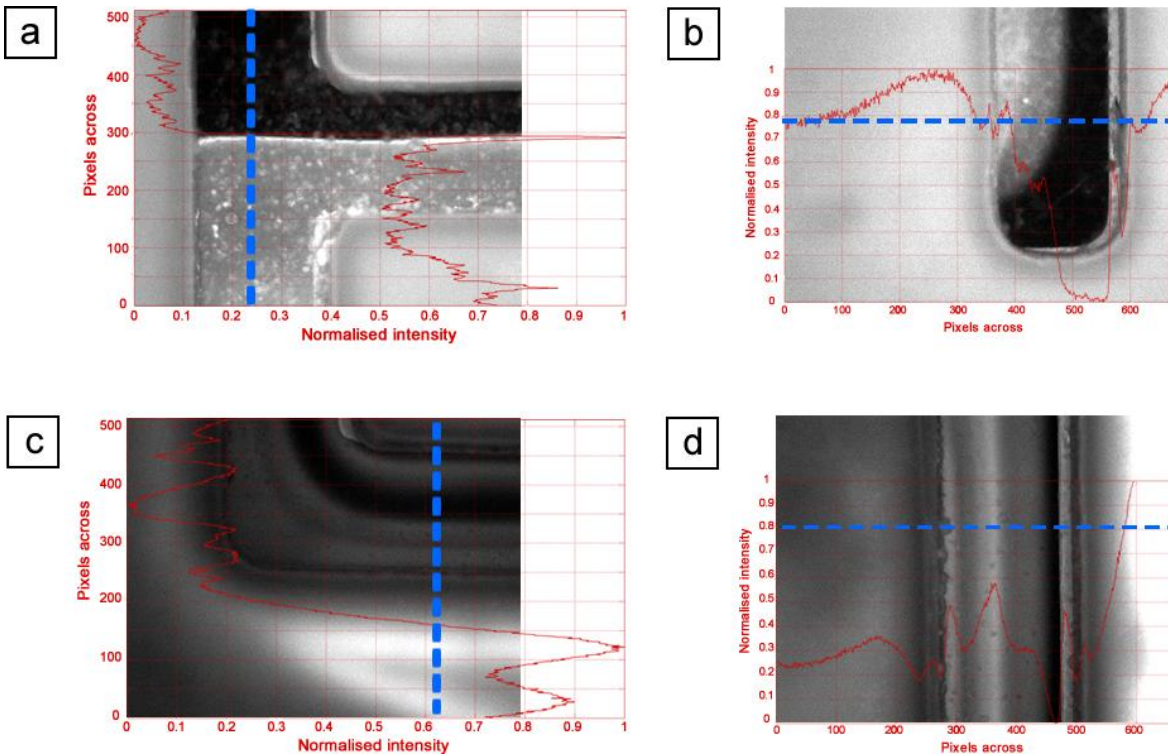
Figure 4.29a, b,c & d – Normalised intensity profiles the 500μm microfluidic channel for a) fluid T junction inlet, b) change in z direction at 2nd finger, c) after 2nd mixer element and d) the detection chamber.

The mixing levels are quantified by calculating the standard deviation of the corrected intensity across the channel width. This accounts for the variation in mixing level across the channel width (i.e. when the standard deviation approaches zero it can be assumed the fluid is fully mixed). The corrected intensity is calculated using Equation 4.32 and uses the dark field (minimum background intensity) and light field images (maximum intensity of fluorescein) to normalise the intensity between zero and one.

$$CI = \frac{(OI-DF)}{(FF-DF)}$$ *Equation 4.32*

Where *CI* is the corrected image, *OI* is the original image, *DF* is the dark field image and FF is the flat-field image. Equation 4.33 allows the mixing level can be expressed as a percentage.

$$ML=(1-2\sigma)\times100 \qquad\qquad \textit{Equation 4.33}$$

Where *ML* is mixing level (%) and σ is the standard deviation. The mixing level (Table 4.8) for the channel at the T junction inlet should be equal to zero but due to inaccuracies in obtaining the dark field and flat fields (due to the changing illumination) it is 27%. Taking this as the base level (i.e. subtracting it from the measured mixing levels) provides a corrected mixing level. The uncorrected and corrected mixing level at each stage is presented in Table 4.8.

Position	Standard deviation	Mixing level (%)	Corrected mixing level (%)
T junction inlet	0.3652	27	0
After 2nd finger	0.2660	47	20
Detection chamber	0.1302	73	46

Table 4.8 – Standard deviation and mixing levels for the T-junction inlet, 2nd finger and detection chamber.

The corrected mixing level after four F shaped elements the fluid is 46% mixed and corresponds to 11.5% mixing per element. To achieve >90% mixing in future designs it will be necessary to increase the number of mixing elements to above eight (assuming linear relationship). However as the amount mixed by each element decreases with an increased mixed percentage (inverse exponential decay [153]) as fluid approaches a fully mixed state more elements may be required.

It should be noted that this measurement of mixing efficiency assumes minimal variation of the mixing with channel depth (i.e. the pixel intensity at each point across the channel width only reflects the environment nearest the microscope lens). Qualitative calculations included in Section 4.3.2 expand the measurement of mixing efficiency to include variations of mixing with channel depth.

4.2.15 Discussion

The principle of being able to measure the absorption of a fluid on the L.O.C. device was confirmed by the use of coloured food dye (Section 4.2.8). It showed an increase in absorption with dye concentration. The use of coloured food dye also allowed rapid confirmation that low cost L.E.D's could be coupled to optical fibres and launch sufficient light into an L.O.C. device to allow a fibre coupled photodiode to measure changes in absorption over a 10mm absorption cell. The optical power launched into the L.O.C. device was measured experimentally (Section 4.2.2.1) and acts as a minimum optical power requirement for the stage III prototype and future sensor development. The difference between the experimental (0.11%) and theoretical (4%) value

for coupling losses from launching light from an L.E.D. into a 250μm polymer fibre was associated with the offset from the L.E.D.'s active area. To maximise the measurement range and enable a longer absorption cell (lower L.O.D.) in the stage III device the optical fibre needs to be coupled as close as possible to the active area. As such an alternative (surface emitting) L.E.D. was adopted in stage III.

Premixed nitrite (in seawater) and reagent samples were used to confirm the chemistry on the microscale and to gain information on the sensitivity and L.O.D. of the device whilst isolated from mixer performance. Using premixed samples the sensor was also shown to have a higher sensitivity than the commercial spectrophotometer (i.e. higher absorption for the same concentration). This can only occur if the effective absorption path length is greater than the 10mm length of the cell and would occur through refraction or reflection (as described in Section 2.2.23). The ability of compact L.O.C. device that could integrate both optical and mixing onto a single platform was also proven. The measurement of nitrite concentrations between 0 and 15μM over three days showed an average L.O.D. (0.838μM) which is within the key performance parameter stated earlier in this study. However the precision (7.801μM) over multiple runs is above that required and was attributed to the variable and incomplete mixing of the reagent and sample. The response times for the on board mixing of nitrite and reagent was 15.64 seconds (1% of the final value).

Visualisation of the on device mixing (Section 4.2.14) showed that fluid in the detection chamber was 46% mixed. A mixing level of 46% over 15mm (3% per mm) is greater than that of the chicane mixer proposed by Gotze et al [160] (1.2% per mm) at similar flow rates. The incomplete mixing was also highlighted by a comparison between the absorption of the premixed nitrite and reagent sample (presented in Section 4.2.9) and the absorption of nitrite concentrations mixed with the reagent on chip (presented in Section 4.2.10) is shown in Figure 4.30. The difference between the mean trend lines (the on device mixed absorption is approximately 40% less) indicates that the mixing can be improved. As such the need to incorporate more than 8 mixing elements into the stage III sensor to ensure >90% mixing was noted.
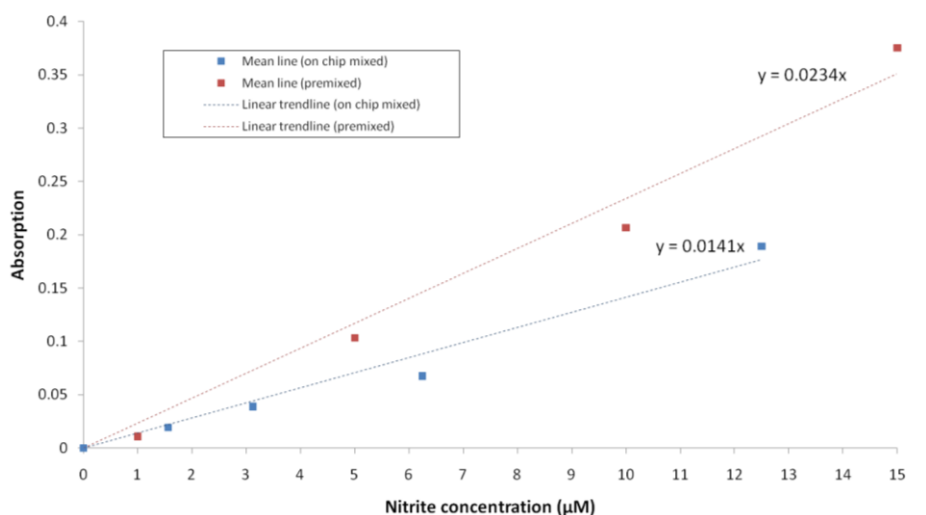
Figure 4.30 – Graph plotting the absorption measurements against nitrite concentration from the premixed and on chip measured experiments where the dashed lines show the linear trend line. The equations of the line are also provided.

Detecting a partially mixed combination of reagent and fluid causes fluctuation in the absorption (fluid streams changing position in the channel) and an increased L.O.D. The accumulation of bubbles within the mixer also alters the flow characteristics. They restrict the flow causing a higher pressure in that section of the channel causing flow to be diverted through the other channels leading to decreased mixing efficiency.

A summary of the limits of detection and precision for systems presented in this section are shown in Table 4.9. Based on the assumption that the sensor will be deployed *in situ* the electronics were not a limiting factor in the measurements as the electronics noise (± 0.0034V or 1.075×10^{-4} Volts per root hertz) is smaller than the standard deviation of the measurements (electronic and chemical noise, 0.0029V or 1.284×10^{-3} Volts per root hertz).

Description	L.O.D. (µM)	Precision (µM)
Onboard mixing of dye and methanol	1.432	n/a
Premixed nitrite & reagent – 1st run	0.083	0.192 (at 10µM)
Premixed nitrite & reagent – 2nd run	0.102	
Onboard mixing of nitrite and reagent – gravity fed – 1st run	0.399	
Onboard mixing of nitrite and reagent – gravity fed – 2nd run	0.730	7.801 (at 12.5µM)
Onboard mixing of nitrite and reagent – gravity fed – 3rd run	1.386	
Onboard mixing of nitrite and reagent - pumped	2	n/a

Table 4.9 – Overview of the limit of detection and precision of the experiments performed in the stage II microscale sensor section.

4.3   Stage III – Bench top prototype sensor

This section details the setup of and results from a custom designed third party manufactured (Epigem Ltd) SU8 and P.M.M.A. L.O.C. device (shown in Figure 4.31a). It was designed as part of the final part, or third step, of the iterative development process. It provided a single platform for fluid handling, mixing of reagents and absorption measurements and a precursor to a fully deployable *in situ* sensor. The performance of this improved L.O.C. device for the detection of nitrite concentrations in seawater is presented in this section.

Following on from stage II the next step in the three stage iterative process was an increase in the number of mixing elements to increase the extent and stability of mixing (decreasing L.O.D. and precision). An increased L.E.D. to fibre coupling efficiency was also used to extend the possible length of the absorption cell to 20mm. The fluid delivery system was re-examined to improve flow rate stability (precision) and provide a pumping system suitable for *in situ* deployment. The effects of the flow rate changes on absorption measurements are also detailed.

Absorption cell design is detailed, along with comparative coupling efficiency results for different optical setups. A qualitative performance review of the on board microfluidic mixer (Figure 4.31b) is carried out using a laser scanning confocal microscope allowing a cross sectional image of the channel to be recorded during fluid flow at an instant in time.
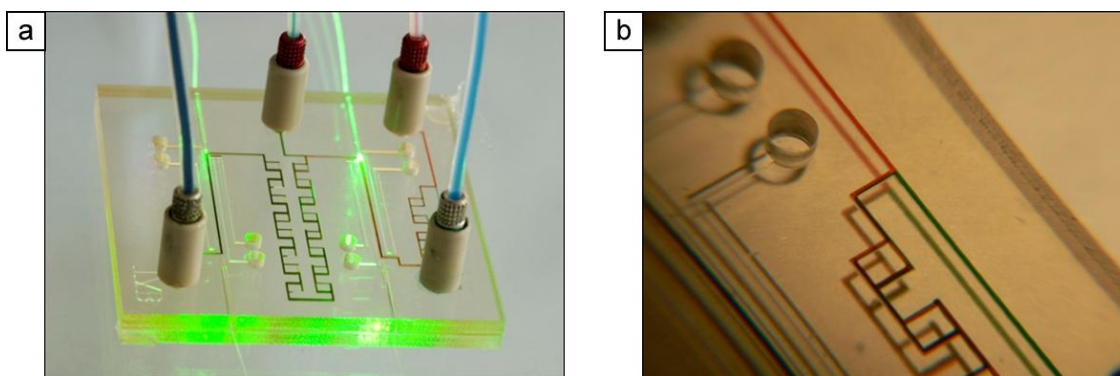
Figure 4.31a & b – Picture of a) the L.O.C. device used within this section of the report with fluid ports and fibre optics attached and b) a red and green food colouring dye entering the first set of mixer elements on the device.

Following confirmation of its ability to detect nitrite a rudimentary test of the L.O.C. to detect nitrate, following its reduction to nitrite in a cadmium column, is also performed. This confirms that the device presented in this study can be developed to detect additional chemical species of scientific interest.

4.3.1 Optical design improvements

This section focuses on three areas of optical design improvement for the stage III L.O.C. device. The first considers the coupling of the light from the source into optical fibre. In the stage II prototype the L.E.D. and photodiode are each butt coupled to an optical fibre, and the free end of the fibre inserted into the L.O.C. device. While the coupling of the fibre to photodiode it is the same as described in Section 4.2.7.2. Modifications to the technique and the use of new components used to couple the fibre to the L.E.D. are described in this section. The second area covers the coupling into the absorption cell and out to the photodiode. The third covers decreasing the propagation loss in the absorption cell and decreasing the possibility of interference from stray light. For both there is an emphasis on using fabrication techniques and designs that are low cost and capable of withstanding deep sea depths.

Any improvement of the coupling efficiency and a decrease in propagation losses will increase the measurement range of the sensor, increase the maximum possible absorption cell length (and hence L.O.D.) and decreases power consumption.

4.3.1.1 L.E.D. to fibre coupling efficiency

To achieve a high coupling efficiency the fibre must be placed as close as possible to the emitting surface of the L.E.D. In a 5mm epoxy packaged L.E.D. (as used in stage II) this is not possible as a conductive wire passes over the top of the emitting surface, and attempts to remove the surrounding epoxy damage the emitter. As such only a fraction of the power can be coupled into the L.O.C. device due to geometrical and angular losses (as reported in Section 4.2.1). A surface emitting L.E.D. allows a higher coupling efficiency. Figure 4.32a shows the Philips Luxeon Rebel surface emitting L.E.D. used within this section. The silicone sphere protecting the 16 emitter matrix (1.5 x 1.5mm) can be clearly identified. The removal of the silicone sphere allows direct butting of the fibre against the emitter matrix (see Figure 4.32b). The fibre was aligned to the centre of the emitter matrix using a 3 axis manual translation stage (Thorlabs PT3) and visual verification (x10 jewellers' loupe).
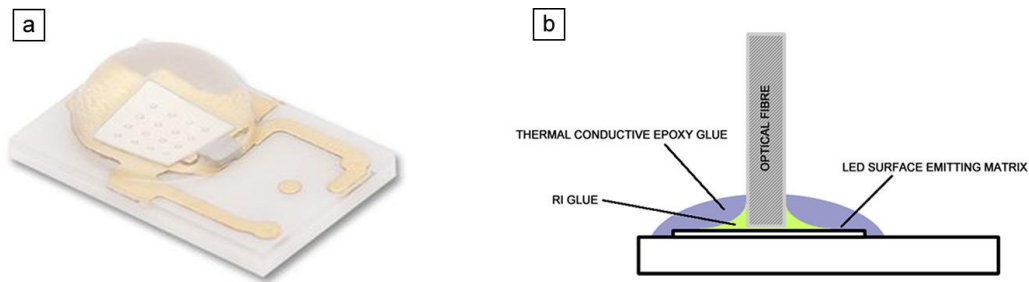
Figure 4.32a & b – a) Philips Lumiled Luxeon Rebel L.E.D. with a 16 emitter matrix and silicone protective sphere, b) Schematic diagram of the LED to fibre butt coupling.

Air gaps present between the fibre and L.E.D. would reduce the coupling efficiency and collapse under pressure causing component failure. Therefore a U.V. curable refractive index matching glue (Norland Optical Adhesive NOA61) was pipetted over the emitter area and used to secure the fibre in place. A portable U.V. gun (Dataman Strobe Eraser) was used to cure the glue. The surface of the L.E.D. produces heat (dependant on voltage but up to 150°C) during operation. To prevent damage to the optical fibre from this high temperature a non-electrically conductive but thermally conductive opaque epoxy (Arctic Alumina Ceramic Thermal Adhesive) was used to cement the fibre onto the L.E.D. It acts to transfer heat away from the emitter and provides additional structural support for the fibre to L.E.D. coupling. The spectrum of light emitted from the L.E.D., through the attached polymer fibre is shown in Figure 4.33.
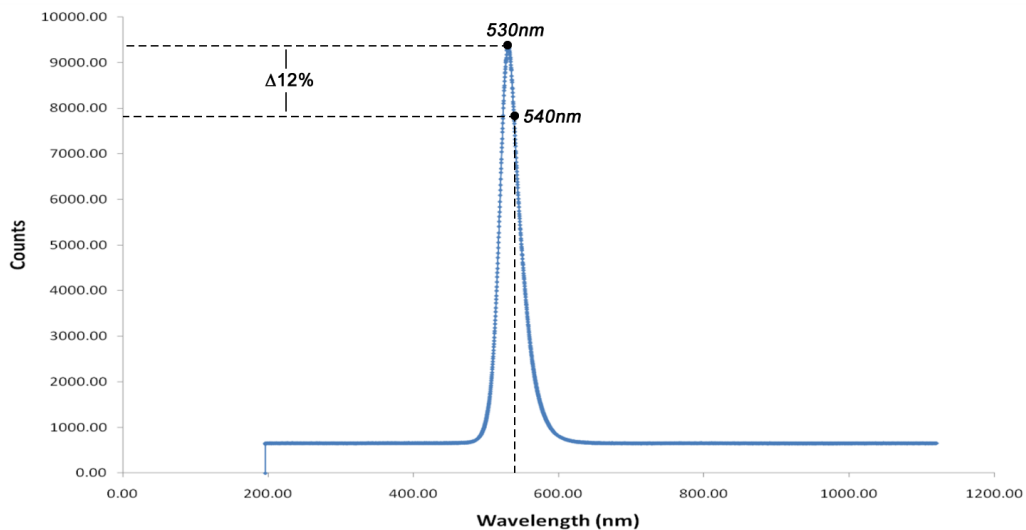
Figure 4.33 – Photon counts versus wavelength for the light emitted from a fibre coupled Philips Luxeon Rebel green LED. The 12% difference between the peak number of counts and that measured at 540nm is indicated.

The optical power output from the L.E.D. and the polymer fibre coupled L.E.D. was measured with a S120UV Thorlabs power meter and is shown in Table 4.10. The coupling efficiency

achieved in stage II prototype was 0.11% and the new setup achieves a coupling efficiency of 6%. This is greater than the theoretical coupling efficiency calculated in 4.3.1.1.

Setup description	Voltage (V)	Optical power output (µW, at 530nm)
L.E.D. only	2.3	550
Fibre coupled L.E.D.	2.1	0.64
	2.2	18.7
	2.3	33.5
	2.4	83.8

Table 4.10 – Measured optical power output level for the Philips Luxeon Rebel L.E.D. at 2.3 Volts and the power output from a fibre butt coupled to the L.E.D. at 530nm.

This low cost, robust and effective method increases the coupling efficiency of the L.E.D. to the fibre by more than an order of magnitude. It can also be used to bond two fibres to the same L.E.D (therefore allowing a common mode signal in both signal and reference absorption cells without the use of a fibre splitter).

The use of a new L.E.D. to fibre assembly method and light source has increased the amount (power) of light entering the absorption cell which in turn enables a longer absorption cell. Fabrication and package size restriction mean the absorption cell in the stage III sensor was limited to 20mm, but it also decreased the electrical power consumption of the optical system as the light source needs only to be driven with a minimal voltage due to a higher coupling efficiency.

4.3.1.2 Fibre to absorption cell coupling efficiency

This section examines improvements to the quantity of light being collected by the output fibre through the use of micro lenses. This would further decrease the amount of power required to drive the L.E.D. (through increasing the coupling efficiency between the optical fibre and L.O.C. device) and increase the possible absorption length. Although literature is available [246,247,248] for the use of micro lenses to reduce the spread of light (i.e. aperture) from a light source they are reliant on air to provide the refractive index difference. The use of air is not possible with deep sea devices. Therefore in this study R.I. fluids (Cargille Laboratories Series A R.I. 1.46 – 1.64) are used to replace the air. To utilise the R.I. fluids in micro lenses new L.O.C. device were designed and fabricated (see Figure 4.34a & b for photographs).
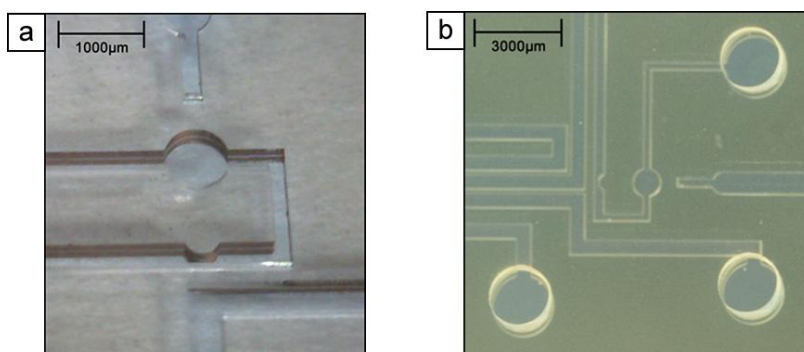
Figure 4.34a & b – Two pictures of the L.O.C. devices used in determining increases in coupling efficiency through the use of microlenses.

To determine any increase or decrease in the coupling efficiency when using a light entry and exit lens they were filled with either 1.46 or 1.64 R.I. fluid and the power output from the absorption cell (via a fibre) was measured using an S120UV Thorlabs power meter. Figure 4.35 shows the measured optical power (output fibre) for each variation with the L.E.D. light source (Philips Lumiled Luxeon Rebel) driven at 2.2V.
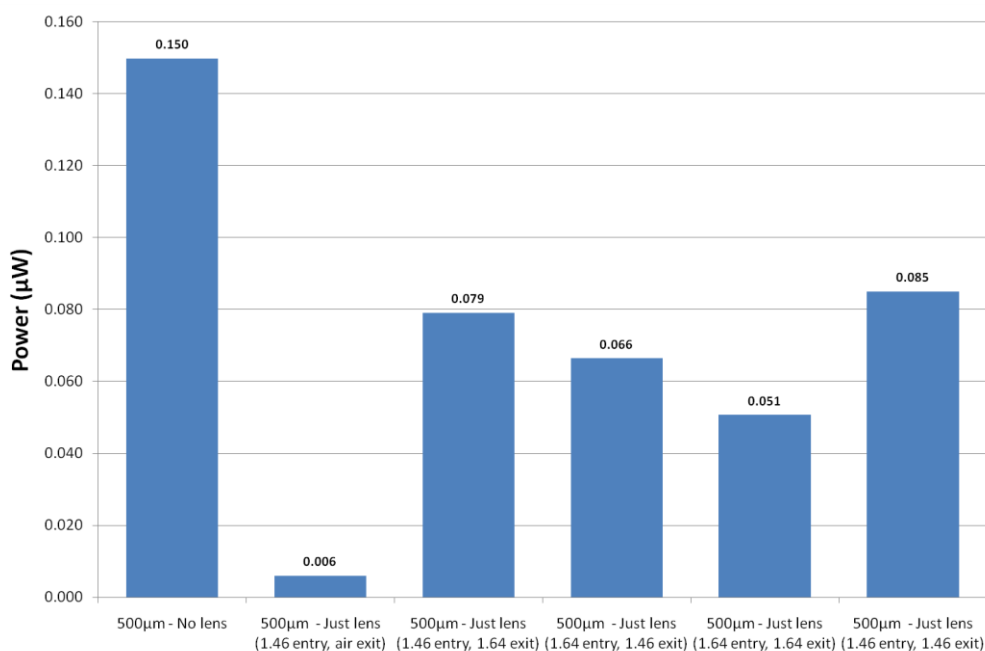
Figure 4.35 – Bar chart of the output power from five variations of lens configurations measured using a S120UV power meter. The output power without a lens is also plotted.

Although the refractive index fluid can be used to act as a lens the losses associated with the introduction of further material boundaries makes the 'no lens' option more suitable for the current L.O.C. device. Therefore micro lenses were not used in the stage III sensor.

4.3.1.3 Absorption cell

The stage I prototype relied upon the black acrylic material that the absorption cell was constructed in to decrease the effect of stray light and propagation losses. The L.O.C. device presented in stage II was made with a dry film resist and glass substrate that did not offer this property. The addition of planar waveguides in the stage III sensor was designed to decrease the effects of stray light (natural light or another channel in the differential measurement system).

Air core waveguides have previously been used to decrease light losses in the L.O.C. absorption cells and decrease interference between the signal and reference cells (as presented in Section 3.2). To be most effective waveguides need to be in both horizontal and vertical planes. It is not possible to create waveguides in both planes using the dry film manufacturing techniques, but single plane waveguides are possible. Waveguides use total internal refraction to constrain the light to one or two planes. In the majority of L.O.C. devices in the literature to date these waveguides use an air core. The difference between the refractive index of water and air is large (≈ 0.3394) therefore the waveguides have a large angle of incidence and are effective. It is not possible to use air core waveguides in this study due to deep sea deployment scenario's (see Section 4.2.1). Instead this study uses a prototype low refractive index fluid (R.I.=1.26) from Cargille Laboratories (Catalogue no.19170 code 126nD) to replace the air. The use of single plane waveguides filled with R.I. fluid were investigated in this section.

The effectiveness of a refractive index fluid filled waveguide can be modelled using a Matlab$^{©}$ script (Appendix 8.5.3.1) and Snell's law. This determines the path of the monochromatic light (e.g. are the waveguides going to act as such) and an average 'real' absorption path length (e.g. the path length that the light takes through the sample). Figure 4.36a shows ray trace for a 20mm air core waveguide and Figure 4.36b shows a 20mm 1.26 refractive index fluid filled waveguide for a point source with no angular dependent variation in output power.
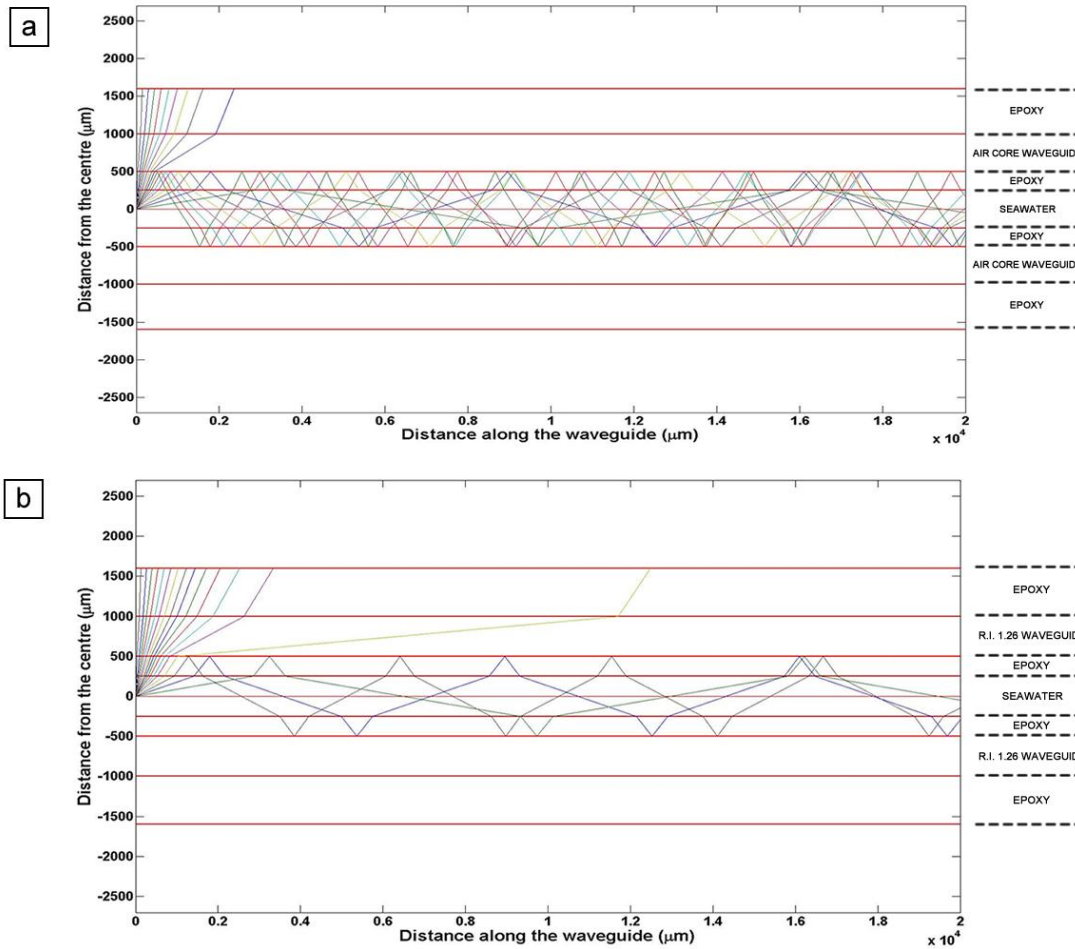
Figure 4.36a & b – Diagram showing the theoretical path of light through a 20mm absorption cell where the waveguide is a) air and b) 1.26RI fluid.

A 1.26 R.I. fluid within the waveguides results in total internal reflection for light entering the absorption cell from up to 20.8 degrees from the horizontal. Light that passes into the epoxy side-walls of the channel alternates between travelling inside and outside the fluid. This reduces the 'real' absorption path length (see Section 2.2.23). For instance a light ray entering at 15 degrees to the horizontal has a real path length of 4.4mm in a 20mm cell. This reduction in path length will lead to a higher limit of detection. In comparison air core waveguides have an acceptance angle of 41.7 degrees. The multiple paths created in both and hence different absorption path lengths will also result in non linearity in the absorbance response. An experiment was used to provide an indication into the difference in coupling efficiencies and propagation losses of air, 1.26 and 1.59 filled waveguides. The voltage of a photodiode (Taos TSLG257) coupled to the output fibre from an L.O.C. device was recorded whilst using a constant intensity light source (L.E.D. driven at 2.2V and 10mA) for each of the combinations is shown in Table 4.11.

Waveguide core	Taos Voltage (V)	Difference from air core (%)
Air	3.2870	-
1.26 R.I. fluid	3.2248	(-1.89)
1.59 R.I. fluid	3.1870	(-3.04)

Table 4.11 – Difference in photodiode voltage when measuring the optical power output from a 20mm water filled absorption cell when varying the waveguide core between air, 1.26 and 1.59 R.I. fluid.

The 1.89% difference in voltages between air and R.I. 1.26 is minimal therefore confirming that use of 1.26 R.I. filled waveguides is a suitable replacement for air core waveguides within a deep sea L.O.C. device. These are integrated into the mask design presented in Section 4.3.3.

4.3.2 Micromixer

The recommendation from the stage II sensor prototype was to increase the number of f-shaped to above 8 elements (500μm wide, 300μm high channels) and that this would result in >90%. This section provides qualitative results to confirm that the mixing of the sample and reagent is taking place effectively in the L.O.C. device (as presented in Section 4.2.3 and shown in Figure 4.37a). A Nikon laser scanning con-focal microscope which was not previously available (EC Plan-Neofluar 5x/0.16 M27 Lens, LP560) was used to provide a three dimensional image of two fluids mixing at different stages of the mixer. Two fluorescent solutions (Fluorescein and Rhodamine B) were pumped (at 40μl/min, similar flow rates to those used during nitrite detection experiments) into the L.O.C. device using a Harvard Apparatus Nanomite syringe pump. Fluorescein and Rhodamine B were chosen as the excitation (488 and 543nm) and emission bands (505-530 and 560) are distinctly separate. Figure 4.37b shows a three dimensional picture imaged at the T junction where fluids A and B combine to form the fluid stream C.
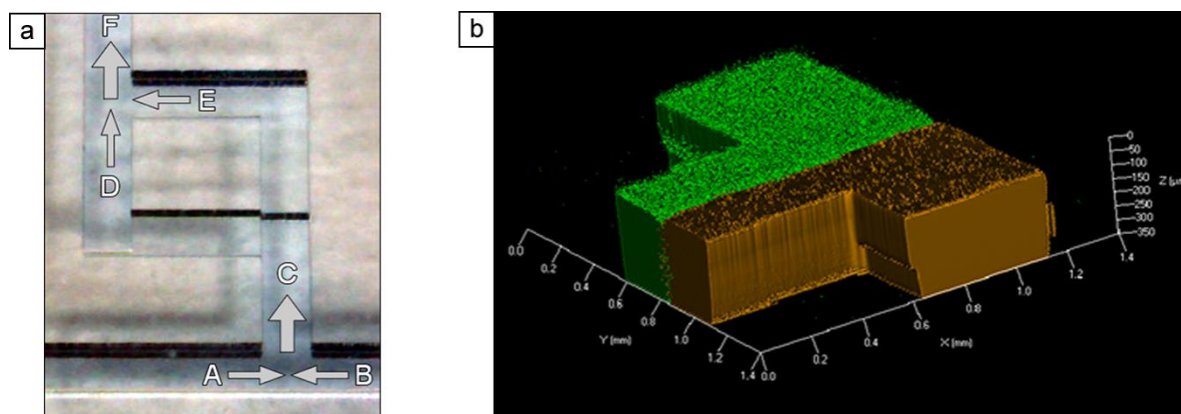
Figure 4.37a & b – Two pictures showing a) an annotated view of an f-shaped mixer segment and b) fluids first coinciding at the microscale T-junction, where the green shows the fluorescein and the brown the rhodamine.

Figure 4.37b shows the laminar effects found on the microscale (no mixing and a sharp and persistent boundary between the two fluids). To determine the degree of mixing it was necessary to take a smaller cross section width (leads to a faster imaging time) at several sections of the mixer. Figure 4.38 shows the imaging at three different locations, the T-junction, after the 1st mixing element, after the 8th mixing element.
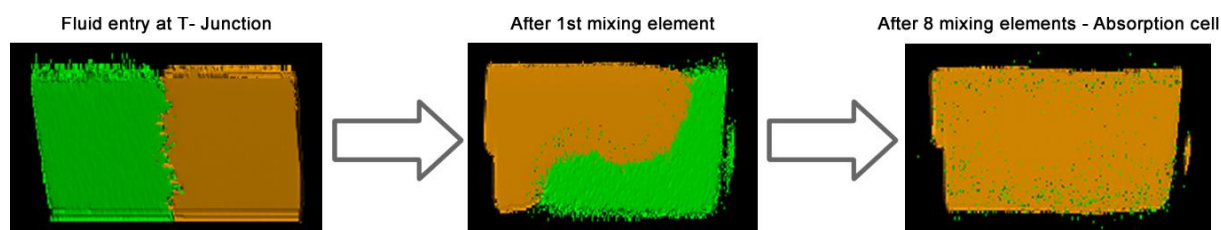
Figure 4.38 – Three images of the two fluids within the L.O.C. device, with the rotation introduced by the mixer clearly seen in the 1st mixing element image.

Work conducted in the stage II prototype found 46% mixing after 4 elements (11.5% per element) and recommended eight elements (11.5μl/sec in 500μm channels). The qualitative results show that this has been achieved and that the fluid entering the absorption cell should be fully mixed. As such the same number of mixing elements where transitioned to the L.O.C. device used in *in situ* trials (see Section 5). It should be noted that while laser scanning confocal measurements can provide qualitative results quantitative results need to be conducted with using seawater and reagent due to pH effects and fluid density variations. These are conducted in the stage III section by a comparison of the absorption measurements from the L.O.C. device and those from a commercial spectrophotometer.

4.3.3   Mask design and device fabrication

Following the identification of improvements to the mask design identified in Section 4.2 and 4.3.1 the mask design shown in this section incorporated these developments and was used in fabrication of the stage III sensor.

The negative dark field mask used during fabrication of the device had two absorption cells, four fluid ports and two different sets of mixer elements. The mask is shown in Figure 4.39. The two absorption cells (each 20mm in length, 500μm wide, and 300μm in height) are used as a reference and signal cells to provide a differential absorption measurement to isolate the measurement from changes in the absorption of the sample carrier (i.e. turbidity).
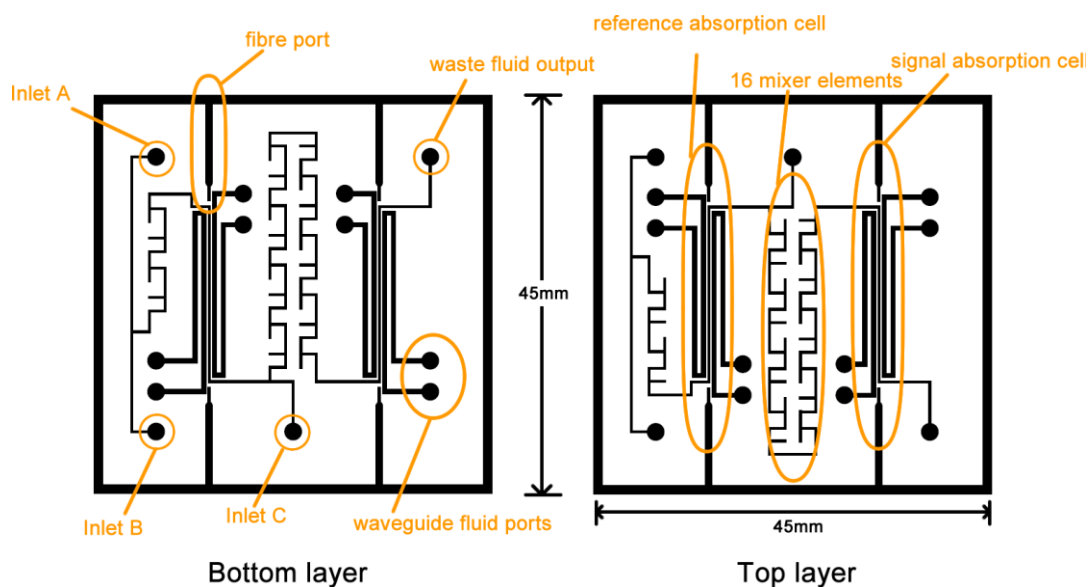
Figure 4.39 – Diagram of the two dark field mask designs used in the fabrication of the L.O.C. device for the stage III sensor with the key sections highlighted.

The design includes an increased number of mixer segments (16), following previous experimental results, to ensure complete mixing (presented in Section 2.6.2). Waveguides have been placed on either side of the absorption cells with the aim of decreasing propagation losses and the effects of stray light (the effects of which are highlighted in Section 2.4.1.1).

While the rapid manufacturing of the device in P.M.M.A. and SU8 was provided by Epigem Ltd the confocal microscope images gained during the qualitative mixer evaluation show misalignment of the lid and base. It is shown in Figure 4.37b as a ridge. This is not ideal as it will increase smearing and residue (therefore increasing minimum resolvable volume) and also possibly the extent of mixing due to design variation. This was accepted as a risk with this design and noted for further work outside the scope of this study.

4.3.3.1   The effects of flow rate variability

In stage I and II work (Section 4.1 and 4.2) it was noted that flow rate changes of either the sample or reagent have a large effect on the measured absorption. Minor variations in the flow rate impact the sample to reagent ratio, the mixing level, the residence time in the system (and therefore the time for the reaction to approach completion) and hence azo dye development. Figure 4.40 shows the variation in absorption with flow rate when drawing a 25μM sample of nitrite in seawater and reagent through (solenoid pump) the L.O.C. device.
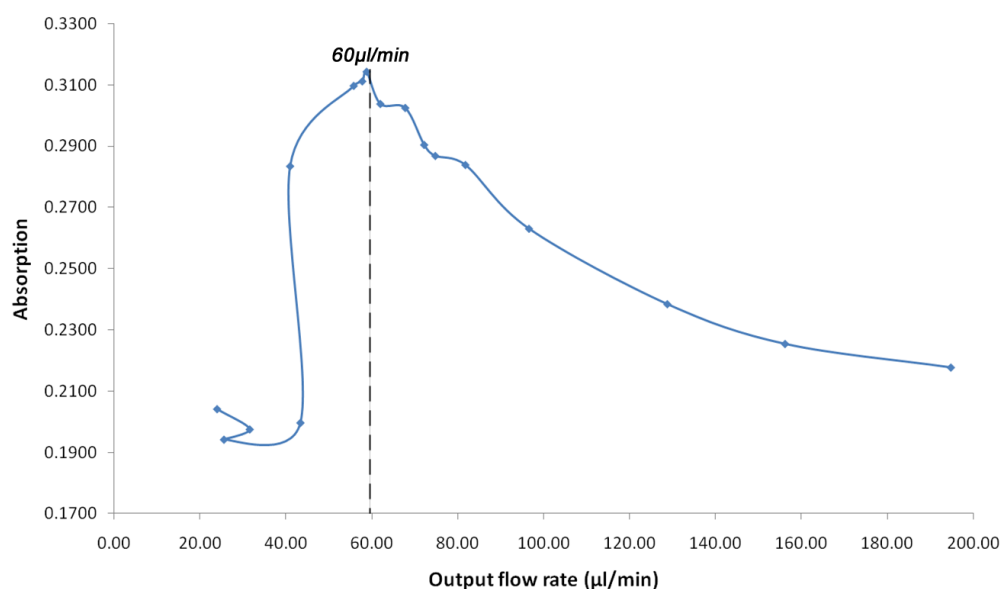
Figure 4.40 – Graph of absorption versus flow rate showing the variation in azo dye formation with flow rate when drawing a 25μM sample of nitrite in seawater and reagent through the stage III L.O.C. device.

The peak absorption (≈0.32A) is at 60μl/min with a rapid decrease in absorption at lower flow rates. The rapid drop in absorption can be attributed to the stopping of flow in either the reagent or sample inlet and insufficient mixing. At flow above 60μl/min the absorption decreases due to insufficient colour development (reagent kinetics and a change in the extent of mixing). The theoretical value for the absorption of a 25μM concentration of nitrite in a 20mm absorption cell is given by Equation 4.34 and Equation 4.35.

$$A = \varepsilon bc \qquad \text{\textit{Equation 4.34}}$$

$$A = (1.5 \times 10^6) \times 0.02 \times (25 \times 10^{-6}) = 0.75A \qquad \text{\textit{Equation 4.35}}$$

Although the maximum absorption value from the experiment is under half that of the theoretical absorption, following the identification of 60μl/min as the optimum flow rate for azo dye development in this L.O.C. device, future experiments were carried out at this value. At this flow rate the reaction will be complete by the time the mixed fluid enters the detection chamber (based on previous literature, see section 2.4.1.1) which will decrease the L.O.D. and precision.

An additional complication in providing a constant flow of sample and reagent is the selectivity between the sample and reagent inlets. In certain scenario's (i.e. low flow rates) it was noted that the flow rate on one inlet would drop to zero whilst the other remained flowing. To monitor this effect the flow rate at the sample and reagent inlets was recorded (Sensiron LG16-1000A) whilst

a syringe pump drew fluid through the L.O.C. device. This was conducted for a variety of tubing lengths and diameters. For each measurement 5 seconds of data was recorded (at 1kHz sampling rate) at a range of flow rates (0 to 500µl/min). Figure 4.41a shows the result when using a 0.8mm tubing diameter (400mm length) and Figure 4.41b using 0.3mm diameter tubing (400mm length).
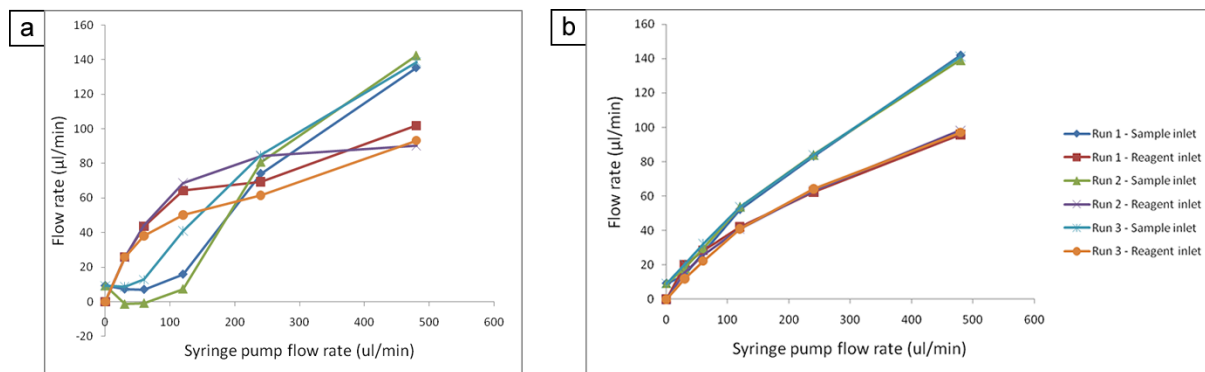
Figure 4.41a & b – Graph showing the variation in flow rate on sample and reagent inlets versus the syringe pump flow rate on the outlet for an inlet tubing of diameter a) 0.8mm and b) 0.3mm.

The precision and linearity of the experiments improved through the use of narrower (Ø0.3mm) tubing. Narrower tubing increases the pressure drop and therefore decreases the percentage effect of external factors (e.g. atmospheric pressure) and geometry of junctions on the system. The variability of the flow rates, shown by Figure 4.41a, is the reason why a push through system is used in stage III experiments.

4.3.4 Detection of nitrite

This section presents nitrite detection results from three bench top experiments following the design modifications to improve L.O.D, and precision. The optical and L.O.C. device design are described in the previous sections of this chapter (Section 4.3.1 and 4.3.3). Fluid delivery is provided by either a syringe pump (used as a reference measurement) or a peristaltic pump (Instech P625 Peristaltic pump capable of 0.34 to 275µl/min, 0.6W power consumption, and 27x32x68mm) and data is recorded by a data acquisition card (NIDAQ) at 1 kHz. No third party electronics were used and the L.E.D. driven directly by the NIDAQ. An illustration of the two fluidic setup and a schematic illustration of the electronics is shown in Figure 4.42.

The syringe pump (i.e. used for reference measurements to isolate the sensor precision from pump oscillations) cannot be packaged into an *in situ* device without significant redesign, and is suitable only for initial bench top testing. Therefore it is necessary to use an alternative pump. Peristaltic pumps have been used *in situ* and are more appropriate for deployment due to their

simplicity, small size and low power hence are also used in the fluid delivery setup. An eight way valve was used during the peristaltic experiments (BioChem 080T812-62-5, internal volume of 373µl) to ensure the same flow rates and experimental conditions for all samples.
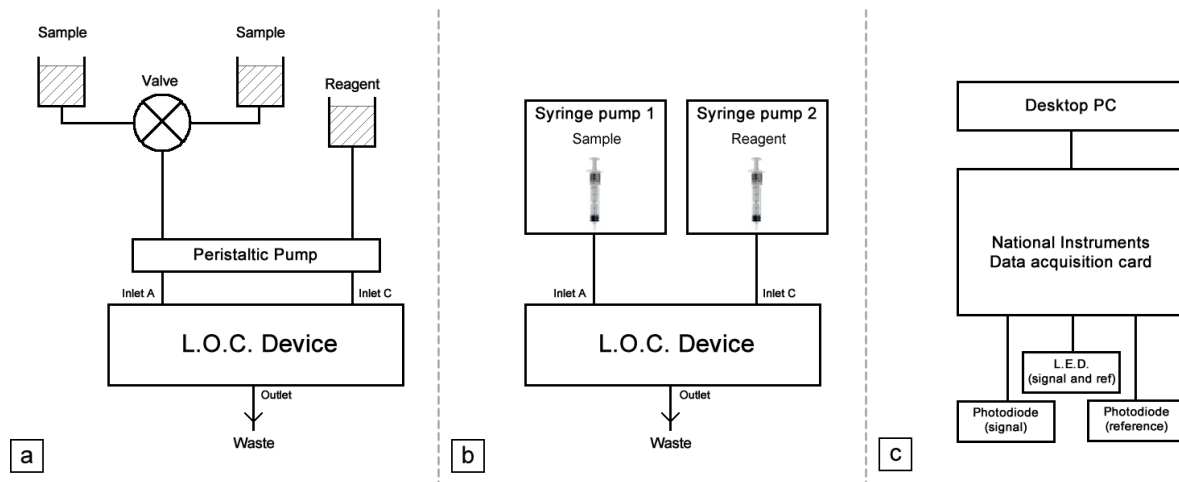
Figure 4.42 - Diagram illustrating a high level schematic of a) peristaltic pump experiment setup, b) syringe pump experiment setup c) the electronics used in the detection of nitrite using the stage III L.O.C. device.

In all experiments the concentration of the nitrite sample (made through the successive dilution of a 100µM nitrite seawater standard, O.S.I.L. Uk Ltd with artificial seawater or M.Q. water) was increased from zero as to minimise the effect of contamination from previous samples. The three experiments detailed are shown in Table 4.12.

No.	Sample		Reagent	Pump
	Species	**Base**		
1	nitrite	M.Q. water	N.E.D, P.V.A, Sulphanilamide	syringe
2	nitrite	M.Q. water	N.E.D, Sulphanilamide	peristaltic
3	nitrite	artificial seawater	N.E.D, Sulphanilamide	peristaltic

Table 4.12 – An overview of the experiments described in this section (Section 4.3.4).

The two reagents used for the detection of nitrite were based on the Tovar et al [92] variant Griess reaction, presented in Section 2.4.1.1. The first is as presented in Section 4.2.6. The second (without P.V.A.) was comprised of 0.06M sulfanilamide, 2M HCl, 0.5% polyvinyl alcohol and 0.05% N-(1-napthyl)ethlenediamine dihydrochloride, all sourced from Fisher Scientific Uk. It was prepared in 200ml batches by mixing together; 2 grams of sulfanilamide dissolved in 35ml of

concentrated HCl and 65ml of deionised water; and 0.1 gram of N.E.D. dissolved in 100ml of deionised water.

4.3.4.1 Full reference run with syringe pump

Using a syringe pump (Harvard Apparatus Nanomite) two fluids (nitrite sample and reagent) were pushed into the L.O.C. device through two microbore (Ø0.8mm) tubes at a combined flow rate of 100µl/min. The voltage output from the reference channel photodiode and the mixed fluid channel photodiode (signal) was measured for ten different nitrite concentrations samples (5µM intervals from 0 to 45µM). A plot of signal minus the reference photodiode voltage versus the nitrite concentration for two runs is shown in Figure 4.43.
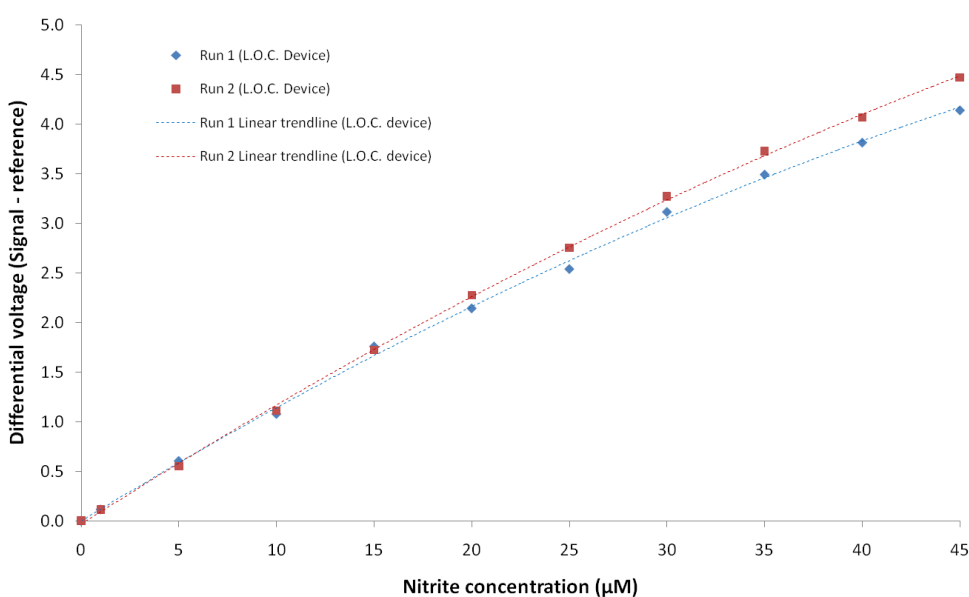
Figure 4.43 – Graph showing two experiment runs for 0 to 45µM nitrite concentrations in MQ water. The differential voltage is plotted against nitrite concentration with the trendlines illustrated for each run.

The average standard deviation (resolution) for run one and two was 0.00337 and 0.0308V respectively. Using the equation for the limit of detection presented in Section 2.2.12, and with k=3, the L.O.D. for run one is 0.0322µM and 0.0308µM for run two. The precision, given by the standard deviation of absorption values measured at 15µM across the two runs (as per Section 2.2.11), was 0.01899V (0.344µM). At 45µM this increases to 0.17169V (45.76µM) as the trendlines deviate. At high concentrations the graph becomes non linear as a result of the non linearity of the Beer-Lambert law at high absorption levels or a combinatorial dilution error. The divergence of the two experiment runs is attributed an unbalanced response of signal and reference channels and subsequent variations in natural light (causing a deviation in the curve, see 2.4.1.1). The level of resolution and limit of detection achieved in this experiment would be

suitable for the detection of nitrite in the ocean as changes in concentration that are of scientific interest could be detected.

4.3.4.2 New reagent and peristaltic pump

This section covers the results from nitrite concentrations in M.Q. water between 0 and 15μM. Three runs were completed at 12 hour intervals and each run was conducted from low to high nitrite concentration. This section also qualitatively examines the effects of removing Poly-Vinyl Alcohol (added to aid colour formation and prevent precipitation when during the detection of ammonium, as per Section 2.4.1.1.1) from the reagent. As a surfactant it contributes to bubble formation and decreases the mixing efficiency. This is a replication of an improvement made in flow segmented analysis system and was suggested by an expert in the field [249]. A decrease in the number of air bubbles entering the L.O.C. device will decrease the number of erroneous readings (see Section 4.3.1). The removal of the P.V.A. should not interfere with the creation of azo dye in the detection of nitrite or nitrate (which is a key objective of this study, as reported in Section 1.1).

Fluid was pumped at a total flow rate of 60μl/min (flow rate identified in Section 4.3.3.1). Figure 4.44 shows a graph of the average of 30 seconds of data at each nitrite concentration. The absorption at 0μM was baselined for each successive run. Between samples and before taking a measurement fluid was pumped for 5 minutes at 120μl/min using an Instec Peristaltic pump to negate any cross sample contamination (i.e. due to smearing, dead volume and dispersion in the sample inlet fluid path).
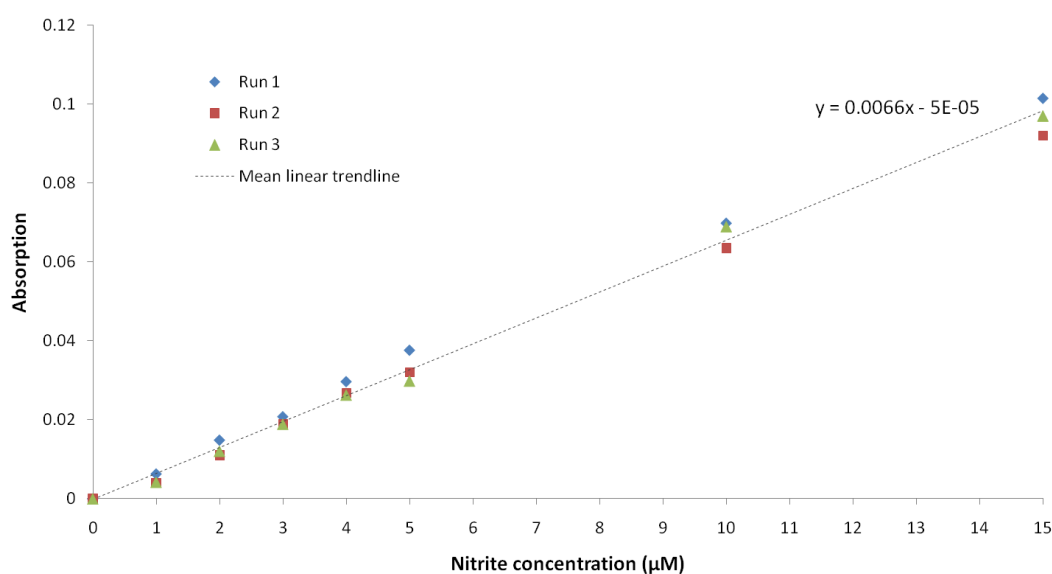
Figure 4.44 – Graph of absorption versus nitrite concentration for three runs using a peristaltic pump

The average standard deviation (resolution) for run one correlates to 0.0005A (83.3nM), run two to 0.0005A (83.3nM), and run three 0.0024A (371nM). Using the equation for the limit of detection presented in Section 2.2.12, and with k=3, the L.O.D. for run one is 0.145μM, run two 0.165μM, and run three 0.840μM. The precision, given by the standard deviation of absorption values measured at 15μM across all the runs (as per Section 2.2.11), was 0.0047A (0.726μM).

To confirm the accuracy of the absorption measurements the waste output for each nitrite concentration from run 1 was collected into a specimen container (100μl) and its absorption measured three times in a Hitachi commercial spectrophotometer. Figure 4.45 plots the measured commercial spectrophotometer absorption against the measured L.O.C. device absorption. This provides a comparator and confirms that the absorption values are accurate and whether the nitrite samples (manually produced from a 100μM standard) have been diluted correctly. Only one run was compared as flow rates and original samples were the same in each.
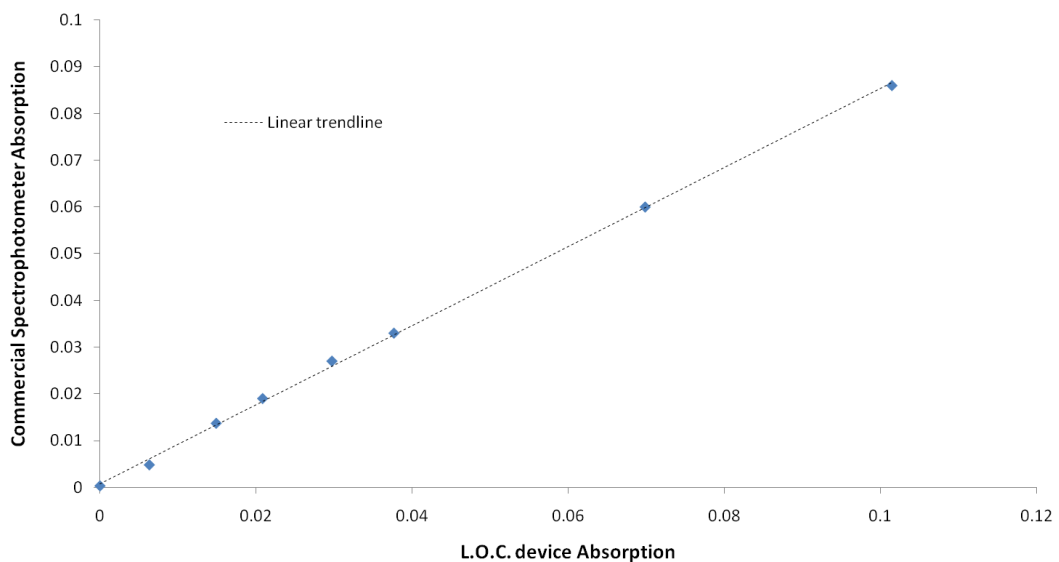
Figure 4.45 – Graph showing the absorption measured (in run one) in the commercial spectrophotometer against the absorption measured in the L.O.C. device during the detection of nitrite using a peristaltic pump and nitrite in M.Q. water.

The comparison between the absorption measured in the L.O.C. device and the commercial spectrophotometer shows slight deviation from a linear trend line. This indicates that the dilution of the nitrite was not accurate. It also indicates that the effective path length is greater in the L.O.C. device.

4.3.4.3   Nitrite in seawater

Previous results presented in this section have used a nitrite in M.Q. water as a standard. The results presented in this section use nitrite in artificial seawater. Three runs with a range of nitrite concentrations between 0 and 15μM were conducted. The absorption values plotted in Figure 4.46 are the average of 30 seconds of data. The experiment was run from low to high concentration.
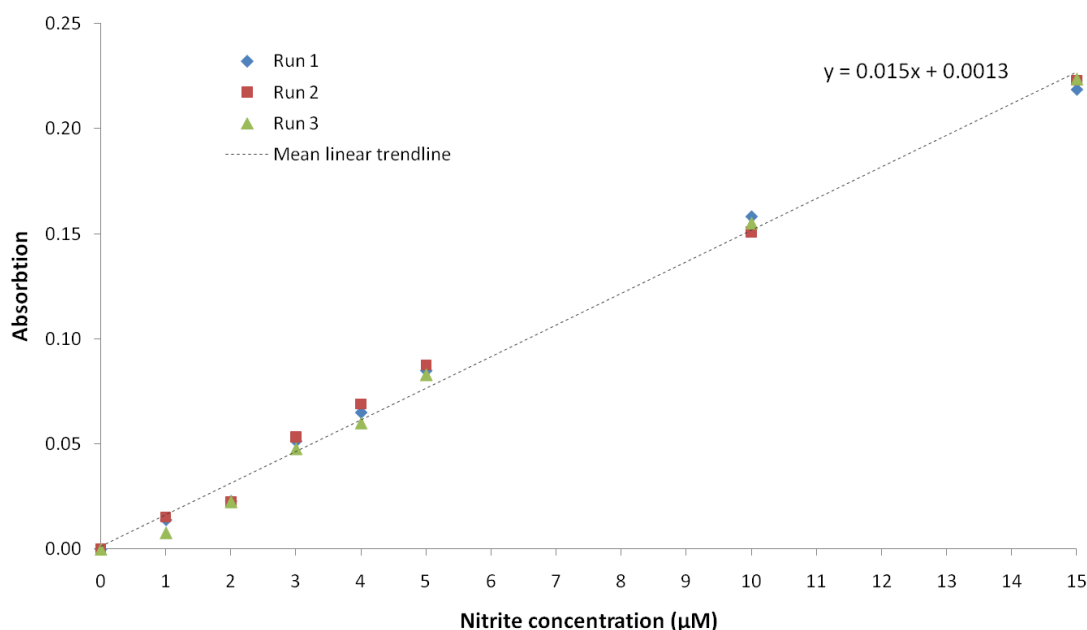
Figure 4.46 – Graph of absorption versus nitrite concentration for three runs conducted with nitrite standard in artificial seawater between 0 and 15μM.

The average standard deviation (resolution) for run one correlates to 0.0024A (157.9nM), run two to 0.003A (197.3nM), and run three 0.0028A (184.2nM). Using the equation for the limit of detection presented in Section 2.2.12, and with k=3, the L.O.D. for run one is 0.0628μM, run two 0.0811μM, and run three 0.0476μM. The precision, given by the standard deviation of absorption values measured at 15μM across all the runs (as per Section 2.2.11), was 0.00264A (0.0893μM).

To confirm that the absorption measurements are accurate the waste output for each nitrite concentration during each run was collected into a specimen container (100μl) and its absorption measured three times in a Hitachi commercial spectrophotometer. The comparison is presented in Figure 4.47.
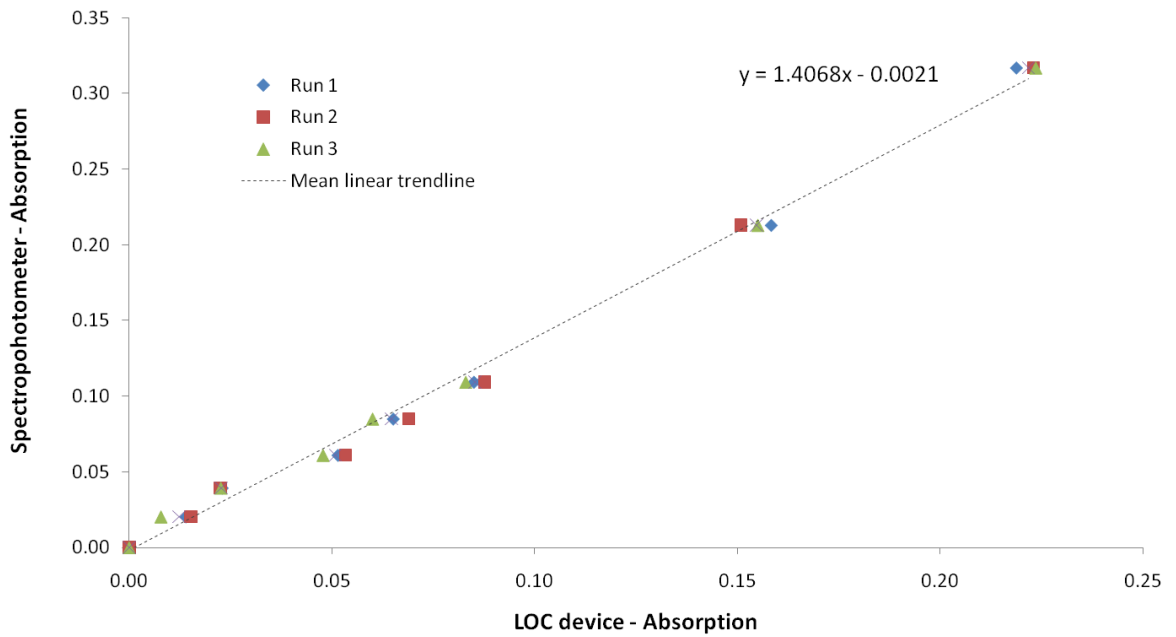
Figure 4.47 – Graph of absorption measured on a commercial spectrophotometer versus absorption measured using the L.O.C. device. The equation of the mean linear trendline of the three runs is also shown.

Once again there is a correlation between the deviation from the linear trend in the L.O.C. device measured absorption values and the spectrophotometer measured values. The first three values (0, 1, 2μM) are all low therefore indicating too little nitrite standard was added to the sample. The following three (3, 4, 5) are all above the linear trend line in both sets of results therefore indicating that too little artificial seawater was added during experiment preparation. Horizontal variation of the measurement points in Figure 4.47 indicates that the commercial spectrophotometer was more precise than the L.O.C. device.

Once again the resolution and precision of the L.O.C. device in this experiment fulfils the requirements set out in Section 2.2. If this device was deployed as an *in situ* package then it would be enable a greater scientific understanding of the ocean and its biogeochemical processes.

4.3.4.4   Discussion

Through design developments it was possible to improve coupling efficiency from 0.11% (stage II) to 6% (stage III). As such it was possible to measure the change in absorption caused by different nitrite concentrations in sweater in a 20mm optical absorption cell. Experiments carried out using a syringe pump proved the L.O.C. device was capable of detecting low concentrations of nitrite (<1μM). However as there are no commercially available syringe pumps suitable for *in situ* deployment it was necessary to use an alternative fluid delivery mechanism. The peristaltic pump used as the alternative causes more fluctuations in the flow rate and hence a lower

sensitivity. Following observations during experiments the removing the Poly Vinyl Alcohol reduced the quantity of air bubbles formed within the L.O.C. device. Minimal effect on the L.O.D. (shown by the difference between the L.O.D's in Section 4.3.4.1 and 4.3.4.2) was seen. A full calibration of the detection of nitrite samples in M.Q. water shows the device is capable of a L.O.D. of <100nM nitrite concentrations, and when nitrite samples in artificial seawater were used the L.O.D. did not decrease. This compares to an absorption L.O.D. of 0.001987A achieved by C.M. Mcgraw et al [1] during a partial *in situ* deployment. Table 4.13 presents an overview of the experimental results gained for the detection of nitrite using the stage III L.O.C. device.

Description	L.O.D. (μM)	Precision (μM)
Full reference run with syringe pump – 1st run	0.0322	0.344 (at 15μM)
Full reference run with syringe pump – 2nd run	0.0308	
New reagent and peristaltic pump – 1st run	0.145	0.726 (at 15μM)
New reagent and peristaltic pump – 2nd run	0.165	
New reagent and peristaltic pump – 3rd run	0.840	
Nitrite in seawater – 1st run	0.0628	0.0893 (at 15μM)
Nitrite in seawater – 2nd run	0.0811	
Nitrite in seawater – 3rd run	0.0476	

Table 4.13 – Overview of the limit of detection and precision of the experiments performed in the stage III bench top sensor section.

In preparation for *in situ* deployment it was noted that a change in height between the L.O.C. device and the sample or reagent inlet can cause a change in flow rate. This will be an issue during *in situ* deployment as the sensor will experience the motion of a ship or waves during near surface deployment scenarios. To identify the level of change in the flow rate caused by a change in height a solenoid pump (2Hz) was used to pump fluid from a sample container (open to the atmosphere) whilst changing the height of the container and recording the output flow rate. Figure 4.48a shows the effect on flow rate as the sample is raised by 20cm and Figure 4.48b during a decrease in height by 20cm.
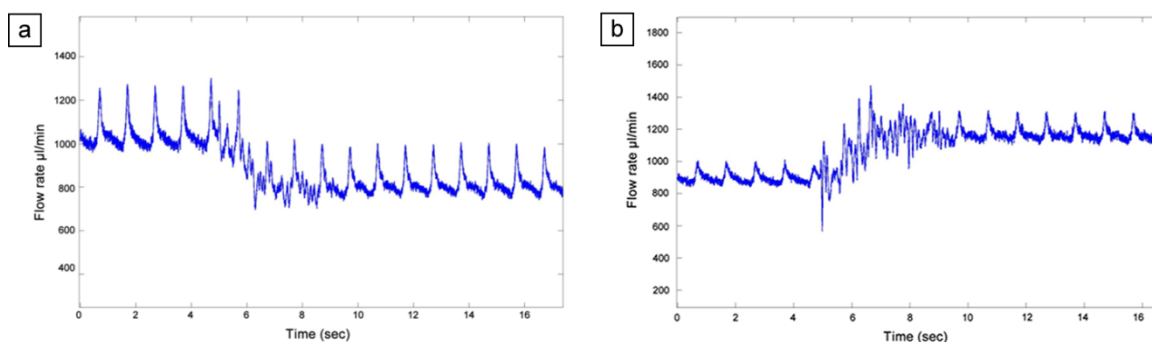
Figure 4.48a & b – Graph of flow rate versus time for the L.O.C. device outlet after the sample inlet height is decreased by 20cm and b) when the height is increased by 20cm.

This highlights one of the issues surrounding fluid delivery to a microscale device. As the L.O.C. device needs to able to operate *in situ* it needs to be resilient to the effects of changes of inlet pressure and in operating conditions. To minimise these effects it is necessary to use a system that draws fluid from the inlet and pushes it through the L.O.C. device. This minimises the quantity of air bubbles (Section 4.1.1.1) and delivers fluid at a repeatable rate to the L.O.C. device. As such it is used during *in situ* deployment in Chapter 5. The disadvantage of a 'push through' system is that it will increase the fluidic delay, dispersion and minimum resolvable volume and hence decrease the sampling frequency. This can be minimised by ensuring the fluidic path length between the sample inlet and absorption cell is minimised. The time taken to change a sample (e.g. from 0-15µM or 15-0µM) in all peristaltic pump runs was 180 seconds. This time is measured from the switching of the fluid inlet streams till the signal from reduces to within 90% of the steady value (T90). Much of this time is due to the large fluid volume in the sample inlet valve (373µl).

4.3.5 Detection of nitrate

By the addition of a macroscale cadmium column (salvaged from a NAS-3X sensor, Section 2.4.9) to the sample inlet path it was possible to prove the principle of detecting nitrate using the same L.O.C. device as used for nitrite. Figure 4.49 shows a schematic of the experimental setup where the salvaged cadmium column is a 15cm (3.2mm I.D.) plastic tube filled with 3.2g of Skalar cadmium granules and sealed using a plug of glass wool at each end of the tube.
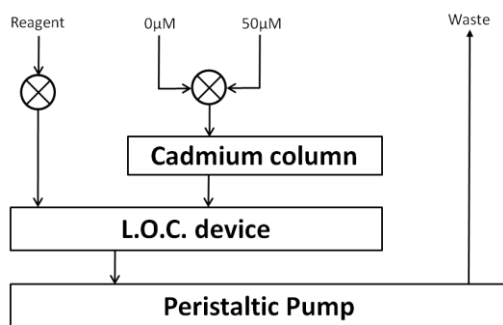
Figure 4.49 - Diagram illustrating a high level schematic of the fluid handling systems used to prove the principle of the detection of nitrate using the L.O.C. device.

The voltage of the signal and reference channel was recorded for a 0 and 100μM sample of nitrate in seawater. The experiment was repeated three times. Figure 4.50 shows a plot of the absorption versus nitrate concentration for the runs.
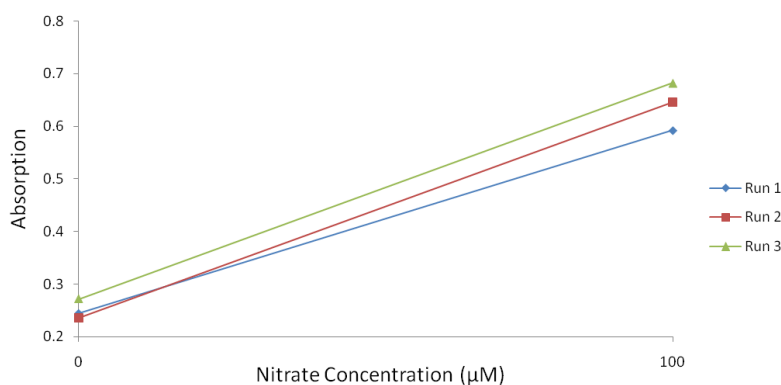
Figure 4.50 – Graph of absorption versus nitrate concentration for a basic proof of principle experiment.

The standard deviation (resolution) for run one correlates to 0.0110A (3.149μM), run two to 0.0074A (1.805μM), and run three 0.0112A (2.732μM). Using the equation for the limit of detection presented in Section 2.2.12, and with k=3, the L.O.D. for run one is 1.745μM, run two 3.955μM, and run three 5.731μM. The precision, given by the standard deviation of absorption values measured at 100μM across all the runs (as per Section 2.2.11), was 0.0454A (1.164μM).

The L.O.D. for all three runs is higher than that found for the detection of nitrite. One of the reasons for the increased L.O.D. is the variability of conversion of the nitrite to nitrate by the cadmium column. The macroscale column is designed for large sample volumes and was past its peak performance leading a variable nitrate to nitrite conversion ratio. Therefore for future work it is necessary to have an appropriately scaled cadmium column. It is acknowledged that this is a basic test of functionality and proof of principle in the detection of nitrate. It provides a basis for future work.

5. TRIAL CRUISE DEPLOYMENT

This section details the construction of a standalone L.O.C. chemical sensor and the results from its testing on a trials cruise. The sea trials undertaken were designed to provide diagnostic data (for example; pressure resistance; robustness) and initial data on the sensor performance and stability (in the detection of nitrite and nitrate) *in situ*. They took place between the 11th and 25th October 2008 off the northwest coast of Africa, in the vicinity of the Canary Islands, onboard the RRS Discovery (research cruise D333 - Figure 5.1).
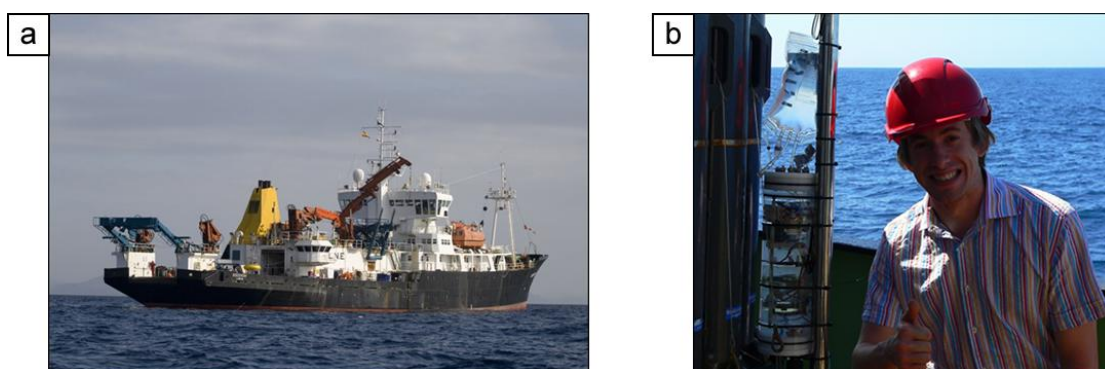
Figure 5.1a & b – Picture of the a) RRS Discovery on the trial cruise and b) the Mk II sensor and author before deployment.

The section is split into two parts. The first covers the design, construction, and setup of the first prototype sensor (Mk I) and how it was taken from a laboratory bench system to a standalone device. Preliminary bench top tests conducted prior to deployment are also included. The second section covers the design, construction, and setup of a second prototype sensor (Mk II). It focuses on the improvements made over and above the first prototype. Results are presented from bench top tests and three successful deployments (casts) on a rosette frame to a maximum depth of 1518m.

5.1   Reagent preparation

The reagent used for the detection of nitrite (based on the Tovar et al [92] variant Griess reaction, presented in Section 2.4.1.1) was comprised of 0.06M sulfanilamide, 2M HCl, and 0.05% N-(1-napthyl)ethlenediamine dihydrochloride, all sourced from Fisher Scientific Uk. It was prepared in 200ml batches by mixing together; 2 grams of sulfanilamide dissolved in 35ml of concentrated HCl and 65ml of deionised water; and 0.1 gram of N.E.D. dissolved in 100ml of deionised water.

Exposure of the reagent to light and reagent ageing (>1month) results in a shift in the baseline absorption measurement (an increase in the absorption for a 0µM nitrite sample). However as this was a short deployment and the natural light at depth was minimal it was not necessary to consider this.

5.2   Mk I sensor

The electronics on the Mk I sensor suffered a severe failure during the first cast leading to the construction of a Mk II sensor. Significant lessons were learnt from the construction of the Mk I sensor and preliminary data gained so it is therefore included within this report. Its construction forms the blueprint for the Mk II sensor, and is broken down into three sections covering fluid delivery, electronics, and packaging. The dual spectrophotometer L.O.C. device and optical detection systems are based on those presented in Section 4.3 (stage III bench top prototype sensor).

5.2.1   Fluid delivery

Fluid delivery is a key aspect in maintaining the accuracy and precision of the sensor (Section 2.2), therefore every effort in the design of the fluid delivery system has been made to reduce; oscillation; variations in flow rates; and 'dead volume' (the benefits of which where identified in stage I, II and III). A high level schematic of the fluidics is shown in Figure 5.2a and described in further detail below. In addition, one of the key elements of fluid delivery that wasn't considered in stages I, II and III was the filtration of the seawater. As such, the design and test of a filter is also included in this section to facilitate the operation of the sensor *in situ*.

Three 500ml blood bags (constructed of an inert FEP material and stored 0.5m above the sensor) were used to store reagent (as per Section 5.1), and two calibrated seawater solutions (0 and 25µM nitrite). The blood bags were connected to 0.3mm Internal Diameter (I.D.) tubing (TTTA3201643A) by Luer Lock to ¼ inch 28 UNF connectors and 062 minstac connectors. The sample (seawater) is filtered through a replaceable 300 copper mesh (50µm hole width, with a mesh diameter of 3.05mm) contained within a P.E.E.K. housing (Section 5.2.1.1), and enters the sensor housing (together with the reagent and two standards) through an end cap (via 062 minstac and ¼ 28UNF adapters). The layouts of these connections are shown in Figure 5.2b.
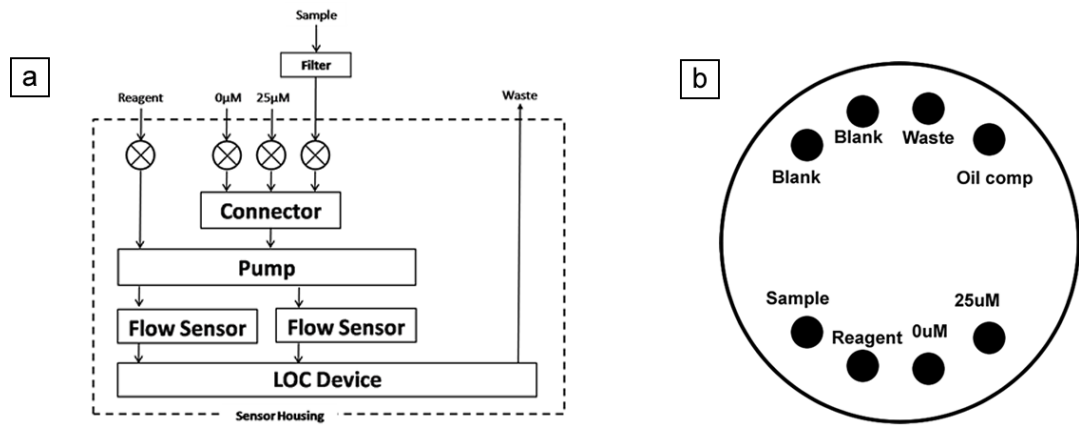
Figure 5.2a & b – Diagrams illustrating a) a high level schematic of the fluid handling systems within the sensor package and b) the layout of the inlets / outlets in the end cap.

Inside the sensor housing the seawater, the 0μM and 25μM inlets are each connected to 2 way valves (Lee Minstac 2 way micro inert valve). The layout of the valves is shown in Figure 5.3. These valves allow the flow of each fluid stream to be completely stopped. They are controlled via a switched 12V output from the data logger board (see Section 5.2.1.1). The fluid output of each valve is connected to a 5 way junction. One entrance of this junction is blocked off with a blanking plug and the other is connected to a pump. The reagent is also connected to a 2 way valve and then directly into a different channel of the same pump.
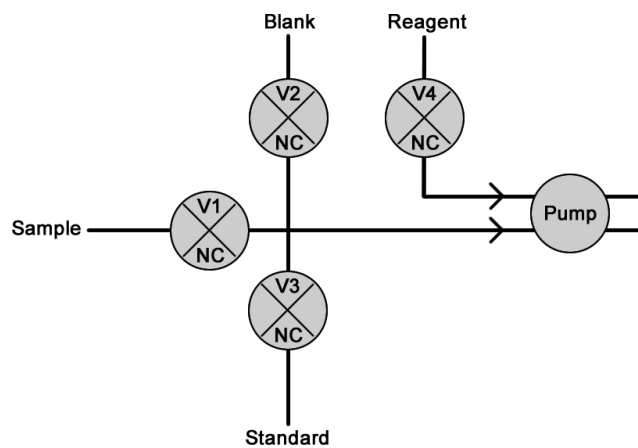
Figure 5.3 – A diagram showing the valve setup and position in the fluid systems, where NC equals normally closed.

The use of 2 way valves, compared with 3 ways, minimises the dead volume (33μl total compared with 450μl total internal volume) and hence minimum sample volume. The total volume of the fluidic pathways in the valves (33μl), pump (39.3μl) L.O.C. device (15.75μl) and the flow sensors (30μl) is 118.05μl. The two way valves also allow a complete stop of the flow. On sample change

this volume has to be replaced by the new sample before a measurement can take place. The volume of new sample to replace the old is larger than the total volume due to sample carry over effects (as illustrated in Section 4.2.13). The purpose of the valve setup is to allow the seawater sample inlet fluid stream to be switched between two known concentrations of nitrite or nitrate used to calibrate the sensor *in situ*. The calibration increases the precision and accuracy of the sensor data. Once deployed the valves are controlled through a preset program to allow calibration during long casts. A state diagram of the program can be found in Appendix 8.4.1. The timings for the valves, pump and data collection were set for each cast.

The performance criteria required of an *in situ* pump for the sensor (pressure compensated, capable of operating in oil, small or no oscillations, as identified in Section 2.2) necessitates a custom solution as no off the shelf pump is available. The pumping setups presented in stage I (size limitations), II (not feasible) and III (pump unable to operate in oil) have not been able to fulfil the criteria set down. Therefore a peristaltic pump was constructed from a stepper motor (Mclennan ID31-004), gearbox (250:1) and custom fabricated roller and body. The pump pulls the fluid from the inlets and pushes it through the L.O.C. device. This setup reduces the variability of inlet flow rates (as presented in Section 4.3.3.1) caused by changes in the orientation of the sensor or height difference between the sample containers. It removes the reliance on the hydrostatic resistance to set the mixing ratio between the sample and reagent. Hence it improves sensor precision. Placing the pump between the L.O.C. device and sample inlets increases the volume by 39.3μl due to the length of tubing required inside the pump. The cyclic flow rate profile over time through the L.O.C. device using this pump is shown in Figure 5.4.
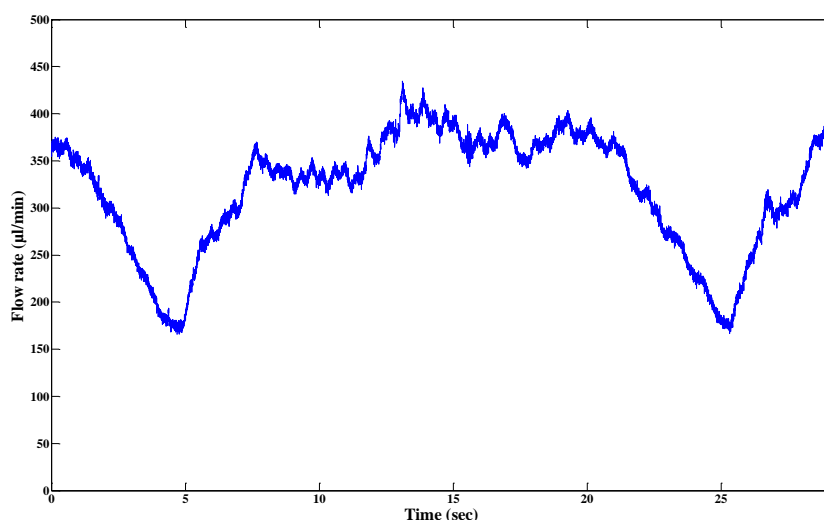
Figure 5.4 – Graph of the flow rate over time of fluid through the L.O.C. device in the sensor. The cyclic nature of the peristaltic pump can be identified but is significantly reduced when compared other pumps (Section 4.1.1.1).

This fluctuating profile is not ideal for high sensitivity but as the only pump suitable and available it was unavoidable. It should be noted that for future work that a smoother profile is preferable and will achieve more consistent mixing and absorption levels.

The flow rates of the reagent and the 0μM, 25μM nitrite or the seawater samples were measured using two OEM micro flow sensors (Sensiron LG16-1000A) whose analogue outputs (2.5V – 5V) are linearly proportional to the flow rate. These voltage outputs were logged. After exiting the flow sensors fluids enter the L.O.C. device through their respective inlets. The waste output from the L.O.C. device is piped to a blood bag (1000ml) that acts as the waste (0.5m below the sensor). The path length of the waste output has no effect on the minimum sample volume as the absorption measurement has already taken place. Although it increases the pressure drop across the fluidics positioning the waste output beneath the sensor can reduce the load on the pump (i.e. siphoning caused by hydrostatic pressure). This will not be possible in future deployment scenarios due to space and orientation issues. However once a suitable pump has been developed it will no longer be necessary.

5.2.1.1 Filter characterisation

To ensure the continued operation of the sensor during *in situ* deployments it was necessary to have a filter on the sea water sample inlet. The filter reduces the quantity and size of particulates and biological matter that would otherwise flow through the sensor and hence decreases the risk of blockages and the amount of biofilm growth (as reported in Section 2.2.17). Over time particulates become trapped in a filter decreasing the flow rate due to increased pressure resistance and can eventually cause a totally blockage. This section details the experiments conducted to determine the length of time that the filter remains usable in an ocean environment. The filter should be suitable for an *in situ* deployment lasting up to 8 hours. Longer deployments will require filter maintenance and mechanical cleaning. This section covers the design of the filter and the experiments carried out to test its suitability for an *in situ* environment and that it was capable of lasting up to 8 hours during *in situ* deployment.

The filter developed in this report (see Figure 5.5a) is a combination of a copper mesh grid and P.E.E.K. holder (both resistant to biofouling). The replaceable 50μm copper mesh (SPI Supplies) is held inside a P.E.E.K. holder (pictured in Figure 5.5b) and allows fluid to enter the sensor whilst restricting the entry of particulates or debris. It is possible to fabricate the 50μm mesh in house using a highly accurate P.C.B. mill (L.P.K.F. ProtoMat S100) however it is cheaper (£2 per mesh compared with £15) and quicker to purchase it pre-fabricated. The mesh is fabricated in copper as the material is resilient to biofilm growth.
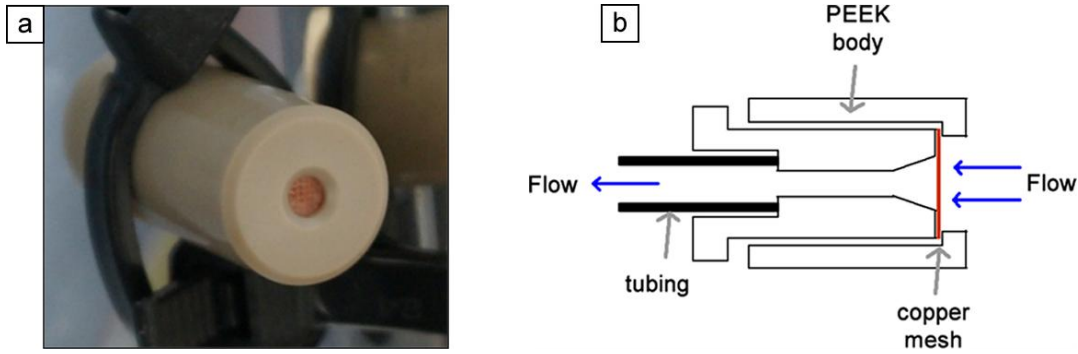
Figure 5.5a & b – a) Picture of the filter and b) an illustration of its design showing the fluid flow direction through the copper mesh and into tubing connected to the sensor.

5.2.1.1.1 Experimental setup

The experimental setup (illustrated in Figure 5.6) was designed to provide a constant pressure head (due to gravity) and not be reliant on a pump. If a pump were to draw the liquid through the filter then when the flow resistance increased (i.e. the filter starts the block) it would try to maintain a constant flow rate and increase the pressure (and require more power). Relying on a gravity feed isolates the performance of the filter from that of the pump.
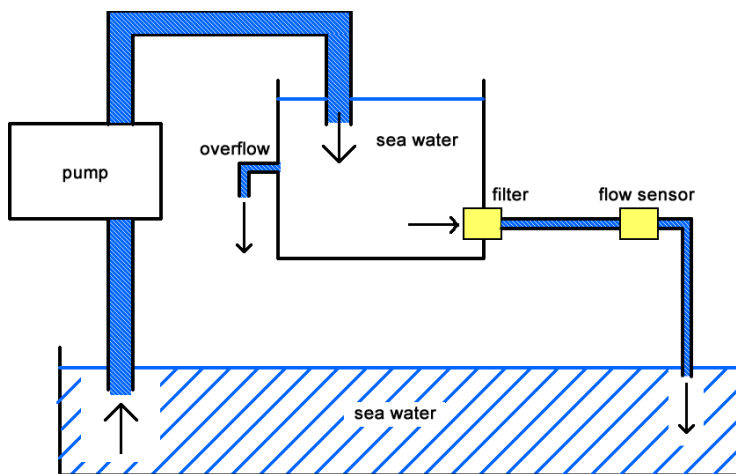
Figure 5.6 – The experimental setup used to determine the length of time the filter would remain useable in an in situ ocean deployment.

5.2.1.1.2 Filter lifetime

Two experiments were conducted. The first measured the flow rate of seawater (collected from Southampton docks) through the filter over 4 hrs to calculate the M.T.T.F. (mean time to failure). The flow rate was measured using a Sensirion flow sensor whose voltage outputs are directly

proportional to the flow rate (previously calibrated in Section 4.1.1). A National Instruments USB DAQ (NI USB-6009) logging at a sample rate of 100Hz is used to record the results. Figure 5.7 shows the results.
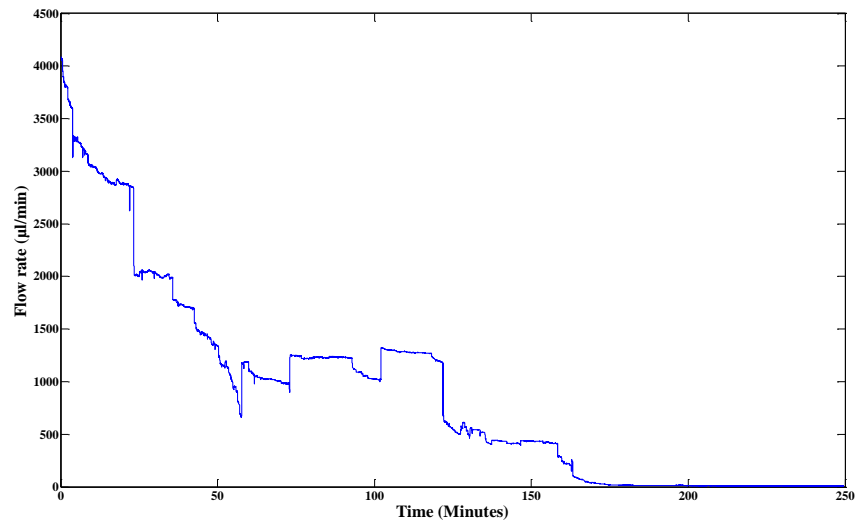
Figure 5.7 – Graph of flow rate against time for continuous seawater flow through the filter. The flow rate falls to zero after 2hrs 45minutes.

The flow rate decreased (at an average rate of 24.25μl/min per minute) to zero after 2 hours 45 minutes. It can be seen that as particles block the mesh there is a sudden drop in flow rate. Equally particles can become entrapped and then become free raising the flow rate. To increase the lifetime of a filter it is possible to back flush water through it (reverse fluid flow, Figure 5.8) to remove some of the particles trapped in the mesh.
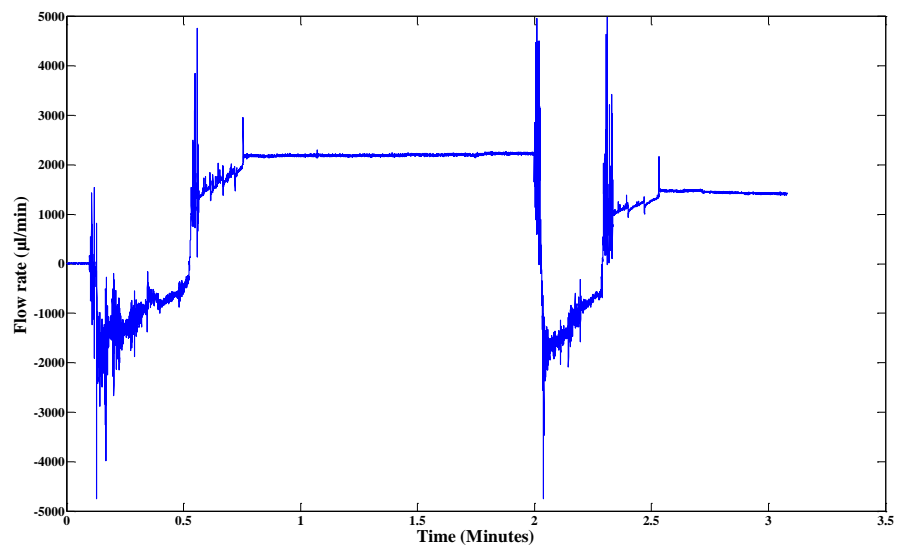
Figure 5.8– Graph showing two back flushing cycles with reverse flow over a total period of 200 seconds.

The second experiment measured the flow rate through the filter over 1 hour, 15 minutes with a periodical back flush cycle. The results are shown in Figure 5.8 and show a significant increase in filter lifetime. The decrease in flow rate over time is reduced to virtually zero.
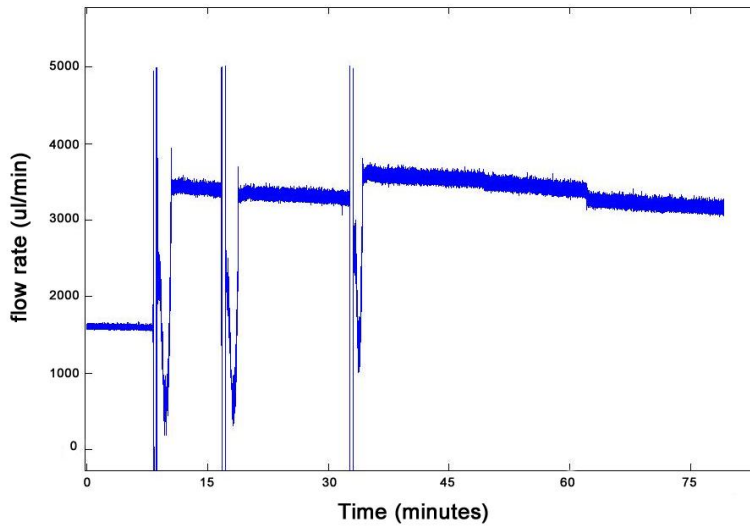
Figure 5.9 – Graph showing the flow rate of seawater through the filter over a 1 hour 15 minutes with three back flush cycles.

Throughout the experiments in this section seawater from a dock area was used. This water can be treated as the worst case scenario due to the high quantity of particulate matter within it (due to frequent shipping activity in the area). As such it is possible to use the experimental results to predict the period for which the filter will last during an *in situ* environment such as the ocean.

The filter will be capable of lasting for an indefinite period with back flushing every 5 to 10 minutes. Without back flushing the filter would only last 180 minutes before complete failure. Given that a typical deployment length is 4 to 8 hours during C.T.D. deployment the filter was deemed suitable for preliminary trials. For longer deployments further tests will need to be carried out to determine its suitability.

5.2.2 Electronics

The overall electronic design is shown in Figure 5.10. This drives the optical components (e.g. L.E.D. and photodiode), powers the flow sensors and logs data. The schematic is expanded upon in the text below from the battery inwards, describing the function of each part and its basic operating parameters.
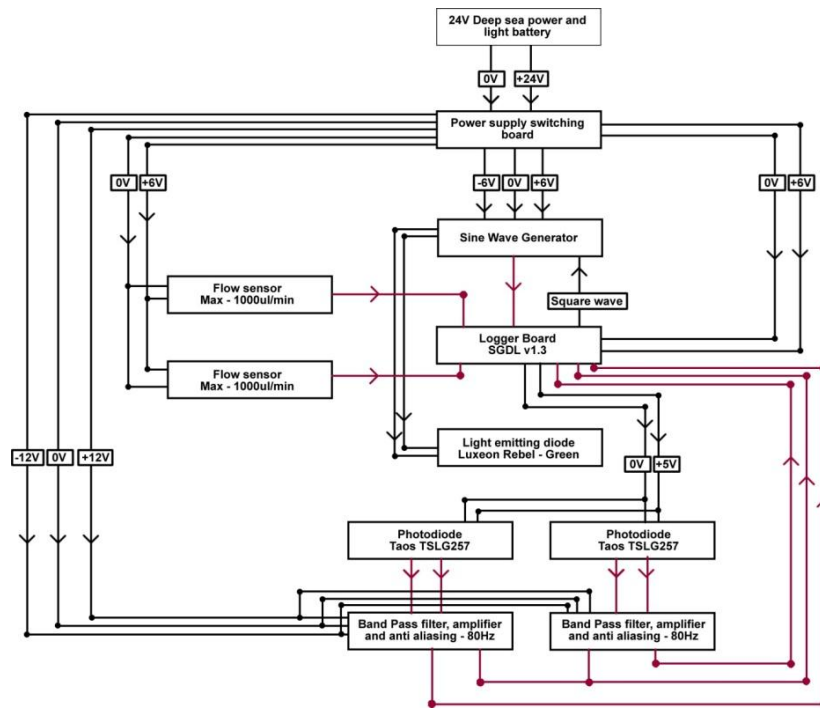
Figure 5.10 – The diagram shows a high level schematic of the electronics for the MkI sensor. The voltage supplies are coloured black and the data flows, red.

The power source for the electronics is a 24V (38 amp hours) Deep Sea Power and Light battery. This full ocean depth rated battery acts an abundant supply of power for the sensor and is a piece of proven technology. Using it will remove a potential failure point or error source from the sensor. Power is transported from the battery into the sensor housing, through a 5 pin bulkhead connector, with water proof connectors and leads (Impulse Wet Pluggable). Four pins provide a dual voltage supply and the fifth acts as a mechanical stability pin.

Inside the sensor housing the 24V battery supply is converted into +6, ±6V and ±12V lines by a Traco power supply. The ±12V supplies two bandpass filters, an anti-aliasing circuit and amplifiers. The ±6V supplies a sinewave generator and the +6V supplies two flow sensors and the data logger board. The flow sensor outputs (analogue 2.5-5V) are recorded by a data logger. For this study the sinewave generator [**250**], bandpass filters [**250**], anti-aliasing circuit [**250**], amplifier [**250**] and data logger board [**251**] were built by third parties. The integration and assembly of all the components was carried out by the author.

The sinewave generator outputs a sinusoidal signal (variable 0-3V peak to peak with 0-2.5V variable offset) to the L.E.D. The frequency of the sinewave output is matched to the square wave input from the data logger. The sinewave generator output to the L.E.D. is also logged by the data logger. A sinewave generator is used to provide the sinusoidal signal as the Peripheral

Interface Controller (P.I.C.) processor on the data logger doesn't have enough processing power to generate a smooth wave form.

Each of the two photodiodes (TAOS TSLG257), which contain integrated transimpedance amplifiers, is driven (+5V supply) directly from the data logger board and output an analogue signal between 0 and 5V (dependant on light level). Each photodiode voltage output passes through a band pass filter (centred around 80Hz – Appendix 8.4.2) and anti-aliasing filter. The two voltage channels are amplified (variable gain) and logged by the data logger. The voltage levels on each channel are logged at 960Hz (with a resolution of 0.1mV) onto a 1Gb flash memory M.M.C. (Multimedia Card). Data is read from the card through an rs232 interface (115,200 baud), downloaded to a PC via a HyperTerminal interface and stored as a text file. Thirty six seconds of data recorded by the data logger takes approximately 1 minute to download and is 1mb in size. A maximum of 10 hours of data can be recorded.

Five channels of data are recorded by the data logger; reference signal, detection signal, sinewave generator output, and two flow sensor outputs. Once downloaded the data is converted to voltage by a simple equation (Equation 5.1). Data logging errors often necessitate the correction of the data. This is performed by a Matlab© script which can be found in Appendix 8.5.4.1 and is based on the removal of non numerical data and values larger than those physically possible on the data logger (e.g. >5V or 32768bits).

$$Voltage = Data \times \left(\frac{5}{2^{16}}\right) + 2.5 \qquad \textit{Equation 5.1}$$

For resilience during deployment all electronic connections are made with multi-core wire (to prevent fatigue failure) and soldered to prevent poor connections and oil seeping between contact surfaces.

5.2.3 Packaging

To protect the sensor from seawater and the environment it is packaged into a sealed housing. The housing is formed of five parts, two end caps (Delrin), two rubber o-ring seals and an acrylic tube (Ø110mm x 350mm). The housing is filled with Carnation oil (RS, mineral oil) to transmit the pressure (i.e. so it doesn't require a pressure resistant shell). Under pressure and with cooling the oil contracts by 1% (based on a volume expansion coefficient of 0.00063m^3/m^3/°C and temperature change from 20 to 5°C) and as such an oil expansion compensation port is included in the end cap. This port is connected (via a 0.8mm internal diameter tube) to an oil filled blood bag which acts as a bladder.

To ensure that the sensitive electronics (specifically the data logger and flow sensors) are pressure resistant they are potted in hard epoxy. The epoxy creates a hard shell that resists the pressure and stops oil being absorbed into the fibre glass circuit boards.
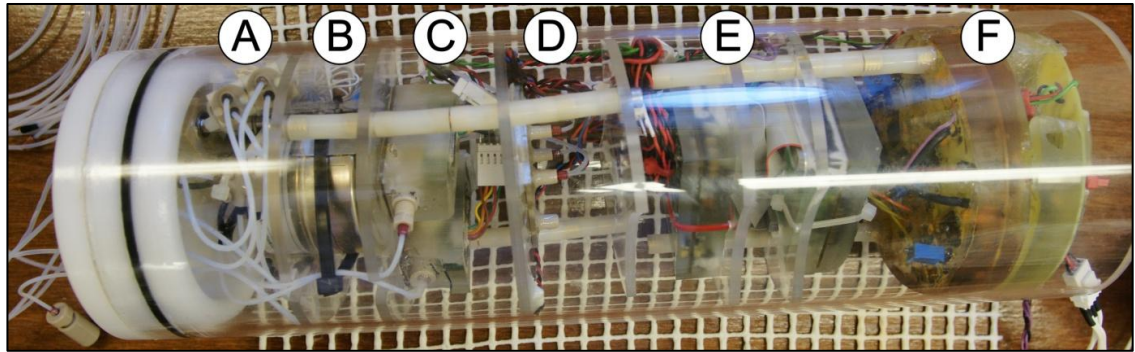
Figure 5.11 – A picture of the Mk I sensor, where A is the valves, B is the pump, C is the flow sensors, D is the L.O.C. device, E is the data logger and driver board and F is the analogue electronics.

5.2.4   On bench calibration

This section details the bench top calibrations and functionality tests conducted on the Mk I sensor before its *in situ* deployment. To confirm that the electronics were functioning correctly a frequency spectrum of the output of the sinewave generator (one of the channels logged) was generated (Figure 5.12). The peak frequency, excluding those close to 0Hz, was calculated to be 82.284Hz.
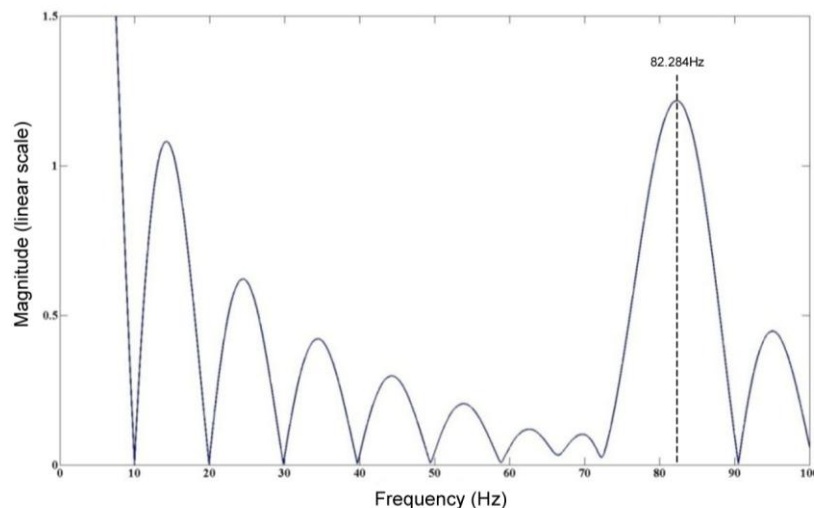
Figure 5.12 – Graph of the frequency spectrum of the 80Hz output from the sinewave generator into the L.E.D, with a peak at 82.284Hz.

Whilst a peak is present at 82.284Hz multiple smaller peaks are present above and below. These are associated with the sin wave generator and complimentary electronics. They should not cause an issue as the bandpass filter was adjusted to match and reject the maximum amount of noise.

Confirmation that all channels were being recorded was also sought. The five channels shown in Figure 5.13 (reference, signal, sinewave output, flow sensor 1 and flow sensor 2) show a sample of data that was recorded. The 80Hz signals can be identified as the thick bands of colour (green, red and blue).
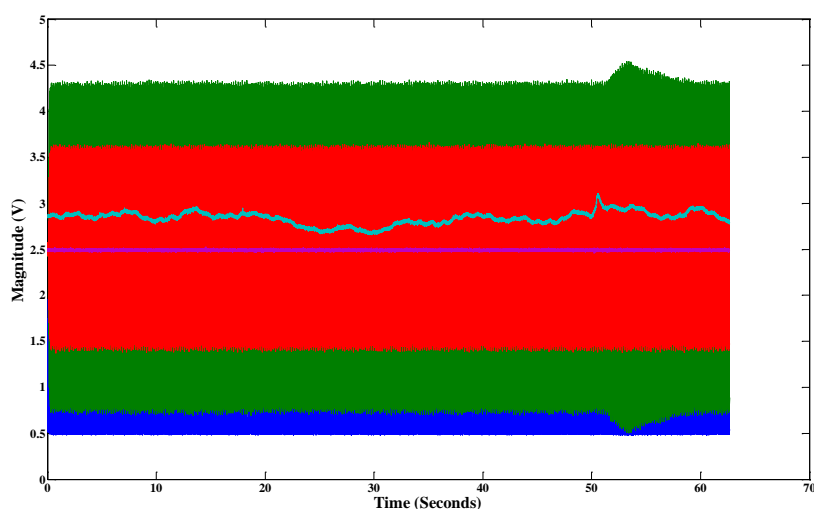
Figure 5.13 – Graph showing voltage against time for all five channels being recorded by the data logger in the Mk I sensor.

The sensor was calibrated by switching the sample inlet between two different concentrations (0 and 100μM) of nitrite in artificial seawater. For each measurement the sample was pumped at 305μl/min (4,000 μs per pulse) for 10 minutes, to ensure no sample carry over, and then at 85μl/min (13,000 μs per pulse) for 5 minutes, to allow for flow rate stabilisation, before a reading (20 seconds) was taken. The over flushing was required to ensure that the performance (i.e. precision) sensor was isolated from the response time (caused by the large fluidic volume in the sample path prior to the L.O.C. device).

The experiment was repeated three times using the same sample sources. Table 5.1 shows the results of the experiments after the data has been filtered to remove high frequencies and the average (1 seconds moving) peak to peak magnitude has been calculated.

Run no.	Nitrite concentration (μM)	Reference magnitude (V)	Signal magnitude (V)	Reference Standard Deviation (3σ)	Signal Standard Deviation (3σ)
1a	0	0.6630	3.4431	0.1779	0.0282
1b	100	0.6740	2.5071	0.1473	0.1323
2a	0	0.6817	3.3021	0.2571	0.0363
2b	100	0.6753	2.6277	0.1977	0.0357
3a	0	0.6997	3.5013	0.1902	0.0342
3b	100	0.6569	2.5744	0.1770	0.0183

Table 5.1 – Nitrite concentrations listed by run number and the resulting reference and signal magnitude, along with their standard deviations.

The average change in voltage between 0 and 100μM is 0.832V, which leads to a sensitivity of 0.00832 Volts per μM (or approximately 8mV). At 100μM the standard deviation (3σ) is 0.0621V (average over the three runs) which translates to 7.46μM. The average standard deviation of the reference channel is an order of magnitude higher than that of the signal. This high standard deviation can be attributed to contamination or high levels of optical or electronic noise in that channel.

The power requirements of the sensor during the bench top test, whilst fully operational, were 7.2W (at 24V). The high power consumption of the sensor is due to the analogue electronics (e.g. the power supply convertor, amplifiers and filters). The L.E.D's and photodiodes account for 0.2W.

5.2.5 *In situ* deployment

The first *in situ* deployment (Cast 001) of the Mk I sensor was on the 21st October at 0906 GMT at station number 16464H. It was deployed to depth of 300m for 2 hours. The depth measurements are from the base of the frame to the sea surface. Details of the deployment location, time and ocean depth can be found in Table 5.2. The timings for the valves, pump and data collection used in the preset data logger program can be found in Appendix 8.4.3.

Stage of deployment	Time (GMT)	Latitude	Longitude	Water depth (m)
In Water	0906	27º 56. 904N	014º 12. 417W	1854
At Bottom	1010	27º 56. 418N	014º 13. 025W	1833
On Deck	1232	27º 55. 543N	014º 15. 138W	1825

Table 5.2 – The details of the Mk I sensor in situ deployment. The latitude and longitude are those of the RRS Discovery Research vessel, and the water depth is the distance from the vessel to the ocean floor.

For deployment the sensor was attached to a rosette frame (≈Ø2m) along with twenty four, 10 litre, Niskin sample bottles. Figure 5.14a & b show the Mk I sensor attached to the rosette frame and being deployed into the ocean. Additional instrumentation was also attached to the rosette frame including a SBE43 Oxygen, CTG Fluorometer, CTG transmissometer, Wetlabs light back scatter, and C.T.D.
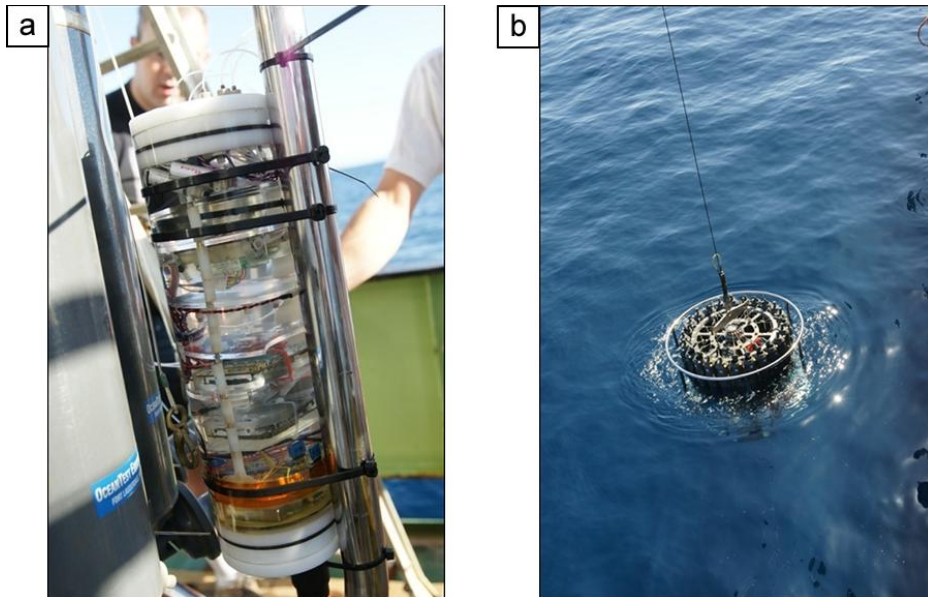
Figure 5.14a & b – Picture showing a)the main Mk I sensor housing attached to the C.T.D. frame before deployment and, b) the C.T.D. frame and sensor being deployed in to the Atlantic ocean.

The first fifteen minutes of the deployment were spent at 3m to allow pressure compensation to begin and air to be purged. The frame then descended to 300m. At 140 minutes the rosette frame ascended and was loaded back onto the vessel.

On retrieval the sensor was found to have failed and a small quantity of water (3-5ml) was present within the housing. The overheating of the electronics (Traco ±6V power convertor) had caused a power surge and was responsible for the short circuiting and disabling of the data logging systems, two micro flow sensors, and the analogue L.E.D. drive, photodiode amplification and filter circuitry. Water ingress was attributed to an insufficient flow of oil between the sensor housing and the pressure compensation bladder. The narrow bore of the fluidic connectors (0.8mm diameter) reduced the velocity of the oil flowing between the compensating bladder and the sensor housing creating a reduced pressure in the housing. The resulting pressure differential across the housing caused water to be drawn in between the seals of the end caps.

5.2.6 Summary of design issues

It was found that neither the L.O.C. device (including oil filled waveguides and L.E.D. fibre inserts) or the fluidic connections to it had failed during deployment. Therefore the failure points can be highlighted as the ancillary components. The design issues encountered with these ancillary components during the deployment of the Mk I sensor were noted as a basis for improvement on the Mk II sensor. A summary of these issues is found below:

- Removal of information from the data logger requires the sensor to be dismantled and oil drained from the housing

- Once filled with oil the end caps are difficult to insert into the acrylic tube.

- The power consumption of the sensor is high (7.2W) due to the large quantity of analogue electronics (notably the power convertor).

- There was insufficient flow of oil between main sensor housing and pressure compensation bladder.

- The fluid flow oscillated flow due to the peristaltic pump (alternative pump not available).

5.3 Mk II sensor

Following the failure of the Mk I sensor a Mk II sensor was built (shown in Figure 5.15) using simplified electronics and an improved pressure compensation system. No band pass filtration or amplification was integrated into the design, larger bore and shorter connections were used on the pressure compensation system, and a RS232 communications port was added into an end cap. To ensure any electronic faults or short circuits did not propagate a custom fabricated, pressure resistant fuse (700mA) was placed inline with the battery connection. The 80Hz sinewave previously generated by analogue electronics was replaced by an 80Hz square wave produced directly by the data logger.
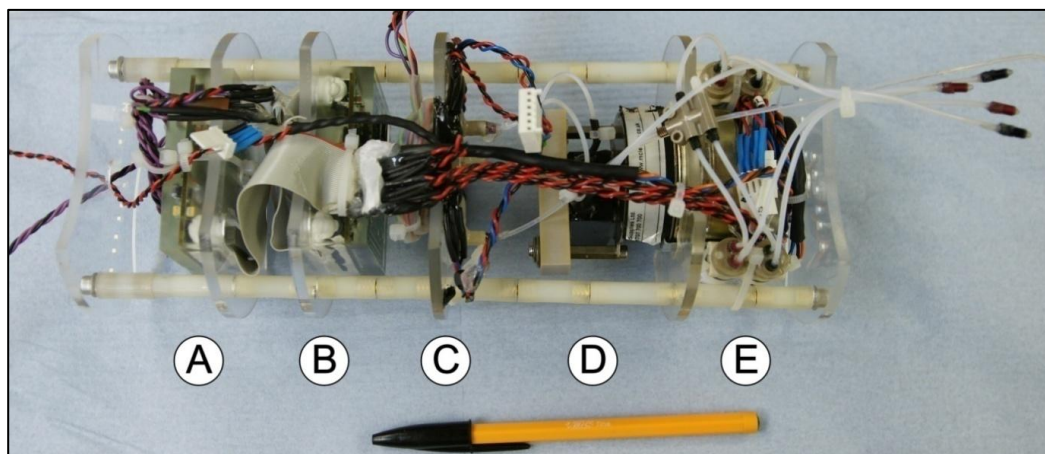
Figure 5.15 – A picture of the Mk II sensor without the protective housing where A is the main data logger processor board, B is the data logger driver board, C is the L.O.C. device, D is the pump, and E is the valves.

As the flow sensors were removed it was no longer necessary for the data logger to record their voltage level output. It was also not necessary to record the output of the sinewave generator. Therefore the number of channels recorded by the data logger was decreased from five to two (channel 1, reference and channel 2, signal). The reduction in the number of components (12 to 8) has three benefits. Firstly the sampling frequency can be increased from 960Hz to 1960Hz. Secondly the length of the sensor decreases to 300mm and thirdly the power consumption of the sensor drops from 7.2W to 1.4W (24V).

Due to the low nitrite levels (<1μM) in the location the Mk II sensor was due to be deployed in, it was converted to measure nitrate which is present at higher concentrations (0-15uM). The conversion entails adding a small (20mm length by 10mm diameter) packed cadmium column to the fluid path. This cadmium column was attached directly to the seawater sample filter using narrow bore tubing. The fluid was then taken directly into the sensor housing, as presented in Figure 5.16.
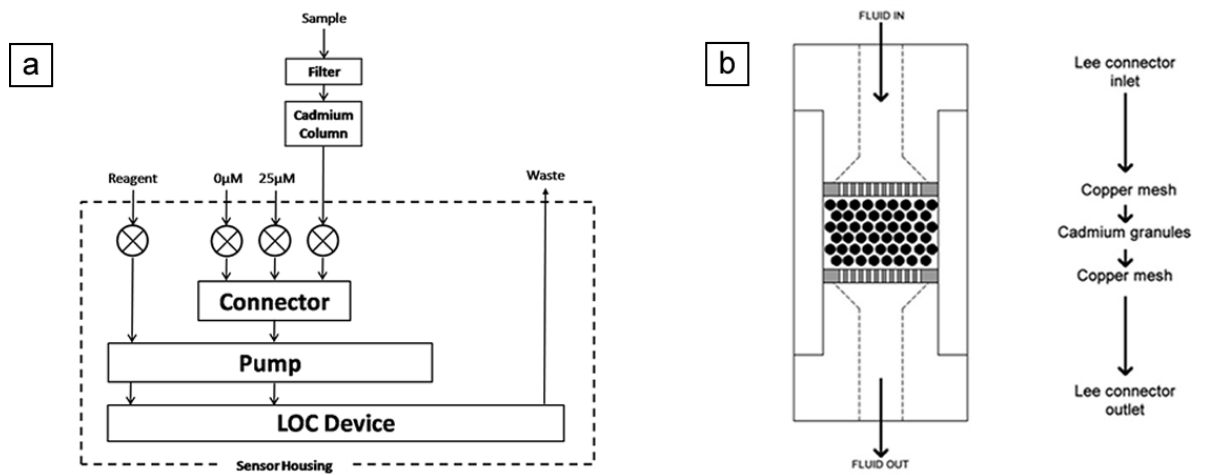
Figure 5.16a & b – Illustrations of the a) Mk II sensor fluid handling systems within the sensor and, b) the cadmium column.

5.3.1 On bench calibration

As with the Mk I sensor, the functionality of the Mk II was tested on the bench before it was deployed. A basic calibration of the sensor was also performed.

In addition to the functionality testing (e.g. testing valve, pump and data logger operation) a spectrum analysis (F.F.T.) was performed on a sample of reference and signal channel data recorded by the data logger. This provided confirmation that the 80Hz square wave was being outputted to the L.E.D. and received by the photodiodes. Data was recorded over 120 seconds with water in both reference and signal fluid paths. The graph of the F.F.T. (see Figure 5.17) shows a clear peak at 80.4299Hz with several orders of magnitude difference between the noise and the signal. The greater the difference between the 80Hz peak and noise, the greater rejection of external noise (i.e. 50Hz mains). This was a significant improvement on the similar unfiltered F.F.T. of the signal from the Mk I sinewave generator (see Figure 5.12).
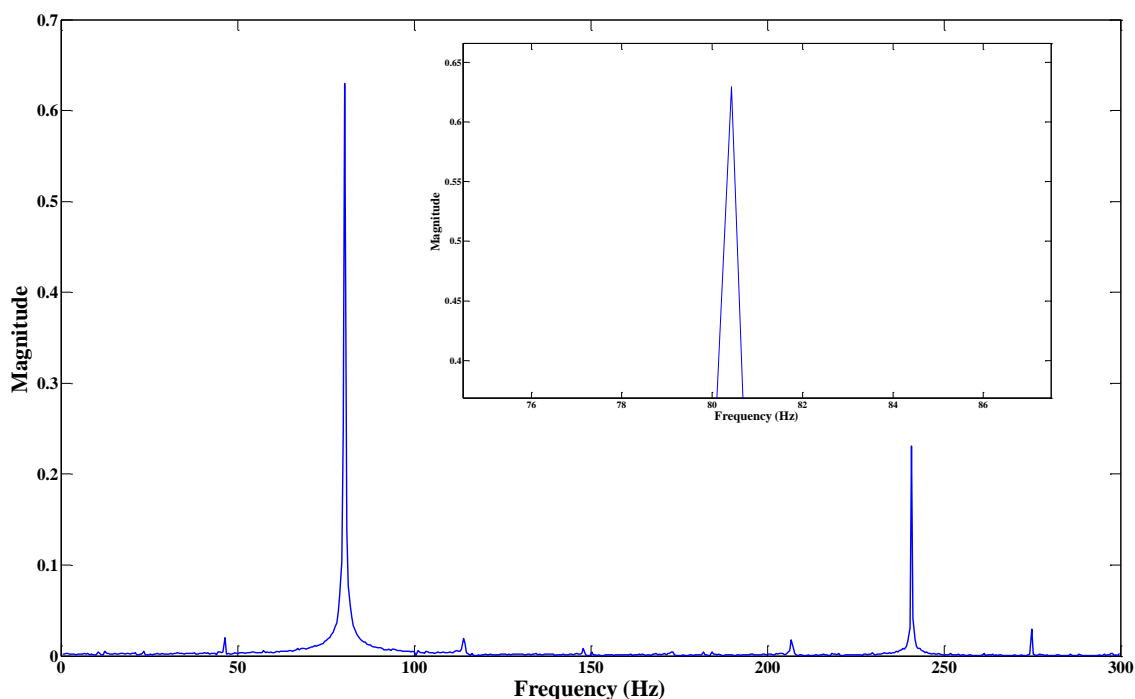
Figure 5.17 – Graph showing the frequency spectrum of a 120 second sample of data, and a peak centred at 80.4299Hz

The calibration of the Mk II sensor was conducted by switching between the seawater sample inlet (connected to a container of 25μM nitrate) and the blank inlet (0μM). Each sample was pumped for 360 seconds at a pump speed of 85.43μl/min (4000μs per pulse) before a 60 second sample of data was recorded. Once again the over flushing (approximately five times the fluidic volume of the sample path length of 88.05μl) was used to ensure that the performance of the sensor (i.e. precision) was isolated from the response time caused by the fluidic delay.

To remove non numerical data and non possible values (e.g. >5V) the data is filtered using a Matlab© script (see Appendix 8.5.4.1). A software bandpass filter centred at 80Hz (see Appendix 8.5.4.2) was used to remove any noise, before the peak to peak amplitude was calculated and a 1 second moving average (See Appendix 8.5.4.3) applied. The reference values are subtracted from the signal values to remove any interference and allow the data to be converted into a single, interpretable, line and value. The average magnitude of the signal and its standard deviation over 60 seconds was then calculated. The table below (Table 5.3) shows the results gained from the 0 and 25uM nitrate concentrations

Concentration (μM)	Signal – Reference (Volts)	Standard deviation (3σ)
0	1.5402	0.2556
25	0.0477	0.0150

Table 5.3– Results from the basic Mk II sensor calibration conducted before in situ deployment.

This gives a sensitivity of 0.00597V per μM and a resolution (3σ) at 25μM of 0.398μM. The resolution and sensitivity is improved compared to the Mk I basic calibration tests. This improvement can be attributed to the removal of the analogue electronics and noise introduced by them. The simplified electronics and square wave output to the L.E.D. decreases the amount of post processing needed and harmonics seen in the spectrum analysis of the recorded signal. Increasing the sampling frequency from 960 to 1960Hz has increased the error rate in the data captured by the data logger (e.g. missed or combined values).

5.3.2 *In situ* deployment

The first deployment (Cast 003) of the Mk II sensor (Figure 5.18) was at station number 16470H off the Canary Islands, on the 22nd October 2008. Table 5.4 shows the details of Cast 003 including the position of the ship at each stage, and when the sensor was powered on (e.g. when the preset program activates). The timings for the pump, valve and data recording for the cast can be found in Appendix 8.4.4.

Stage of deployment	Time (GMT)	Latitude	Longitude	Water depth (m)
Sensor Powered On	1330	-	-	-
In Water	1344	27º 58. 594N	014º 02. 699W	1715
At Bottom	1353	27º 58. 566N	014º 05. 916W	1717
On Deck	1448	27º 58. 186N	014º 05. 814W	1730

Table 5.4– Deployment details for Cast 003, where the latitude and longitude is that of the RRS Discovery and the water depth is the vertical distance between the surface and the ocean floor.

The first fifteen minutes of the cast were spent at 3m to allow pressure to start equalising within the sensor and air bubbles to be purged. It was then lowered to a depth of 32m and held in position for 60 minutes.
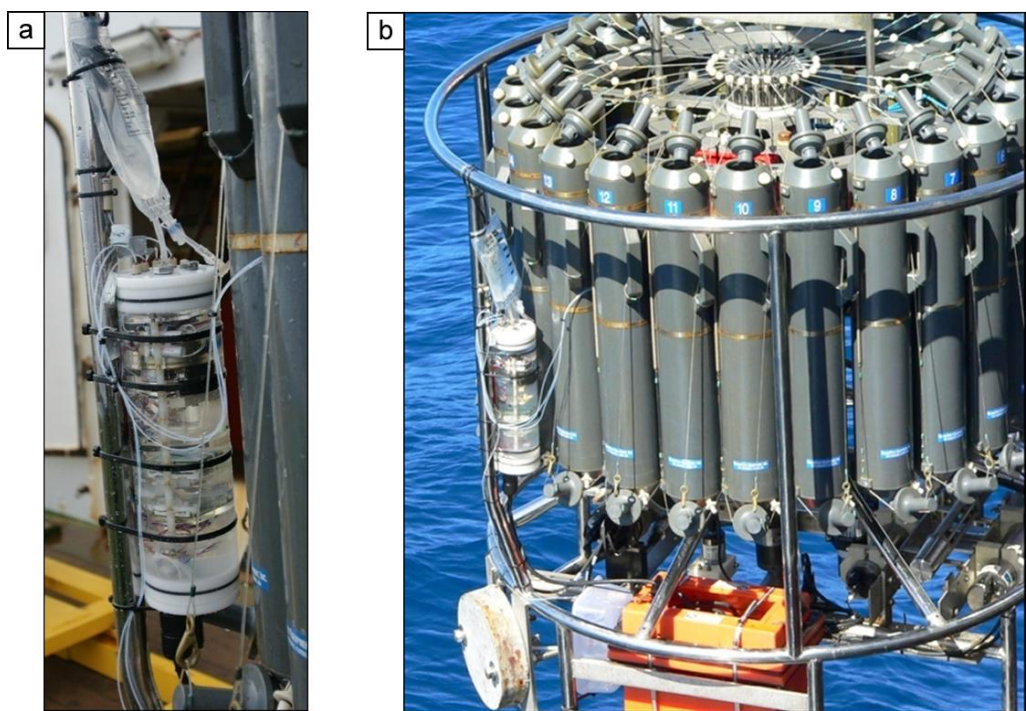
Figure 5.18a & b – Pictures of the Mk II sensor a) attached to the CTD frame with the pressure compensation blood bag directly above and b) being deployed.

On retrieval the sensor was still operating and communicating via RS232, and no water ingress had occurred. It was also noted (through visual inspection) that neither the filter nor the cadmium had been blocked or obstructed by particulates or organic matter. A total of 480 seconds of data over 78 minutes had been recorded. The elapsed time and depth at which each segment of data recorded is shown in Table 5.5 along with the type of sample being analysed. It should be noted that the data recorded does not include waiting time, as the data logger is not recording during these periods.

Time (Seconds)	Time Elapsed (min)	Depth (m)	Stage
0-60	42-43	32	0μM
60-120	50-51	32	25μM
120-180	53:11-54:11	32	seawater
180-240	58:22:59:22	32	seawater
240-300	63:33-64:33	32	seawater
300-360	68:44-69:44	32	seawater
360-420	73:55:74:55	32	seawater
420-end	79:06-80:06	32-0	seawater

Table 5.5 – Data segments recorded for Cast 003 along with the elapsed relative time, depth and sample type being analysed during data recording.

The graph shown in Figure 5.19 is the magnitude (Voltage) of the signal and reference against the time (data recorded) for the entire cast. To interpret the data additional post processing was carried out, in the same manner as in the bench top calibration. A software bandpass filter was used to remove any noise and a one second moving average (Appendix 8.5.4.3) applied. Figure 5.20 shows the data after the post processing.
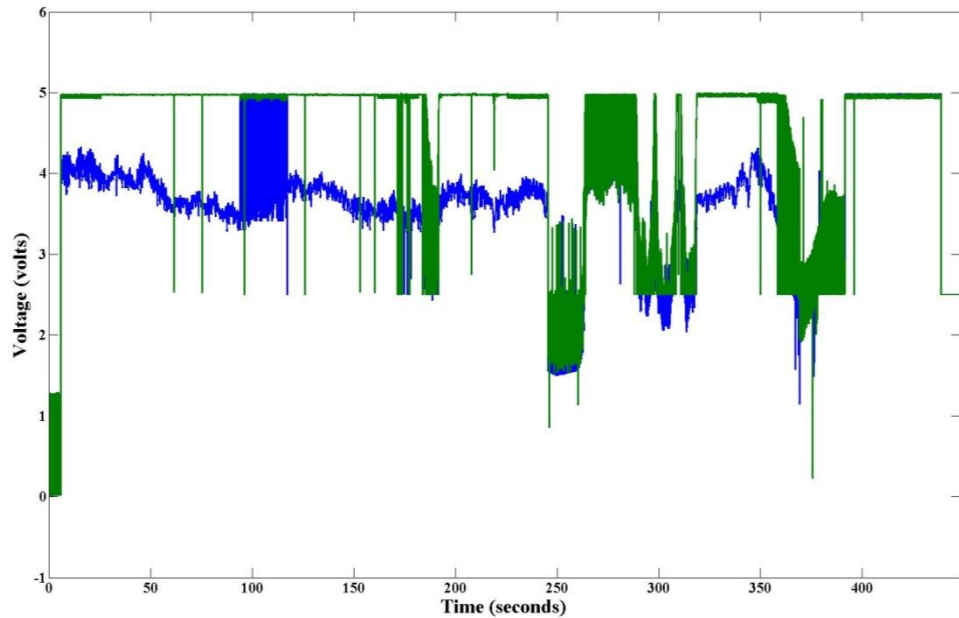
Figure 5.19 – Graph of combined raw data segments for Cast 003 where the blue trace is the reference channel and green is the signal.
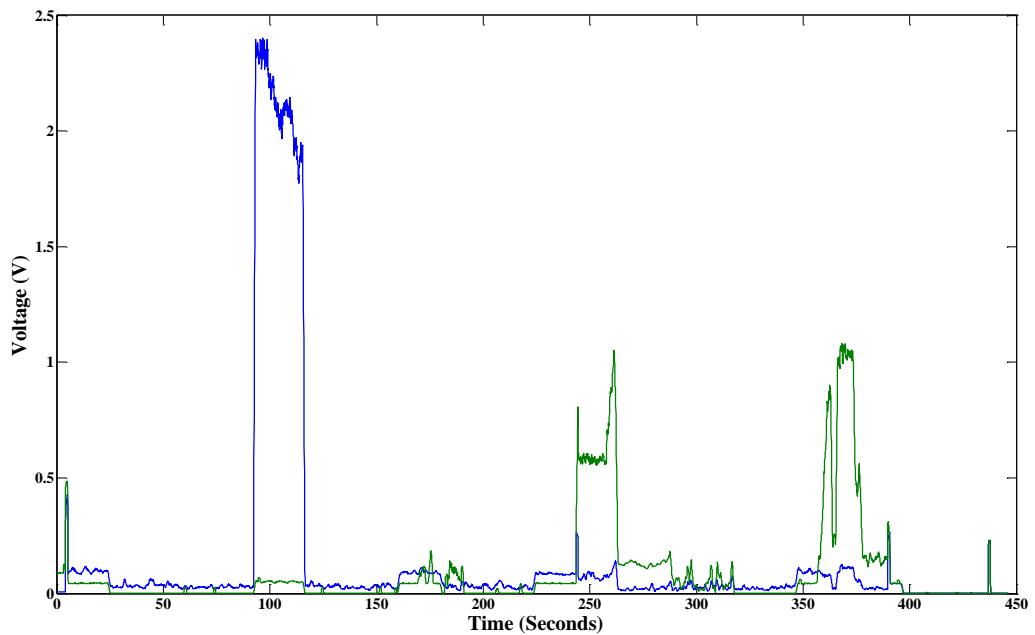
Figure 5.20 – Graph of combined the Cast 003 data after post processing where the blue trace is the reference channel and green is the signal.

It can be seen from the raw data that when the sensor is initially deployed and close to the surface a square wave of 1.2V in amplitude is recorded. However in a short space of time (<10 seconds) the signal channel becomes saturated (>5V). This increase in signal is attributed to an increase in the coupling efficiency between the L.E.D. and fibre and fibre and photodiode. As the photodiode is saturated the magnitude (voltage) in post processed data decreases to zero. Additionally at several points (i.e. at 100, 250 and 380 seconds) the signal and reference channel responses have similar profiles. Although they are of different magnitudes this indicates that there is a common effect. This most probable cause for this effect is a change in the L.E.D. to fibre coupling. To increase the quality of data and remove the saturation issue the intensity of the L.E.D. was decreased for the next deployment. Variation in the reference and signal data could also be attributed to pump oscillations, although without the flow sensors attached (destroyed in the MkI sensor) this is impossible to conclude.

On confirmation of that data had been successfully downloaded after Cast 003, the sensor was launched again (Cast 004) at station number 16471H. This time a depth of 1518m was reached over a total cast length of 2 hours. Table 5.6 shows the details of Cast 004 including the position of the ship at each stage.

Stage of deployment	Time (GMT)	Latitude	Longitude	Water depth (m)
Sensor Powered On	1545	-	-	-
In Water	1557	27º 58. 046N	014º 04. 884W	1745
At Bottom	1647	27º 58. 172N	014º 05. 323W	1743
On Deck	1754	27º 58. 472N	014º 05. 414W	1740

Table 5.6 – Deployment details for Cast 004, where the latitude and longitude is that of the RRS Discovery and the water depth is the distance between the surface and the ocean floor.

To reduce the length of the cast (due to trial cruise time restraints) the time for pumping to change sample (e.g. flush out the previous) was reduced from an average of 420 to 150 seconds. The revised timings for the pump, valve and data recording for the cast can be found in Appendix 8.4.5. An increased winch speed of 45m/min was also used. The elapsed time and depth at which each segment of data recorded is shown in Table 5.7 along with the type of sample being analysed.

Time (Seconds)	Time Elapsed (min)	Depth (m)	Stage
0-60	10-11	0	0μM
60-120	18-19	45-90	25μM
120-180	24-25	315-360	seawater
180-240	30-31	585-630	seawater
240-300	36-37	855-900	seawater
300-360	42-43	1125-1170	seawater
360-420	48-49	1395-1440	seawater
420-480	55:30-56:30	1518	0μM
480-540	63:30-64:30	1518	25μM
540-600	69:30-70:30	1518	seawater
600-660	75:30-76:30	1103-1058	seawater
660-720	81:30-82:30	765-720	seawater
720-780	87:30-88:30	405-360	seawater
780-840	93:30-94:30	45-0	seawater
840-900	101-102	0	0μM
900-960	109-110	0	25μM
960-end	117-end	0	seawater

Table 5.7 – Log of data segments recorded for Cast 004, the elapsed relative time, depth and sample type being analysed during data recording.

Once again, on retrieval, there had been no water ingress, the data had been recorded successfully, and there was no visual evidence of the filter or cadmium column being obstructed by foreign objects. Figure 5.21 shows the combined raw data segments from the cast, where the solid block of colour is the 80Hz square wave.
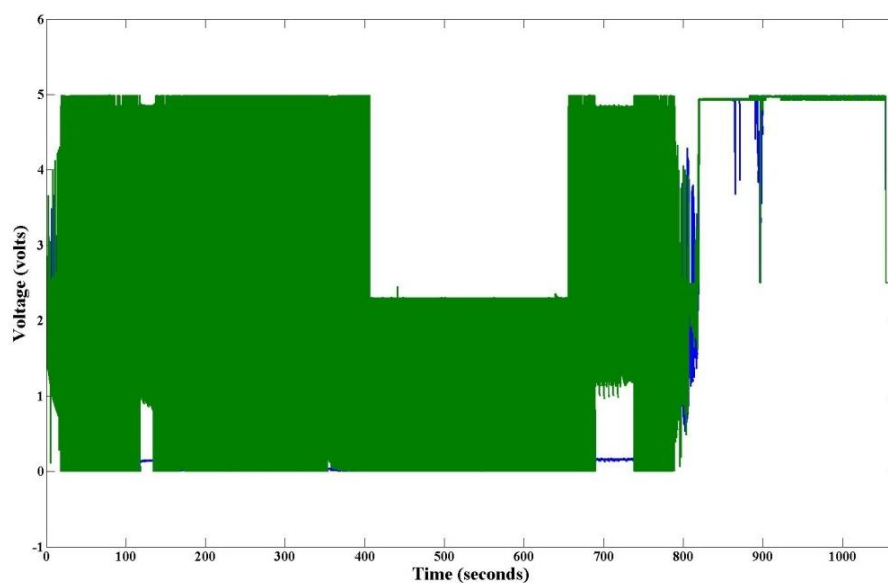
Figure 5.21 – Graph of combined raw data segments for Cast 004 where the blue line is the reference channel and green is the signal.

The last 200 seconds of data is at +5V as the photodiode has become saturated. This is the result of the sensor being winched onto the research vessel whilst data is being recorded and natural daylight hitting the photodiode. The post processed data is shown in Figure 5.22
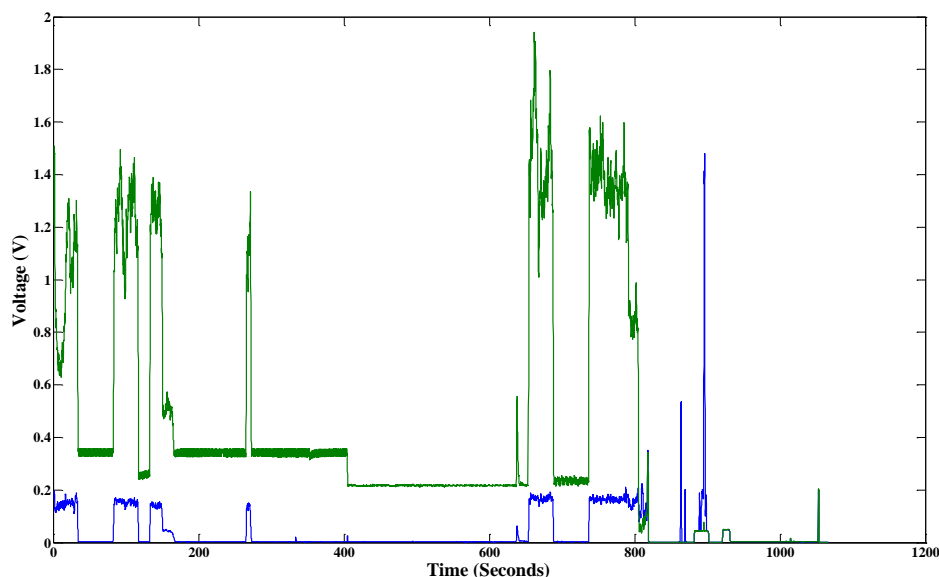
Figure 5.22 – Graph of combined the Cast 004 data after post processing where the blue trace is the reference channel and green is the signal.

The final cast on the 23rd October (Cast 005) was to a depth of 998m at station number 16475H. Table 5.8 shows the details of Cast 005 including the position of the ship at each stage.

Stage of deployment	Time (GMT)	Latitude	Longitude	Water depth (m)
Sensor Powered On	1310	-	-	-
In Water	1314	27º 34. 509N	015º 41. 213W	1609
At Bottom	1416	27º 34. 122N	015º 40. 781W	1711
On Deck	1526	27º 34. 771N	015º 40. 774W	1807

Table 5.8 – Deployment details for Cast 005, where the latitude and longitude is that of the RRS Discovery and the water depth is the distance between the surface and the ocean floor.

The elapsed time and depth at which each segment of data recorded is shown in Table 5.9 along with the type of sample being analysed. The timings for the pump, valve and data recording for the cast can be found in Appendix 8.4.6. On retrieval the sensor data was successfully downloaded and the raw data is shown in Figure 5.23.

Time (Seconds)	Time Elapsed (min)	Depth (m)	Stage
0-60	75:40 – 76:40	997	0μM
60-120	83:40 – 84:40	997	25μM
120-end	91:40 – 120	997-0	seawater

Table 5.9 – Log of data segments recorded for Cast 005, the elapsed relative time, depth and sample type being analysed during data recording.
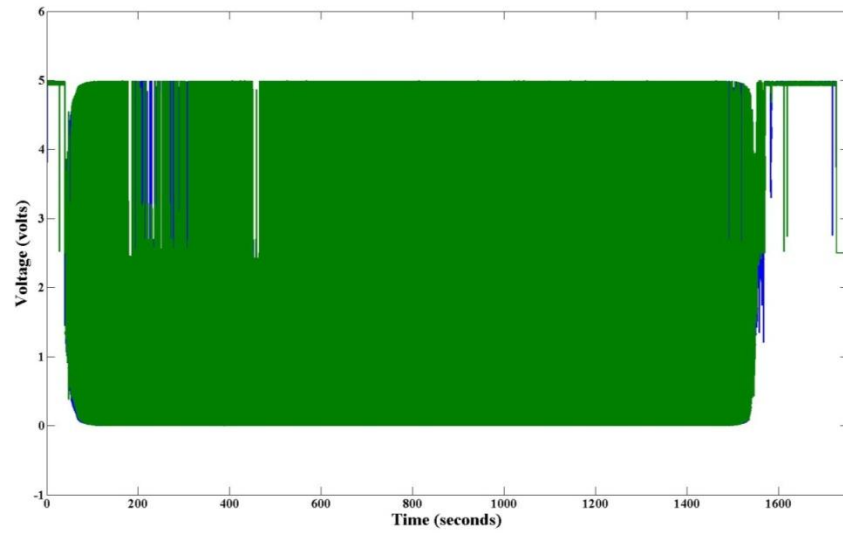
Figure 5.23 – Graph of combined raw data segments for Cast 004 where the blue line is the reference channel and green is the signal.
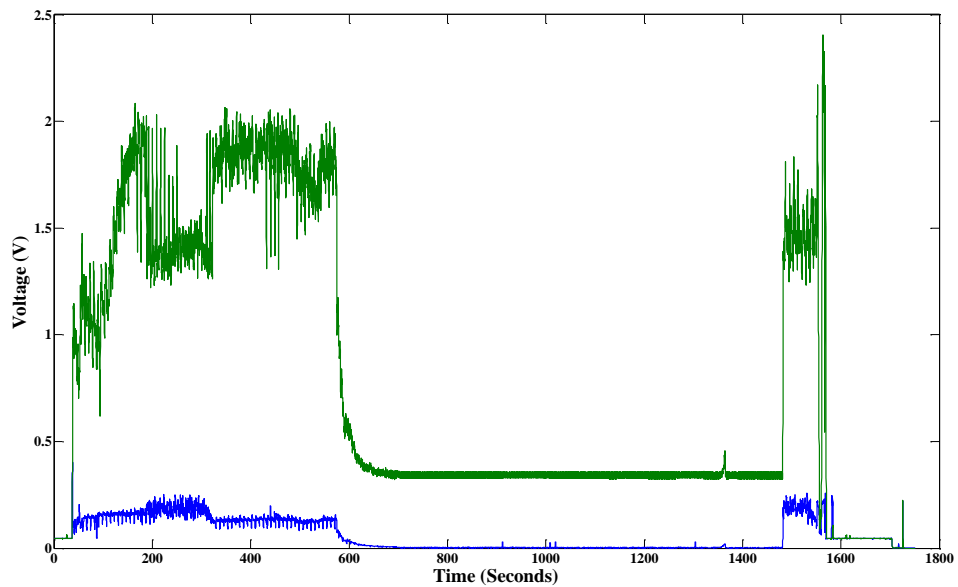
Figure 5.24 - Graph of combined the Cast 005 data after post processing where the blue trace is the reference channel and green is the signal.

The sensor begins to ascend from 997m at 300 seconds into Figure 5.24 and continues ascend for 1329 seconds. The last 100 (one hundred) seconds of data in both Figure 5.21 and Figure 5.23 is saturated due to exposure to ambient light whilst the sensor was still operating and being loaded back on to the RRS Discovery.

With both cast 003 & cast 004 there is cross talk between the signal and reference channels. This is seen when the magnitude of the voltage from a photodiode on one channel decreasing inline with that of another. In addition, and once again the common effect could also result from the failing of the L.E.D. to fibre coupling. The coupling efficiency or a significant change in flow rates could also result in the change in both signal and reference channels between 600 and 1400 seconds.

5.4   Summary

Two bench top calibrations and three *in situ* deployment tests (Figure 5.25) were conducted on the D333 trials cruise. The failure of the first prototype sensor (Mk I) led to the construction of an improved (lower power consumption and smaller size) Mk II sensor. The bench top tests and deployments of both sensors showed the L.O.C. sensor is viable but the associated ancillary components need to be improved before quantitative results are gained during *in situ* deployment.

Figure 5.25 – Picture showing the three in situ deployment locations (Cast 003, Cast 004 and Cast 005), positioned of the coast of Africa and around the Canary Islands.

Bench top tests performed using the Mk I and Mk II gave a sensor sensitivity of 7.46µM and 0.398µM respectively. The improvement in sensitivity was attributed to a simplification of the

absorption measurement electronics, and hence a decrease in noise. The *in situ* tests, although not able to provide a vertical profile of the nitrite or nitrate level in the ocean, provided valuable information on the design and construction improvements required to commercialise the sensor. The *in situ* tests also confirmed that there was no performance degradation in the seawater filter (Section 5.2.1.1) during repeated C.T.D. deployments in oligotrophic water. The successful operation of the L.O.C. sensor at depths of up to 1.5km (approximately 1 mile) also means that it is the world's first deep sea L.O.C. sensor.

Several design issues were highlighted throughout this section of the report. Firstly that the data requires significant analysis to determine the nitrite concentration due to lack of indicators between data segments (e.g. 0μM, 25μM or seawater) and the large quantity of data errors caused by the data logger and stored on the M.M.C. Secondly, for shallow ocean work (<10m) which is of scientific interest the influence of natural daylight is an issue (this could be rectified by using an opaque sensor housing). In addition common mode effects would indicate that there was some form of optical failure at depth. Since this study was conducted this has been associated with partially cured U.V. glue used to increase the coupling efficiency between the polymer fibre and L.O.C. device [240].

6. DETECTION OF OTHER CHEMICALS

There are many other chemicals, apart from nitrite and nitrate, within the water column that are of scientific interest. Three examples that can be detected using spectrophotometric techniques include manganese, phosphate and silicate. Manganese is the most sensitive indicator of hydrothermal activity. Current C.T.D. sampling does not allow scientists to resolve the range, variability or resolution of the manganese concentrations in the plumes [38,252]. Phosphate is an essential macronutrient required for living organisms in terrestrial or aquatic environments. Ecosystems are sensitive to its levels and high levels can lead to eutrophication and low levels limit primary production [253,254]. Silicate or silicon is another essential macronutrient in both the fresh and marine environment. Low levels limit the productivity of diatoms which effect carbon export [255]. It would be of scientific interest to measure the concentration of the three chemicals *in situ* to a higher spatial and temporal resolution than is currently possible

The basic detection principles for these three chemicals and the L.O.C. device schematic setup necessary are covered in this chapter. An optimised, 2nd generation, L.O.C. dark field mask design is also proposed for the detection of the each of the chemicals.

6.1   Basic detection principles

6.1.1   Manganese

Manganese is detected using the solubilisation method of Watanabe (1974). The sample is mixed (ratio of 5.3:1) with a solution of 1-(2-pyridylazo)-2-naphtholor (PAN), Triton X100, sodium hydroxide, boric acid and an iron-specific cheating agent desferrioxamine B (used to suppress interference from iron) [256]. The absorption of the solution at 560nm is proportional to the concentration of manganese. The L.O.C. device setup necessary for the process is shown in Figure 6.1.
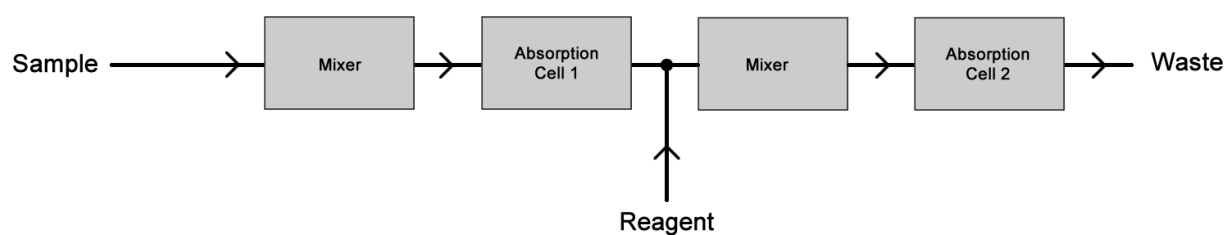
Figure 6.1 – Schematic diagram of the L.O.C. device setup for the detection of Manganese, where the reagent is a solution of 1-(2-pyridylazo)-2-naphthol or (PAN), Triton X100, sodium hydroxide, boric acid and desferrioxamine B.

6.1.2   Phosphate

A 12-molybdophosphate acid is formed in the reaction between phosphate in a sea water sample and an ammonium molybdate solution (acidic pH=1.0) in the presence of potassium antimony tartrate. The 12-molybdophosphate acid is reduced by ascorbic acid to a phosphomolybdenum blue complex [257]. The absorption of the resulting solution at 710nm is proportional to the concentration of phosphate. The L.O.C. device setup necessary for the process is shown in Figure 6.2.
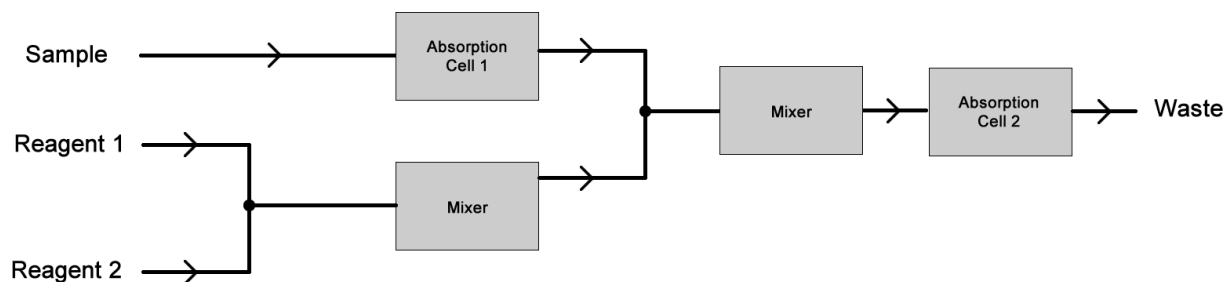
Figure 6.2 – Schematic diagram of the L.O.C. device setup for the detection phosphate, where reagent 1 is a solution of ammonium molybdate and potassium antimonyl tartrate and sulphuric acid, and reagent 2 is ascorbic acid.

6.1.3   Silicate

Silicate can be detected using a method based on the reaction of silicate with ammonium molybdate to form a yellow silicomolybdate complex. It is then reduced to silicomolybdenum blue by ascorbic acid [258]. The absorption of the solution at either 660 or 800nm is proportional to the concentration of silicate. The L.O.C. device setup necessary for the process is shown in Figure 6.3.
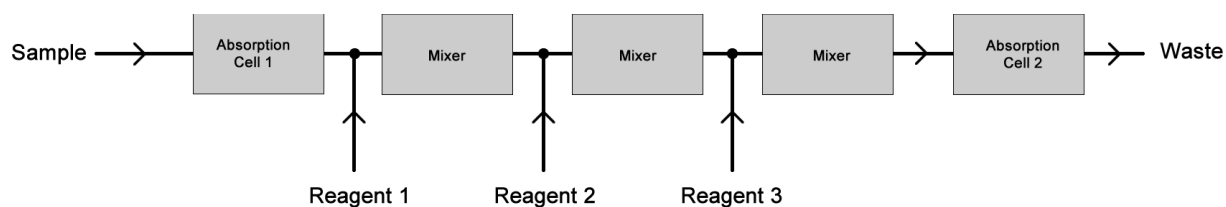
Figure 6.3 – Schematic diagram of the L.O.C. device setup for the detection of silicate, where reagent 1 is an ammonium molybdate solution, reagent 2 is Oxalic acid and reagent 3 is Ascorbic acid.

6.2 Second generation L.O.C. device

Although the Mk II sensor is capable of detecting all these chemicals, the configuration would not be optimal (e.g. long fluid path lengths and order of mixers in fluid path). A longer path length is also required for the detection of Manganese due to it's the low absorption ($44000 \, l \, mol^{-1} \, cm^{-1}$) and low concentration (0.2nM to 4.5x10-6nM). Therefore a 2nd generation L.O.C. device is proposed in this section. Four variants have been designed for future use, the first a configurable design (using jumpers between inlets) is capable of being used to detect nitrite, nitrate, silicate, phosphate and manganese. The second, third and fourth, are each capable of detecting a single chemical and hence optimised to have minimum fluid path lengths to reduce smearing and the minimum sample volume.

The configurable chemical analyser (C.C.A., Figure 6.4), has been designed with either 2 or 5cm absoption call path lengths. The channels are 250μm in width and height with a minimum wall thickness of 250μm. Depending on the configuration microbore tubing can link the inlet ports, which are spaced to allow the use of the fluid connectors used in previous chapters of this report where required. The L.O.C. device has a total footprint of 60 x 60mm comparable to that of the data logger.
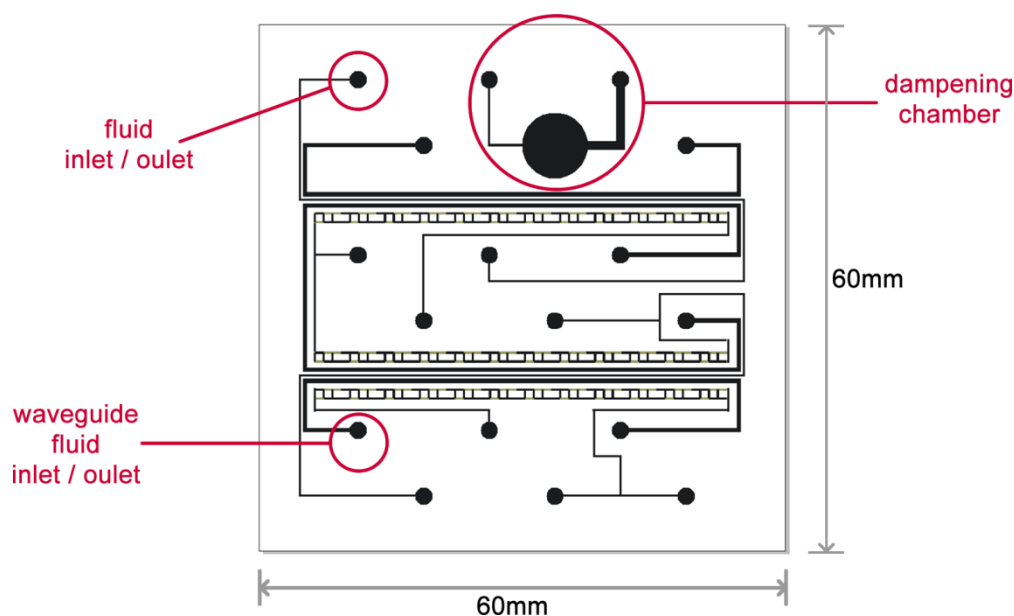
Figure 6.4 – The configurable chemical analyser with two 5cm absorption path lengths, 3 mixer stages and a dampening chamber to reduce oscillation when pumping.

The chemical specific versions of the 2nd generation device (see Figure 6.5) are designed to minimise dead volumes, and path lengths when the fluid is not being mixed (i.e. reduce

smearing). The fibre channels were adapted to push the fibre into the same position within the gap on each insertion. These variants are also designed to decrease the footprint of the device and allow more to be fabricated per glass wafer (e.g. lower the fabrication cost per device).
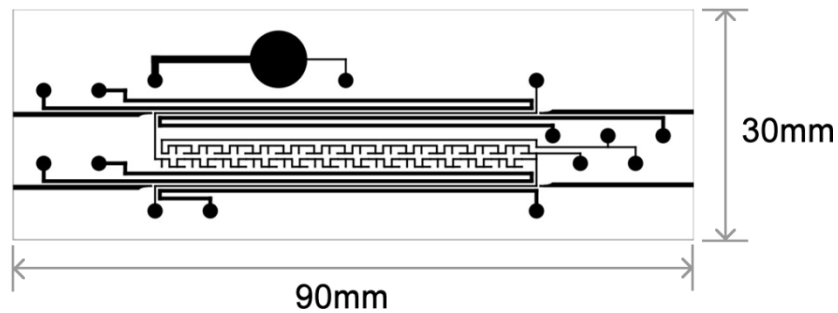
Figure 6.5 – Diagram showing the dark field mask for phosphate specific version of the 2nd generation L.O.C. device.

6.3   Summary

Although significant design improvements are achieved with the 2nd generation designs it is outside the scope of this report to progress them any further. However the suitability of the mask designs for manufacture was confirmed and this report suggests that the next step would be to batch manufacture the devices for testing and comparison. The Philips Luxeon Rebel L.E.D. is available in 5nm intervals between 440 to 645nm so would also be suitable for use in the detection of all chemicals mentioned apart from phosphate.

7. CONCLUSION

The viability of colourmetic spectrophotometric detection of nitrite and nitrate has been proven on a microscale and at a depth of up to 1.5km *in situ* during ocean deployment. A dual channel spectrophotometric L.O.C. sensor was able to detect nanomolar (L.O.D. of <100nM) concentrations of nitrite and low micromolar (L.O.D. <3.8μM) concentrations of nitrate in a laboratory environment. Whilst only diagnostic data was retrievable from the *in situ* deployments the sensor package was capable of detecting nanomolar concentrations of nitrate (≈398nM resolution) whilst on board the research vessel. In summary this study has developed a device that progresses scientific understanding of measuring nitrite concentration on a microscale *in situ* and can help improve the quality and quantity of data available. At the early stage and without the development of ancillary components the sensor is already able to match and exceed the performance of some commercial spectrophotometers reviewed earlier in this report (see Section 2.5)

The study identifies the scientific and commercial reasons to develop a L.O.C. chemical sensor and the impact change in nitrite, nitrate and ammonium changes can have on the environment and human health. It also provides evidence as to the novelty of such a device in the world to date. To provide a building block for future work and assess the suitability of any device for an *in situ* environment key performance drivers were set out. These drivers set the scope for this study.

To enable the technology readiness level [31] of the sensor to improve this study has identified key areas of technology that development effort should be the focused upon in the future. It is suggested that a 'design freeze' be enforced on the L.O.C. device to allow the development and performance comparison of new ancillary microscale components (such as pumps and value) to be conducted. The large impact of pump and valve characteristics on the sensitivity, precision and accuracy has been highlighted through this study. It will be vital for any future device that the interfaces between these components are examined.

Finally the overriding conclusion is that there is a need to develop ancillary components (i.e. pump and valves) that are of a similar scale and reliability whilst being capable of operating in the ocean. Whilst this study has developed low cost and robust optics and L.O.C. devices with integrated mixing it has been shown that the flow control of micro litres of fluid in a reliable manner is of key importance in creating a reliable sensor capable of detecting ultra-low concentrations of nitrite or nitrate. Further work is also required on the pumping scheme to reduce delay, flushing time and response times.

8. APPENDIX

8.1 Fabrication using fluoropolymers

8.1.1 Fluorescence measurement data

8.1.1.1 Spectra of Fluorescein
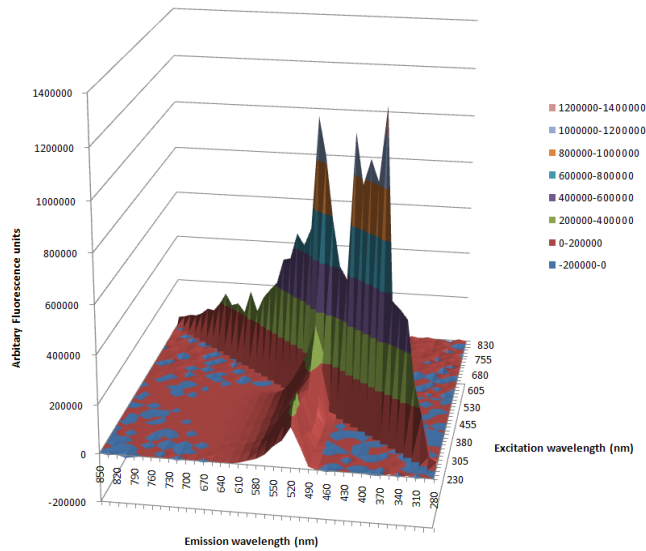
8.1.1.2 Spectra of P.T.F.E.

8.1.1.2.1 Untreated
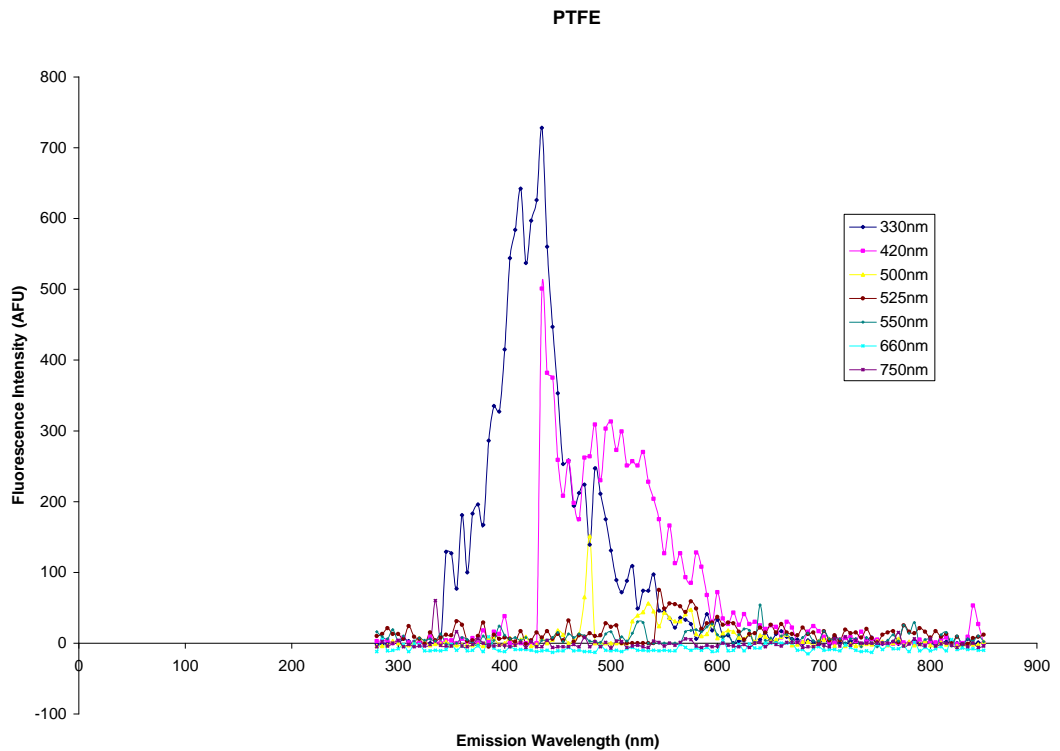
8.1.1.2.2   Treated with uncured epoxy laminate

Fluoroscence Intensity of Etched PTFE & Uncured Epoxy
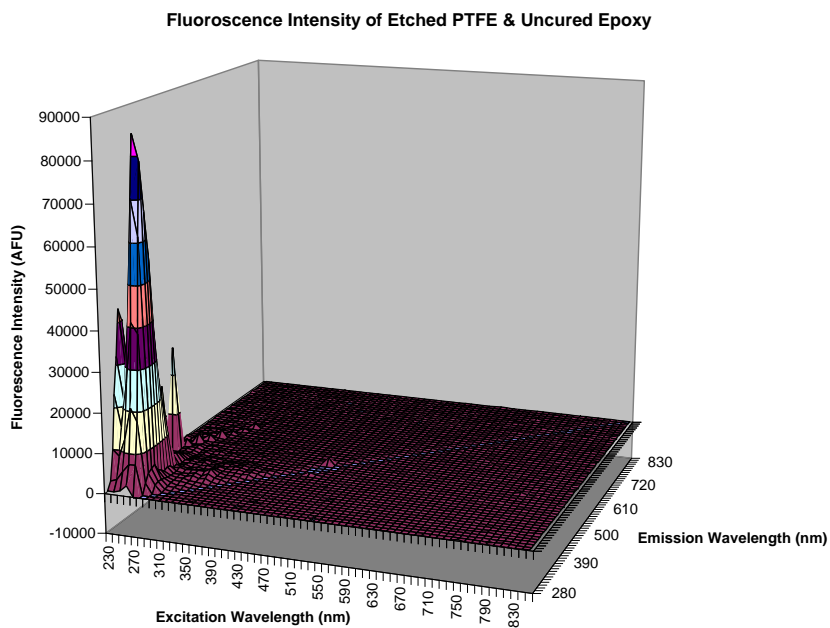
8.1.1.2.3   Treated With cured epoxy laminate

Fluoroscence Intensity of Etched PTFE & Cured Epoxy
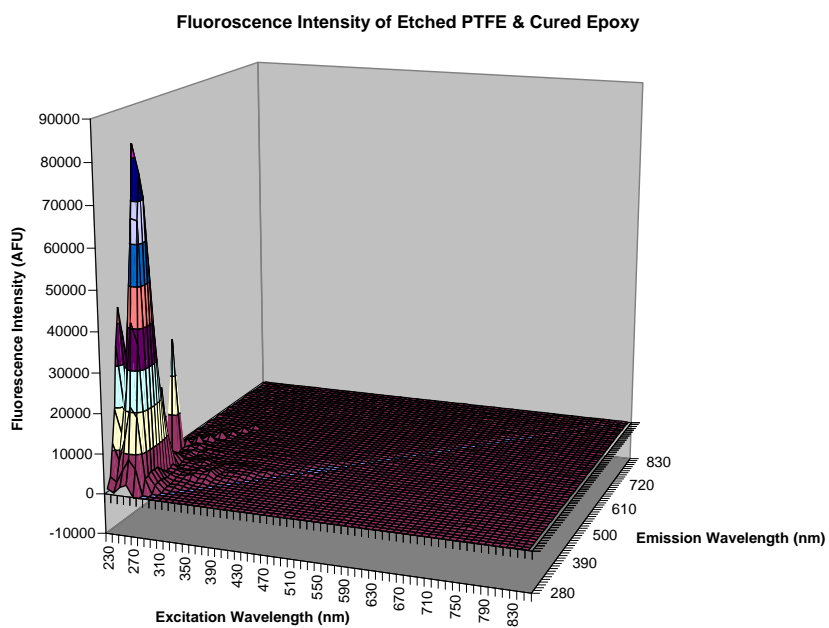
8.1.1.3 Spectra of P.C.T.F.E.

PCTFE

8.1.1.3.1 With uncured epoxy laminate

Fluoroscence Intensity of Etched PCTFE & Uncured Epoxy

8.1.1.3.2 With cured epoxy laminate

Fluoroscence Intensity of Etched PCTFE & Cured Epoxy
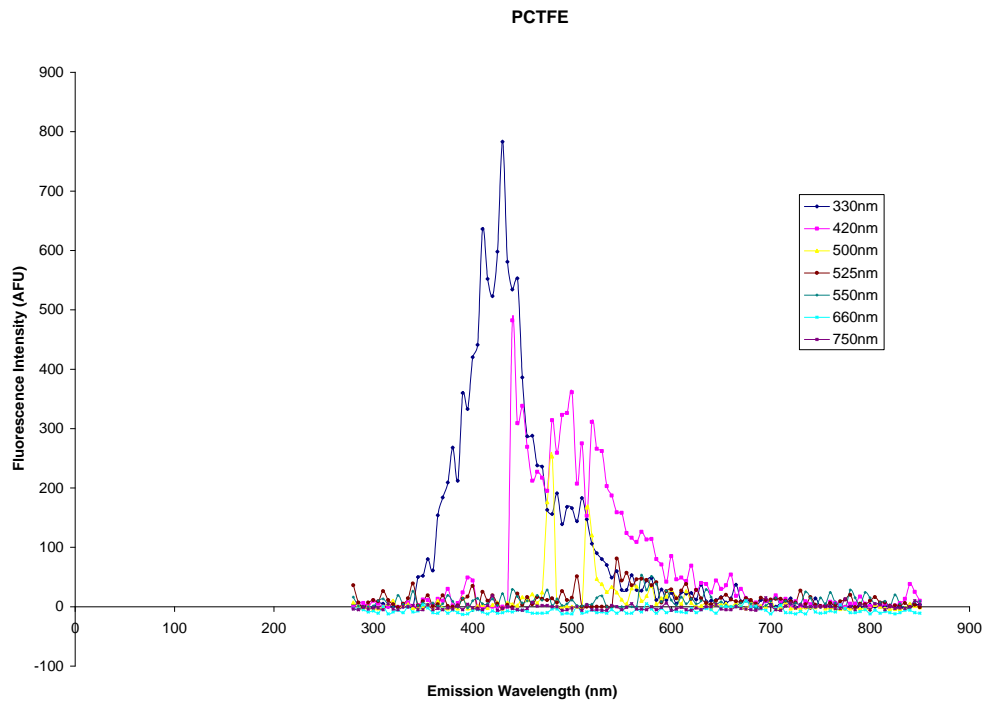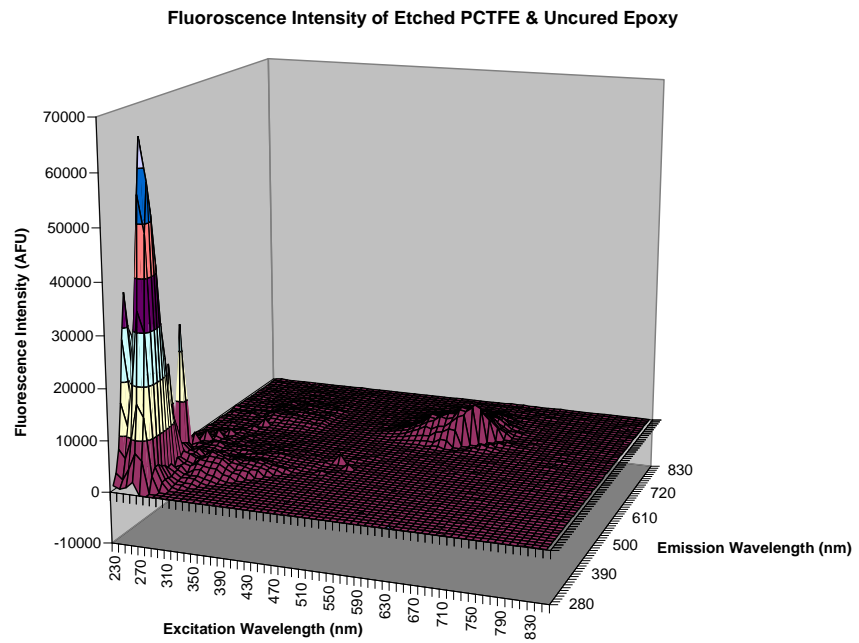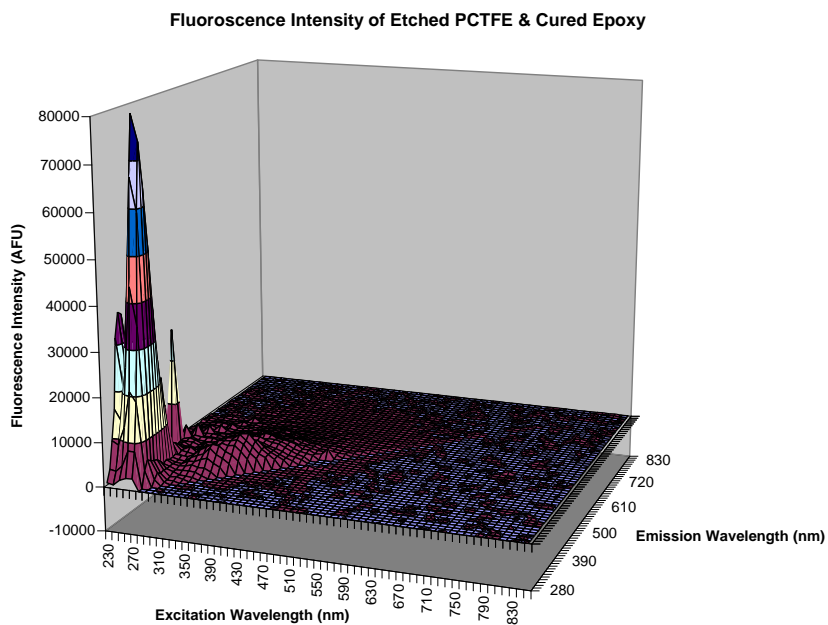
8.1.1.4 Spectra of F.E.P.

8.1.1.4.1 Untreated

FEP

8.1.1.4.2 With uncured epoxy laminate

Fluoroscence Intensity of Etched FEP & Uncured Epoxy

8.1.1.4.3 With cured epoxy laminate

Fluoroscence Intensity of Etched FEP & Cured Epoxy
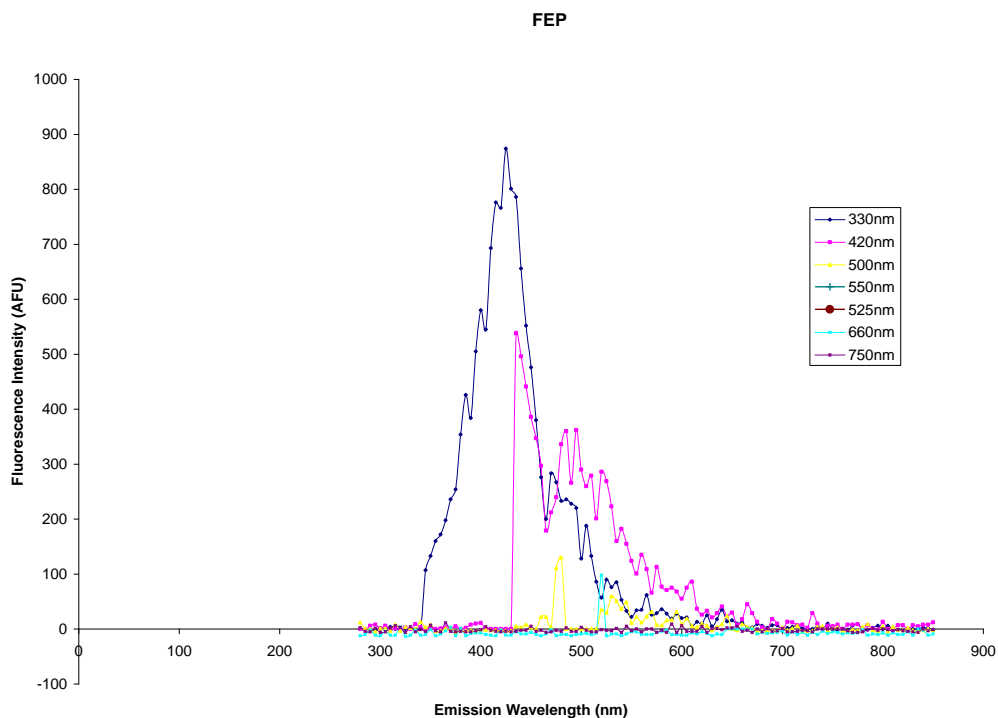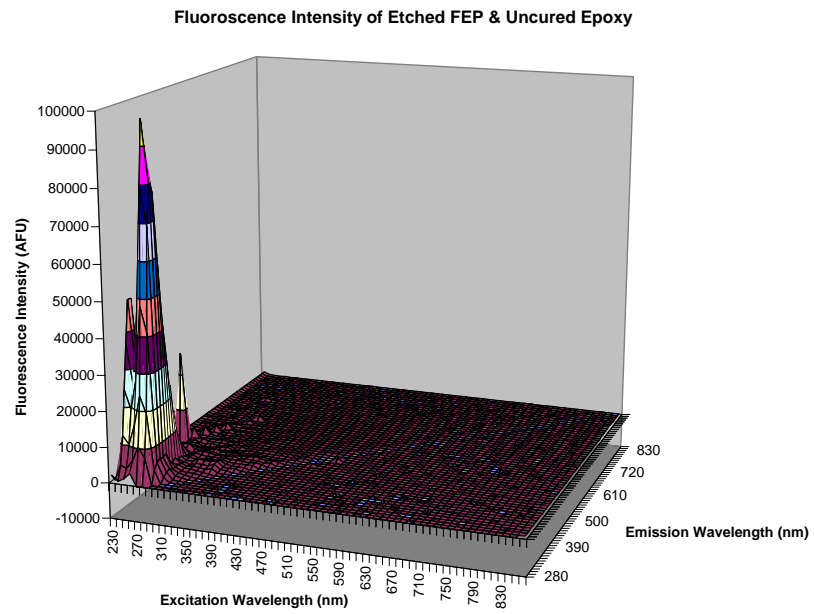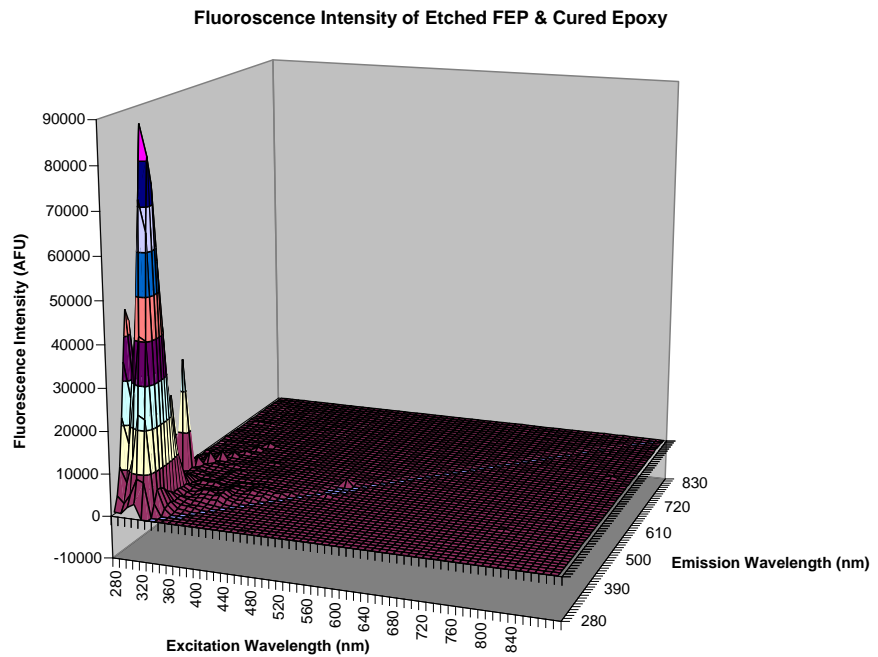
8.1.2 Surface profiles

8.1.2.1 Glass microscope slide
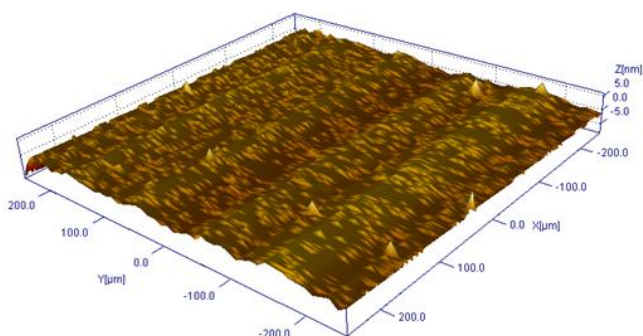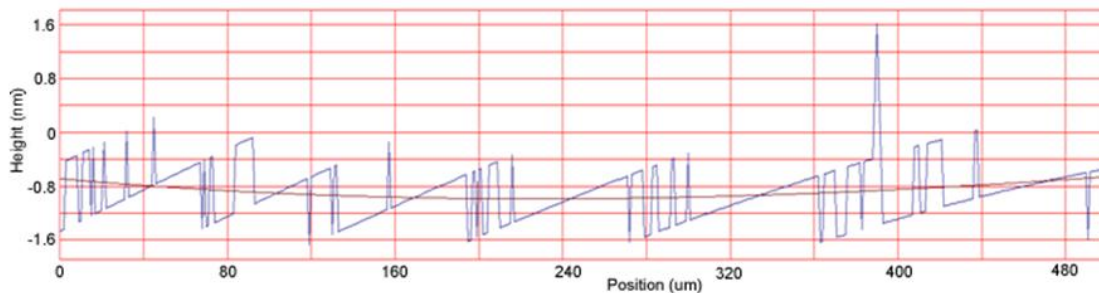
Roughness Average	0.872nm
Minimum height	-8.32nm
Maximum height	5.96nm

8.1.2.2 FEP
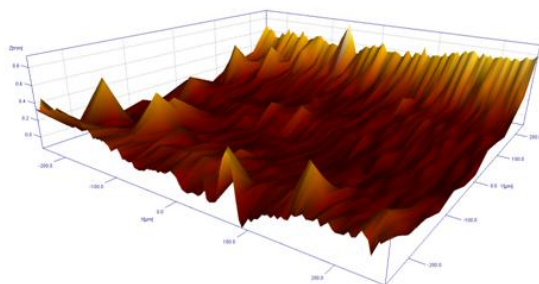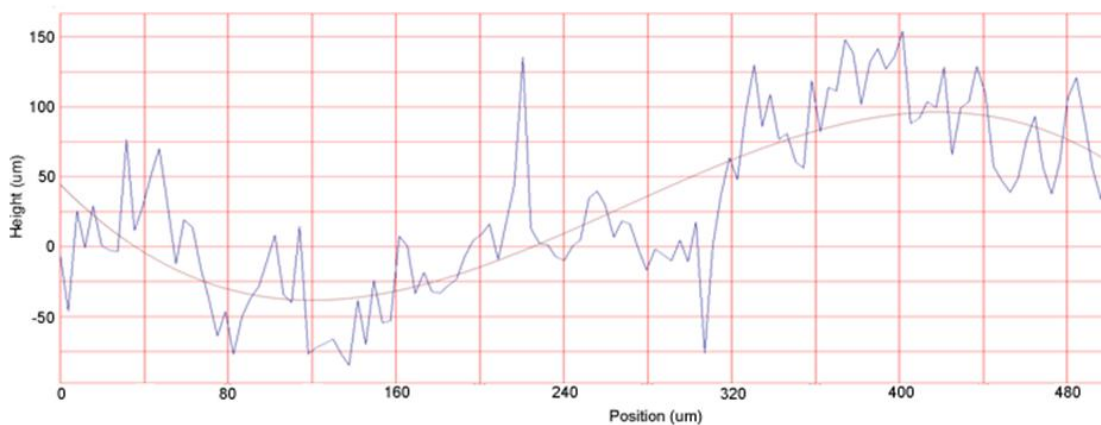
Roughness average	20748nm
Minimum height	-41102nm
Maximum height	113000nm

8.1.2.3   FEP compressed and etched
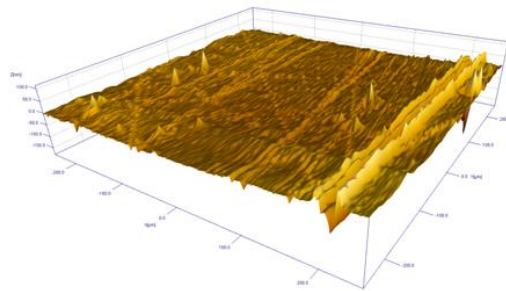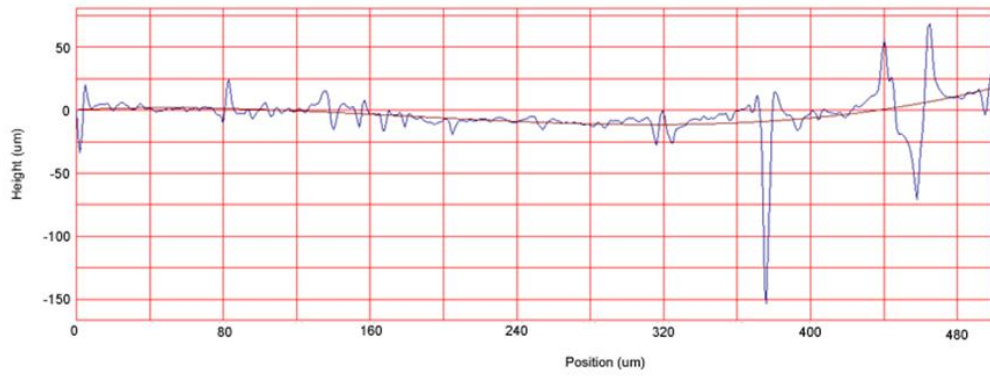
Roughness average	3.54nm
Minimum height	-28.4nm
Maximum height	3.80nm

8.1.2.4   PTFE
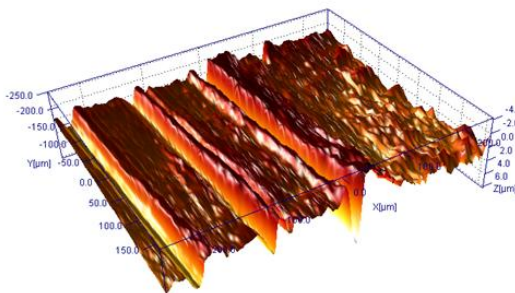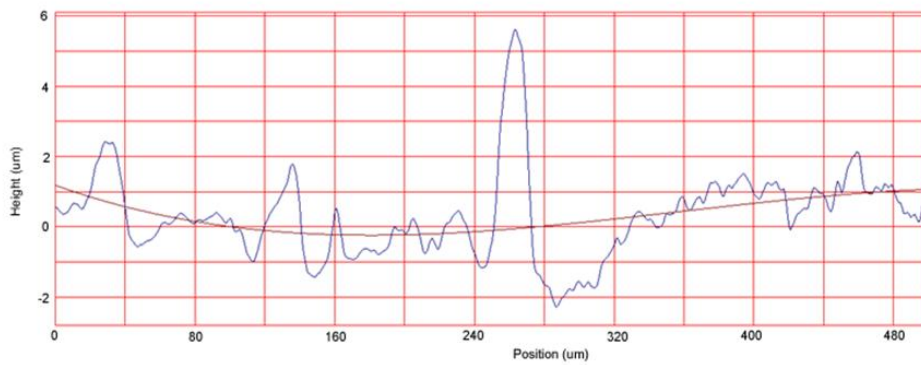
Roughness average	888nm
Minimum height	-4.212um
Maximum height	6.241um

8.1.2.5   PTFE etched
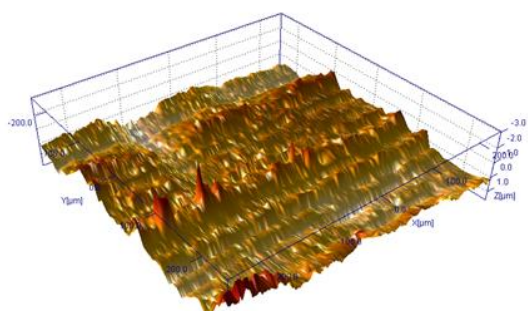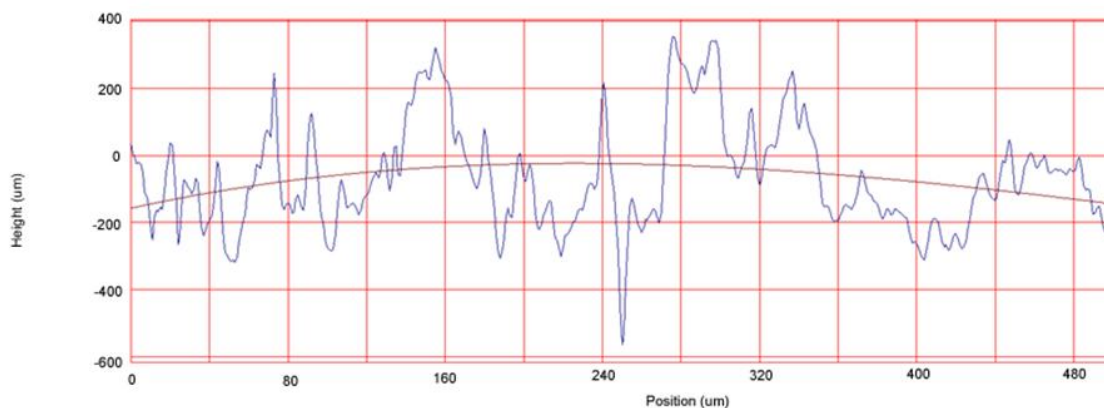
Roughness average	387nm
Minimum height	-3.072um
Minimum height	1.578um

8.1.2.6   PTFE compressed and etched
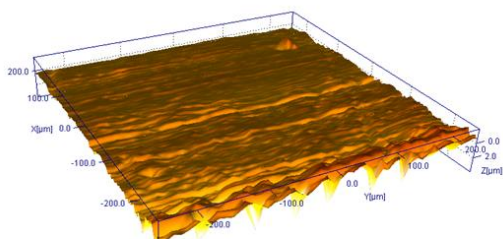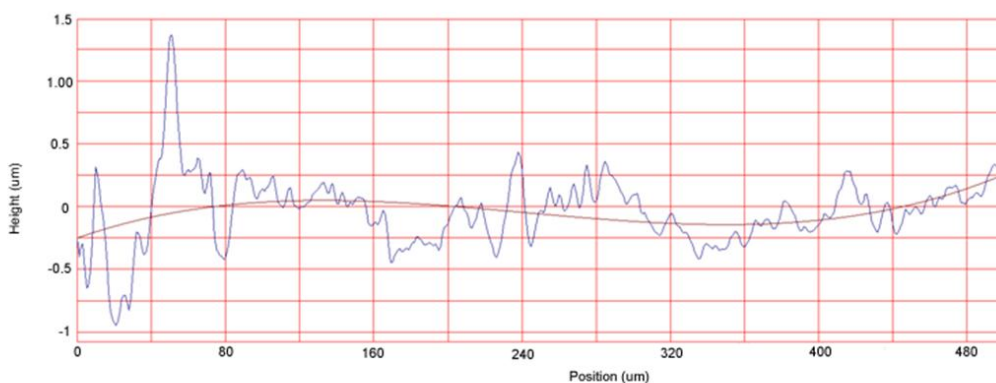
Roughness average	270nm
Minimum height	-1.951um
Maximum height	3.937um

8.2   Nitrite detection

8.2.1   Stage I – macro and microscale sensor

8.2.1.1   Sensiron LG16-1000A calibration

Flow rate (µl/min)	Average Voltage (V)	Standard Deviation (1σ)
0	2.4884	0.0019
10	2.5068	0.0063
20	2.5128	0.0083
30	2.5184	0.0018
40	2.5233	0.0018
50	2.5280	0.0019
60	2.5325	0.0018
100	2.5499	0.0024
1000	2.9696	0.0114
1500	3.2110	0.0166

8.2.1.2   Detection of coloured dye

Concentration (%)	Elapsed time (min)	Voltage (V)	Average Voltage (V)	Standard deviation (σ)
0.1	20	0.970215	-	-
	40	0.966797		
	41	0.968937	0.9682236	0.068237
	42	0.961051		
0.05	20	1.791504	-	-
	41	1.791674		
	42	1.791992	1.794108	0.067454
	43	1.798658		
0.04	20	1.963867	-	-
	41	1.953613		
	42	1.953982	1.956198	0.068647
	43	1.961000		
0.03	20	1.982910	-	-
	41	1.9799**		
	42	1.963915	1.971908	0.089401
	43	-		
0.03	20	2.617188	-	-
	41	2.592773		
	42	2.651899	2.635676	0.207142
	43	2.662366		
0.02	20	2.682129	-	-
	41	2.756598		
	42	-	2.756598	-
	43	-		
0.02	20	3.202148	-	-
	41	3.312536		
	42	3.256122	3.284329	0.2375163
	43	-		
0.01	20	2.6846191	-	-

	41	2.876943		
	42	2.891602	2.8847623	0.088427
	43	2.885742		
0.008	20	3.82324	-	-
	20	3.304688	-	-
	41	3.359375		
	42	3.345642	3.3525085	0.117188
	43	-		
0.006	20	3.640137	-	-
	41	3.626465		
	42	3.626468	3.6229173	0.084261
	43	3.615816		
0	41	4.110840		
	42	4.131348	4.118466	0.113494
	43	4.113212		

8.2.1.2.1 Spectrophotometer readings

Concentration (%)	Absorption at 532nm before Epigem	Absorption at 532nm after Epigem	Dilution (%)
0.1	2.99084759	2.94506025	1.01562
0.05	1.64399529	0.84554797	1.943262
0.04	1.38990688	0.70637554	1.968839
0.03	1.40649378	0.69375211	2.025937
0.03	0.57219523	0.31358248	1.821656
0.02	0.66496569	0.3058615	2.173203
0.02	0.35106194	0.16320722	2.153374
0.01	0.37992111	0.19086736	1.989529
0.008	0.24372482	0.11934465	2.05042
0.006	0.13522784	0.07480287	1.8

8.2.1.3 Detection of nitrite

8.2.1.3.1 Systems 2-4

Concentration (µM)	Time elapsed (min)	Voltage (V)
Ethanol	10	4.247070
	15	4.178223
Blank	0	3.781250
	10	3.84515
	15	3.818848
	20	3.842773
5uM	0	3.82
	10	3.860352
	15	3.862793
	20	3.910645
System 3 – extra 500 delay		
5uM	11	3.9711911
	15	3.997070
	20	3.977539
Blank	11	3.9882422
System 4 – delay of 50 on NED channel		
Blank	10	3.882324
	15	3.661621
	20	4.134766
	25	4.132324
System 5 – increase NED delay to 200		
5uM	15	3.973145
	16	4.095
	20	4.092

Concentration	Time elapsed	Voltage
Blank	12	4.110311
	15	4.112793

8.2.1.3.2   Systems 6-7

Concentration (µM)	Time elapsed (min)	Voltage (V)
Blank	5	3.908610
	8	3.955078
	10	3.940430
	15	3.920928
5uM	10	3.888184
	15	3.885724
Sample and sodium citrate delay to 200		
Ethanol	15	4.145020
Blank	15	4.175293
	20	3.9
	25	3.822754
	30	3.979004
5uM	10	3.873535
	15	3.882813
	20	3.846680
10uM	10	3.918457
	15	3.904297
	20	3.907227
	25	3.860352

8.2.1.3.3   System 8

Concentration (µM)	Time elapsed (min)	Pressure (kPa)	Voltage (V)	Average Voltage (V)	Standard deviation (σ)
First run					
0	15	21.0	3.056102	-	
	20	21.5	3.121582		
	25	19.6	3.603027	3.46468	0.58575
	30	20.0	3.669434		
5	5	20.0	3.422566	-	
	15	20.3	3.387207	-	
	20	20.0	3.123535		
	25	18.6	3.120117	3.11792	0.07890
	30	19.5	3.114746		
	35	20.0	3.113281		
10	20	20.5	3.026855		
	25	19.0	3.104004	3.05485	0.22171
	30	19.0	3.033691		
Second run					
0	20	20.0	3.82080		
	25	19.8	3.81267	3.81848	0.07627
	30	20.0	3.82198		
5	10	20.0	2.82910	-	
	15	21.7	2.95459	-	
	20	20.0	3.06024		
	25	20.0	3.06845	3.06390	0.06745
	30	20.0	3.06301		
7	20	20.0	2.94030		
	25	20.2	2.90944	2.92013	0.14307
	30	20.0	2.91005		
10	10	19.3	3.82275	-	
	15	20.0	3.77396	-	
	30	20.6	2.68115		
	35	20.7	2.84473	2.76489	0.28940
	40	20.0	2.76881		

8.2.2 Stage II – microscale sensor

8.2.2.1 Sample heights 1

Sample container	Height (m)	Flow rate (µl/sec)
Methanol inlet	0.38	2.00
Dye mix inlet	0.67	7.75
Reference outlet	0.27	0.63
Mixed outlet	0.01	9.11

8.2.2.2 Sample heights 2

Sample container	Height (m)	Flow rate (µl/sec)
Methanol inlet	0.67	7.75
Dye mix inlet	0.38	2.00
Reference outlet	0.27	0.63
Mixed outlet	0.01	9.11

8.2.2.3 Dye & methanol

Concentration (µM)	First run average voltage (V)	First run standard deviation (σ)	Second run average voltage (V)	Second run standard deviation (σ)
200	0.5237	0.0029	0.0839	4.50×10^{-04}
100	0.3683	0.0083	0.0689	0.0056
50	0.3113	3.72×10^{-04}	0.0533	2.60×10^{-04}
25	0.2896	2.87×10^{-04}	0.0444	1.78×10^{-04}
12.5	0.2636	5.22×10^{-04}	0.0398	5.60×10^{-03}
6.25	0.2568	2.10×10^{-04}	0.0379	5.60×10^{-03}
3.125	0.2522	2.95×10^{-04}	0.0378	5.60×10^{-03}
1.5625	0.2411	2.91×10^{-04}	-	-
0.78125	0.2338	3.85×10^{-04}	-	-
0.390625	0.2306	3.19×10^{-04}	-	-
0	0.2185	2.80×10^{-03}	0.0377	2.06×10^{-04}

8.2.2.4 Pre-mixed 1

Concentration (µM)	Voltage (V)
5 x amplified	
0.1	0.21
0.5	0.25
1	0.3
1 x amplified	
1	0.04
5	0.09/0.08
10	0.13
15	0.18
20	0.21

25	0.30
30	0.33
35	0.35
40	0.47
45	0.52/0.51
50	0.56

8.2.2.5   Pre-mixed 2

Concentration (µM)	Voltage (V)	Average voltage (V)	Standard deviation (σ)
50	4.44598	4.440081	0.004041
	4.43665		
	4.44199		
	4.44131		
	4.43723		
	4.43888		
	4.43268		
	4.43892		
	4.44517		
	4.44200		
45	4.07977	4.076373	0.003797
	4.07466		
	4.07383		
	4.08173		
	4.08021		
	4.07835		
	4.07559		
	4.07087		
	4.07235		
40	3.74784	3.750256	0.003029
	3.75082		
	3.75285		
	3.75418		
	3.75073		
	3.75373		
	3.74609		
	3.74542		
	3.74935		
	3.75014		
	3.74798		
	3.75394		
35	3.43281	3.42828	0.00398
	3.43011		
	3.43318		
	3.43058		
	3.43028		
	3.42705		
	3.42122		
	3.42190		
	3.42960		
	3.42559		
	3.42876		
30	3.05215	3.051961	0.005483
	3.05359		
	3.05717		
	3.05938		
	3.05762		
	3.05437		

	3.05029		
	3.04471		
	3.04490		
	3.04543		
25	2.48047	2.476619	0.002803
	2.47863		
	2.48113		
	2.47774		
	2.47416		
	2.47400		
	2.47352		
	2.47586		
	2.47851		
	2.47352		
	2.47527		
20	2.07529	2.080413	0.005479
	2.06733		
	2.08033		
	2.08147		
	2.08366		
	2.08242		
	2.07985		
	2.08302		
	2.08484		
	2.08592		
15	1.69939	1.696479	0.004261
	1.70204		
	1.70229		
	1.70031		
	1.69735		
	1.69383		
	1.69322		
	1.69210		
	1.69185		
	1.69241		
10	1.01766	1.016323	0.001078
	1.01641		
	1.01562		
	1.01605		
	1.01652		
	1.01641		
	1.01467		
	1.01760		
	1.01749		
	1.01480		
5	0.54233	0.543065	0.002112
	0.54370		
	0.54353		
	0.54562		
	0.54647		
	0.54568		
	0.54409		
	0.54196		
	0.54105		
	0.54156		
	0.54021		
	0.54058		
1	0.05458	0.054642	0.001090
	0.05488		
	0.05346		
	0.05554		

	0.05626		
	0.05594		
	0.05543		
	0.05475		
	0.05365		
	0.05322		
	0.05335		
0	-0.05940	-0.06092	0.003353
	-0.05646		
	-0.05821		
	-0.06096		
	-0.06060		
	-0.06009		
	-0.05903		
	-0.05845		
	-0.06731		
	-0.06562		
	-0.06400		

8.2.2.6   Pre-mixed 3

Concentration (µM)	Voltage (V)	Average voltage (V)	Standard deviation (σ)
50	5.48457	5.48457	0.003128
	5.48014		
	5.47839		
	5.47422		
	5.48042		
	5.47855		
	5.47804		
	5.47895		
	5.47826		
	5.47340		
45	4.41207	4.410322	0.002588
	4.41380		
	4.41132		
	4.41107		
	4.41006		
	4.41142		
	4.40670		
	4.40753		
	4.41200		
	4.41199		
	4.40558		
40	4.01038	4.000473	0.007868
	4.01126		
	4.00493		
	4.00875		
	4.00751		
	4.00346		
	4.00239		
	3.99501		
	3.99000		
	3.99728		
	3.99791		
	4.00457		
	4.00205		
	3.99820		
	3.98976		

	3.98410		
35	3.65648	3.662539	0.006508
	3.65660		
	3.65534		
	3.66701		
	3.67328		
	3.66891		
	3.66933		
	3.66742		
	3.66829		
	3.65956		
	3.65625		
	3.65641		
	3.65813		
30	3.21971	3.211358	0.004961
	3.21774		
	3.21578		
	3.21288		
	3.20481		
	3.20942		
	3.20919		
	3.20859		
	3.20912		
	3.20634		
25	2.69473	2.690967	0.004916
	2.69404		
	2.69186		
	2.69331		
	2.69300		
	2.69123		
	2.69262		
	2.69815		
	2.68246		
	2.68499		
	2.68425		
20	2.21618	2.213591	0.002766
	2.21571		
	2.21643		
	2.21575		
	2.21313		
	2.21153		
	2.20734		
	2.21242		
	2.21366		
	2.21376		
15	1.68837	1.670808	0.01369
	1.69070		
	1.68611		
	1.68716		
	1.69014		
	1.68418		
	1.67660		
	1.66458		
	1.66388		
	1.65835		
	1.65946		
	1.65894		
	1.65762		
	1.65855		
	1.65903		
	1.65984		

	1.66022		
10	1.04868	1.047511	0.002891
	1.04881		
	1.05149		
	1.05132		
	1.04834		
	1.04883		
	1.04465		
	1.04504		
	1.04420		
	1.04375		
5	0.49415	0.488733	0.003862
	0.49279		
	0.49283		
	0.48953		
	0.48685		
	0.48599		
	0.48281		
	0.48422		
	0.48762		
	0.49054		
1	0.05372	0.053822	0.001692
	0.05422		
	0.05319		
	0.05268		
	0.05233		
	0.05306		
	0.05239		
	0.05297		
	0.05650		
	0.05716		
0	0.02598	0.023775	0.002779
	0.02156		
	0.02435		
	0.02654		
	0.02491		
	0.02456		
	0.02848		
	0.02126		
	0.01998		
	0.02396		
	0.01994		

8.2.2.7 Nitrite 1

First run		
Concentration (μM)	Average voltage (V)	Standard deviation (σ)
12.5	1.206	0.002
6.25	1.0902	0.0032
3.125	1.0691	0.0019
1.5625	1.0438	0.0022
0	1.02	0.0019

Second run		
Concentration (μM)	Average voltage (V)	Standard deviation (σ)
12.5	1.1065	0.0014
6.25	0.9967	0.0025

3.125	0.9605	0.0053
1.5625	0.9463	0.0013
0	0.9319	0.0026

Third run		
Concentration (µM)	Average voltage (V)	Standard deviation (σ)
0	-0.0975	0.006
10	0.0356	0.0028
12.5	0.1225	0.0023

Standard deviations	
Run number	Average standard deviation (σ)
1	0.0024
2	0.0026
3	0.0037

8.2.2.8 Nitrite 2

Concentration (µM)	Average voltage (V)	Standard deviation (σ)
50	0.1193	0.022
25	-0.0553	0.0173
12.5	-0.1188	0.0192
6.25	-0.2586	0.0211
0	-0.3256	0.0063

8.3 Stage III - Bench top experiments

8.3.1 Flow stability

Inlet tubing diameter (mm)	Run number	Flow rate (µl/min)	Sample inlet		Reagent inlet	
			Average	Std Dev	Average	Std Dev
0.8		0	2.5061	0.0015	2.4976	0.0018
	1	30	2.5051	0.0015	2.5105	0.0017
		60	2.505	0.0016	2.5194	0.0016
		120	2.5094	0.0016	2.5297	0.0017
		240	2.5385	0.0018	2.5323	0.0017
		480	2.5691	0.0022	2.5485	0.0019
	2	30	2.5008	0.0016	2.5104	0.0017
		60	2.5011	0.0015	2.5196	0.0016
		120	2.5052	0.0018	2.5319	0.0018
		240	2.5419	0.0022	2.5397	0.0019
		480	2.5727	0.002	2.5427	0.0018
	3	30	2.5058	0.0016	2.5105	0.0017
		60	2.5079	0.0016	2.5167	0.0017

		120	2.522	0.0018	2.5227	0.0017
		240	2.5439	0.0019	2.5284	0.0017
		480	2.5708	0.002	2.5442	0.0018
		0	2.5061	0.0015	2.4976	0.0018
	1	30	2.5085	0.0016	2.5076	0.0018
		60	2.5151	0.0016	2.5118	0.0016
		120	2.5276	0.0018	2.5186	0.0016
		240	2.5431	0.0017	2.5288	0.0017
		480	2.5724	0.0020	2.5455	0.0018
	2	30	2.5105	0.0016	2.5053	0.0017
0.3		60	2.5163	0.0016	2.5105	0.0017
		120	2.5284	0.0017	2.5180	0.0016
		240	2.5435	0.0018	2.5292	0.0017
		480	2.5711	0.0020	2.5467	0.0018
	3	30	2.5117	0.0016	2.5036	0.0018
		60	2.5176	0.0016	2.5087	0.0017
		120	2.5283	0.0017	2.5181	0.0016
		240	2.5434	0.0018	2.5297	0.0017
		480	2.5721	0.0020	2.5461	0.0018

8.4 Trials cruise deployment

8.4.1 Data logger state diagram

SET ST=0 - All valves closed

Wait for T1 minutes

Open Valve 1

Pump On - Backwards - PS1 speed

Wait for T2 minutes

Pump On - Foward - PS2 speed

Wait for T3 minutes

Close Valve 1, Open Valve 2

Wait for T4 minutes

Open Valve 4

Wait for T5 minutes

Pump Change - Foward - PS3 speed

Wait for T6 minutes

Start reading

Wait for T7 minutes

Stop reading

Close Valve 2, Open Valve 3

Pump On - Foward - PS2 speed

Wait for T8 minutes

Pump Change - Foward - PS3 speed

Wait for T9 minutes

Start reading

Wait for T10 minutes

Stop reading

Close Valve 3, Open Valve1, Open Valve 4

Pump Change - Foward - PS2 speed

Wait for T11 minutes

Pump Change - Foward - PS3 speed

Wait for T12 minutes

Start reading

Wait for T13 minutes

Stop reading

Close Valve 4

Pump Change - Backwards - PS1 speed

Wait for T14 minutes

ST=0

ST=ST+1

ST<5   ST=5

8.4.2   80Hz filter characteristics
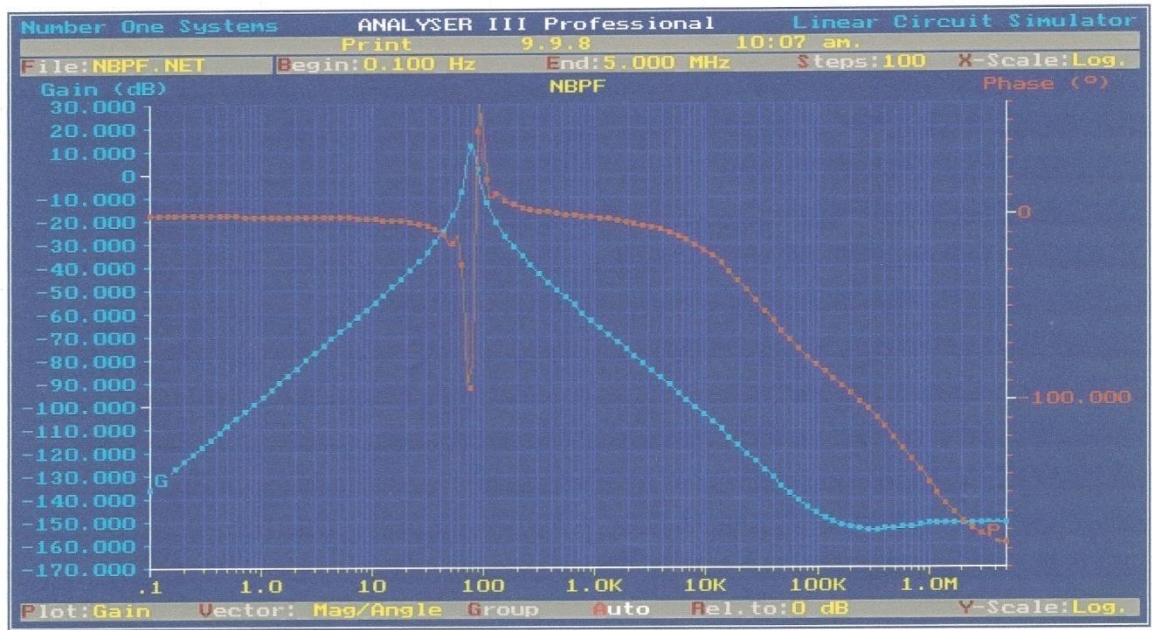
8.4.3   Cast 001

8.4.3.1   Niskin bottle timings

Firing Order	Bottle No.	Depth (m)	Time	Sensor running time (min)
1	1	203	0952	49
2	2	203	0953	50
3	6	253	1005	62
4	7	254	1006	63
5	9	304	1018	75
6	10	304	1019	76
7	15	304	1031	88
8	16	304	1032	89
9	19	304	1044	101
10	20	304	1045	102
11	22	304	1057	114
12	23	304	1058	115

8.4.3.2   Sensor timing settings

Event	Description of event	Waiting period (secs)
T1	Initial start up pause	900
T2	Pump backwards from waste to sea	300
T3	Pump forwards from sea	300
T4	Pump from 0µM	300
T5	Pump from reagent and 0µM	300

T6	Pump at lower speed ready for reading	120
T7	Taking data	60
T8	Pump from 25µM	300
T9	Pump at lower speed ready for reading	120
T10	Taking data	60
T11	Pump from seawater	300
T12	Pump at lower speed ready for reading	120
T13	Taking data	60
T14	Pump backward from waste to sea	120
T15	Pump forwards ready for callibration	180

8.4.3.3   Pump Settings

Event	Description of event	Set pulse period (µs)
PS1	Pump forwards – fast	4000
PS2	Pump backwards – fast	4000
PS3	Pump forwards – slow	14000

8.4.4   Cast 003

8.4.4.1   Niskin bottle timings

Firing Order	Bottle No.	Depth (m)	Time	Sensor running time (min)
1	6	32	1443	49
2	18	32	1443	49

8.4.4.2   Sensor timing settings

Event	Description of event	Waiting period (secs)
T1	Initial start up pause	900
T2	Pump backwards from waste to sea	600
T3	Pump forwards from sea	300
T4	Pump from 0µM	300
T5	Pump from reagent and 0µM	300
T6	Pump at lower speed ready for reading	120
T7	Taking data	60
T8	Pump from 25µM	300
T9	Pump at lower speed ready for reading	120
T10	Taking data	60
T11	Pump from seawater	11
T12	Pump at lower speed ready for reading	120
T13	Taking data	60
T14	Pump backward from waste to sea	120
T15	Pump forwards ready for calibration	15

8.4.4.3   Pump speed settings

Event	Description of event	Set pulse period (µs)
PS1	Pump forwards – fast	5000

PS2	Pump backwards – fast	5000	
PS3	Pump forwards – slow	14000	

8.4.5 Cast 004

8.4.5.1 Niskin bottle timings

Firing Order	Bottle No.	Depth (m)	Time
1	1	1518	1649
2	2	1518	1649
3	5	1265	1700
4	6	1265	1700
5	9	1014	1712
6	10	1014	1712
7	17	762	1722
8	18	762	1723
9	21	509	1734
10	22	509	1734

8.4.5.2 Sensor timing settings

Event	Description of event	Waiting period (secs)
T1	Initial start up pause	120
T2	Pump backwards from waste to sea	60
T3	Pump forwards from sea	120
T4	Pump from 0μM	120
T5	Pump from reagent and 0μM	120
T6	Pump at lower speed ready for reading	60
T7	Taking data	60
T8	Pump from 25μM	120
T9	Pump at lower speed ready for reading	60
T10	Taking data	60
T11	Pump from seawater	120
T12	Pump at lower speed ready for reading	60
T13	Taking data	60
T14	Pump backward from waste to sea	90
T15	Pump forwards ready for calibration	120

8.4.5.2.1 Pump speed settings

Event	Description of event	Set pulse period (μs)
PS1	Pump forwards – fast	4000
PS2	Pump backwards – fast	4000
PS3	Pump forwards – slow	14000

8.4.6 Cast 005

8.4.6.1 Niskin bottle timings

Firing	Bottle	Depth	Time

Order	No.	(m)	
1	2	997	1445
2	3	998	1446
3	10	755	1456
4	11	756	1456
5	18	508	1506
6	19	508	1507

8.4.6.2 Sensor timings

Event	Description of event	Waiting period (secs)
T1	Initial start up pause	3600
T2	Pump backwards from waste to sea	10
T3	Pump forwards from sea	300
T4	Pump from 0µM	300
T5	Pump from reagent and 0µM	120
T6	Pump at lower speed ready for reading	30
T7	Taking data	60
T8	Pump from 25µM	300
T9	Pump at lower speed ready for reading	120
T10	Taking data	60
T11	Pump from seawater	300
T12	Pump at lower speed ready for reading	120
T13	Taking data	2400
T14	Pump backward from waste to sea	10
T15	Pump forwards ready for calibration	120

8.4.6.3 Pump speed settings

Event	Description of event	Set pulse period (µs)
PS1	Pump forwards – fast	4000
PS2	Pump backwards – fast	4000
PS3	Pump forwards – slow	14000

8.5 Matlab© scripts

The following sections contains Matlab© (Mathworks™) code segments are the scripts used within this report.

8.5.1 Beer-Lambert-Bouger plot

```
% Create figure
figure1 = figure('PaperSize',[20.98 29.68],'Color',[1 1 1]);

% Create axes
axes('Parent',figure1,'FontWeight','bold','FontSize',20,'FontName','Arial')
;
box('on');
hold('all');

clear all
```

```matlab
Ia=1;Ib=1;EPa=1350000;EPb=10000;L=0.01;st=0.1;
Startconc=0;Endconc=0.001;res=0.00001;
x=[];y=[];x2=[];y2=[];

%Solve for x & y

%Polychromatic
count=1;
for x=Startconc:res:Endconc;
y(count)=log10((Ia+Ib)/((Ia*10^(-EPa*L*x))+(Ib*10^(-EPb*L*x))));
count=count+1;
end
x=(Startconc:res:Endconc)*(1e6);

%Monochromatic
count=1;
for x2=Startconc:res:Endconc;
y2(count)=EPa*L*x2;
count=count+1;
end
x2=(Startconc:res:Endconc)*(1e6);

%Stray light
count=1;
for x3=Startconc:res:Endconc;
y3(count)=-log10((Ia*10^(-EPa*L*x3)+st)/Ia);
count=count+1;
end
x3=(Startconc:res:Endconc)*(1e6);

plot(x,y,x2,y2,x3,y3,'LineWidth',2)
axis([0,100,-0.1,1])
xlabel('Concentration
(µM)','FontWeight','bold','FontSize',24,'FontName','Arial')
ylabel('Absorption','FontWeight','bold','FontSize',24,'FontName','Arial')
```

8.5.2   Stage II - microscale

8.5.2.1   Filter load function

```matlab
function [Hd01]=filterload(samplerate);

Fs01=samplerate;  % Sampling Frequency

Fpass01 = 0.2;         % Passband Frequency
Fstop01 = 0.5;         % Stopband Frequency
Apass01 = 1;           % Passband Ripple (dB)
Astop01 = 60;          % Stopband Attenuation (dB)
match01 = 'passband';  % Band to match exactly

% Fs02 = 1024;  % Sampling Frequency
%
% Fstop02 = 0.01;        % Stopband Frequency
% Fpass02 = 1;        % Passband Frequency
% Astop02 = 3;         % Stopband Attenuation (dB)
% Apass02 = 1;           % Passband Ripple (dB)
% match02 = 'passband';  % Band to match exactly


% Construct an FDESIGN object and call its BUTTER method.
```

```matlab
h01  = fdesign.lowpass(Fpass01, Fstop01, Apass01, Astop01, Fs01);

Hd01 = design(h01, 'butter', 'MatchExactly', match01);

Hd01.persistentmemory=true;
Hd01.states=1;
```

8.5.2.2   Graphical user interface
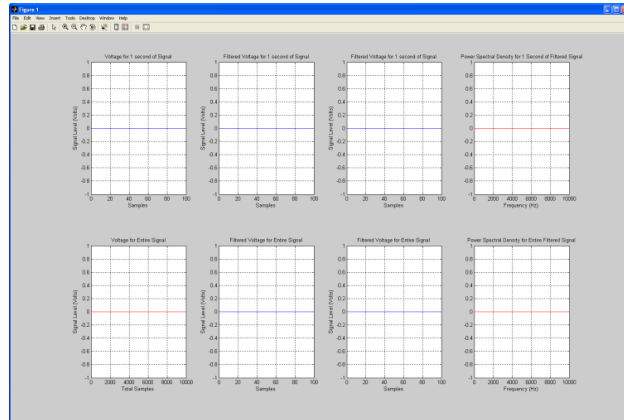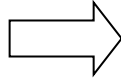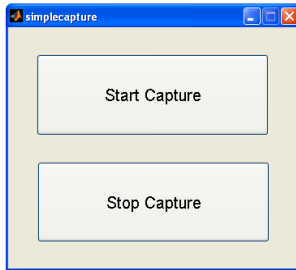

```matlab
function varargout = simplecapture(varargin)
gui_Singleton = 1;
gui_State = struct('gui_Name',       mfilename, ...
                   'gui_Singleton',  gui_Singleton, ...
                   'gui_OpeningFcn', @simplecapture_OpeningFcn, ...
                   'gui_OutputFcn',  @simplecapture_OutputFcn, ...
                   'gui_LayoutFcn',  [] , ...
                   'gui_Callback',   []);
if nargin && ischar(varargin{1})
    gui_State.gui_Callback = str2func(varargin{1});
end

if nargout
    [varargout{1:nargout}] = gui_mainfcn(gui_State, varargin{:});
else
    gui_mainfcn(gui_State, varargin{:});
end

function simplecapture_OpeningFcn(hObject, eventdata, handles, varargin)
handles.output = hObject;
guidata(hObject, handles);

function varargout = simplecapture_OutputFcn(hObject, eventdata, handles)
varargout{1} = handles.output;

function startbutton_Callback(hObject, eventdata, handles)

hw=daqhwinfo('nidaq');
ID=hw.InstalledBoardIds;

switch isempty(ID)
    case 0
    case 1
        waitfor(msgbox({'No Board IDs Found!'},'Program Error','error'));
        return
end

hw.BoardNames;
```

```matlab
ADNAME=hw.AdaptorName;
ID=char(ID);

 global ai01
global ai02

%Add hardware channel 0 from board
ai01 = analoginput(ADNAME,ID);
addchannel(ai01,0);

%setting the logging mode & filename
set(ai01,'LoggingMode','Disk&Memory');
set(ai01,'LogToDiskMode','Index');

%Folder and file name creation
datefolder=date;
if exist(datefolder);
else
    mkdir(datefolder);
end

files01=dir(fullfile(datefolder,'*.daq'));

switch isempty(files01);
    case 0
        [a,b]=size(files01);
        runnumber=a+1;
        runnumber=num2str(runnumber);
    case 1
        runnumber='1';
end

set(ai01,'LogFileName',[datefolder,'\',runnumber,'.daq']);

%Set maximum amount of memory usage
daqmem(ai01,400e6); %400mb max

%Showing amount of memory used, 0 for none 100 max
out=daqmem;
memorypercentage=out.MemoryLoad;
 set(ai01,'InputType','SingleEnded'); %- configure for single end mode

try
    close(figure(1))
catch
end

scrsz = get(0,'ScreenSize');
figure('Position',[20 50 scrsz(3)/1.2 scrsz(4)/1.2])
H=figure(1);

%Unfiltered Signal Short
figure(1)
subplot(2,4,1)
set(gcf,'doublebuffer','on'); %Reduce plot flicker
P1=plot(zeros(100,1));
T=title('Voltage for 1 second of Signal');
xlabel('Samples');
ylabel('Signal Level (Volts)');
grid on

%Unfiltered Signal Long
subplot(2,4,5)
```

```matlab
set(gcf,'doublebuffer','on'); %Reduce plot flicker
P2=plot(zeros(10000,10));
T=title('Voltage for Entire Signal');
xlabel('Total Samples');
ylabel('Signal Level (Volts)');
grid on

%Filtered Signal Short
subplot(2,4,2)
set(gcf,'doublebuffer','on'); %Reduce plot flicker
P3=plot(zeros(100,1));
T=title('Filtered Voltage for 1 second of Signal');
xlabel('Samples');
ylabel('Signal Level (Volts)');
grid on

%Filtered Signal Long
subplot(2,4,6)
set(gcf,'doublebuffer','on'); %Reduce plot flicker
P4=plot(zeros(100,1));
T=title('Filtered Voltage for Entire Signal');
xlabel('Samples');
ylabel('Signal Level (Volts)');
grid on

%Filtered Signal Short
subplot(2,4,3)
set(gcf,'doublebuffer','on'); %Reduce plot flicker
P5=plot(zeros(100,1));
T=title('Filtered Voltage for 1 second of Signal');
xlabel('Samples');
ylabel('Signal Level (Volts)');
grid on

%Filtered Signal Long
subplot(2,4,7)
set(gcf,'doublebuffer','on'); %Reduce plot flicker
P6=plot(zeros(100,1));
T=title('Filtered Voltage for Entire Signal');
xlabel('Samples');
ylabel('Signal Level (Volts)');
grid on


%Don't need to calculate the fft till the end of the collection, at the
%moment it is the the filtered

%FFT graph for filtered signal short
subplot(2,4,4)
set(gcf,'doublebuffer','on'); %Reduce plot flicker
P7=plot(zeros(10000,10));
T=title('Power Spectral Density for 1 Second of Filtered Signal');
xlabel('Frequency (Hz)')
grid on

%FFT graph for filtered signal long
subplot(2,4,8)
set(gcf,'doublebuffer','on'); %Reduce plot flicker
P8=plot(zeros(10000,10));
T=title('Power Spectral Density for Entire Filtered Signal');
xlabel('Frequency (Hz)')
grid on
```

```matlab
%Setting the sample rate and storing actual rate
duration=300;
previewrate1=1024;
samplerate=1024;

[Hd01]=filterload(samplerate);

try
    set(ai01,'SampleRate',samplerate);
    actualrate=get(ai01,'SampleRate')
    set(ai01,'SamplesPerTrigger',duration*actualrate);
catch
end

set(ai01,'BufferingMode','Auto');
ai01.BufferingMode;

out=daqhwinfo(ai01);
out.NativeDataType;
out01=daqmem(ai01);

ai01.TransferMode;
set(ai01,'TransferMode','DualDMA');
ai01.TransferMode;

ValidRates=propinfo(ai01,'SampleRate');

%Start accquisition
try
    start(ai01)
%catch
end
pause(2)

%determine if logging is taking place - returns 1 if is
islogging(ai01);
isrunning(ai01);

%Starting the preview after the first preview batch has been logged
startpausesamplenumber=previewrate1;
while ai01.SamplesAcquired < startpausesamplenumber;
    acc=ai01.SamplesAcquired;
end

try
%Creating preview plot while still running
while ai01.SamplesAcquired < (duration*actualrate)
    acc=ai01.SamplesAcquired;
    [data1]=peekdata(ai01,previewrate1);
    averagevoltage=sum(data1)/previewrate1;
    averagevoltage=num2str(averagevoltage);
    previewrate2=ai01.SamplesAcquired;
    [data2]=peekdata(ai01,previewrate2);
    time01=previewrate2/actualrate;
    time=num2str(time01);
    data3=filter(Hd01,data1);
    data4=filter(Hd01,data2);

    F=1024/10;
    data5=movingaverage01(data3,F);
    data6=movingaverage01(data4,F);
    [data7x,data7y]=fftcalc(data3,1/1024);
```

```matlab
    [data8x,data8y]=fftcalc(data4,1/1024);
    set(P1,'ydata',data1);
    set(P2,'ydata',data2);
    set(P3,'ydata',data3);
    set(P4,'ydata',data4);
    set(P5,'ydata',data5);
    set(P6,'ydata',data6);
    set(P7,'xdata',data7x);
    set(P7,'ydata',data7y);
    set(P8,'xdata',data8x);
    set(P8,'ydata',data8y);
    set(H,'name',['Time    Elapsed   =   ',time,'   Average   Voltage   =
',averagevoltage]);
    drawnow;
end
%catch
end

%Aqquire data into the matlab workspace

if ai01.SamplesAcquired==(actualrate*duration);
[data01,time01]=getdata(ai01);
end

wait(ai01,2)

%Cleaning up
stop(ai01)
delete(ai01)

function stopbutton_Callback(hObject, eventdata, handles)
global ai01

try
    stop(ai01)
catch
end
```

8.5.2.3   Image analysis program
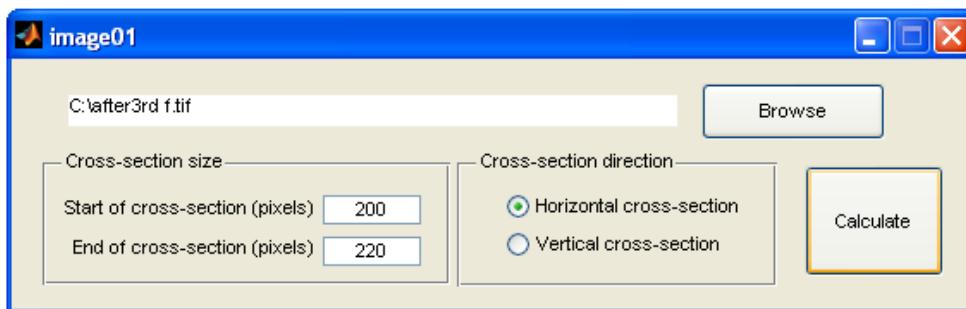

```matlab
function varargout = image01(varargin)
gui_Singleton = 1;
gui_State = struct('gui_Name',       mfilename, ...
                   'gui_Singleton',  gui_Singleton, ...
                   'gui_OpeningFcn', @image01_OpeningFcn, ...
                   'gui_OutputFcn',  @image01_OutputFcn, ...
                   'gui_LayoutFcn',  [] , ...
                   'gui_Callback',   []);
if nargin && ischar(varargin{1})
    gui_State.gui_Callback = str2func(varargin{1});
```

```matlab
end

if nargout
    [varargout{1:nargout}] = gui_mainfcn(gui_State, varargin{:});
else
    gui_mainfcn(gui_State, varargin{:});
end

% --- Executes just before image01 is made visible.
function image01_OpeningFcn(hObject, eventdata, handles, varargin)
handles.output = hObject;
guidata(hObject, handles);

if exist('imagedefaults.mat');
    load('imagedefaults.mat');
else
    waitfor(msgbox({'Defaults    file    cannot    be    found!'},'Program
Error','error'));
    return
end

global filelocationfullfile
global crosssection01
global crosssection02
global horizontal

if exist('filelocationfullfile')
    set(handles.filelocationbox,'string',filelocationfullfile)
end

if exist('crosssection01')
    set(handles.crosssection01box,'string',crosssection01);
end

if exist('crosssection02')
    set(handles.crosssection02box,'string',crosssection02);
end

if exist('horizontal')
    set(handles.horizontalradio,'value',horizontal);
end

% --- Outputs from this function are returned to the command line.
function varargout = image01_OutputFcn(hObject, eventdata, handles)
varargout{1} = handles.output;

% --- Executes on button press in browsebutton.
function browsebutton_Callback(hObject, eventdata, handles)

global filelocationfullfile
global filelocationfilename
global filelocationfolder

savepath=pwd;
if isempty(filelocationfolder);
else
    try
        cd(filelocationfolder);
    catch
    end
end
[file,folder]=uigetfile({'*.*'},'Choose the image file');
if file==0;
```

```matlab
else
    filelocationfilename=char(file);
    filelocationfolder=char(folder);
end
filelocationfullfile=strcat(filelocationfolder,filelocationfilename);
set(handles.filelocationbox,'string',filelocationfullfile);
cd(savepath);

switch exist('imagedefaults.mat')
    case 0
        save('imagedefaults.mat','filelocationfullfile');
        save('imagedefaults.mat','filelocationfilename','-append');
        save('imagedefaults.mat','filelocationfolder','-append');
    case 2
        save('imagedefaults.mat','filelocationfullfile','-append');
        save('imagedefaults.mat','filelocationfilename','-append');
        save('imagedefaults.mat','filelocationfolder','-append');
    otherwise
        waitfor(msgbox({'Failed    to    save    defaults    file'},'Program
Error','error'));
        return
end

function crosssection01box_Callback(hObject, eventdata, handles)
function crosssection01box_CreateFcn(hObject, eventdata, handles)
if       ispc       &&       isequal(get(hObject,'BackgroundColor'),
get(0,'defaultUicontrolBackgroundColor'))
    set(hObject,'BackgroundColor','white');
end


function crosssection02box_Callback(hObject, eventdata, handles)
function crosssection02box_CreateFcn(hObject, eventdata, handles)
if       ispc       &&       isequal(get(hObject,'BackgroundColor'),
get(0,'defaultUicontrolBackgroundColor'))
    set(hObject,'BackgroundColor','white');
end


function calculatebutton_Callback(hObject, eventdata, handles)

global horizontal
global crosssection01
global crosssection02
global filelocationfullfile
global filelocationfilename
global filelocationfolder

horizontal=get(handles.horizontalradio,'value');
crosssection01=get(handles.crosssection01box,'string');
crosssection02=get(handles.crosssection02box,'string');

switch exist('imagedefaults.mat')
    case 0
        save('imagedefaults.mat','filelocationfullfile');
        save('imagedefaults.mat','filelocationfilename','-append');
        save('imagedefaults.mat','filelocationfolder','-append');
        save('imagedefaults.mat','horizontal','-append');
        save('imagedefaults.mat','crosssection01','-append');
        save('imagedefaults.mat','crosssection02','-append');
    case 2
        save('imagedefaults.mat','filelocationfullfile','-append');
        save('imagedefaults.mat','filelocationfilename','-append');
```

```matlab
        save('imagedefaults.mat','filelocationfolder','-append');
        save('imagedefaults.mat','horizontal','-append');
        save('imagedefaults.mat','crosssection01','-append');
        save('imagedefaults.mat','crosssection02','-append');
    otherwise
        waitfor(msgbox({'Failed    to    save    defaults    file'},'Program
Error','error'));
        return
end

calculate
```

8.5.2.3.1 Intensity calculation function

```matlab
clear array
clear arrayline
clear arrayaveraged

if exist('imagedefaults.mat');
    load('imagedefaults.mat');
else
    waitfor(msgbox({'Defaults    file    cannot    be    found!'},'Program
Error','error'));
    return
end

global crosssection01
global crosssection02
global filelocationfullfile

crosssection01=str2num(crosssection01);
crosssection02=str2num(crosssection02);

if exist(filelocationfullfile)
    array=imread(filelocationfullfile);
    info=imfinfo(filelocationfullfile);
end

switch horizontal
    case 1
        crossdirection='x';
    case 0
        crossdirection='y';
end

%Size of strip to use and position
width=info.Width;
height=info.Height;

switch crossdirection
    case 'x'
        %Horizontal cross-section
        array=array(crosssection01:crosssection02,1:width);
    case 'y'
        %Vertical cross-section
        array=array(1:height,crosssection01:crosssection02);
end

%Measuring intensity of cross section
[rows,columns]=size(array);
rowsno=double(rows);
columnsno=double(columns);
```

```matlab
switch crossdirection
    case 'x'
        %Horizontal cross-section
        count=1;
        for count=1:columns
            arrayline=sum(array(1:end,count));
            average=arrayline/rowsno;
            arrayaveraged(:,count)=average;
            count+1;
        end
    case 'y'
        %Vertical cross-section
        count=1;
        for count=1:rows
            arrayline=sum(array(count,1:end));
            average=arrayline/columnsno;
            arrayaveraged(:,count)=average;
            count+1;
        end
end

%get global max and min so can normalise to 0-1
abs_max=max(arrayaveraged(:));
abs_min=min(arrayaveraged(:));
arrayaveraged=arrayaveraged-abs_min;
abs_max=max(arrayaveraged(:));
abs_max=double(abs_max);
value01=double(1);
arrayaveraged=arrayaveraged*(value01/abs_max);

figure(2)

switch crossdirection
    case 'x'
        plot(1:width,arrayaveraged(1,1:end),'LineWidth',2);
        grid;
        xlabel('Pixels across');
        ylabel('Normalised Intensity');
        h=get(gcf,'CurrentAxes');
        set(h,'FontSize',22);
        set(get(h,'XLabel'),'FontSize',22);
        set(get(h,'YLabel'),'FontSize',22);
        set(get(h,'XLabel'),'FontSize',22);
        xlim([0,width]);
        ylim([0,1]);
        set(gcf,'Color',[1,1,1])
    case 'y'
        arrayaveraged=fliplr(arrayaveraged);
        plot(arrayaveraged(1,1:end),1:height,'LineWidth',2);
        grid;
        xlabel('Normalised Intensity');
        ylabel('Pixels across');
        h=get(gcf,'CurrentAxes');
        set(h,'FontSize',22);
        set(get(h,'XLabel'),'FontSize',22);
        set(get(h,'YLabel'),'FontSize',22);
        set(get(h,'XLabel'),'FontSize',22);
        xlim([0,1]);
        ylim([0,height]);
        set(gcf,'Color',[1,1,1])
end
```

8.5.3   Stage III - Bench top experiments

8.5.3.1   Ray tracing program

```matlab
clear all
cla

n0width=500;
n1width=250;
n2width=500;
n3width=600;
numberofcladdings=3;
n0refi=1.3394;
n1refi=1.59;
n2refi=1.26;
n3refi=1.59;
anglestep=5;
beginangle=0;
endangle=90;
angleofinterest=75;
clear position


for angle=(beginangle:anglestep:endangle)
    nwidth=n0width;
    direction='up';
    xend=20000;
    stepend=20000;
    halt=0;
    step=1;
    x=0;
    y=0;
    anglein=angle;
    tir='';
    direction='up';
    xpos=[];
    ypos=[];
    xpos(1)=0;
    ypos(1)=0;
    length=0;

    xpos(2)=(nwidth/2)/tand(90-angle);
    ypos(2)=nwidth/2;

    if xpos(2)==Inf
        xpos(2)=xend;
        ypos(2)=0;
        length=xend;
        halt=1;
        tir='endoftrace';
    else
        newx=xpos(2)-xpos(1);
        length=newx/sind(angle);
    end

    layer=0;
    n1=eval(['n',num2str(abs(layer)),'refi']);
    n2=eval(['n',num2str(abs(layer+1)),'refi']);
```

```
%Tracing function for single light path
while step<stepend & halt==0

    cangle=asind(n2/n1);
    if isreal(cangle)==0
        tir=0;
    else
        if cangle==90
            tir=0;
        else
            if angle>=cangle
                tir=1;
            else
                tir=0;
            end
        end
    end


    switch tir
        case 0
            switch direction
                case 'up'
                    n1=eval(['n',num2str(abs(layer)),'refi']);
                    n2=eval(['n',num2str(abs(layer+1)),'refi']);
                    nwidth=eval(['n',num2str(abs(layer+1)),'width']);
                    angle=asind((n1*sind(angle))/n2);
                    x=x+(nwidth/tand(90-angle));
                    y=y+nwidth;
                    xpos(step+2)=x+xpos(2);
                    ypos(step+2)=y+n0width/2;
                    if xpos(step+2)>=xend
                        halt=1;
                        tir='endoftrace';
                        outofbounds=find(xpos>xend);
                        if isempty(outofbounds)
                        else
                            x1=xpos(1,outofbounds(1,1)-1);
                            x2=xpos(1,outofbounds(1,1));
                            y1=ypos(1,outofbounds(1,1)-1);
                            y2=xpos(1,outofbounds(1,1));
                            newx=xend-x1;
                            newy=newx/tand(angle);
                            xpos(step+2)=xpos(step+1)+newx;
                            ypos(step+2)=ypos(step+1)+newy;
                        end
                    end
                    if layer==0
                        newx=xpos(step+2)-xpos(step+1);
                        newlength=newx/sind(angle);
                        length=length+newlength;
                    else
                    end
                    step=step+1;
                    layer=layer+1;
                    if layer==numberofcladdings
                        halt=1;
                        tir='endoftrace';
                    else
                        n1=eval(['n',num2str(abs(layer)),'refi']);
```

```matlab
                        n2=eval(['n',num2str(abs(layer+1)),'refi']);
                end
            case 'down'
                n1=eval(['n',num2str(abs(layer)),'refi']);
                n2=eval(['n',num2str(abs(layer-1)),'refi']);
                nwidth=eval(['n',num2str(abs(layer-1)),'width']);
                angle=asind((n1*sind(angle))/n2);
                x=x+(nwidth/tand(90-angle));
                y=y-nwidth;
                xpos(step+2)=x+xpos(2);
                ypos(step+2)=y+n0width/2;
                if xpos(step+2)>=xend
                    halt=1;
                    tir='endoftrace';
                    outofbounds=find(xpos>xend);
                    if isempty(outofbounds)
                    else
                        x1=xpos(1,outofbounds(1,1)-1);
                        x2=xpos(1,outofbounds(1,1));
                        y1=ypos(1,outofbounds(1,1)-1);
                        y2=xpos(1,outofbounds(1,1));
                        newx=xend-x1;
                        newy=newx/tand(angle);
                        xpos(step+2)=xpos(step+1)+newx;
                        ypos(step+2)=ypos(step+1)-newy;
                    end
                end
                if layer==0
                    newx=xpos(step+2)-xpos(step+1);
                    newlength=newx/sind(angle);
                    length=length+newlength;
                else
                end
                step=step+1;
                layer=layer-1;
                if layer==numberofcladdings
                    halt=1;
                    tir='endoftrace';
                else
                    n1=eval(['n',num2str(abs(layer)),'refi']);
                    n2=eval(['n',num2str(abs(layer-1)),'refi']);
                end
        end
    case 1
        switch direction
            case 'up'
                direction='down';
                x=x+(nwidth/tand(90-angle));;
                y=y-nwidth;
                xpos(step+2)=x+xpos(2);
                ypos(step+2)=y+n0width/2;
                if xpos(step+2)>=xend
                    halt=1;
                    tir='endoftrace';
                    outofbounds=find(xpos>xend);
                    if isempty(outofbounds)
                    else
                        x1=xpos(1,outofbounds(1,1)-1);
                        x2=xpos(1,outofbounds(1,1));
                        y1=ypos(1,outofbounds(1,1)-1);
                        y2=xpos(1,outofbounds(1,1));
                        newx=xend-x1;
                        newy=newx/tand(angle);
```

```matlab
                            xpos(step+2)=xpos(step+1)+newx;
                            ypos(step+2)=ypos(step+1)-newy;
                        end
                    end
                    if layer==0
                        newx=xpos(step+2)-xpos(step+1);
                        newlength=newx/sind(angle);
                        length=length+newlength;
                    else
                    end
                    step=step+1;
                    n1=eval(['n',num2str(abs(layer)),'refi']);
                    n2=eval(['n',num2str(abs(layer-1)),'refi']);
                case 'down'
                    direction='up';
                    x=x+(nwidth/tand(90-angle));
                    y=y+nwidth;
                    xpos(step+2)=x+xpos(2);
                    ypos(step+2)=y+n0width/2;
                    if xpos(step+2)>=xend
                        halt=1;
                        tir='endoftrace';
                        outofbounds=find(xpos>xend);
                        if isempty(outofbounds)
                        else
                            x1=xpos(1,outofbounds(1,1)-1);
                            x2=xpos(1,outofbounds(1,1));
                            y1=ypos(1,outofbounds(1,1)-1);
                            y2=xpos(1,outofbounds(1,1));
                            newx=xend-x1;
                            newy=newx/tand(angle);
                            xpos(step+2)=xpos(step+1)+newx;
                            ypos(step+2)=ypos(step+1)+newy;
                        end
                    end
                    if layer==0
                        newx=xpos(step+2)-xpos(step+1);
                        newlength=newx/sind(angle);
                        length=length+newlength;
                    else
                    end
                    step=step+1;
                    n1=eval(['n',num2str(abs(layer)),'refi']);
                    n2=eval(['n',num2str(abs(layer+1)),'refi']);
            end
        end

    end

    anglein=num2str(anglein);
    anglein(findstr(anglein,'.'))='p';
    position.(['xcoord',anglein])=xpos;
    position.(['ycoord',anglein])=ypos;
    absorptionlength.(['A',anglein])=length;
end


for a=(beginangle:anglestep:endangle)
    a=num2str(a);
    a(findstr(a,'.'))='p';
    x1=position.(['xcoord',a]);
    y1=position.(['ycoord',a]);
    plot(x1,y1);
```

```matlab
    hold all
end


%Axis labels
xlabel('Distance along the waveguide ( \mum)');
ylabel('Distance from the centre ( \mum)');


hold all

%Draw material boundaries
xmarker=[0,xend];
yn1marker=[(n0width/2),(n0width/2)];
line(xmarker,yn1marker,'Linewidth',2,'Color','red');
yn1marker=[(n0width/2)+n1width,(n0width/2)+n1width];
line(xmarker,yn1marker,'Linewidth',2,'Color','red');
yn1marker=[(n0width/2)+n1width+n2width,(n0width/2)+n1width+n2width];
line(xmarker,yn1marker,'Linewidth',2,'Color','red');
yn1marker=[(n0width/2)+n1width+n2width+n3width,(n0width/2)+n1width+n2width+
n3width];
line(xmarker,yn1marker,'Linewidth',2,'Color','red');
yn1marker=[(-n0width/2),(-n0width/2)];
line(xmarker,yn1marker,'Linewidth',2,'Color','red');
yn1marker=[(-n0width/2)-n1width,(-n0width/2)-n1width];
line(xmarker,yn1marker,'Linewidth',2,'Color','red');
yn1marker=[(-n0width/2)-n1width-n2width,(-n0width/2)-n1width-n2width];
line(xmarker,yn1marker,'Linewidth',2,'Color','red');
yn1marker=[(-n0width/2)-n1width-n2width-n3width,(-n0width/2)-n1width-
n2width-n3width];
line(xmarker,yn1marker,'Linewidth',2,'Color','red');

%Set axis view
sumwidths=((n1width+n2width+n3width));
axis([0,xend,-2*sumwidths,2*sumwidths]);



%Calculating the absorption path lengh (e.g. through the core)

%Edge lengths to look at e.g. when starts and when finishes

for a=(beginangle:anglestep:endangle)
    a=num2str(a);
    a(findstr(a,'.'))='p';
    x1=position.(['xcoord',a]);
    y1=position.(['ycoord',a]);
    plot(x1,y1);
    hold all;
end
%
% if angle=='90'
%     absorptionlength.(['A',angle])=xend;
% else
% end

n=0;
for a=(beginangle:anglestep:endangle)
    ab=num2str(a);
    ab(findstr(ab,'.'))='p';
    if a==beginangle
        anglemaxlength=a;
    else
```

```matlab
        ac=num2str(a-anglestep);
        ac(findstr(ac,'.'))='p';
        if absorptionlength.(['A',ab])>absorptionlength.(['A',ac])
            anglemaxlength=a;
        end
        if absorptionlength.(['A',ab])==absorptionlength.(['A',ac])
            n=n+1
            anglemaxlength.n=a;
        end
    end
end


absorptionlength
anglemaxlength
H=figure(1);
angleofinterest=num2str(angleofinterest);
set(H,'name',['Absorption length =
',num2str(absorptionlength.(['A',angleofinterest]))]);
```

8.5.4   Trials cruise

8.5.4.1   Data error correction

```matlab
% Create figure
figure1 = figure('PaperSize',[20.98 29.68],'Color',[1 1 1]);

% Create axes
axes('Parent',figure1,'FontWeight','bold','FontSize',18,...
    'FontName','Times New Roman');
box('on');
hold('all');

clear all

load('cast003clean.mat')
data01=cast003clean;

%Frequency that the logger stored data at
freqlog=1960;

%Peaks over 32768 (e.g. +5V) in first col
overset=find(data01(:,1)>32768);
[a,b]=size(overset);
for count=1:1:a
    data01(overset(count),1)=data01(overset(count)-1,1);
end

%Peaks over 32768 (e.g. +5V) in second col
overset=find(data01(:,2)>32768);
[a,b]=size(overset);
for count=1:1:a
    data01(overset(count),2)=data01(overset(count)-1,2);
end

%Peaks under -32768 (e.g. -5V) in first col
overset=find(data01(:,1)<-32768);
[a,b]=size(overset);
for count=1:1:a
    data01(overset(count),1)=data01(overset(count)-1,1);
end
```

```matlab
%Peaks under -32768 (e.g. -5V) in second col
overset=find(data01(:,2)<-32768);
[a,b]=size(overset);
for count=1:1:a
    data01(overset(count),2)=data01(overset(count)-1,2);
end

%Convert to voltage
data01a=data01*(5/2^16)+2.5;


[sizea,sizeb]=size(data01a);
totaltime=sizea/freqlog;

%Calculate time steps
a=(0:1/freqlog:totaltime-1/freqlog)';

%Plot the results
plot(a,data01a,'LineWidth',2)

save(data01a)

axis([a(1) a(end) -1 6])

xlabel('Time (seconds)','FontWeight','bold','FontSize',24,...
    'FontName','Times New Roman')
ylabel('Voltage (volts)','FontWeight','bold','FontSize',24,...
    'FontName','Times New Roman')
```

8.5.4.2   80Hz filter

```matlab
function [Hd01]=filterload(samplerate);


Fs01=samplerate;   % Sampling Frequency


Fpass01 = 80;            % Passband Frequency
Fstop01 = 100;           % Stopband Frequency
Apass01 = 1;             % Passband Ripple (dB)
Astop01 = 90;            % Stopband Attenuation (dB)
match01 = 'passband';    % Band to match exactly




% Construct an FDESIGN object and call its BUTTER method.
h01  = fdesign.lowpass(Fpass01, Fstop01, Apass01, Astop01, Fs01);
%h02  = fdesign.highpass(Fstop02, Fpass02, Astop02, Apass02, Fs02);

Hd01 = design(h01, 'butter', 'MatchExactly', match01);
%Hd02 = design(h02, 'butter', 'MatchExactly', match);

Hd01.persistentmemory=false;
Hd01.states=1;
```

8.5.4.3   Peak to peak

```matlab
function x255000bplayload(X1,Y1)

% Create figure
```

```matlab
figure1 = figure('PaperSize',[20.98 29.68],'Color',[1 1 1]);

% Create axes
axes('Parent',figure1,'FontWeight','bold','FontSize',18,...
    'FontName','Times New Roman');
box('on');
hold('all');

clear all


%Load data file
load('x25nitrate5000b.mat');

samplerate=1960; %Samples per second
L=60; %Length of signal being used

dataA=x25nitrate5000b;
data=(dataA(samplerate*39:samplerate*41,:));
[sizea,sizeb]=size(data);

%Convert data to voltage
data01=data(1:end,:)*(5/2^16)+2.5;

%%%%%%%%%%%%%%%%%%%%%%%%%%%%%%%%%%%%%%%%%%%%%%%%%%%%%%%%%%%%%%%%%%%%%%%%

%Remove frequencies
[Hd01]=filterload(samplerate);
data02=filter(Hd01,data01);

%%%%%%%%%%%%%%%%%%%%%%%%%%%%%%%%%%%%%%%%%%%%%%%%%%%%%%%%%%%%%%%%%%%%%%%%

%Calculating total magnitude
for col=1:1:2
count=1;
for x=1:L:(sizea-L)
data02a=data02(x:x+L,col);

maxpeak=max(data02a);
minpeak=min(data02a);
mag=maxpeak-minpeak;

%Add the magnitude to the entire file
data03(count,col)=mag;
count=count+1;
end
end

a=(0:(L/samplerate):((sizea-L)/samplerate))';

stddev=std(data03)
average=mean(data03)

plot(a,data03,'LineWidth',2)

xlabel('Time','FontWeight','bold','FontSize',24,...
    'FontName','Times New Roman')
ylabel('Magnitude','FontWeight','bold','FontSize',24,...
    'FontName','Times New Roman')
```

9. REFERENCES

1 McGraw M, Stitzel SE, Cleary J, Slater C, Diamond D. Autonomous microfluidic system for phosphate detection. Talanta. 2006;71(3):1180-1185.

2 Libes SM. An introduction to marine biochemistry. John Wiley and sons; 1992.

3 Timmerman A. Phytoplankton influences on tropical climates. Geophysical research letters. 2002;29:1-4.

4 Jones LSF. Enhanced carbon dioxide uptake by the world's oceans. Energy Conversion and Management. 1996;37(6-7):1049-1052.

5 Maso M, Carces E. Harmful microalgae blooms (HAB); problematic and conditions that induce them. Marine Pollution Bulletin. 2006;53:620-630.

6 Gruber N, Galloway JN. An Earth-system perspective of the global nitrogen cycle. Nature. 2008;451:293-296.

7 Vitousek PM, Aber J, Howarth RW, Likens GE, Matson PA, Schindler DW, Schlesinger WH, Tilman GD. Human Alteration of the Global Nitrogen Cycle: Causes and Consequences. Issues in Ecology. 2000.

8 NC State University. NCSU Water Quality Group. [Internet]. 2007 Available from: http://www.bae.ncsu.edu/programs/extension/wqg/.

9 Rittmann BE, Siripong S. Diversity study of nitrifying bacteria in full scale municipal treatment. Water Research. 2007;41:1110-1120.

10 Becker EW. Microalgae: Biotechnology and microbiology. Vol 3. Cambridge: Cambridge university press; 1994.

11 Carvalho AP, Meireles LA, Malcata FX. Rapid spectrophotometric determination of nitrates. Analusis. 1998;26:347-351.

12 United Nations. United Nations Environment program (UNEP) millennium report of the environment. London: Earthscan publications; 1999.

13 Moorcroft MJ. Detection and determination of nitrate and nitrite: a review. Talanta. 2001;54:785-803.

14 Swann PF. Carcinogenic risk from nitrite, nitrates and N-nitrosamines in food. Proc R Soc Med. 1977;70:113.

15 Tarafder PK, Rathore DPS. Spectrophotomteric determination of nitrite in water. Analyst. 1988;113:1073-1076.

16 Lijinsky W, Epstein SS. Nitrosamines as Environmental Carcinogens. Nature. 1970;225:21-

23.

17 Dutt J, Davies J. Current strategies in nitrite detection and their application to field analysis. J. Environ. Monit. 2002;4:465-471.

18 Cherian T, Narayana B. A new system for the spectrophotometric determination of trace amounts of nitrite in environmental samples. Journal of the Brazilian Chemical Society. 2006;17(3):577-581.

19 Badea M, Amine A, Palleschi G, Moscone D, Volpe G, Curulli A. New electrochemical sensors for detection of nitrites and nitrates. Journal of Electroanalytical Chemistry. 2001 66-72.

20 Gabbay J, Almog Y, Davidson M, Donagi AE. Rapid Spectrophotometric micro-determination of nitrites in water. Analyst. 1977;102:371-376.

21 Miro M, Cladera A, Estela JM, Cerda V. Sequential injection spectrophotometric analysis of nitrite in natural waters using an on-line solid-phase extraction and preconcentration method. Analyst. 2000;125(5):943-948.

22 Moncada S, Higgs EA. Molecular mechanisms and therapeutic strategies related to nitric oxide. Faseb Journal. 1995;9(13):1319-1330.

23 Maeda H, Akaike EA. Nitric oxide and oxygen radicals in infection, inflammation and cancer. Biochemistry-Moscow. 1998;63(7):854-865.

24 Tsikas D. Analysis of nitrite and nitrate in biological fluids by assays based on the Griess reaction: Appraisal of the Griess reaction in the L-arginine/nitric oxide area of research. Journal of Chromatography B-Analytical Technologies in the Biomedical and Life Sciences. 2007;851(1-2):51-70.

25 Ignarro LJ, Fukuto JM, Griscavage JM, Rogers NE, Byrns RE. Oxidation of Nitric-Oxide in Aqueous-Solution to Nitrite but Not Nitrate - Comparison with Enzymatically Formed Nitric-Oxide from L-Arginine. Proceedings of the National Academy of Sciences of the United States of America. 1993;90(17):8103-8107.

26 Griess JP. Colouring matters. Journal of American Chemical Society. 1879;1(4):126-126.

27 Browning S. Potential applications for bio-sensing technology for environmental testing/monitoring.; 2008.

28 Dickey TD, Bidigare RR. Interdisciplinary oceanographic observations: the wave of the future. Scientia Marina. 2005;69(23-42):23-42.

29 Prein RD. The future of chemical in situ sensors. Marine Chemistry. 2007;107(3):422-432.

30 Dickey TD. The role of new technology in advancing ocean biogeochemical research.

Oceanography. 2001;14(4).

31 Wikipedia Foundation. Wikipedia. [Internet]. 2007 Available from: http://www.wikipedia.org.

32 Yuan-Hui L, Menviel L, Peng T. Nitrate deficits by nitrification and dentrification processes in the Indian Ocean. Deep-Sea Research I. 2005 94-110.

33 Wada E, Hattori A. Nitrite metabolism in the euphotic layer of the central north pacific ocean. Limnology and oceanography. 1971;16(5):766-772.

34 Mowlem M, Hartman S, Harrison S, Larkin KE. Intercomparison of biogeochemical sensors at ocean observatories. Research and Consultancy. Southampton: National Oceanographic Centre; 2008.

35 International Union of Pure and Applied Chemistry. Nomenclature in evaluation of analytical methods, including detection and quantification capabilities. 1995;67:1699-1723.

36 Dore JE, Karl DM. Nitrification in the euphotic zone as a source for nitrite, nitrate, and nitrous oxide at station aloha. Limnology and Oceanography. 1996;41(8):1619-1628.

37 Grunwald M, Dellwig O, Liebezeit G, Schnetger B, Reuter R, Brumsack H. A novel time-series station in the Wadden Sea (NW Germany): First results on continuous nutrient and methane measurements. Marine Chemistry. 2007;107(3):411-421.

38 Statham PJ, Connelly DP, German EB, Millard N, McPhail S, Pebody M, Perrett J, Squires M, Stevenson P, Webb A. Mapping the 3D spatial distribution of dissolved manganese in coastal waters using an in situ analyser and the autonomous underwater vehicle Autosub. Underwater Technology. 2003;25(3):129-134.

39 Whelan A, Regan F. Antifouling strategies for marine and riverine sensors. Journal of Environmental Monitoring. 2006;8(9):880-886.

40 Johnson KS, Coletti LJ. In situ ultraviolet spectrophotometry for high resolution and long-term monitoring of nitrate, bromide and bisulfide in the ocean. Deep-Sea Research Part I-Oceanographic Research Papers. 2002;49(7):1291-1305.

41 Sheldon RW, Evelyn TPT, Parsons TR. On the occurrence and formation of small particles in seawater. Limnology and Oceanography. 1967;XII(3):367-375.

42 Shilfrin KS. Physical Optics of Ocean Water. New York: American Institute of Physics; 1988.

43 Maddux WS, Kanwisher JW. An in situ particle counter. Limnology and Oceanography. 1965;10:162-168.

44 Gad-el-Hak M. MEMS: Design and Fabrication. 2nd ed. CRC; 2005.

45 Geschke O, Klank H, Telleman P. Microsystem Engineering of Lab-on-a-chip Devices. 1st

ed. Wiley-VCH; 2004.

46   Petersen W, Colijn F, Hydes D, Schroeder F. Report on the Functionality of the FerryBox Systems Onboard of the Ferries. EuroGOOS; 2002-2005.

47   British Oceanographic Data Centre. British Oceanographic Data Centre (BODC) - oceanographic and marine data. [Internet]. 2007 Available from: http://www.bodc.ac.uk/.

48   Chelsea Technolgies Group Ltd. AquaLine FerryBox System - Autonomous Environmental Measurements from Ferries. [Internet]. 2007 Available from: http://www.chelsea.co.uk/LFerryBox07.pdf.

49   Mcphail SD. Private communication [Internet]. 2008.

50   Argo Project Office. Argo, an array of profiling flaots observing the coean in real-time. [Internet]. 2006 Available from: http://w3.jcommops.org/FTPRoot/Argo/Doc/Argo_new_brochure.pdf.

51   Davis RE. Observing the General-Circulation with Floats. Deep-Sea Research Part a-Oceanographic Research Papers. 1991;38:531-571.

52   Swallaw JC. A neutral-buoyancy float for measuring deep currents. Deep-sea Research. 1955;3(1):93-104.

53   Southampton Oceanography Centre. Profiling floats at SOC. [Internet]. 2006 Available from: http://www.noc.soton.ac.uk/JRD/HYDRO/argo/index.php.

54   AIC. Argo Information Centre. [Internet]. 2008 Available from: http://wo.jcommops.org/cgi-bin/WebObjects/Argo.

55   Webb Research Corporation. Webb Research: Slocum Glider. [Internet]. 1999 Available from: http://www.webbresearch.com/slocum.htm.

56   Griffiths G, Jones CP, Ferguson J, Bose N. Undersea Gliders - ECOR Specialist Panel on Underwater Vehicles. Journal of Ocean Technology. 2007.

57   Auroux PA, Iossifidis D, Reyes DR, Manz A. Micro total analysis systems. 2. Analytical standard operations and applications. Analytical Chemistry. 2002;74(12):2637-2652.

58   Sommer L. Analytical absorption spectrophotometry in the visible and ultraviolet. Elsevier; 1989.

59   Dakin J, Culshaw B. Optical Fiber Sensors - Applications, Analysis, and Future Trends. Vol 4. Artech House; 1997.

60   Lothian GF. Absorption spectrophotometry. London: Hilger & Watts; 1958.

61   Skoog DA, Holler FJ, Nieman TA. Principles of Instrumental Analysis. Fifth Edition ed. Saunders College Publishing; 1998.

62 Shimadzu Scientific Instruments. UV-VIS Spectophotometers - UV-3600. [Internet]. 2009 Available from: http://www.ssi.shimadzu.com/products/product.cfm?product=uv3600.

63 Jasco UK limited. V-670 Research UV-Visible NIR Spectrophotometer. [Internet]. 2009 Available from: http://www.jasco.co.uk/UV_Visible_NIR_spectrophotometer.asp.

64 Spectronic Analytical Instruments. The Camspec M550 Double Beam Scanning UV/Vis Spectrophotometer. [Internet]. 2009 Available from: http://www.spectronic.co.uk/uv-vis-spectrophotometers/m550.htm.

65 Hach Company. DR 5000 UV-Vis Spectrophotometer. [Internet]. 2009 Available from: http://www.hach.com.

66 Beckman Coulter. DU® 800 UV/Visible Spectrophotometer. [Internet]. 2009 Available from: http://www.beckman.com/products/instrument/analytical/uvvis/du800_inst_dcr.asp.

67 Hitachi-hitec. U-4100 UV-Visible-NIR Spectrophotometer. [Internet]. 2009 Available from: http://www.hitachi-hitec.com/global/science/uv_vis/u4100.html.

68 Suzuki N, Kuroda R. Direct Simultaneous Determination of Nitrate and Nitrite by Ultraviolet 2nd-Derivative Spectrophotome. Analyst. 1987;112(7):1077-1079.

69 Wetters JH, Uglum KL. Direct Spectrophotometric Simultaneous Determination of Nitrite and Nitrate in Ultraviolet. Analytical Chemistry. 1970;42(3):335-.

70 Tsikas D, Rossa S, Sandmann J, Frolich JC. High-performance liquid chromatographic analysis of nitrite and nitrate in human plasma as S-nitroso-N-acetylcysteine with ultraviolet absorbance detection. Journal of Chromatography B. 1999;724(1).

71 Finch MS, Hydes DJ, Clayson CH, Weigl B, Dakin J, Gwilliam P. A low power ultra violet spectrophotometer for measurement of nitrate in seawater: introduction, calibration and initial sea trials. Analytica Chimica Acta. 1998;377(2-3):167-177.

72 Gupta RP. Remote Sensing Geology. Springer; 2003.

73 Nagashima K, Qian XX, Suzuki S. 2nd-Derivative Spectrophotometric Determination of Nitrite and Nitrate at 10-8-M Concentrations. Analyst. 1986;111(7):771-775.

74 Karpinska J. Derivative spectrophotometry - recent applications and directions of developments. Talanta. 2004;64(4):801-822.

75 Bratton C, Marshall EK. A new coupling component for sulfanilamide determination. The Johns Hopkins University; 1939.

76 Yao W, Byrne RH, Waterbury RD. Determination of Nanomolar Concentrations of Nitrite and Nitrate in Natural Waters Using Long Path Length Absorbance Spectroscopy. ENVIRONMENTAL SCIENCE & TECHNOLOGY. 1998;32(17):2646-2649.

77 AOAC. Offical Methods of Analysis. 1995. p. 8-9.

78 Rathore DPS, Tarafder PK. Journal of the Indian Chemistry Society. 1989;26:185.

79 Kaur P, Gupta VK. Journal of the Indian Chemistry Society. 1987;64:428.

80 Kaveeshwar R, Cherian L, Gupta VK. Extraction–spectrophotometric determination of nitrite using 1-aminonaphthalene-2-sulphonic acid. Analyst. 1991;116:667-669.

81 Kesari R, Gupta VK. Journal of the Indian Chemistry Society. 1998;75:416.

82 Revanasiddappa HD, Kumar K, Bilwa M. A facile spectrophotometric determination of nitrite using diazotization with p-nitroaniline and coupling with acetyl acetone. Mikrochimica Acta. 2001;137(3-4):249-253.

83 Zatar NA, Maher AA, Abdullah FE. ectrophotometric determination of nitrite and nitrate using phosphomolybdenum blue complex. Talanta. 1999;50(4):819-826.

84 Sreekumar NV, Narayana B, Hegde P, Manjunatha BR, Sarojini BK. Determination of nitrite by simple diazotization method. Microchemical Journal. 2003;74(1):27-32.

85 Revanasiddappa HD, Kiran Kumar TN. New spectrophotometric method for the determination of ntrite in water. 2001 October.

86 Sukumar C, Sunitha MB, Gupta VK. Journal of the Indian Chemistry Society. 2004;81:522.

87 Reddy MC. New reagent for determination of trace levels of nitrite in environmental samples. Journal of Scientific & Industrial Research. 2004;63(2).

88 Revanasiddappa HD, Kiran Kumar TN. A highly sensitive spectrophotometric determination of chromium using leuco Xylene cyanol FF. Talanta. 60(1):1-8.

89 Sunita S, Gupta VK. Extractive Photometric Determination of Nitrite in Polluted Water in ppm Level Using p -Nitroaniline and Guaiacol. International Journal of Environmental Analytical Chemistry. 1984;19(1):11-18.

90 Baveja AK, Jagadeesan N, Gupta VK. Extraction-spectrophotometric determination of sub-microgram amounts of nitrite using 4-nitroaniline and naphth-1-ol. Analyst. 1981;106:955-959.

91 Steimle ET, Kaltenbacher EA, Byrne RH. In situ nitrite measurements using a compact spectrophotometric analysis system. Marine Chemistry. 2002;77(4):255-262.

92 Tovar A, Moreno C, Manuel-Vez MP, Garcia-Vargas M. A simple automated method for the speciation of dissolved inorganic nitrogen in seawater. Analytica Chimica Acta. 2002;469(2):235-242.

93 Fox Jr JB. Kinetics and Mechanisms of the Griess Reaction. Analytical Chemistry. 1979 August;51(9):1493-1502.

94 Sieben VJ, Floquet CFA, Ogilivie IRG, Mowlem MC, Morgan H. Microfluidic colourimetric chemical analysis system: Application to nitrite detection. Analytical methods. 2010.

95 Richards FA, Kletsch RA. The spectrophotometric determination of ammonia and labile amino compounds in fresh and seawater by oxidation to nitrite. Seattle: University Of Washington; 1963.

96 Matsunaga K, Nishimura M. A rapid and sensitive method for determination of submicrogram amounts of ammonia in fresh and sea waters. Analytica Chimca Acta. 1974;73:204-208.

97 Adornato LR, Kaltenbacher EA, Villareal TA, Byrne RH. Continuous in situ determinations of nitrite at nanomolar concentrations. Deep-Sea Research Part I-Oceanographic Research Papers. 2005;52(3):543-551.

98 Liu RM, Wang HS, Sun AL, Liu DJ. Reversed flow injection spectrophotometric determination of trace amount of ammonia in natural water by oxidation of ammonia to nitrite. Talanta. 1997;45(2):405-410.

99 Campbell WH, Song P, Barbier GG. Nitrate reductase for nitrate analysis in water. Environmental Chemistry Letters. 2006;4(69-73).

10 Miranda KM, Espey MG, Wink DA. A Rapid, Simple Spectrophotometric Method for
0   Simultaneous Detection of Nitrate and Nitrite. NITRIC OXIDE: Biology and Chemistry. 2001;5(1):62-71.

10 Gapper LW, Fong BY, Otter DE, Indyk HE, Woollard DC. Determination of nitrite and
1   nitrate in dairy products by ion exchange LC with spectrophotometric detection. International Diary Journal. 2004;14:881-887.

10 Johnson KS, Petty RL. Determination of nitrate and nitrite in seawater by flow injection
2   analysis. Limnology and Oceanography. 1983;28(6):1260-1266.

10 Zhang JZ, Fischer CJ, Ortner PB. Comparison of open tubular cadmium reactor and packed
3   cadnium column in automated gas-segmented continous flow nitrate analysis. International Journal of Environmental Analytical Chemistry. 1999;76(2):99-113.

10 Morais IPA, Toth IV, Rangel AOSS. An overview on flow methods for the
4   chemiluminescence determination of phosphorus. Talanta. 2005;66(2):341-347.

10 Yaqoob M, Nabi A, Worsfold PJ. Determination of nanomolar concentrations of phosphate
5   in freshwaters using flow injection with luminol chemiluminescence detection. Analytica Chimica Acta. 2004;510:213-218.

10 Desouky AEH, Ripp S, Zaki S, Sayler GS. Detection of nitrate/nitrite bioavailability in

106 wastewater using a luxCDABE-based Klebsiella oxytoca bioluminescent bioreporter. Journal of Microbiology and Biotechnology. 2007;17(8):1254-1261.

107 Cox RD. Determination of Nitrate and Nitrite at the Parts per Billion Level by Chemiluminescence. Analytical Chemistry. 1980;52:332-335.

108 Garside C. A Chemi-Luminescent Technique for the Determination of Nanomolar Concentrations of Nitrate and Nitrite in Sea-Water. Marine Chemistry. 1982;11(2):159-167.

109 Ojeda CB, Rojas FS. Recent development in optical chemical sensors coupling with flow injection analysis. Sensors. 2006;6(10):1245-1307.

110 Kerouel R, Aminot A. Fluorometric determination of ammonia in sea and estuarine waters by direct segmented flow analysis. Marine Chemistry. 1997;57:265-275.

111 Fernandez-Arguelles MT, Canabate B, Costa-Fernandez JM, Pereiro R, Sanz-Medel A. Flow injection determination of nitrite by fluorescence quenching. Talanta. 2004;62(5):991-995.

112 Novak L, Neuzil P, Pipper J, Zhang Y, Lee SH. An integrated fluorescence detection system for lab-on-a-chip applications. Lab on a Chip. 2007;7(1):27-29.

113 Masserini RT, Fanning KA. A sensor package for the simultaneous determination of nanomolar concentrations of nitrite, nitrate, and ammonia in seawater by fluorescence detection. Marine Chemistry. 2000;68(4):323-333.

114 Zhang JZ. Shipboard automated determination of trace concentrations of nitrite and nitrate in oligotrophic water by gas-segmented continuous flow analysis with a liquid waveguide capillary flow cell. Deep-Sea Research Part I-Oceanographic Research Papers. 2000;47(6):1157-1171.

115 EIC Laboratories, Inc. In-Situ Monitoring of Nuclear Waste. Application summary. Norwood 2002.

116 Brewer PG, Malby G, Pasteris JD, White SN, Peltzer ET, Wopenka B, Freeman J, Brown MO. Development of a laser Raman spectrometer for deep-ocean science. Deep-Sea Research Part I-Oceanographic Research Papers. 2004;51(5):739-753.

117 Landers JP. Clinical Capillary Electrophoresis. Clinical Chemistry. 1995;41(4):495-509.

118 Morcos E, Wiklund NP. Nitrite and nitrate measurement in human urine by capillary electrophoresis. Electrophoresis. 2001;22(13):2763-2768.

119 Gaspar A, Juhasz P, Bagyi K. Application of capillary zone electrophoresis to the analysis and to a stability study of nitrite and nitrate in saliva. Journal of Chromatography A. 2005;1065(2):327-331.

120 Miyado T, Tanaka Y, Nagai H, Takeda S, Saito K, Fukushi K, Yoshida Y, Wakida S, Niki E. Simultaneous determination of nitrate and nitrite in biological fluids by capillary electrophoresis and preliminary study on their determination by microchip capillary electrophoresis. Journal of Chromatography A. 2004;1051(1-2):185-191.

121 Kim D, Goldberg IB, Judy JW. Micromachined amperometric nitrate sensor with an anion permeable membrane. Univeristy Of California; 2005.

122 Fulda MO. Detection of nitrite ion in plutonium nitrate solutions. Technical Report. Aiken: Du Pont de Nemours (E.I.) & Co.; 1958.

123 Cattarin S. Electrochemical reduction of nitrogen oxyanions in 1 M sodium hydroxide solutions at silver, copper and CuInSe2 electrodes. Journal of Applied Electrochemistry. 1992;22(11):1077-1081.

124 Nyholm L. Electrochemical techniques for lab-on-a-chip applications. Analyst. 2005;130(5):599-605.

125 Harmon RS, DeLucia FC, McManus CE, McMillan NJ, Jenkins TF, Walsh ME, Miziolek A. Laser-induced breakdown spectroscopy - An emerging chemical sensor technology for real-time field-portable, geochemical, mineralogical, and environmental applications. Applied Geochemistry. 2006;21(5):730-747.

126 Lazic V, Colao F, Fantoni R, Spizzichino V, Jovicevic S. Underwater sediment analyses by laser induced breakdown spectroscopy and calibration procedure for fluctuating plasma parameters. Spectrochimica Acta Part B-Atomic Spectroscopy. 2007;62(1):30-39.

127 Daly KL, Byrne RH, Dickson AG, Gallager SM, Perry MJ, Tivey MK. Chemical and biological sensors for time-series research: Current status and new directions. Marine Technology Society Journal. 2004;38(2):121-143.

128 Dwivedi P, Matz LM, Atkinson DA, Hill HH. Electrospray ionization-ion mobility spectrometry: a rapid analytical method for aqueous nitrate and nitrite analysis. Analyst. 2004;129(2):139-144.

129 EnviroTech LLC. NAS-3X In-Situ Nutrient Analyzer. [Internet]. 2007 Available from: http://envirotechinstruments.com/files/datasheets/nas3x.pdf.

130 Villagarcia MG. Calibration of Biogeochemical data from sensors - Nitrate. Atlantic Network of Interdisciplinary Moorings and Time series for Europe; 2005.

131 Systea S.r.l. Water chemical analyzers - In Situ Probes. [Internet]. 2006 Available from: http://www.systea.it/systea/index.php?option=com_content&task=category&sectionid=4&id=16&Itemid=28.

13 SubChem Systems, Inc. The SubChemPak Analyzer. [Internet]. 2008 Available from:
2 http://www.subchem.com/prod01.htm.

13 Chelsea Instruments Ltd. Chelsea Instruments' AQUAsensor Monitors Nitrate Levels at
3 Thames   Water.   [Internet].   2008   Available   from:
   http://www.chelsea.co.uk/AQUAsensor%20Thames%20Water%20Jan%202001.pdf.

13 Photon Systems, Inc. Targeted Ultraviolet Chemical Sensor. [Internet]. 2005 Available from:
4 http://www.photonsystems.com/sub/products/instruments.php.

13 Herold KE, Rasooly A. Lab-on-a-Chip Technology (Vol. 1): Fabrication and Microfluidics.
5 Caister Academic Press; 2009.

13 Li PCH. Microfluidic Lab-on-a-Chip for Chemical and Biological Analysis and Discovery.
6 2005.

13 Whitesides GM. The origins and the future of microfluidics. Nature. 2006;442:368-373.
7

13 Stone HA, Stroock AD, Ajdari A. Engineering flows in small devices: Microfluidics toward a
8 lab-on-a-chip. Annual review of fluid mechanics. 2004;36:381-411.

13 Adornato L, Cardenas-Valencia A, Kaltenbacher E, Byrne RH, Daly K, Larkin K, Hartman S,
9 Mowlem M, Prien RD, Garcon V. In situ nutrient sensors for ocean observing systems. 2009.

14 Mogensen KB, El-Ali J, Wolff A, Kutter JP. Integration of polymer waveguides for optical
0 detection in microfabricated chemcial analysis systems. Applied Optics. 2003;42(19):4072-
   4079.

14 Bargiel S, Górecka-Drzazga A, Dziuban JA, Prokaryn P, Chudy M, Dybko A, Brzózka Z.
1 Nanoliter detectors for flow systems. Sensors and Actuators A. 2004;115:245-251.

14 Manor R, Datta A, Dhar A, Holtz M, Berg J, Gangopadhyay S, Dasgupta P, Temkin H,
2 Veeraraghavan V, Vijayaraghavan R, et al. Microfabricated liquid core waveguides for
   microanalysis systems. In: IEEE Sensors; 2002. p. 660-664.

14 Manor R, Datta A, Ahmad I, Holtz M, Gangopadhyay S, Dallas T. Microfabrication and
3 Characterization of Liquid Core Waveguide Glass Channels Coated With Teflon AF. IEEE
   SENSORS. 2003;3(6):687-692.

14 Zhang JZ. Enhanced Sensitivity in Flow Injection Analysis Using a Long Pathlength Liquid
4 Waveguide capillary floe Cell for Spectrophotometric detection. although not commercially
   available). 2006;22:57-60.

14 Taberham A, Kraft M, Mowlem M, Morgan H. The fabrication of lab-on-chip devices from
5 fluoropolymers. J. Micromech. Microeng. 2008.

146 Chin LK, Liu AQ, Zhang JB, Lim CS, Soh YC. An on-chip liquid tunable grating using multiphase droplet microfluidics. Applied Physics Letters. 2008;93.

147 Lim J, Kim S, Choi J, Yang S. Fluorescent liquid-core/air-cladding waveguides towards integrated optofluidic light sources. Lab on a Chip. 2008;8:1580-1585.

148 Hawkins AR, Schmidt H. Optofluidic waveguides: II. Fabrication and structures. Microfluidics and Nanofluidics. 2008;4:17-32.

149 deMello AJ. Control and detection of chemical reactions in microfluidic systems. Nature. 2006;442:394-402.

150 Ottino JM, Wiggins S. Introduction: mixing in microfluidics. Philosophical Transactions of the Royal Society of London Series a-Mathematical Physical and Engineering Sciences. 2004;362(1818):923-935.

151 Schonfeld F, Hessel V, Hofmann C. An optimised split-and-recombine micro-mixer with uniform 'chaotic' mixing. Lab on a Chip. 2004;4(1):65-69.

152 Yang JT, Huang K, Lin Y. Geometric effects on fluid mixing in passive grooved micromixers. Lab on a Chip. 2005;5:1140-1147.

153 Kim DS, Lee SH, Kwon TH, Ahn CH. A serpentine laminating micromixer combining splitting/recombination and advection. Lab on a Chip. 2005;5(7):739-747.

154 Stroock AD, Dertinger SKW, Ajdari A, Mezic I, Stone HA, Whitesides GM. Chaotic mixer for microchannels. Science. 2002;295(5555):647-651.

155 Stroock AD, Dertinger SK, Whitesides GM, Ajdari A. Patterning flows using grooved surfaces. Analytical Chemistry. 2002;74(20):5306-5312.

156 Johnson TJ, Ross D, Locascio LE. Rapid microfluidic mixing. Analytical Chemistry. 2002;74(1):45-51.

157 Johnson TJ, Locascio LE. Characterization and optimization of slanted well designs for microfluidic mixing under electroosmotic flow. Lab on a Chip. 2002;2(3):135-140.

158 Fu X, Liu SF, Ruan XD, Yang HY. Research on staggered oriented ridges static micromixers. Sensors and Actuators B-Chemical. 2006;114(2):618-624.

159 Wang HZ, Iovenitti P, Harvey E, Masood S. Numerical investigation of mixing in microchannels with patterned grooves. Journal of Micromechanics and Microengineering. 2003;13(6):801-808.

160 Götze H, Gaßmann S, Pagel L. Design and Testing of static laminar diffusion mixer with convective cross mixture based on PCB technology. In: Micromechanics Europe; 2005; Göteborg. p. 334-337.

16
1   Mengeaud V, Josserand J, Girault HH. Mixing Processes in a Zigzag Microchannel: Finite Element Simulations and Optical Study. Analytical Chemistry. 2002;74(16):4279-4286.

16
2   Koch M, Chatelain D, Evans AGR, Brunnschweiler A. Two simple micromixers based on silicon. Journal of Micromechanics and Microengineering. 1998;8(2):123-126.

16
3   Chang S, Cho YH. Static micromixers using alternating whirls and lamination. Journal of Micromechanics and Microengineering. 2005;15(8):1397-1405.

16
4   Melin J, Gimenez G, Roxhed N, van der Wijngaart W, Stemme G. A fast passive and planar liquid sample micromixer. Lab on a Chip. 2004;4(3):214-219.

16
5   Zhao L, Ting W, Lefevre J, Leray I, Delaire J. Fluorimetric lead detection in a microfluidic device. Lab on a Chip. 2009;9:2818-2823.

16
6   Tiggelaar RM, Veenstra TT, Sanders RGP, Berenschot E, Gardeniers H, Elwenspoek M, Prak A, Mateman R, Wissink JM, van den Berg A. Analysis systems for the detection of ammonia based on micromachined components modular hybrid versus monolithic integrated approach. Sensors and Actuators B-Chemical. 2003;92(1-2):25-36.

16
7   Koroleff F, Grasshoff K, Ehrhardt M, Kremling K. Methods of Seawater Analysis. 2nd ed. Verlag Chemie; 1983.

16
8   Tiggelaar RM, Veenstra TT, Sanders RGP, Gardeniers JGE, Elwenspoek MC, Van den Berg A. A light detection cell to be used in a micro analysis system. Talanta. 2002;56:331-339.

16
9   Balslev S, Jorgensen AM, Bilenberg B, Mogensen KB, Snakenborg D, Geschke O, Kutter JP, Kristensen A. Lab-on-a-chip with integrated optical transducers. Lab on a chip. 2006;6(2):213-217.

17
0   Madou MJ, Lee LJ, Daunert S, Lai S, Shih CH. Design and fabrication of CD-like Microfluidic Platforms for Diagnostics: Microfluidic Functions. Biomedical Microdevices. 2001;3(3):245-254.

17
1   Madou MJ, Kellogg G. The LabCD, A centrifuge-based microfluidic platform for diagonistics. In: SPIE Proceedings; 1998.

17
2   Ducree J, Haeberle S, Lutz S, Pausch S, Stetten FV, Zengerle R. The centrifugal microflduic Bio-Disk platform. Journal of Micromechanics and Microengineering. 2007;17:103-115.

17
3   Madou MJ, Zoval J, Jia G, Kido H, Kim J, Kim N. Lab on a CD. Annual Review of Biomedical Engineering. 2006;8:601-628.

17
4   Wicht Technologie Consulting. NEXUS Market Analysis for MEMS and Microsystems III, 2005-2009. [Internet]. 2006 Available from: http://www.wtc-consult.com.

17   Tropini C. Living la vida loc(a): A brief insight into the world of "lab on a chip" and

5   microfluidics. The Science Creative Quarterly. 07-08.

17   Maluf N. An Introduction to Microelectromechanical Systems Engineering. 2nd ed. Artech
6   House Publishers; 2002.

17   Fiorini GS, Jeffries GDM, Lim DSW, Kuyper CL, Chiu DT. Fabrication of thermoset
7   polyester microfluidic devices and embossing masters using rapid prototyped
     polydimethylsiloxane molds. Lab on a Chip. 2003;3(3):158-163.

17   Lasby JB. Wafer bonding for silicon on insulator technologies. Applied Physics Letters.
8   1986;48(1):78-80.

17   Yu L, Tay FEH, Xu G, Chen B, Avram M, Iliescu C. Adhesive bonding with SU-8 at wafer
9   level for microfluidic devices. Journal of Physics: Conference Series. 2006;34:776-781.

18   Yussuf AA, Sbarski I, Hayes JP, Solomon M, Tran N. Microwave welding of polymeric-
0   microfluidic devices. Journal of Micromechanics and Microengineering. 2005;15(9):1692-
     1699.

18   McDonald JC, Duffy DC, Anderson JR, Chiu DT, Wu HK, Schueller OJA, Whitesides GM.
1   Fabrication of microfluidic systems in poly(dimethylsiloxane). Electrophoresis. 2000;21(1):27-
     40.

18   Rolland JP, Van Dam RM, Schorzman DA, Quake SR, DeSimone JM. Solvent-resistant
2   photocurable "liquid teflon" for microfluidic device fabrication. Journal of the American
     Chemical Society. 2004;126(8):2322-2323.

18   Mukhopadhyay R. When PDMS isn't the best. Analytical Chemistry. 2007 May 1 3249-3253.
3

18   Toepke MW, Beebe DJ. PDMS absorption of small molecules and consequences in
4   microfluidic applications. Lab on a Chip. 2006;6(12):1484-1486.

18   Klintberg L, Svedberg M, Nikolajeff F, Thornell G. Fabrication of a paraffin actuator using
5   hot embossing of polycarbonate. Sensors and Actuators A. 2003;103:307-316.

18   Leech PW. Hot embossing of cyclic olefin copolymers. Journal of Micromechanics and
6   Microengineering. 2009;19:1-5.

18   Toh AGG, Wang ZF, Wang ZP. Ambient hot embossing of polycarbonate,
7   polymethylmethacrylate and cyclic olefin co-polymer for micro fluidc applications. Design,
     Test, Integration and Packaging of MEMS/MOEMS. 2009.

18   Ahn CH, Choi J, Beaucage G, Nevin JH, Lee J, Puntambekar A, Lee JY. Disposable Smart
8   Lab on a Chip for Point-of-Care Clinical Diagnostics. Proceedings of the IEEE.
     2004;92(1):154-173.

18 Nikcevic I, Lee SH, Piruska A, Ahn CH, Ridgway TH, Limbach PA, Wehmeyer KR,
9 Heineman WR, Seliskar CJ. Characterization and performance of injection molded
   poly(methylmethacrylate) microchips for capillary electrophoresis. Journal of
   Chromatography A. 1154(1-2):444-453.

19 Svedberg M, Pettersson A, Nilsson S, Bergquist J, Nyholm L, Nikolajeff F, Markides K.
0 Sheathless Electrospray from Polymer Microchips. Analytical Chemistry. 2003;75(15):3934-
   3940.

19 Lamonte RR, McNally D. Cyclic Olefin Copolymers. Advanced Materials & Processes. 2001
1 March.

19 Liquidia Technologies. Perfluoropolyethersas Enabling Materials in Micro and Nano-
2 technologies [Internet]. 2005.

19 Ukita Y, Kishihara M, Kanda K, Matsui S, Mochiji K, Utsumi Y. Fabrication of
3 Poly(tetrafluoroethylene) Microparts by High-Energy X-ray-Induced Etching. Japanese
   Journal of Applied Physics. 2008;47(1):337-341.

19 Hira S, Wang Z, Yoshioka M, Zhang Y, Nobukawa Y. Study on Replication of Micro
4 Channel Structures onto Polytetrafluoroethylene (PTFE) Substrate Employing Two-Stage
   Hot Embossing. Advanced Materials Research. 2009;76-78:526-531.

19 Bhansali S, Han A, Patel M, Oh KW, Ahn CH, Henderson HT. Resolving chemical/bio-
5 compatibility issues in microfluidic MEMS systems. In: SPIE Conference on Microfluidic
   Devices and Systems II; 1999; Santa Clara. p. 101-109.

19 Rye RR, Howard AJ, Ricco AJ. Photolithographic Metallization of Fluorinated Polymers.
6 Thin Solid Films. 1995;262(1-2).

19 Wang W, Soper SA. Bio-MEMS: technologies and applications. CRC; 2006.
7

19 Koch M, Evans A, Brunnschweiler A. Microfluidic Technology and Applications. Research
8 Studies Press Ltd; 2000.

19 Kang ET, Zhang Y. Surface modification of fluoropolymers via molecular design. Advanced
9 Materials. 2000;12(20):1481-1494.

20 Paint Research Association. Surface Energy and Contact Angle Measurements on Solids.
0 [Internet]. 2001 Available from:
   http://www.pra.org.uk/technical/testingphysicalsurfacetension.htm.

20 Broughton W. Assessment of surface characterization techniques for adhesive bonding.
1 MATC (MN). 2002;24.

20 Ebnesajjad S, Khaladkar P. Fluoropolymer Applications in the Chemical Processing
2   Industries: The Definitive User's Guide and Databook. Vol s1. Plastic Design Library; 2004.

20 Boittiaux V, Boucetta F, Combellas C, Kanoufi F, Thiebault A, Delamar M, Bertrand P.
3   Surface modification of halogenated polymers 3. Influence of additives such as alkali cations
    or nucleophiles on the magnesium reductive treatment of polytetrafluoroethylene. Polymer.
    1999;40(8):2011-2026.

20 Noh I, Goodman SL, Hubbell JA. Chemical modification and photograft polymerization
4   upon expanded poly(tetrafluoroethylene). Journal of biomaterials science, Polymer edition.
    1998;9(5):407-426.

20 Marchesi JT, Ha K, garton A, Swei GS, Kristal KW. Adhesion to Sodium Napthalenide
5   Treated Fluoropolymers. Part II. Effects of Treatment conditions and Fluoropolymer
    Structure. Journal of Adhesion. 1991;36:55-69.

20 Costello CA, McCarthy TJ. Surface modification of poly(tetrafluoroethylene) with benzoin
6   dianion. Macromolecules. 1984;17(12):2940-2942.

20 Kavan L, Janda P, Weber J. Surface modification of poly(tetrafluoroethylene) by magnesium
7   amalgam. Journal of Materials Science. 2004;879(885):879-885.

20 Badey JP, Espuche E, Jugnet Y, Chabert B, Duct TM. Influence of chemical and plasma
8   treatments on the adhesive properties of PTFE with an epoxy resin. International Journal of
    Adhesion and Adhesives. 1996;16(3):173-178.

20 Rye RR, Martinez RJ. Photolithography of Polytetrafluoroethylene for Adhesion. Journal of
9   Applied Polymer Science. 1989;37(9):2529-2536.

21 Pillar Technologies. Corona, Plasma, Flame - How do you determine what's right for you?
0   [Internet]. 2007 Available from: http://www.pillartech.com/treaters/trwn11.htm.

21 Haubert K, Drier T, Beebe D. PDMS bonding by means of a portable, low cost corona
1   system. Lab on a Chip. 2006;6:1548-1549.

21 Chan CM, Ko TM, Hiraoka H. Polymer surface modification by plasmas and photons.
2   Surface Science Reports. 1996;24(1-2):3-54.

21 Bhattacharyya A, Klapperich CM. Mechanical and chemical analysis of plasma and ultraviolet-
3   ozone surface treatment for thermal bonding of polymeric microfluidic devices. Lab on a
    Chip. 2007;7:876-882.

21 Introduction to Plasma Technology. [Internet]. [cited 2008]. Available from:
4   http://www.plasmatechsystems.com.

21 Sterigenics. Material Considerations - Irradiation Processing. [Internet]. 2004 Available from:

215 http://www.sterigenics.com/library.

216 Piruska A, Nikcevic I, Lee SH, Ahn C, Heineman WR, Limbach PA, Seliskar CJ. The autofluorescence of plastic materials and chips measured under laser irradiation. Lab on a Chip. 2005;5(12):1348-1354.

217 Hawkins KR, Yager P. Nonlinear decrease of background fluorescence in polymer thin-films - a survey of materials and how they can complicate fluorescence detection in u-TAS. Lab on a Chip. 2003;3(4):248-252.

218 Olympus. Fluorescence Microscopy Interactive Java Tutorials. [Internet]. 2008 Available from: http://www.olympusmicro.com/primer/.

219 Tangram Technology Ltd. Consulting Engineers for Plastics Products. [Internet]. 2006 Available from: http://www.tangram.co.uk/.

220 Callister WD. Materials Science & Engineering - an Introduction. Wiley & Sons; 1997.

221 Woodward RP. Contact Angle Measurements Using the Drop Shape Method. Portsmouth: First Ten Angstroms.

222 Hopp B, Kokavecz J, Kresz N, Smausz T, Schieferdecker H, Döring A, Marti O, Bor O. Adhesive and morphological characteristics of surface chemically modified polytetrafluoroethylene films. Applied Surface Science. 2004;221(1-4):437-443.

223 Cubaud T, Ulmanella U, Ho C. Two-phase flow in microchannels with surface modifications. Fluid Dynamics Research. 2006;38:772-786.

224 Meng D, Kim J, Kim C. A degassing plate with hydrophobic bubbles capture and distributed venting for microfluidic devices. Journal of Micromechanics and Microengineering. 2006;16:419-424.

225 Tecan Trading AG. Tecan Group Ltd. [Internet]. 2009 Available from: http://www.tecan.com.

226 Chavagnac V. Miniaturisation of analytical techniques for oceanographic in-situ MEMS lab-on-chip devices. University Of Southampton; 2006.

227 Epigem Ltd. Microfluidic Chip Connections. [Internet]. 2008 Available from: http://www.epigem.co.uk/index.htm.

228 Prien R. Private Communication [Internet]. 2006.

229 Nakayama T, Kurosawa Y, Furui S, Kerman K, Kobayashi M, Rao SR, Yonezawa Y, Nakano K, Hino A, Yamamura S, et al. Circumventing air bubbles in microfluidic systems and

quantitative continuous-flow PCR applications. Analytical and Bioanalytical Chemistry. 2006;386(5):1327-1333.

230 Ramsey WL. Bubble growth from dissolved oxygen near the sea surface. Limnology and Oceanography. 1962 January;VII(1):1-7.

231 University of Minnesota. Dissolved Oxygen. [Internet]. 2007 Available from: http://www.waterontheweb.org/under/waterquality/oxygen.html.

232 Office of Water Quality. Correction factor for oxygen solubility and salinity. In: National Field Manual for the Collection of Water-Quality Data - Book 9. 2007.

233 Lugli F, Zerbetto F. An introduction to bubble dynamics. Physical Chemistry Chemical Physics. 2007;9:2447-2456.

234 Deep Ocean. Decompression Theory - Bubble Models. [Internet]. 2000 Available from: http://www.deepocean.net/deepocean/index.php?science04.php.

235 The Open University. 2.2 Dissolved oxygen - Potable water treatment - OpenLearn - The Open University. [Internet]. 2009 Available from: http://openlearn.open.ac.uk/mod/resource/view.php?id=185880.

236 Texas Advanced Optoelectronic Solutions. TSLB257, TSLG257, TSLR257 High Sensitivity Colour Light-To-Voltage Convertor. Data Sheet. 2001.

237 Hardy K, Pebdani P, Weber P, Sanderson J. Deep Sea Power and Light. [Internet]. 2009 Available from: http://www.deepsea.com/pdf/articles/PressureCompensatedJuly_Aug09.pdf.

238 Gong W, Mowlem M, Kraft M, Morgan H. A Simple, Low-Cost Double Beam Spectrophotometer for Colorimetric Detection of Nitrite in Seawater. IEEE SENSORS. 2009;9(7).

239 Doric Lenses Inc. AN04. fiber Coupling effeciency calculation. [Internet]. 2005 Available from: http://www.doriclenses.com/lire/40.html.

240 Mowlem M. Private Communication [Internet]. 2008.

241 Gong W. Ocean sensors for marine environmental monitoring. MPhil / PhD Transfer. University Of Southampton; 2007.

242 PerkinElmer Instruments. Specifying Lock-in Amplifiers - TN 1001. Technical Note. Wokingham 2000.

243 Bentham Instruments Ltd. Lock-in Amplifiers. Reading 2002.

24 Hasenhuetti GL, Hartel RW. Food Emulsifiers and Their Applications. 2nd ed. Springer;
4   2008.

24 Park SJ, Kim JK, Park J, Chung S, Chung C, Chang JK. Rapid three-dimensional passive
5   rotation micromixer using the breakup process. Journal of Micromechanics and
     Microengineering. 2004;14(1):6-14.

24 Wang Z, El-Ali J, Engelund M, Gotsaed T, Perch-Nielsen IR, Mogensen KB, Snakenborg D,
6   Kutter JP, Wolff A. Measurements of scattered light on a microchip flow cytometer with
     integrated polymer based optical elements. Lab Chip. 2004;4:372-377.

24 Seo J, Lee LP. Disposable integrated microfluidics with self-aligned planar microlenses.
7   Sensors and Actuators B. 2004;99:615-622.

24 Dong L, Jiang H. Tunable and movable liquid microlens in situ fabricated within microfluidic
8   channels. Applied Physics Letters. 2007;91.

24 Bennett S. Private Communication [Internet]. 2008.
9

25 Harris A. Ancillary electronics [Internet]. 2008.
0

25 Waugh E. Data logger electronics [Internet]. 2008.
1

25 Stratham PJ, Connelly DP, German CR, Brand T, Overnell JO, Bulukin E, Millard N,
2   Mcphail S, Pebody M, Perrett J, et al. Spatially Complex Distribution of Dissolved Manganese
     in a Fjord as Revealed by High-Resolution in Situ Sensing Using the Autonomous
     Underwater Vehicle Autosub. Environmental Science Technology. 2005;39:9440-9445.

25 Westheimer FH. Why nature chose phosphates. Science. 1987;235(4793):1173-1178.
3

25 Ryther JH, Dunstan WM. Nitrogen, Phosphorus, and Eutrophication in the Coastal Marine
4   Environment. Science. 1971;171(3975):1008-1013.

25 Sigmon DE, Nelson DM, Brzezinski MA. The Si cycle in the Pacific sector of the Southern
5   Ocean: seasonal diatom production in the surface layer and export to the deep sea. Deep Sea
     Research Part II: Topical Studies in Oceanography. 2002;49(9-19):1747-1763.

25 Chin CS, Johnson KS, Coale KH. Spectrophotometric Determination of Dissolved
6   Manganese in Natural Waters with 1-(2-Pyridylazo)-2-Naphthol - Application to Analysis in
     Situ in Hydrothermal Plumes. Marine Chemistry. 1992;37(1-2):65-82.

25 Zhang JZ, Fischer C, Ortner PB. Optimization of performance and minimization of silicate

7   interference in continuous flow phosphate analysis. Talanta. 1999;49:293-304.

25   Mullin JB, Riley JP. The colorimetric determination of silicate with special reference to sea

8   and natural waters. Analytica Chimica Acta. 12:162-176.